Bimetallic Metal-Organic Frameworks (MOFs) as Precursor Electrocatalysts for Enhancing the Oxygen Evolution Reaction (OER)

Inaugural thesis presented to the Faculty of Mathematics and Natural Sciences
of Heinrich Heine University of Düsseldorf
for degree of
Doctor of Philosophy (Ph.D.) in Natural Science
presented by

Thi Hai Yen Beglau
from Thanh Hoa, Vietnam

Düsseldorf, August 2024

from the ACI Section for nanoporous and nanoscale materials
of the Heinrich-Heine-University Düsseldorf

Published by permission of the Faculty of Mathematics and Natural Sciences of the Heinrich Heine University Düsseldorf

Examiners:

1. Prof. Dr. Christoph Janiak

2. Prof. Dr. Christian Ganter

Tag der mündlichen Prüfung: 08.08.2024

Eidesstaatliche Erklärung

Ich, Thi Hai Yen Beglau, versichere an Eides statt, dass die vorliegende Dissertation von mir selbstständig und ohne unzulässige fremde Hilfe unter Beachtung der „Grundsätze zur Sicherung guter wissenschaftlicher Praxis“ an der Heinrich-Heine-Universität Düsseldorf erstellt worden ist.

Die aus fremden Quellen direkt oder indirekt übernommenen Gedanken sind als solche kenntlich gemacht.

Die Arbeit wurde bisher weder im Inland noch im Ausland in gleicher oder ähnlicher Form einer anderen Prüfungsbehörde vorgelegt. Es wurden keine früheren erfolglosen Promotionsversuche unternommen.

Düsseldorf, 08.08.2024

(Ort, Datum) (Unterschrift)

Acknowledgements

First and foremost, I would like to express my heartfelt appreciation to my *Doktorvater*, Prof. Dr. Christoph Janiak, for offering me the invaluable opportunity to finish my PhD in his research group at Heinrich Heine University Düsseldorf. I am very grateful for his solid guidance, support and patience over the last three years, and also for the inspiration and scientific discussions that he provided throughout my research work.

I would also like to extend my gratitude to Prof. Dr. Christian Ganter for being my co-supervisor. My sincere thanks go to Jun-Prof. Dr. Markus Suta, Dr. Gündoğ Yücesan, Dr. Istvan Boldog, Marcus N. A. Fetzer for his unwavering scientific support and his invaluable assistance in elucidating the structures of the newly synthesized MOFs during my tenure at Heinrich Heine University Düsseldorf. Many thanks for your constructive feedback and profound discussions. I appreciate Birgit Tommes's contributions to the IR measurements, Anette Ricken's expertise in AAS measurements, and Marcell Demandt's technical support. I extend my thanks to Jutta Bourgeois for her invaluable assistance with all organizational matters.

Furthermore, I would like to express my gratitude to Dr. Ulrich Hagemann (ICAN, Duisburg University) for introducing the X-ray absorption spectroscopy methodology and assisting me with the measurements. I thank Dr. Lars Rademacher and Linda Sondermann for their guidance and support in measurements with the Gamry potentiostat/galvanostat. A special acknowledgement is due to Dr. Alex Spieß teaching me how to operate the SEM-EDX device. I thank Dr. Alex Spieß and Dr. Daniel Komisarek for their assistance with Powder X-ray diffraction measurements and Robert Oestreich's assistance in gas-sorption measurements using the BELSORP device.

I would like to extend my thanks to all members of the nano group Dr. Lars Rademacher, Dr. Dennis Woitassek, Linda Sondermann, Till Strothmann and Dr. Soheil Abdpour for the fruitful discussions and the precious advice on my research works. I learned a lot from our group seminars and frequent scientific discussions, providing me with new insight into my research topic.

I sincerely appreciate my colleagues Dr. Alex Spieß, Marcus N. A. Fetzer, Marilyn Kaul, Dr. Dennis Woschko, Dietrich Püschel, Annette Vollrath and Maximilian Vieten for making my working life so much more colourful. Your friendship has been a true gift and I'll cherish the memories we've made together. Besides, your support and encouragement have made work feel like a second home.

My gratitude also goes out to the entire AC1 group for their warm welcome, unwavering support, and the friendly atmosphere they provided. I am thankful to a multitude of individuals within the working group, with special recognition for Dr. Christian Jansen, Dr. Stefanie Bügel,

Dr. Dustin Jordan, Dr. Vasily Gvilava, Philipp Seiffert, Hanibal Othman, Tim Müller, Aysenur Limon, Dr. Vasily Gvilava, Lukas Eisenhuth, David Geller, Takin Haj Hassani Sohi, Jonas Fabrizi, Dr. Tobie Matemb Ma Ntep, Peter Ferber, Tobias Heinen, Sarah Merzenich, Julia Michalski, Abdulrahman Mohabbat, Brenda Flore Kenyim, Kenika Khotchasanthong ... for the friendly welcome at the Institute and everything else.

I would like to thank my students: Tim Malskorn and Yanyan Fei for their great contribution to the experimental works.

Last but not least, I want to thank my family in Vietnam and also my second family in Germany for their support and endless love. Thanks to them for always having faith in me and allowing me as ambitious as I wish. I would like to express my sincere gratitude to Dr. Le Chi Hieu (Associate Professor at the University of Greenwich, United Kingdom), I feel so lucky to have him as my personal tutor. He's the best supporter I could ask for. He's always there for me, encouraging me and offering his understanding and love.

The deepest gratitude goes to my husband Martin V. Beglau, who steadfastly supports my scientific dream and stands by me with encouragement and unwavering love, especially in moments of travail. I also know that no matter what happens in my life, you will always be my strongest support. Anh!, em yêu anh và cảm ơn anh rất nhiều!

Kurzfassung

Die Sauerstoffentwicklungsreaktion (OER) stellt den Engpass der elektrolytischen Wasserspaltung dar. Es besteht daher Bedarf an der Entwicklung innovativer, kostengünstiger Ansätze zur Erzeugung aktiver und langlebiger Elektrokatalysatoren auf der Grundlage häufig vorkommender Übergangsmetalloxide. Obwohl bereits zahlreiche Anstrengungen unternommen wurden, um dieses Ziel zu erreichen, erfordern die meisten Materialien mit hoher katalytischer Aktivität zeit- und energieaufwendige, mehrstufige Syntheseverfahren. Der effektivste Ansatz wäre die einstufige Herstellung hochaktiver Elektrokatalysatoren ohne komplizierte Templatbildung und energieintensive Kalzinierungsprozesse. MOFs werden als vielversprechende Ausgangsstoffe für aktive Mischmetalloxid-/hydroxid-Elektrokatalysatoren erachtet, da sie eine definierte Mischmetallzusammensetzung mit einer gleichmäßigen Verteilung der Metalle im Nanometerbereich ermöglichen.

Im Rahmen des ersten Forschungsschwerpunkts dieser Arbeit wurden die bimetallischen NiFeMOF der Formeln [(Ni,Fe)$_2$(BDC)$_2$DABCO] (BDC = 1,4-Benzoldicarboxylat, DABCO) sowie ihre modifizierten Ketjenblack (mKB)-Verbindungen durch ein einstufiges solvothermisches Verfahren hergestellt. Im Anschluss wurden die Materialien hinsichtlich ihrer Aktivität bezüglich der OER in einem alkalischen Medium (1 mol L^{-1} KOH) untersucht. Die Einbindung eines elektrisch leitfähigen mKB-Zusatzes führte zu einem synergistischen Effekt, der die katalytische Aktivität der MOF/mKB-Verbundstoffe erhöhte. Im Vergleich zu reinen MOFs und mKB zeigten alle MOF/mKB-Komposite (7, 14, 22, 34 Gew.-% mKB) eine signifikant verbesserte Leistung hinsichtlich der OER. Das Ni-MOF/mKB14-Komposit (14 Gew.-% mKB) wies bei einer Stromdichte von 10 mA cm^{-2} eine Überspannung von 294 mV und eine Tafelsteigung von 32 mV dec^{-1} auf, vergleichbar mit kommerziellem RuO_2, einem Referenzmaterial für die OER. Eine weitere Steigerung der katalytischen Leistung konnte mit dem Ni(Fe)MOF/mKB14-Komposit (0,57 Gew.-% Fe) erzielt werden, welches eine Überspannung von 279 mV bei einer Stromdichte von 10 mA cm^{-2} aufweist. Die elektrochemische Impedanzspektroskopie (EIS) ergab eine niedrige Tafelsteigung von 25 mV dec^{-1}. Die Imprägnierung des Ni(Fe)MOF/mKB14-Elektrokatalysators in kommerziell erhältlichen Nickelschaum (NF) resultierte in einer Überspannung von 291 mV, welche über einen Zeitraum von 30 Stunden bei einer Stromdichte von 50 mA cm^{-2} aufrechterhalten wurde. Besonderes Augenmerk wurde auf die Aufklärung der *in situ* Umwandlung von Ni(Fe)DMOF in OER-aktives α/β-$Ni(OH)_2$ sowie β/γ-NiOOH und FeOOH mit der von der MOF-Struktur teilweise beibehaltenen Porosität gelegt. Diese konnte durch PXRD, FTIR, SEM und N_2-Sorptionsanalyse bestätigt werden. Die Nickel-Eisen-Katalysatoren, die die Porositätsstruktur des MOF-Vorläufers nutzen, weisen eine überlegene katalytische Aktivität und Langzeitstabilität in der OER auf und übertreffen aufgrund von Synergieeffekten Katalysatoren auf reiner Ni-Basis. Des Weiteren ermöglicht die Integration von mKB als leitfähiges

Kohlenstoffadditiv in die MOF-Struktur den Aufbau eines homogenen Netzwerks, welches im Vergleich zum reinen MOF eine erhöhte elektrische Leitfähigkeit aufweist. Das elektrokatalytische System, das auf der Basis der häufig vorkommenden Metalle Ni und Fe entwickelt wurde, ist vielversprechend für die Entwicklung effizienter, praktischer und wirtschaftlicher Energieumwandlungsmaterialien hinsichtlich der OER.

Im Rahmen eines weiteren Forschungsprojektes konnten zwei neue isotypische halbleitende Metallphosphonatgerüste Co_2[1,4-NDPA] und Zn_2[1,4-NDPA] (1,4-NDPA4 ist 1,4-Naphthalindiphosphonat) präsentiert werden. Die optischen Bandlücken von Co_2[1,4-NDPA] und Zn_2[1,4-NDPA] liegen bei 1,7 bzw. 2,5 eV und befinden sich somit im halbleitenden Bereich. Der aus Co_2[1,4-NPDA] als Präkatalysator abgeleitete Elektrokatalysator erreichte bei der Sauerstoffentwicklungsreaktion (OER) eine niedrige Überspannung von 374 mV bei einer Stromdichte von 10 mA cm^{-2} und einer Tafelsteigung von 43 mV dec^{-1} im alkalischen Elektrolyten (1 mol L^{-1} KOH), was für eine bemerkenswert gute Reaktionskinetik spricht. Die OER Aktivität von Co_2[1,4-NPDA]-Materialien als Präkatalysator in Verbindung mit Nickelschaum (NF) zeigte eine bemerkenswerte Langzeitstabilität bei einer Stromdichte von 50 mA cm^{-2} verglichen mit dem aktuellen Stand der Technik Pt/C/RuO_2@NF nach 30 h in 1 mol L^{-1} KOH. Zur weiteren Ergründung des OER-Mechanismus wurde die Umwandlung von Co_2[1,4-NPDA] in seine elektrokatalytisch aktive Spezies untersucht.

Der letzte Forschungsschwerpunkt umfasst eine Reihe von monometallischen Ni-, Co- und Zn-MOFs sowie bimetallischen NiCo-, NiZn- und CoZn-MOFs der Formeln $M_2(BDC)_2DABCO$ und $(M,M')_2(BDC)_2DABCO$ (M, M' = Metall), die alle die gleichen Säulen- und Schicht-Linker DABCO und BDC beinhalten, welche durch eine schnelle mikrowellenunterstützte thermische Umwandlungssynthesemethode (MW) innerhalb von nur 12 Minuten hergestellt wurden. Die mono- und bimetallischen MOFs wurden ausgewählt, um die katalytische Aktivität der von ihnen abgeleiteten Metalloxide/Hydroxide für die Sauerstoffentwicklungsreaktion (OER) systematisch zu untersuchen. Unter den untersuchten bimetallischen MOF-Katalysatoren zeigt der NiCoMOF die höchste katalytische Aktivität für die Sauerstoffentwicklungsreaktion (OER) mit der niedrigsten Überspannung von 301 mV und einer Tafelsteigung von 42 mV dec^{-1} bei einer Stromdichte von 10 mA cm^{-2}, was mit kommerziell erhältlichem RuO_2 vergleichbar ist, das üblicherweise als Referenzmaterial für die OER verwendet wird. Die Untersuchung erfolgte an einer Glaskohlenstoffelektrode (GCE) in einem 1 mol L^{-1} KOH-Elektrolyten. Darüber hinaus wurde NiCoMOF in situ auf der Oberfläche von Nickelschaum (NF) mit unterschiedlichen Massenbeladungen durch MW-Synthese in nur 25 min synthetisiert. Dabei wurden Überspannungen von 313 und 328 mV bei Stromdichten von 50 bzw. 300 mA cm^{-2} erzielt. Zudem weist das Material eine hervorragende Langzeitstabilität für praktische OER-Anwendung auf. Die niedrige Tafel-Steigung von 27 mV dec^{-1} sowie der niedrige Reaktionswiderstand aus der elektrochemischen Impedanzspektroskopie (EIS) (R_{far} = 2 Ω)

bestätigen die hervorragende OER-Leistung dieses NiCoMOF/NF-Komposits. Die dargestellten Ergebnisse belegen nicht nur die Möglichkeit, die Eigenschaften von MOFs durch den Einbau eines zweiten Metalls in die MOF-Struktur maßzuschneidern, sondern auch die Eignung der Mikrowellenerwärmung als neue Strategie für die Entwicklung vielversprechender hocheffizienter in situ gewachsener Elektrokatalysatoren auf leitfähigen Substraten für praktische Anwendungen. In der vorliegenden Studie wird zudem die Umwandlung des NiCoMOF-Precursors von ungeordneter α- in geordnete β-$(NiCo)(OH)_2$ über einen Zeitraum von zwei Stunden untersucht, bei welcher es sich vermutlich um die aktive Spezies in der OER handelt. Das einfache, schnelle und kontrollierbare MW-Synthesekonzept ist sehr flexibel und kann auch auf verschiedene strukturierte Materialien, einschließlich verschiedener Arten von MOFs, ausgedehnt werden, welche für die Wasserspaltung eingesetzt werden können. Dadurch eröffnet sich ein großes Potenzial für die praktische Kommerzialisierung des Prozesses.

Abstract

The oxygen evolution reaction (OER) is considered the bottleneck of electrolytic water-splitting. Thus, there is a need for the development of innovative, low-cost approaches to design active and durable electrocatalysts based on abundant transition metal oxides. Although much effort has been devoted to this goal, most materials reported with high catalytic activity require time and energy-demanding, multi-step synthetic approaches. The most effective strategy would be the one-step preparation of highly active electrocatalysts without any complicated templating and energy-intensive calcination processes. Metal-organic frameworks (MOFs) are considered to be good precursors for active mixed-metal oxide/hydroxide electrocatalysts, as they allow to achievement of a defined mixed-metal composition with a uniform distribution of metals at the nanoscale.

In the first research focus of this work its bimetallic nickel-iron counterpart [Ni(Fe)(BDC)$_2$DABCO], (BDC = 1,4-benzenedicarboxylate, DABCO = 1,4-diazabicyclo[2.2.2]octane).and their modified Ketjenblack (mKB) composites through a facile one-step solvothermal method. These materials were then evaluated for their performance in the OER in an alkaline medium (1 mol L^{-1} KOH). The incorporation of a conductive mKB additive resulted in a synergistic effect, enhancing the catalytic activity of the MOF/mKB composites. Compared to individual MOFs and mKB, all MOF/mKB composite samples (7, 14, 22, 34 wt.% mKB) exhibited significantly improved OER performance. Notably, the Ni-MOF/mKB14 composite (14 wt.% mKB) demonstrated an overpotential of 294 mV at a current density of 10 mA cm^{-2} and a Tafel slope of 32 mV dec^{-1}, comparable to commercial RuO_2, a benchmark material for OER. Further enhancement in catalytic performance was achieved with the Ni(Fe)MOF/mKB14 composite (0.57 wt% Fe), showing an overpotential of 279 mV at a current density of 10 mA cm^{-2} and a low Tafel slope of 25 mV dec^{-1}, corroborated by electrochemical impedance spectroscopy (EIS) measurements. Impregnating the Ni(Fe)MOF/mKB14 electrocatalyst into commercial nickel foam (NF) resulted in overpotentials of 291 mV and maintained for 30 hours at a current density of 50 mA cm^{-2}. Importantly, this work elucidates the in situ transformation of Ni(Fe)DMOF into OER-active α/β-$Ni(OH)_2$, β/γ-NiOOH, and FeOOH with residual porosity inherited from the MOF structure, as confirmed by PXRD, FTIR, SEM and N_2 sorption analysis. Leveraging the porosity structure of the MOF precursor, the nickel-iron catalysts exhibit superior catalytic activity and long-term stability in OER, outperforming solely Ni-based catalysts due to synergistic effects. Additionally, the introduction of mKB as a conductive carbon additive in the MOF structure enables the construction of a homogeneous conductive network, improving the electronic conductivity of the MOF/mKB composites. This earth-abundant Ni and Fe-based electrocatalytic system holds promise for the development of efficient, practical and economical energy conversion materials for OER activity.

Furthermore, we report two new isotypic semiconductive metal phosphonate frameworks Co_2[1,4-NDPA] and Zn_2[1,4-NDPA] (1,4-$NDPA^{4-}$ is 1,4-naphthalenediphosphonate). Co_2[1,4-NDPA] and Zn_2[1,4-NDPA] have optical bandgaps of 1.7 eV and 2.5 eV respectively, are within the semiconductive regime. The electrocatalyst derived from Co_2[1,4-NPDA] as a precatalyst generated a lower overpotential of 374 mV in the OER with a Tafel slope of 43 mV dec^{-1} at a current density of 10 mA cm^{-2} in the alkaline electrolyte (1 mol L^{-1} KOH), which is indicative of remarkably superior reaction kinetics. The OER of Co_2[1,4-NPDA] materials as precatalyst coupled with NF showed exceptional long-term stability at a current density of 50 mA cm^{-2} for water splitting compared to the state-of-the-art Pt/C/RuO_2@NF after 30 h in 1 mol L^{-1} KOH. To further understand the OER mechanism, the transformation of Co_2[1,4-NPDA] into its electrocatalytical active species was investigated.

The last research focus, a series of monometallic Ni-, Co- and Zn-MOFs and bimetallic NiCo, NiZn- and CoZn-MOFs of formula $M_2(BDC)_2DABCO$ and $(M,M')_2(BDC)_2DABCO$ (M, M' = metal) with the same pillar and layer linkers DABCO and BDC were prepared through a fast microwave-assisted thermal conversion synthesis method (MW) within only 12 min. The mono- and bimetallic MOFs were selected to systematically explore the catalytic activity of their derived metal oxide/hydroxides for the OER. Among all tested bimetallic MOF-derived catalysts, the NiCoMOF exhibits superior catalytic activity for the OER with the lowest overpotentials of 301 mV and Tafel slopes of 42 mV dec^{-1} on a glassy carbon electrode (GCE) in 1 mol L^{-1} KOH electrolyte at a current density of 10 mA cm^{-2}, which is comparable with commercial RuO_2 commonly used as a benchmark material for OER. In addition, NiCoMOF was in situ grown in just 25 min by the MW synthesis on the surface of NF with different mass loadings, where overpotentials of 313 and 328 mV at current densities of 50 and 300 mA cm^{-2}, respectively, were delivered and superior long-term stability exists for practical OER application. The low Tafel slope of 27 mV dec^{-1} as well as a low reaction resistance from EIS measurement (R_{far} = 2 Ω) confirm the excellent OER performance of this composite NiCoMOF/NF. These promising results not only prove that the properties of MOFs can be tailored by the incorporation of a second metal into the MOF structure but also that microwave heating presents a new strategy for developing promising highly efficient in situ grown electrocatalysts on conductive substrates for practical applications. In this study, we also follow the NiCoMOF precursor conversion over disordered α- to ordered β-$(NiCo)(OH)_2$ over the time period of 2 hours which probably presents the active species in the OER. The simple, rapid and controllable MW synthetic concept is very flexible and also can be extended to various structured materials including different types of MOFs to be applied for water-splitting, which has great potential for practical commercialization of the process as well.

List of publications

This cumulative dissertation was completed between February 2021 and July 2024 at the Institute of Inorganic Chemistry and Structural Chemistry I of the Heinrich Heine University Düsseldorf under the supervision of Prof Dr Christoph Janiak. This work resulted from the following publications:

First authorships:

(1) Beglau, T.H.Y.; Rademacher, L.; Oestreich, R.; Janiak, C., Synthesis of Ketjenblack Decorated Pillared Ni(Fe) Metal-Organic Frameworks as Precursor Electrocatalysts for Enhancing the Oxygen Evolution Reaction. *Molecules* ***2023****, 28,* 4464. doi:10.3390/molecules28114464.

(2) Beglau, T.H.Y.; Fetzer, M.N.A.; Boldog, I.; Heinen, T.; Suta, M.; Janiak, C.; Yücesan, G. Exceptionally stable and super-efficient electrocatalysts derived from semiconducting metal phosphonate frameworks. *Chem. Eur. J.* **2023**, e202302765, doi:10.1002/chem.202302765.

(3) Beglau, T.H.Y.; Fei, Y. ; Janiak, C. Microwave-assisted ultrafast Synthesis of Bimetallic Nickel-Cobalt Metal-Organic Frameworks for Application in the Oxygen Evolution Reaction. *Chem. Eur. J.* **2024***, e202401644.* doi:10.1002/chem.202401644.

Co-authorships:

(4) Menzel, S.; Heinen, T.; Boldog, I.; Beglau, T. H. Y.; Xing, S.; Spieß, A.; Woschko, D.; Janiak, C. Metal–organic framework structures of fused hexagonal motifs with cuprophilic interactions of a triangular Cu(i)3(pyrazolate-benzoate) metallo-linker. *CrystEngComm* **2022**, *24* (20), 3675–3691. doi:10.1039/D2CE00268J.

(5) Rademacher, L.; Beglau, T. H. Y.; Karakas, Ö.; Spieß, A.; Woschko, D.; Heinen, T.; Barthel, J.; Janiak, C. Synthesis of tin nanoparticles on Ketjen Black in ionic liquid and water for the hydrogen evolution reaction. *Electrochem.commun.* **2022**, 136, 107243. doi:10.1016/j.elecom.2022.107243.

(6) Rademacher, L.; Beglau, T. H. Y.; Heinen, T.; Barthel, J.; Janiak, C. Microwave-assisted synthesis of iridium oxide and palladium nanoparticles supported on a nitrogen-rich covalent triazine framework as superior electrocatalysts for the hydrogen evolution and oxygen reduction reaction. *Front. Chem.* **2022**, 10. doi:10.3389/fchem.2022.945261.

(7) Bügel, S.; Hähnel, M.; Kunde, T.; Sousa Amadeu, N. de; Sun, Y.; Spieß, A.; Beglau, T. H.Y; Schmidt, B. M.; Janiak, C. Synthesis and Characterization of a Crystalline Imine-Based Covalent Organic Framework with Triazine Node and Biphenyl Linker

and Its Fluorinated Derivate for CO_2/CH_4 Separation. *Materials* **2022**, *15* (8). doi:10.3390/ma15082807.

(8) Ghasemzadeh, S.; Hosseini-Monfared, H.; Ghorbanloo, M.; Beglau, T. H. Y.; Rademacher, L.; Spieß, A.; Woschko, D.; Janiak, C. Scalable synthesis of SWCNT via CH_4/N_2 gas: The effects of purification on photocatalytic properties of CNT/TiO_2 nanocomposite. *J. Environ. Chem. Eng.* **2022**, *10* (5), 108440. doi:10.1016/j.jece.2022.108440.

(9) Tholen, P.; Wagner, L.; Ruthes, J. G. A.; Siemensmeyer, K.; Beglau, T. H. Y.; Muth, D.; Zorlu, Y.; Okutan, M.; Goldschmidt, J. C.; Janiak, C.; Presser, V.; Yavuzçetin, Ö.; Yücesan, G. A New Family of Layered Metal-Organic Semiconductors: Cu/V-Organophosphonates. *Small* **2023**, *19* (47), 2304057. doi:10.1002/smll.202304057.

(10) Abdpour, S.; Rademacher, L.; Fetzer, M. N. A.; Beglau, T. H. Y; Janiak, C. Iron-Containing Nickel Cobalt Sulfides, Selenides, and Sulfoselenides as Active and Stable Electrocatalysts for the Oxygen Evolution Reaction in an Alkaline Solution. *Solids* **2023**, *4* (3), 181–200. doi:10.3390/solids4030012.

(11) Fouda, J. Y. S.; Ntoumba, A. A.; Kedi, P. B. E.; Beglau, T. H. Y.; Fetzer, M.; Strothmann, T.; Florian, T. A.; Bertin, S. E.; Deli, V.; Mbosso, E. J. T. Impregnation of textile cotton material with Cymbopogon citratus-mediated silver nanoparticles and investigations by light, electron and hyperspectral microscopies. *J. Pharmacogn. Phytochem.* **2023**, *12* (5), 135–146. doi:10.22271/phyto.2023.v12.i5b.14722.

(12) Fokou, J. B. H.; Nsegbe, A. C.; Beglau, T. H. Y; Fetzer, M. N. A.; Mbogbe, E. N.; Nkouankam, M. J. C.; Mponge, P. N.; Balłeng, Marie Tryphene Magaly Ngo Yomkil; Songue, S. P.; Kuissi, C. R. N. Anti-inflammation study of cellulose-chitosan biocomposite-based Tetrapleura tetraptera (Taub) dried fruits aqueous extract, *BioNanoSci.* **2024**. doi:10.1007/s12668-024-01364-6.

(13) Rademacher, L.; Beglau, T. H. Y.; Ali, B.; Sondermann, L.; Strothmann, T.; Boldog, I.; Barthel, J.; Janiak, C. Ruthenium nanoparticles on covalent triazine frameworks incorporating thiophene for the electrocatalytic hydrogen evolution reaction. *Journal of J. Mater. Chem. A* **2024**, *12* (4), 2093–2109. doi:10.1039/D3TA05597C.

(14) Abdpour, S.; Fetzer, M. N. A.; Oestreich, R.; Beglau, T. H. Y.; Boldog, I.; Janiak, C. Bimetallic CPM-37(Ni,Fe) metal–organic framework: enhanced porosity, stability and tunable composition. *Dalton Trans.* **2024,** *53*, 4937-4951.doi:10.1039/D3DT03695B.

(15) Sondermann, L.; Smith, Q.; Strothmann, T.; Vollrath, A.; Beglau, T. H. Y.; Janiak, C. Mechanochemical synthesis and application of mixed-metal copper–ruthenium HKUST-1 metal–organic frameworks in the electrocatalytic oxygen evolution reaction. *RSC Mechanochem.* **2024.** doi:10.1039/D4MR00021H.

List of abbreviations

Symbol	Definition
MOFs	Metal-Organic Framework(s)
DABCO	1,4-diazabicyclo[2.2.2]octane
H_2BDC	1,4-benzenedicarboxylate
1,4-$NDPA^{4-}$	1,4-naphthalenediphosphonate
DMF	Dimethylformamide
DMSO	Dimethylsulfoxide
KB	KetjenBlack
mKB	modified Ketjenblack
Pt/C	Platinum on activated carbon
CNT(s)	Carbon nanotube(s)
MWCNT(S)	Multi-Walled Carbon Nanotubes
LDH	Layered Double Hydroxides
η	Overpotential
θ	Diffraction angle or Bragg angle
Ω	Electrical resistance
°C	Celsius Degrees
Å	Ångström (10^{-10} m)
A	Ampere
a.u.	arbitrary unit
b	Tafel-Slope
cm	Centimetre (10^{-2}m)
h	Hour
E	Potential
eV	Electron volt
F	Faraday- constant
g	gram
G	Free enthalpy or Gibbs energy
wet.%	weight percent
L	Liter
m	Meter
mA	Milliampere (10^{-3} A)
mbar	Millibar (10^{-3} bar)
mg	Milligram (10^{-3} g)
min	Minute
mmol	Millimol (10^{-3} mol)
mol	Mol
mV	Millivolt (10^{-3} V)
nm	Nanometer (10^{-9} m)
µL	Mikroliter (10^{-6} L)
ppm	parts per million
rpm	rounds per minute
s	Second
T	Temperature
V	Volt

W	Watt
z	Electron number
AAS	Atomic absorption spectrometry
BET	Brunauer-Emmett-Teller
COD	Crystallography Open Database
CHNS	Elemental analysis
CV	Cyclic voltammetry
EDX	Energy-Dispersive X-Ray Spectroscopy
EIS	Electrochemical Impedance Spectroscopy
PXRD	Powder X-ray diffraction
OER	Oxygen Evolution Reaction
HER	Hydrogen Evolution Reaction
HOR	Hydrogen Reduction Reaction
FTIR	Fourier-transform infrared spectroscopy
IUPAC	International Union of Pure & Applied Chemistry
LSV	Linear Sweep Voltammetry
M	Metal
MS	Mass Spectrometry
NMR	Nuclear Magnetic Resonance Spectroscopy
NLDFT	Non-linear Density Functional Theory
OCV	Open Circuit Potential
ORR	Oxygen Reduction Reaction
RD-GCE	Rotating-Disk Glassy Carbon Electrode
SEM	Scanning Electron Microscopy
RHE	Reversible Hydrogen Electrode
PXRD	Powder X-ray Diffraction
SHE	Standard Hydrogen Electrode
TGA	Thermogravimetric Analysis
XPS	X-Ray Photoelectron Spectroscopy

Table of Contents

1. Introduction

1.1. Electrocatalysis

The growing energy crises and environmental degradation have intensified the search for renewable and green energy sources as viable alternatives to fossil fuels.[1,2] According to the "Renewables Global Status Report 2024 Collection," despite their significant environmental impact and the economic and political dependence on their market, fossil fuels accounted for over 80% of total energy consumption in 2022.[3] This highlights the pressing necessity to develop essential novel methods and materials for enhancing the efficiency, sustainability, and environmental friendliness of energy-intensive chemical and energy-producing processes.[4] Despite the considerable potential of alternative energy technologies such as geothermal, hydro, wind, solar, and tidal, they are occasionally constrained by climatic and geographic factors.[5] The dependability of the electrical grid is adversely affected by the drawback of intermittency.[6] Hydrogen energy has received significant attention as a prospective energy transporter and storage medium due to its high energy density and inexpensive, abundant supply. Hydrogen energy has gained considerable attention as a potential energy carrier and storage medium due to its high energy density and abundant and inexpensive supply. From a technical perspective, water splitting is seen as a promising method for hydrogen production because of its numerous advantages, including the abundance of resources, the absence of greenhouse gas emissions and the high efficiency of the process.[7,8] The International Energy Agency (IEA) predicts that the market share of hydrogen production through electrocatalytic water splitting by 2030 is expected to reach approximately 50% larger than it was at the time of 2022.[9] Over the past few decades, steam methane reforming and water-gas shift reactions have met the demand for hydrogen. However, the water electrolysis method only becomes competitive when electricity prices are low.[10] The field of electrocatalytic water splitting has recently garnered significant interest, largely due to the introduction of the "hydrogen economy" concept. Water splitting involves two half-reactions: water reduction at the cathode for the hydrogen evolution reaction (HER) and water oxidation at the anode for the oxygen evolution reaction (OER) and this is important in terms of energy production.[11] Thermodynamic equilibrium voltage indicates that, under standard conditions (1 bar and 25°C), a voltage of 1.23 V is required to electrolyze water into hydrogen and oxygen.[12] However, in practice, even with an excellent catalyst, a significantly larger overpotential is necessary.[13] Therefore, developing efficient, stable, and affordable electrocatalysts is crucial for the large-scale industrial application.[14]

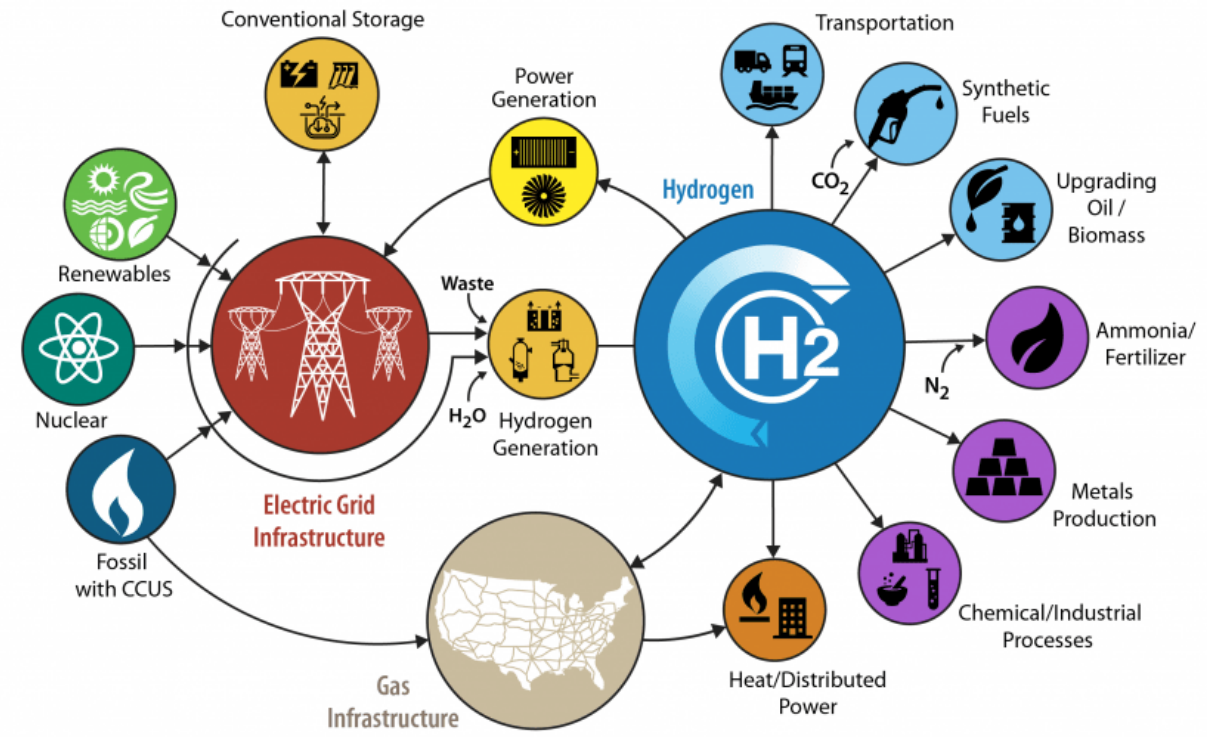

Figure 1. Multiple proposals for the production routes and applications of renewable hydrogen and electricity: concept at the foundation of a sustainable hydrogen economy. *Reproduced with permission from ref.*[15]

Electrocatalysis is a promising technology for storing and converting renewable energies. It offers sustainable ways of producing chemical-based materials and fuels (Figure 1).[16] As mentioned above, the electrochemical splitting of water (H_2O) to produce hydrogen (H_2) and oxygen (O_2) is a promising green pathway that is perfectly aligned with the clean energy technologies of the future.[17] Furthermore, the recent development in fuel cell and metal-air battery research has led to rapid progress in the hydrogen oxidation reaction (HOR), the oxidation of reduced nitrogen compounds (ORR), CO_2 reduction reaction (CO_2RR) and N_2 reduction into valuable base chemicals (e.g. methanol, ammonia and light olefins).[18] The use of platinum and/or other noble metals is particularly relevant to achieving benchmark electrocatalyst performance through stable, robust electrocatalysts. The search for cost-effective, powerful and stable electrocatalysts which do not require the use of valuable noble group metals is currently of great importance in realising the HER and OER pair.[19,20] Using sustainable electrochemical methods to produce synthetic chemicals and replace fossil resources will allow us to minimize CO_2 emissions which is considered as an affordable and clean energy strategy (Figure 2). To achieve a sustainable hydrogen-centric energy industry, it is crucial to advance energy-efficient and cost-effective electrocatalysts designed for electrolysers and fuel cells.[21]

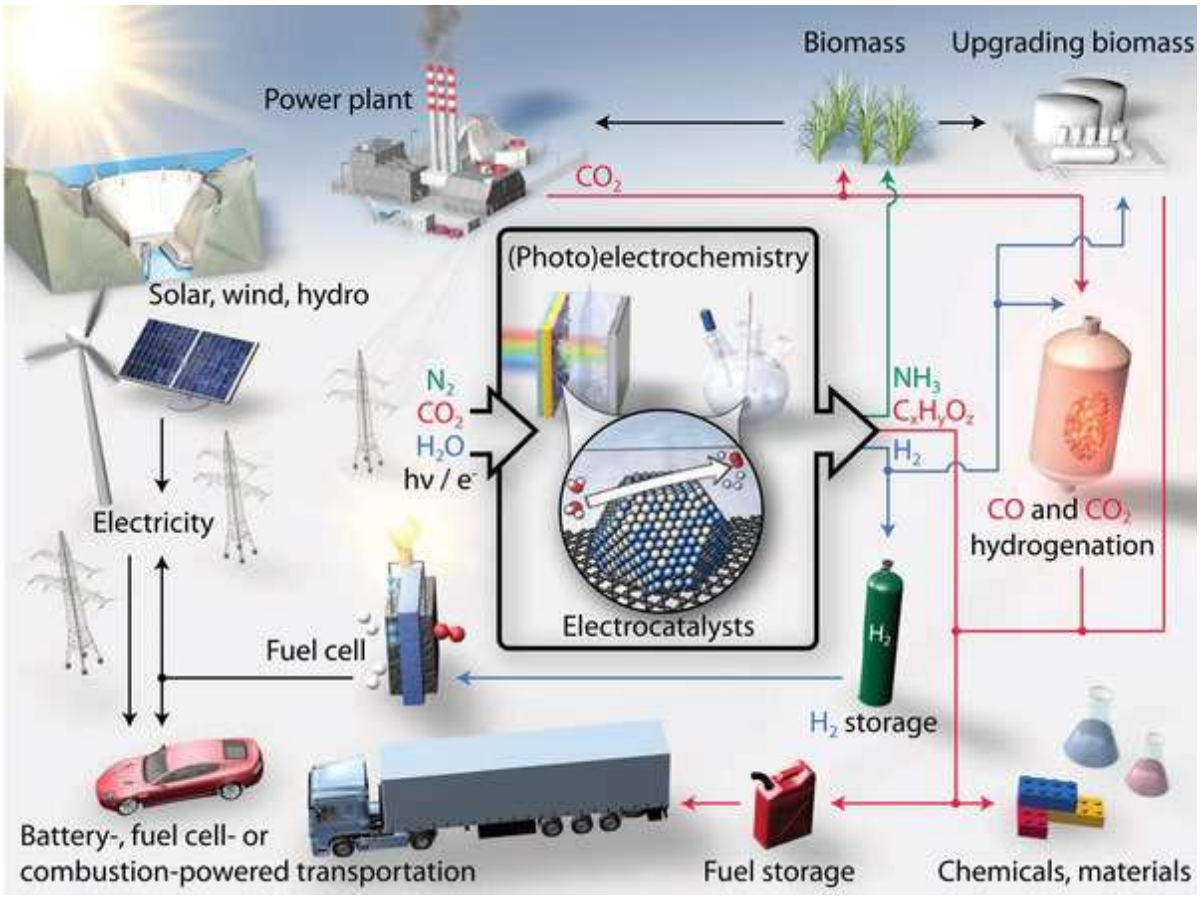

Figure 2. Schematic of hydrogen production methods and application in the fuel cell. *Reproduced with permission from ref.*[22]*. Copyright © 2017, Science.*

1.1.1. Electrochemical water splitting

For hydrogen production by electrochemical conversion of water to oxygen and hydrogen, the free energy of ΔG 238 kJ mol^{-1} is required for the reaction (eqn (1)).

Overall Water Splitting

$$2H_2O \rightarrow 2H_2 + O_2 \quad (1)$$

Water splitting includes two half-reactions, water reduction at the cathode for the HER and water oxidation for the OER at the cathode.[23,24]

Cathode (HER):

$$2\,H^+ + 2e^- \rightarrow H_2 \qquad (E^0_{Reduction} = 0.00\ V) \quad (2)$$

Anode (OER):

$$2H_2O \rightarrow O_2 + 4H^+ + 4e^- \qquad (E^0_{Oxidation} = 1.23\ V) \quad (3)$$

OER in particular requires significantly more energy than HER due to comparably more intermediates and reaction steps involved.[25] Despite recent advances, OER remains a significant challenge in overall water splitting. Consequently, there has been a concerted effort in recent years to identify alternative materials that can effectively reduce the kinetic limitation of OER and enable optimal reaction conditions.[26] Both reactions occur at the electrode surface (anode and cathode) with the electrolyte which requires consideration of the inner and outer

Helmholtz layers.[27] The performance of these reactions can be quantified and evaluated separately using electrochemical techniques, which can be employed to determine the precise values of the applied potentials.[28] In this context, the electrochemical HER and OER can be expressed in terms of two redox pairs. In the case of the OER, the reduced form of water (H_2O) and the oxidised form of oxygen (O_2) form the redox couple (O_2/H_2O). Similarly, the HER is composed of the reduced form of hydrogen (H_2) and the oxidised form of the proton (H^+), which forms the redox couple (H^+/H_2). Each of the two redox systems exhibits varying degrees of reducing and oxidising power, as described in Equations (2) and (3). These redox systems can be described electrochemically by the redox potential E of the redox system.[29] The redox potential is described mathematically by the Nernst equation (see Equation (4))[30]

$$\mathrm{E} = E^0 + \frac{R \cdot T}{z \cdot F}\, ln \frac{c_{Ox}}{c_{Red}} \qquad (4)$$

E^0 is the formal potential of the overall reaction, the constant *z* describes the number of electrons occurring in the redox system, R is the ideal gas constant, F is the Faraday constant and c_{Oxi} and c_{Red} are the concentration of the oxidized and reduced reagents, respectively.[36] The standard potentials are characteristic of each redox system which serve to quantify the reductive or oxidative effect of a given system, thereby indicating whether electrons are being absorbed or released. Only the total potential of a galvanic element can be measured, while the potential difference between two redox pairs can be determined relative to an overpotential.[29]

The reaction process is essentially determined by the pH value of the electrolyte and the catalyst material.[31]

<u>In Alkaline Solution:</u>

$$2H_2O + 2e^- \rightarrow H_2 + 2OH^- \quad (\text{HER at the cathode}) \qquad (5)$$

$$4OH^- \rightarrow O_2 + 2H_2O + 4e^- \quad (\text{OER at the anode}) \qquad (6)$$

<u>In Acid Solution:</u>

$$4H^+ + 4e^- \rightarrow 2H_2 \quad (\text{HER at the cathode}) \qquad (7)$$

$$2H_2O \rightarrow O_2 + 4H^+ + 4e^- \quad (\text{OER at the anode}) \qquad (8)$$

At present, the precious metals platinum, iridium, rhodium and rhenium catalysts exhibit the best electrocatalysis performance in most cases. However, their high cost and limited availability question their large-scale application. It is therefore important to develop earth-abundant, non-noble metal-based catalysts.[32] Many strategies and compounds have been explored in the past decade to develop efficient and affordable electrocatalysts, such as transition metal compounds, carbon-based or heteroatom-doped carbon materials, and conducting polymers.[33,34,35]

1.1.2. Oxygen evolution reaction (OER)

1.1.2.1. Reaction Mechanism and Kinetics

The anodic-half-cell reaction, OER is a far more complex process, which involves either four-electron ($4e^-$) or two-step two-electron ($2e^-$) transfer. OER electrocatalyst design plays a crucial role in efficient water splitting. To understand the activity of OER, several mechanisms have been proposed according to the intermediates identified at the electrolyte–catalyst interface during the reaction. OER can be carried out under either acid or alkaline conditions and the proposed adsorbate evolution mechanism (AEM) can be written as follows.[36, 37]

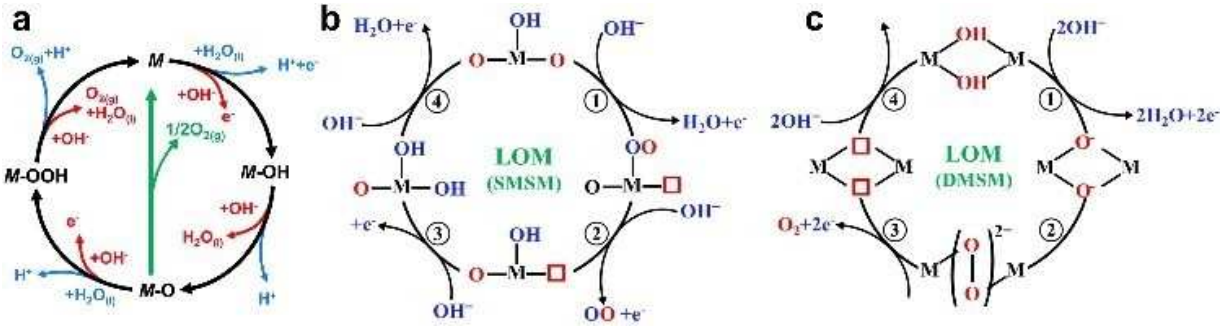

Figure 3. Illustration of the OER mechanisms. (A) Adsorbate evolution mechanism (AEM) of OER on a single active site for acidic (blue route) and alkaline (red route) conditions. (B and C) Lattice-oxygen-participating mechanism (LOM) of OER in alkaline conditions, involving single-metal-site (SMSM) and dual-metal-site (DMSM). M represents the active site, and red squares are the oxygen vacancies. *Reproduced with permission from ref.[38]. Copyright © 2017, Royal Society of Chemistry.*

<u>In acidic solution:</u>

$$M + H_2O \rightarrow M\text{–}OH + H^+ + e^- \quad (9)$$

$$M\text{–}OH \rightarrow M\text{-}O + H^+ + e^- \quad (10)$$

$$2M\text{–}O \rightarrow O_2 + 2M^+ + 2e^- \text{ or } M\text{–}O + H_2O \rightarrow M\text{–}OOH + H^+ + e^- \quad (11)$$

$$M\text{–}OOH \rightarrow M + O_2 + H^+ + e^- \quad (12)$$

<u>In alkaline solution:</u>

$$M + OH^- \rightarrow M\text{–}OH + e^- \quad (13)$$

$$M\text{–}OH + OH^- \rightarrow M\text{-}O + H_2O + e^- \quad (14)$$

$$2M\text{–}O \rightarrow O_2 + 2M^+ + 2e^- \text{ or } M\text{–}O + OH^- \rightarrow M\text{–}OOH + e^- \quad (15)$$

$$M\text{–}OOH + OH^- \rightarrow M + H_2O + O_2 + e^- \quad (16)$$

The proposed reaction mechanisms of the OER proceed through the initial elementary steps of water or hydroxide ion adsorption in an acidic or alkaline solution on the catalytically active site (M) (Figure 3a). In the second step, the adsorbed hydroxide ions (*OH) form oxygen moieties (MO). There are two different approaches to form O_2 from the MO intermediates: Two possible reaction mechanisms have been proposed for the OER. The first involves the direct

combination of two adjacent MO intermediates to produce O_2. The second involves the formation of a peroxide (MOOH) intermediate (3rd electron transfer), which subsequently decomposes after the fourth electron transfer process to release O_2. The kinetic barriers related to each elementary step contribute to the overall required activation overpotential. In general, overpotential (η), exchange current density (j_0), and Tafel slope (b) are the parameters used to evaluate the reaction kinetics of an OER electrocatalyst. These parameters are critical for obtaining insightful information on the OER mechanism, which is discussed in more detail below. Given that the OER involves the transfer of four electrons and protons, as well as the possible formation of a range of adsorbed intermediates (e.g. *O, *OH, *OOH), it may give rise to a multitude of possible pathways with varying rate-determining reaction steps.[38]

The dynamic structural changes observed on the surface of OER catalysts have led to the proposal of a lattice oxygen oxidation mechanism or lattice oxygen-mediated mechanism for OER. This is directly related to the growing attempts to develop perovskite-based electrocatalysts. In the LOM pathway, the catalytic surface is no longer a stable platform but changes dynamically with the oxygen evolution process. The oxidation, exchange, and release of lattice oxygen ligands on the catalyst surface in the OER cycle form the basis for the LOM. As illustrated in Figure 3b and 3c, it is postulated that activated lattice oxygen in the vicinity of the active metal site can be directly coupled to deprotonated M-O intermediates to form M-OO species. The M-OO species can then be converted to O_2 molecules in a subsequent step. It should be noted that the oxygen vacancies resulting from the consumption of lattice oxygen can be ultimately replenished by OH^-.[39,40] This pathway is known as the single-metal-site mechanism (SMSM). Additionally, a dual-metal-site mechanism (DMSM) has been developed, depending on the number of lattice oxygen atoms participating in the reaction around the active metal site. In this mechanism, adjacent activated lattice oxygen atoms are capable of coupling to form the M-OO-M. Subsequently, the O_2 molecule is directly evolved, and OH^- refills the generated two oxygen vacancies.[41,42] Over the past decades, the development of advanced techniques has led to a significant increase in the number of studies devoted to the investigation of the LOM for state-of-the-art OER electrocatalysts (Figure 4), including perovskite oxides, RuO_2,[43,44] IrO_2,[45,46] $NiCo_2O_4$,[47] ….

While theoretical and experimental techniques have facilitated a deeper comprehension of the OER catalytic mechanism, the design of efficient, robust electrocatalysts and the elucidation of the fundamental relationship between catalytic activity and structure remain the primary objectives of future research.

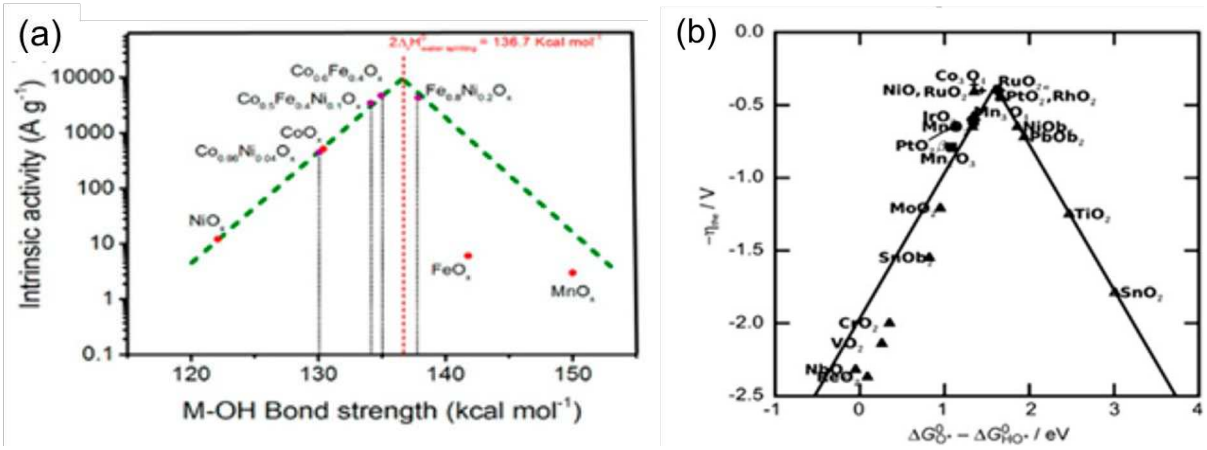

Figure 4. Volcano plot of the intrinsic activities against descriptors of: (a) the M–OH bond strength in transition metal (oxy)hydroxides, (b) the calculated activities against descriptor of the $\Delta G_{O^*} - \Delta G_{HO^*}$ for rutile, anatase, Co_3O_4, Mn_xO_y oxides. *Reproduced with permission from ref.[48] Copyright © 2018, Journal of the American Chemical Society.*

1.1.2.2. Activity evaluation criteria

The activity, efficiency, and stability of a catalyst are the most important factors to evaluate the catalyst activity (Figure 5). In the electrochemical process, the overpotential refers to the extra potential needed to initiate the intended reaction at the thermodynamically determined reversible potential (E_0) in optimal circumstances.[49] The overpotential (η) at a current density of 10 mA cm^{-2} (η_{10}) derived from cyclic voltammetry (CV) or linear sweep voltammetry (LSV) is typically employed as a reference point for comparing the activities of electrocatalysts and corresponds to the ~10% solar-to-chemicals efficiency.[50,51] Conversely, as the field of research has expanded exponentially, researchers have begun to assess and compare η_{100} and η_{500}, in addition to η_{10}, which is highly recommended for catalysts that operate at high current densities. This approach enables the evaluation of a catalyst's activity to be conducted in a manner that is more closely aligned with the standards typically employed in industrial applications.[52,53]

The Tafel slope provides a lot of information about the properties of the catalyst material and is recommended to be measured under steady-state conditions.[54] The Tafel slope can provide insights into the dynamics of the catalytic processes taking place on the surface and provide information about kinetics and inhibitions during the water oxidation catalysis. The Tafel slope indicates the potential for increasing the resulting current (j) by an order of magnitude. It provides an indication of the efficiency and dynamic response of an electrode or the catalyst applied to it to an applied potential, resulting in the generation of a catalytic current. This also considers any alterations to the mechanism resulting from different η values. It can therefore be used to ascertain which is the rate-determining step in the reaction mechanism. The Tafel

slope quantifies the required change in the potential for a one-decade change in current density. Exchange current densities are in turn used to determine the activity or reaction rate of an electrocatalyst at equilibrium potential, i.e. at a net current of zero. [55]

Electrochemical impedance spectroscopy (EIS) is a valuable tool for investigating mechanisms in electrochemical reactions, charge transfer processes in materials, and surface properties of electrodes.[56] It provides highly precise results on the electrical conductivity of a material and is a frequently employed technique. The impedance spectra thus obtained permit the ability of materials to store electrical energy and transfer electrical charge to be determined. The electrodes are measured with a two- or three-electrode set-up, the potentiostat transmitting an alternating potential with varying frequency (ω) to the sample.[57] A signal is generated that is proportional to the current generated. An analyzer then determines the impedance z of the system from the alternating current that passes through the sample and the alternating voltage generated by a generator.[57]

Another valuable insight is the faradaic efficiency (FE), which is defined as the efficiency of electron transfer provided by the external circuit to promote the electrochemical HER or OER reaction. At a constant current density applied for a certain period of the experiment, a gas sample is taken with a gas-tight syringe and analysed with a gas chromatograph (GC) calibrated for H_2 or O_2. The faradaic efficiency is then calculated from the volume of the generated gas during electrocatalysis, in comparison to the current over time. It directly correlates with the number of electrons needed to generate a mole of gas.[58], The turnover frequency (TOF) is another important descriptor to evaluate the catalytic activity, providing the generated H_2 or O_2 molecules per second at a single active site. Nevertheless, the precise determination of TOF remains challenging due to the complexity involved in identifying the total number of such active sites, which precludes the possibility of a precise estimation.[59]

Ideally, electrocatalysts operate close to the thermodynamic equilibrium potential of an electrochemical reaction, i.e. with a low overpotential, a low Tafel slope, a high exchange current density, high stability and high selectivity. In addition, electrocatalysts should have a high mass activity about the load.[60]

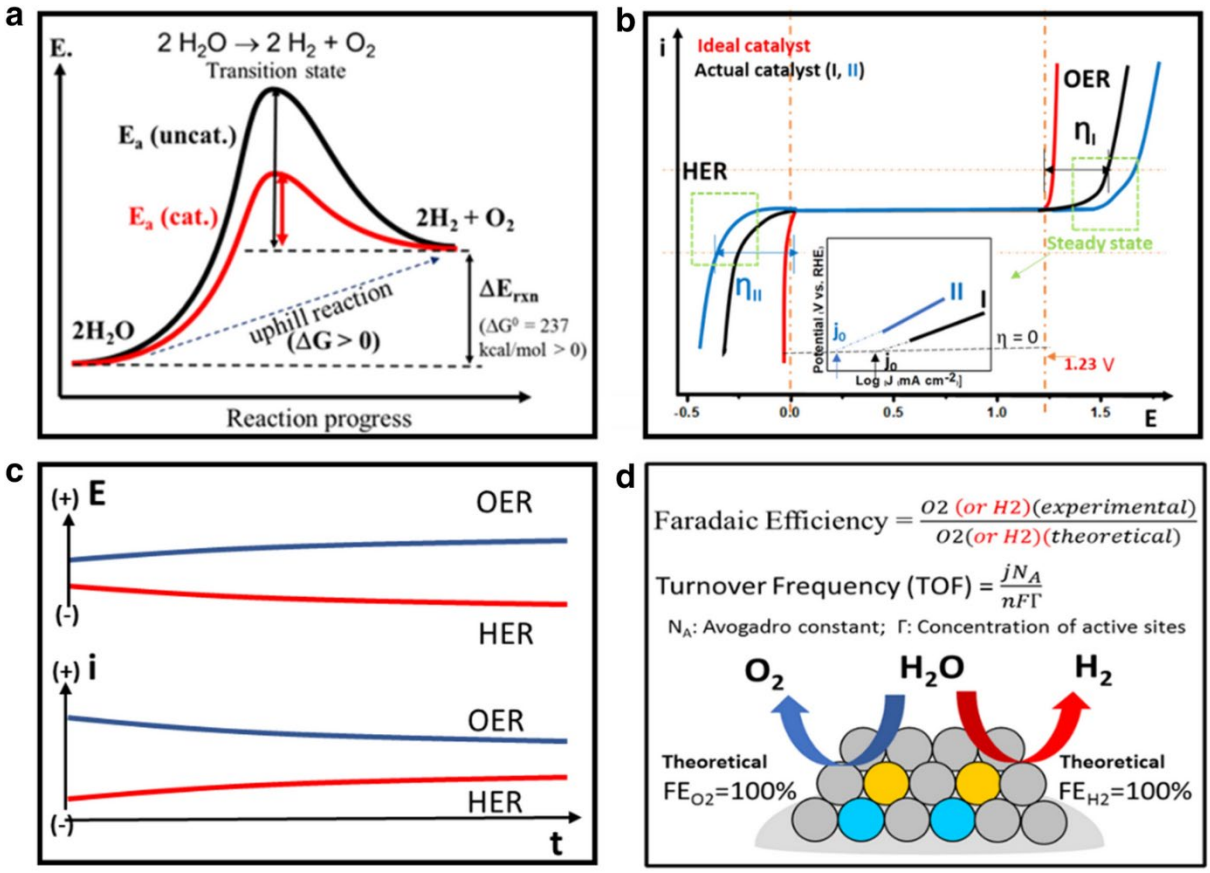

Figure 5: Schematic representation of the energy diagram of water splitting in the absence and presence of an electrocatalyst. *Reproduced with permission from ref.*[61]*. Copyright © 2021, Nano Convergence.*

To characterise the electrocatalytic properties of a material, a three-electrode setup consists of a working electrode, a reference electrode and a counter electrode (Figure 6). A glassy carbon electrode can be used as the working electrode. This serves as an electrically conductive substrate for the electrocatalyst to be applied and enables the controlled investigation of the electrochemical processes taking place with the aid of a potentiostat, which regulates the potential measured at a reference point. Under standard conditions, the redox potential E_0 of the respective redox pair of an electrode side is referenced to the standard hydrogen electrode (SHE). It is more common to use the reversible hydrogen electrode (RHE) as a reference point, which operates independently of the pH value of the electrolyte. The counter electrode closes the circuit and enables the reference electrode to operate almost current-free. A current flow between the working and reference electrodes would cause a voltage drop and prevent the exact determination of the processes at the working electrode.

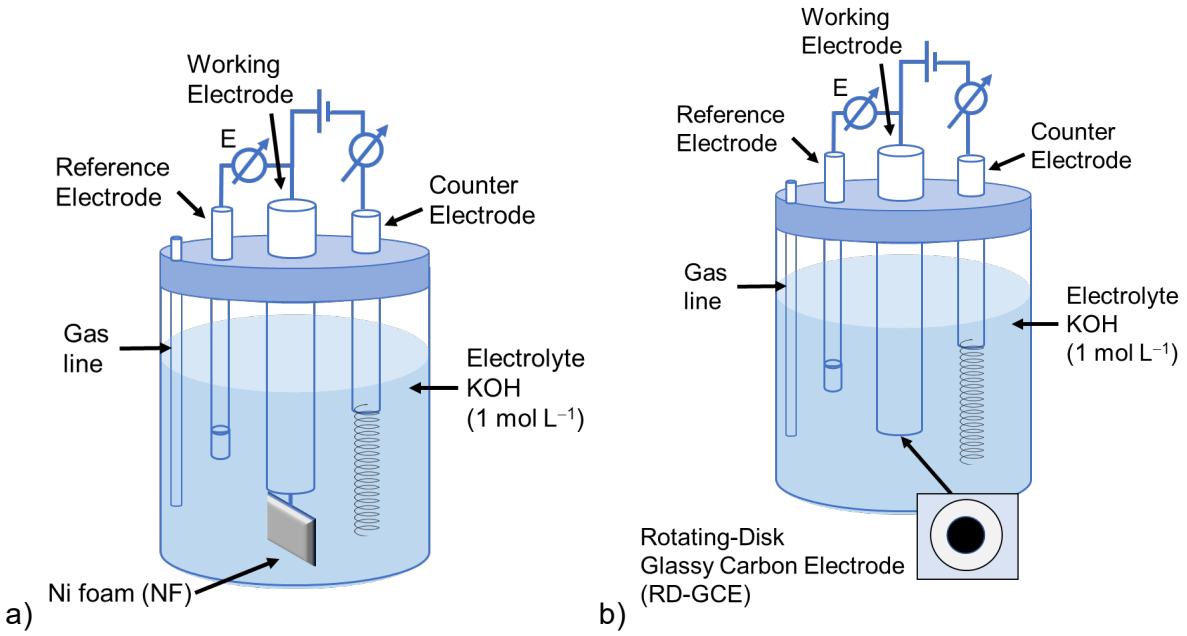

Figure 6: Schematic representation of a typical electrochemical measuring cell with a three-electrode configuration (a) Ni foam as a working electrode, (b) Rotating-Disk Glassy Carbon Electrode (RD-GCE) as a working electrode.

1.2. Metal-organic frameworks for OER

1.2.1. Metal-organic frameworks

Metal-organic frameworks (MOFs) are hybrid materials constructed from metal-based inorganic secondary building units (SBUs or nodes) and organic linkers, using strong coordinative bonding to create open crystalline frameworks with permanent porosity.[62,63] In considering the origin of MOFs, it can be seen that MOFs are a subset of coordination networks and that coordination networks constitute a further subset of coordination polymers. MOFs' construction depends on the linkage of metal nodes via organic ligands through the formation of coordination bonds (Figure 7). In the 1990s, Hoskins and Robson made a significant contribution to the development of coordination polymer chemistry.[64] They demonstrated the construction of structures with specific topologies through the use of metals and ligands with appropriate coordination geometries. Since then, this class of materials has continued to be studied, leading to the investigation of new-generation MOF materials. The term 'metal-organic framework' was first used by Yaghi et al. in 1995, when they introduced the crystalline $[Cu(I)(4,4'\text{-Bipy})_{1,5}\ NO_3]\cdot(H_2O)_{1,25}$ framework with an extended channel system and non-permanent microporosity.[65] In 1997, Kitagawa reported the first permanently porous framework, $Co_2(bipy)_3(NO_3)_4$, which could reversibly adsorb non-polar gases (N_2, O_2 and CH_4) in the framework.[66] Two years later, two well-known MOFs were synthesized: HKUST-1 ($Cu_3(btc)_2$, btc= 1,3,5-benzenetricarboxylate) and MOF-5 ($Zn_4O(bdc)_3$, bdc= 1,4-benzenedicarboxylic acid).[67,68] The rapid development of further highly porous networks was

facilitated by the discovery of MOFs. As of January 2024, more than 100,000 MOF structures have been synthesized in the Cambridge Structural Database (CSD) and about 680,000 structures were predcited.[69] The abundance of available metal ions or clusters, combined with the almost infinite possible organic linkers, offers a vast variety of MOFs, which can be controlled in terms of their topology. MOFs exhibit many outstanding properties, including crystallinity and porosity. In particular, they are capable of forming uniform micro- and mesopore structures with high surface areas (BET = Brunauer-Emmett-Teller), reaching up to 6000 m^2/g.[70] Additionally, they can be tuned to create pores of varying sizes and topologies. Furthermore, they can exhibit flexible structures in response to external stimulation, such as temperature, pressure, or guest molecules. These properties demonstrate the superiority of MOFs in comparison to other porous materials such as zeolites and activated carbon, rendering them promising candidates for a diverse range of applications.[71,72,73]

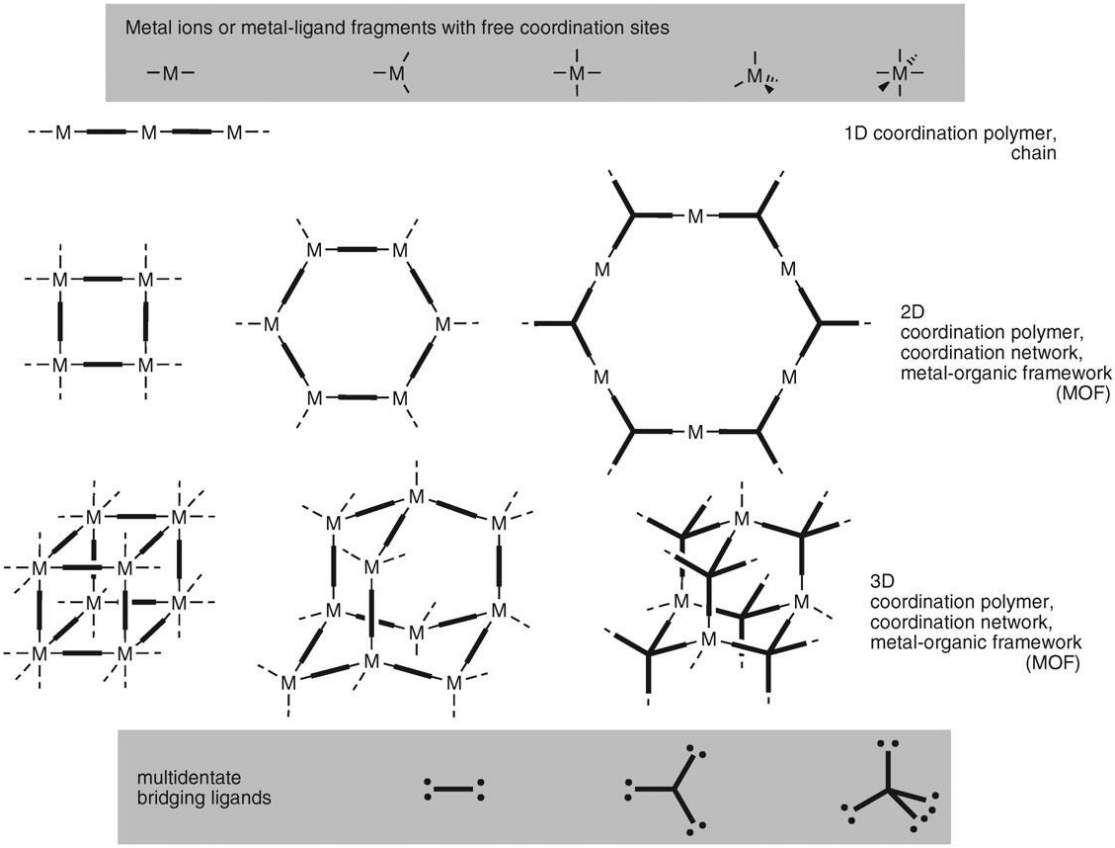

Figure 7: Schematic illustration of the construction of coordination polymers, coordination networks and metal organic frameworks. *Reprinted from ref.[62], Copyright 2010, with permission of The Royal Society of Chemistry (RSC).*

The synthesis of MOFs is typically achieved through hydro/solvo-thermal methods. In addition, microwave-assisted, electrochemical, mechanochemical and sonochemical synthesis methods are widely employed (Figure 8). The choice of metal salts and linkers, the synthesis methods and the conditions have a significant impact on the final MOF structure and morphology. In the traditional hydrothermal (water as solvent) and solvothermal (organic

solvent) synthesis of MOFs, the reaction is carried out in an autoclave (a gas-tight, closed vessel) at autogenous pressure, which enables the process to be conducted above the boiling point of the solvent used.[74] The reaction of a metal salt with the organic molecules in suitable solvents inside an autoclave at elevated temperatures leads to the as-synthesized (as) MOF, which contains the solvent molecules inside the framework.[75, 76] The solvent/guest molecules present within the pore cavity of the as-synthesized MOF must be removed through an activation process. The most commonly employed method of activation is the replacement of high-boiling solvent molecules by volatile solvents, followed by thermal activation under vacuum. This process results in the void space of the pore of the activated MOF becoming accessible.

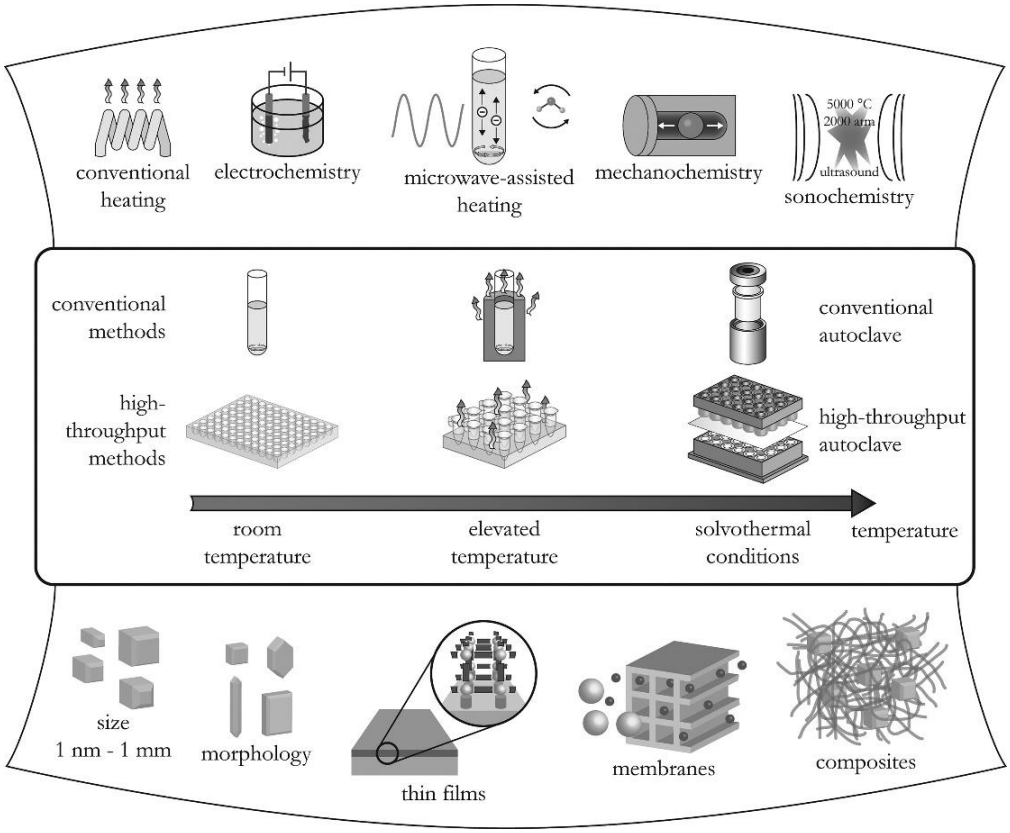

Figure 8: Schematic illustration of the construction of coordination polymers, coordination networks and metal-organic frameworks. *Reprinted from ref.[77], Copyright 2012, with permission of the American Chemical Society.*

Metal–organic frameworks (MOFs) are a promising class of materials with diverse structural and compositional properties, high porosity, and tunable properties (Figure 9). They have been extensively studied for their potential applications in gas storage and selective gas separation. Many MOFs have demonstrated excellent performance in hydrogen storage,[78] methane storage,[79] carbon dioxide capture,[80] and gas separation.[81] In addition, MOFs are also potential candidates in a number of other applications, including drug delivery,[82] sensing,[83] electronics,[84] optics,[85] water sorption for heat transformation,[86] and catalysis.[87] In addition to

the MOFs themselves, MOF composites and MOF derivatives can also act as catalysts for desired reactions. Furthermore, MOFs can be used as supports for catalytically active species. The literature contains numerous examples of MOFs employed as catalysts in a variety of catalytic reactions, including hydrogenation,[88] photocatalysis,[89] and electrocatalysis.[90] Additionally, the potential of MOFs as alternatives for electrochemical energy conversion and storage has drawn attention.

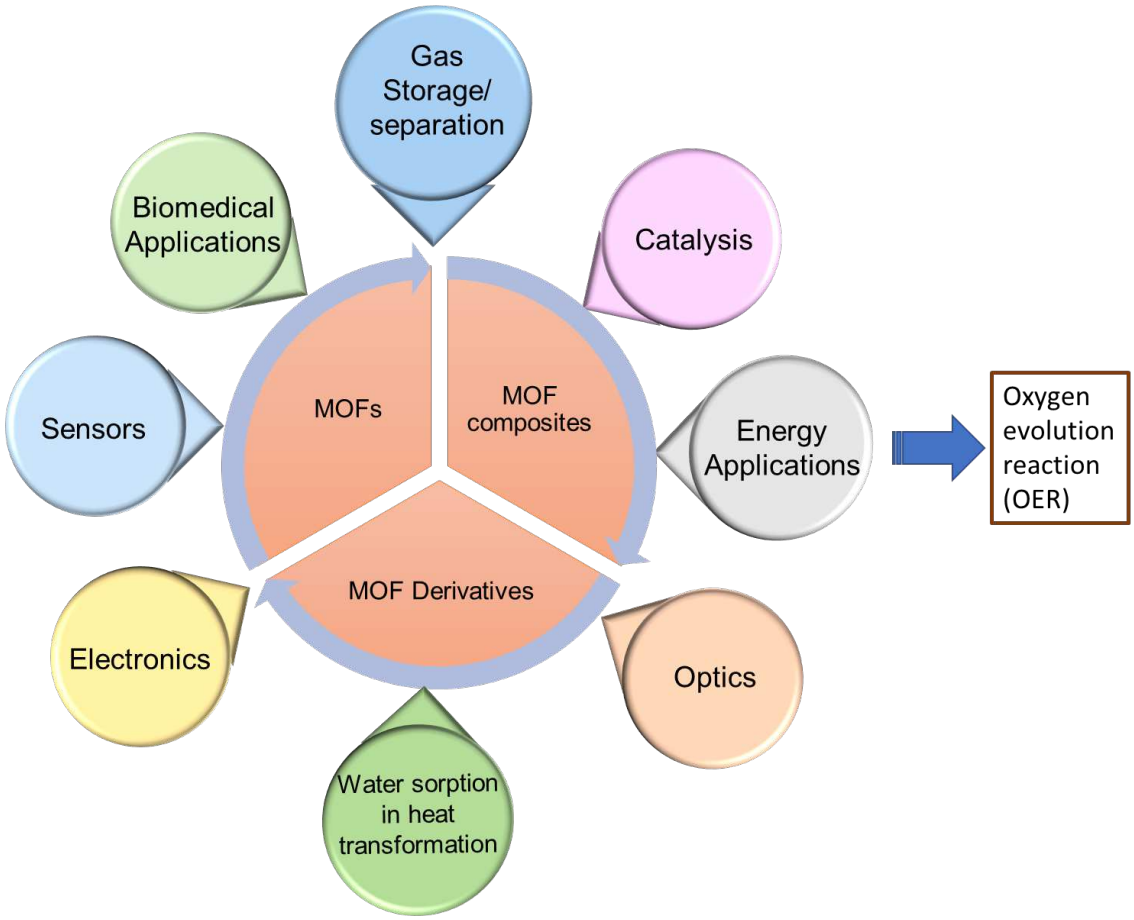

Figure 9. Application areas of MOFs, MOF composites and MOF derivatives.

Metal-organic frameworks (MOFs) have been extensively studied in the fields of energy conversion and storage devices, as well as electrocatalysts in water splitting. This is due to their high surface area, tunable pore size, and variable metal nodes/organic ligands.[91,92,93] The majority of MOF compositions comprise inexpensive first-row transition metals, such as Mn(II)/Mn(III), Fe(III), Co(II), Ni(II), Cu(II), and Zn(II), and inexpensive, commercially available organic ligands (mostly carboxylates).[94,95] This compositional aspect renders MOFs promising earth-abundant electrocatalysts. Despite an enormous amount of research in the last decade, major challenges remain, leaving several opportunities for the use of MOFs as electrocatalysts.[96] While MOF-carbonised or MOF-pyrolysed carbon matrices tend to maintain electrocatalytic performances under the corresponding high temperature and high pressure with inner atmosphere conditions, these indirect post-treatments imply that intrinsic metal-

ligand bonds in the MOFs would be exposed to such harsh reaction conditions. However, most pure MOFs have poor electrical conductivity and lack stability in a highly acidic or basic aqueous electrolyte.[97] The instability of MOFs hybrids in the presence of water or harsh chemicals is largely because they consist of typically labile metal-organic bonds and are accompanied by coordinatively unsaturated and reactive metal centres. Performance is compromised by generally poor selectivity whereas metal complex-based molecular OER catalysts are decomposed under OER conditions to yield metal oxide/hydroxide catalysts.

In contrast, organic linkers in MOFs could be oxidised under OER conditions, leading to framework collapse. In such cases, MOFs will only play the role of precursors, i.e. the "precatalysts", which will eventually generate the true OER catalysts (Figure 10).[98] The precatalyst represents that the pristine MOFs underwent structure transformation and generation of active phases during the alkaline immersion and the electrochemical treatment. Therefore, to utilise MOFs in OER catalysis or other oxidations, surface-sensitive structural characterisations should be employed. Consequently, in order to enhance the catalytic activity and expand the application area of MOFs, future research should focus on the deliberate introduction of defects or unsaturated active sites, size tuning and improvement of conductivity. Furthermore, it is critical to identify the catalytically active species and investigate the link between MOF structure, electrolyte composition, and OER performance.

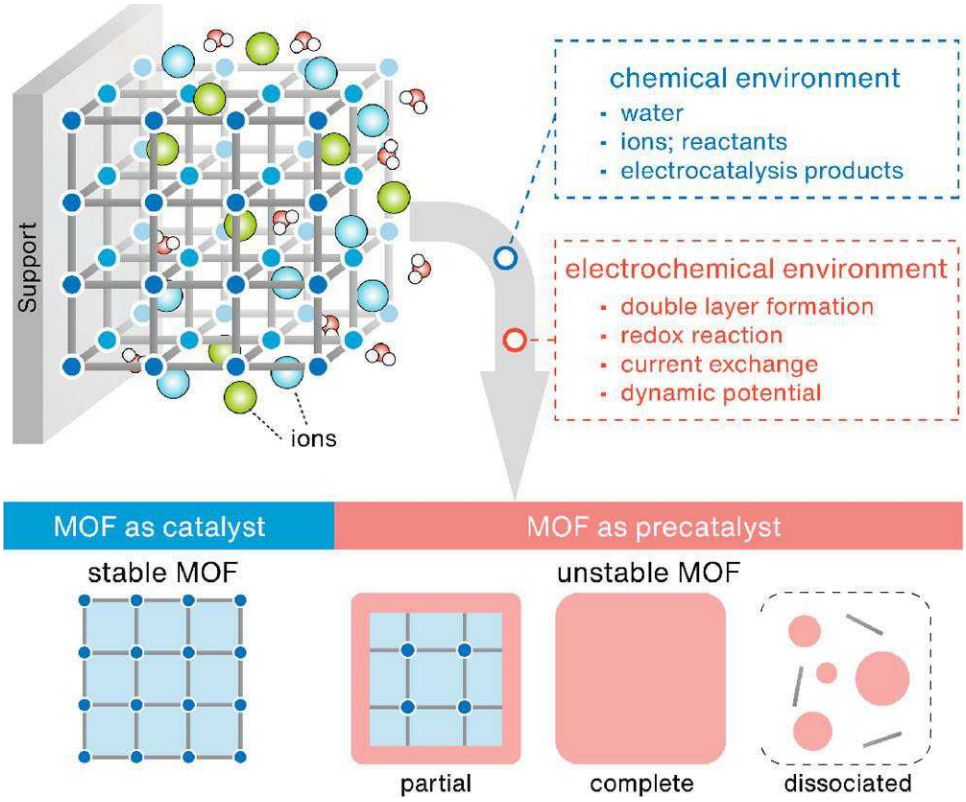

Figure 10: Schematic representation of the possible states of a MOF in a specific chemical and electrochemical environment: catalyst or pre-catalyst. *Reproduced with permission from ref. 98. Copyright © 2021, ACS Energy Letters.*

1.2.2. Pristine Metal-Organic Frameworks for OER

The most significant advantages of MOFs in the OER are their tunable and well-defined porous structure, which is beneficial for electron transfer and mass transport. However, the majority of MOFs exhibit low electrical conductivity values, excessively microporous structures and the blocking of active metal sites by organic ligands, which limits their application in electrocatalysis. Therefore, the development of pristine MOFs as electrocatalysts is described below:

(a) *Improvement of conductivity*: The conductivity of electrocatalysts has a significant impact on the efficiency of electrochemical systems. Most of the identified MOFs are semiconductors or insulators. Conductive MOFs were created by incorporating conjugated organic ligands to improve electrocatalytic activity.[99] For example, In 2016 a new form of conductive Co-based MOF catalyst was found as cobalt porphyrin and phosphonate complexes, named Co-TpBpy, which has been characterised as a novel type of electrocatalyst for water oxidation at neutral pH.[100] In addition, a cobalt conductive MOF (UTSA-16) was reported by Ai and co-workers.[101] UTSA-16contained an open framework structure composed of tetranuclear cobalt citrate clusters as linkers and tetrahedral Co(II) atoms as nodes and the overpotential for the UTSA-16 is 408 mV at the current density of 10 mA cm^{-2}.[101] Later, the conductive Co-based MOFs, named $Co_3(HITP)_2$ (HITP is 2,3,3,7,10,11-hexaaminotriphenylene) was successfully synthesized by Huang and coworkers.[102] The overpotential of $Co_3(HITP)_2$ needed 254 mV vs RHE at a current density of 10 mA cm^{-2}, as small as the Tafel slope of 86.5 mV dec^{-1} in alkaline electrolyte.[102] The efficient OER performance is closely related to the choice of conductive conjugated organic ligands, synergistic effects between the metals, S, and N and the 2D structure. Besides, combining MOFs with highly conductive carbon materials (*e.g.*, graphene, activated carbon) or conductive metal substrates (e.g., Ni foam, Au foil, Pt foil…) is also a common strategy (see more information below).

(b) *Creation of unsaturated sites*: In catalysis, MOFs are ideal candidates for exploring structure-property relationships. Previous studies have shown that introducing defects or creating additional unsaturated metal sites in MOFs can lead to a higher number of catalytically active sites and higher catalytic performance.[103,104,105] Based on this strategy, the electrocatalytic performance of ZIF-67 was enhanced significantly by using plasma etching to create more coordinatively unsaturated metal sites in the chemically and thermally stable.[106]

(c) *Design of ultrathin nanosheets*: The majority of MOFs are characterised by a high density of micropores, which accounts for their exceptionally high specific surface area. This property is advantageous for the adsorption of gases by tiny molecules, but detrimental to electrocatalytic reactions in a liquid environment due to the micropores limiting the diffusion of reactant and product gas molecules. As a result of their distinctive physicochemical features,

ultra-thin two-dimensional nanosheet electrocatalysts are becoming a popular area of study. In general, 2D materials tend to be more coordinatively unsaturated and are more easily accessible to reactants. Consequently, the fabrication of ultrathin MOF nanosheets represents an optimal approach to enhance the accessibility of active metal sites and accelerate the reaction process. Therefore, 2D MOFs have attracted widespread interest in the field of electrocatalysis. For instance, the stable 2D-NiFeMOF was successfully synthesized and then used as an efficient electrocatalyst with an overpotential of η_{10}: 221 mV.[107]

(d) *Generation of lattice strain*: Strain engineering is a typical approach for designing catalysts with excellent performance. According to current research, one of the most important aspects influencing catalyst performance is its electronic structure. The addition of strain to the catalyst surface allows for the fine-tuning of the electronic structure and the modification of the active site's capacity to adsorb reactants, reaction intermediates, and/or products. Recently, the lattice strain in NiFe-MOFs allows for obtaining high OER activity with an overpotential of 300 mV was introduced by Liu and coworkers.[108] The research observed that the superoxide *OOH intermediate emerging on Ni^{4+} sites is responsible for high OER activity.[108]

1.2.3. Metal-Organic Frameworks Derivatives for OER

The term "MOF-derivatives" refers to a wide range of materials. However, this discussion will concentrate on MOF-derived electrocatalysts produced without using pyrolysis or carbonization methods. In MOFs, the coordination bonds between metal ions (or clusters) and organic ligands tend to dissociate under extreme conditions. This leads to the reformation of the released metal ions or clusters in either ordered or disordered metal hydroxides. Due to the low stability of MOFs, the electronic interactions between metal centres and organic ligands in MOFs are weaker than those in conventional solid-state materials.[109] While some MOFs demonstrate strong coordination bonds in concentrated acetic or alkaline electrolytes, this does not ensure their electrochemical stability.[98] Besides, at low or high bias voltages, the metal nodes in MOFs are susceptible to reduction or oxidation, which can also break the coordination bonds.[110,111] Considering the MOF's hydrolytic stability in extremely acidic or alkaline electrolytes, more studies are focusing on the pre-catalytic chemical processing of the pristine MOFs. For example, it has been shown that carboxylate-based MOFs are relatively unstable under strongly alkaline conditions. Especially, carboxylate-based MOFs are relatively fragile under strongly alkaline conditions (that OER entails), while OH^- ions can cleave the coordination bonds holding the carboxylate linkers to the metal sites, resulting in the formation of metal hydroxides.[112,113,114] These metal hydroxides play a crucial role in the subsequent electrocatalytic process. Accordingly, some recent works have reported an alkaline hydrolysis strategy for delivering derived-MOF OER electrocatalysts.[115,116] As an example, Li and coworkers developed a facile alkali-etched method to obtain the defect-rich ultrathin Ni-MOF

nanosheet array for OER.[117] In alkaline electrolytes, partially coordinated Ni-O bonds of 2D MOFs could be broken due to KOH invasion, producing open unsaturated Ni^{2+} XRD patterns demonstrating an increased space between the metal oxide layers after post-alkali etching treatment, evidence of framework stability.[118] Two possible reasons for this observation are: a) the breaking of the partially coordinated Ni-O bonds, and b) the weakening of interactions between the neighboring layers. To enhance the OER performance of MOF-derived electrocatalysts and to clarify their structural conversion mechanisms, more studies are focusing on the completely reconstructed MOFs following alkaline hydrolysis.[116, 119] Using a combination of FeMOF and NiMOFs, the active species and reaction mechanisms were investigated systematically by Bu and co-workers.[112] Their results demonstrated that most organic ligands in MOFs were replaced by OH^- ions in alkaline electrolytes, leading to the generation of NiFeLDH (LDH: layered double hydroxides).[120] The derived NiFeLDH acts as an active species during water oxidation. Multiple reports also demonstrated that some MOFs displayed relatively high stability over a short period of the alkali immersion treatment.[121,122] Such a conjecture in terms of the relationships between the real active sites in MOF-derived catalysts and the pristine MOFs needed to be resolved. Attentively, albeit alkaline hydrolysis could partially or destroy MOF structures, accurate information on the post-destruction phases vis-à-vis during (and/or after) the OER remains missing. In addition to the alkaline hydrolysis, recently, Lee and co-workers systematically studied the transformation process of ZIF-67 during both cyclic voltammetry and amperometry.[123] Their in-situ spectroelectrochemistry results demonstrated that the strong transformation of tetrahedral Co sites in ZIF-67 to tetrahedral α-$Co(OH)_2$ and octahedral β-$Co(OH)_2$ occurs gradually during the electrochemical treatment. The active center of OER lies in CoOOH species, generated by the oxidation of α/β-$Co(OH)_2$, rather than from the metal nodes in ZIF-67.[123]

1.2.4. MOFs composites for OER

The majority of disadvantages of MOFs in the OER are low electrical conductivity, excessively microporous structures, and organic ligands that block active metal sites, thereby limiting their use in electrocatalysis. Therefore, to overcome the drawbacks of MOFs and enhance the electrocatalytic activity, MOFs could be combined with high-conductive materials. The common supporting materials for constructing the MOF composites can be devised into two categories: conductive metallic substrates (e.g. Ni foam, NiFe alloy foam, Cu foam, Au foil, Fe foil, Pt foil….), and conductive carbon materials (e.g. graphene, graphene, graphene oxide (GO), reduced graphene oxide (RGO), or carbon nanotubes (CNT)). The reasons are discussed as follows. Firstly, the utilisation of conductive substrates enhances the electro-conductivity of composite systems. The in situ growth of MOFs on conductive substrates in an oriented arrangement may facilitate the establishment of a synergistic effect between MOF

and the conductive substrate, thereby enhancing electron transport and improving structural stability.[124, 125] Secondly, MOFs that have been in situ grown on substrates such as Ni foam and carbon cloth can be employed as working electrodes for OER tests without binder materials (e.g. Nafion and polytetrafluoroethylene), which could reduce the active sites of the electrocatalysts. In particular, a large amount of oxygen will bubble on the surface of the catalysts at high current density during the OER procedure, which will accelerate the electrocatalyst's detachment from the electrodes, further leading to reduced OER performance.[126] Thirdly, the dispersion of MOFs by the supporting materials may result in the exposure of more active sites.[127] Finally, the MOF/support composites with complex hierarchical structures will facilitate mass transfer and charge carrying.[128] Consequently, the fabrication of MOF/support composites is a potential technique for developing efficient and stable electrodes in OER. Thus, the development of the combination of high-conductive carbon materials or substrates and MOFs is described as follows:

1.2.4.1. Metallic Substrates

To date, various strategies have been developed to modulate the morphologies, compositions, and electronic structures of MOF-based electrocatalysts. To address the drawbacks of poor electroconductivity and instability in MOFs, the in situ growth of MOFs on metal foam has been demonstrated to be an effective approach for the development of high-performance OER materials. This strategy has the potential to prevent catalyst aggregation and shedding, expose more active sites, and reduce charge transfer resistance. For instance, Cu substrate-supported 3 D bimetallic MOF $M_2(BDC)_2TED$ (M = Co, Ni, and Ni/Co; BDC = 1,4-benzenedicarboxylate; TED = triethylenediamine) were synthesized (CoNi-MOFs) via a using a layer-by-layer method.[129] The morphology and structure of this NiCoMOF by tuning the molar ratio of metal ions and reaction time. The optimized CoNi (1:1)-MOF electrode achieved an overpotential of 265 mV at a current density of 10 mA cm^{-2} in 1 mol L^{-1} KOH.[129] Thus, the combination of Ni and Co nodes effectively reduces energy barriers and enhances OER performance. The high conductivity and numerous active sites of the integrated electrode were major factors contributing to the observed high OER activity.[129]

Ni foam (NF), which possesses high mechanical strength, flexibility, and high electrical conductivity, is one of the ideal metallic substrates for the growth of MOFs. Benefiting from these advantages, the NF-supported electrodes normally exhibit better mass transport, more efficient charge transfer and longer durability concerning electrodes supported by flat substrates.[126,130,131] MOF/NF composites with nanosheet array structures could be prepared via a one-pot solvothermal process, during which the metal ions and organic ligands self-assemble on the surface of NF. For instance, the excellent OER catalytic activityof NiFe-MOF74/NF was achieved with an overpotential of 223 mV at a current density of 10 mA cm^{-2}

as well as excellent stability in alkaline solution throughout 65h.[132] The NF-supported NH_2-MIL-88B (Fe_2Ni)MOF electrode was reported by Lu and coworkers with a low overpotential at 10 mA cm^{-2} of 240 mV.[133]. Besides the excellent OER catalytic activity, the stability test under high current densities of 250 and 500 mA cm^{-2} maintained steady for at least 30 h.

1.2.4.2. Carbon-based composites

Similar to the metallic substrates, the hybridization of MOF and carbon-based substrates, which exhibit excellent electrical conductivity, high special surface area and favourable stability, is an effective and viable approach to improve OER activity. To date, numerous MOF/carbon-based substrate hybrids have been successfully obtained by assembling MOFs with 1D, 2D, and 3D carbon materials, such as graphene,[134] graphene oxide (GO),[135] reduced graphene oxide (RGO),[136] or carbon nanotubes (CNT)[137] to overcome the low electrical conductivity of MOFs. Ketjenblack carbon (KB) has a high surface area (1300 $m^2 g^{-1}$), low cost, excellent charge-transport properties, and superior chemical stability.[138] Currently, there are various reports on MOFs and nanoparticles with Ketjenblack carbon that were used as catalysts for OER.[139] For instance, the bimetallic $Ni_{10}Co$-BTC/KB composite gave an overpotential of 344 mV at a current density of 10 mA cm^{-2} and a Tafel slope of 47 mV dec^{-1} in 1 mol L^{-1} KOH.[140] The Ni(Fe)-MOF-74 with KB for OER in an alkaline media reached an overpotential to achieve a current density of 10 mA cm^{-2} was only 274 mV and the Tafel slope was 40 mV dec^{-1}.[141] Ketjenblack carbon materials can not only be well dispersed on the MOFs, affording an improved conductivity of the composites but also close contact between MOFs and the Ketjenblack carbon for enhanced electron transfer. Therefore, the carbon-based materials could highly disperse MOFs or serve as the supports for the growth of MOFs, thus the MOF/carbon-based hybrids display superior OER performances under highly alkaline conditions by taking advantage of both conductive carbon materials and active MOFs.

2. Motivation

MOFs are considered to be promising precursors for active metal oxide/hydroxide electrocatalysts, as they enable the precise control of the metal composition and a uniform distribution of metal at the nanoscale. Bimetallic MOFs present enhanced opportunities for tailoring the properties of MOF properties, generating significant interest between pristine bimetallic MOFs and their derived metal hydroxide electrocatalysts for OER, it also widely underpins the general understanding of MOF as pre-electrocatalysts This work offers a perspective on the development of bimetallic MOF pre-electrocatalysts in an energy-efficient and environmentally friendly manner, thereby avoiding the use of pyrolysis and/or calcination-derived carbonised hybrids. However, the MOFs constructed by earth-abundant metal ions and two kinds of organic ligands MOFs are rarely reported for OER. In this work, the majority of bimetallic MOF compositions comprise the low-cost first-row transition metals such as Fe(III), Ni(II), Co(II), Zn(II), *etc*. as well as inexpensive and commercially accessible organic ligands, including BDC = 1,4 benzenedicarbonxylate, DABCO = 1,4 diazabicyclo [2.2.2] octane. Furthermore, in order to overcome the intrinsic limitations of pristine MOFs, several strategies have been employed to develop catalysts derived from MOFs, to enhance the electrochemical OER catalyst as follows: (i) adopting of bimetallic or multivariate MOFs, (ii) the combination of conductive carbon materials with MOFs, and (iii) the in situ growth of MOFs on conductive Ni foam substrates.

Project 1: In this work, we report on the synthesis of the various pillared-layered MOF [M_2(BDC)$_2$DABCO], (BDC = 1,4 benzenedicarbonxylate, DABCO = 1,4 diazabicyclo [2.2.2] octane), known as DMOF. NiDMOF consists of {$Ni_2(O_2C\text{-})_4$} paddle-wheel clusters connected by BDC linkers to form two-dimensional layers that are pillared by DABCO ligands to a three-dimensional structure. NiDMOF as well as with the addition of iron as Ni(Fe)DMOF and a composite with a conductivity carbon material as modified Ketjenblack carbon (mKB) through a facile one-pot synthesis method. The pretreatment of KB with nitric acid adds hydrophilic oxygen-containing groups that are beneficial to improving the wettability and interfacial area, promoting electrolyte accessibility. The Ni(Fe)DMOF/mKB materials were employed as precursors to OER electrocatalysts in a KOH electrolyte. Stability tests of the MOF in KOH and post-mortem analyses showed the transformation of the precursor into α/β-Ni(OH)$_2$ and β/γ-NiOOH, albeit with the retention of the MOF morphology.

Project 2: we report two new isotypic semiconductive metal phosphonate frameworks Co_2[1,4-NDPA] and Zn_2[1,4-NDPA] (1,4-NDPA^{4-} is 1,4-naphthalenediphosphonate). In order to investigate the electrochemical properties of Co_2[1,4-NDPA] and Zn_2[1,4-NDPA], the optical bandgaps as a semiconductive valuation factor, electrocatalyst OER performances in both accurate RD-GCE and NF systems were investigated.

Project 3: Herein, the bimetallic $(M,M')_2(BDC)_2DABCO$ (M, M´= Ni, Co, Zn) are prepared systematically through a facile and effective microwave synthesis method. Taking advantage of the microwave synthesis method, thanks to its highly tunable mass loading, controllable growth orientation and binder-free processing, the bimetallic NiCoMOF was grown on NF by microwave irradiation and used directly as a working electrode for a practical application at high current densities of 300 mA cm^{-2} and long-term stability of 50 h for OER. The integrated MOFs on the NF electrode could be optimized by adjusting the mass loading of the MOFs on NF through the microwave synthesis time. To understand the influence of secondary metal on MOF structure for OER, the transformation of bimetallic MOFs during OER under an alkaline electrolyte KOH (1 mol L^{-1}) and electrochemical reaction was investigated. This study aims to understand the synergistic effect of the second metal in nanoscale in bimetallic MOFs-based pre-electrocatalysts on OER using both working electrodes, namely the rotating disk glassy carbon electrode (RD-GCE) and the NF electrode.

3. Cumulative part

The following units 3.1, 3.2, and 3.3 contain the three publications that have been published in scientific publications as first authorships. The publications are first introduced by a graphic summary and brief summary, as well as a description of the contribution of all authors to the publication. Each publication is listed separately and chronologically according to their date of publication. Further contributions of other publications as co-authors are given in chapter 4.

3.1. Synthesis of Ketjenblack Decorated Pillared Ni(Fe)Metal-Organic Frameworks as Precursor Electrocatalysts for Enhancing the Oxygen Evolution Reaction

Thi Hai Yen Beglau, Lars Rademacher, Robert Oestreich, Christoph Janiak

Molecules ***2023****, 28,* 4464. DOI: 10.3390/molecules28114464.

Abstract:

This study presents the synthesis of a nickel-based pillared MOF [$Ni_2(BDC)_2DABCO$] and bimetallic [$(Ni/Fe)_2(BDC)_2DABCO$] (BDC = 1,4-benzenedicarboxylate, DABCO = 1,4-diazabicyclo[2.2.2]octane), and their modified Ketjenblack (mKB) composites through a simple solvothermal synthesis method. These materials were investigated for their OER performance in an alkaline medium (1 mol L^{-1} KOH). The incorporation of a conductive mKB additive resulted in a synergistic effect that enhanced the catalytic activity of the MOF/mKB composites. Compared to single MOFs and mKB, all MOF/mKB composite samples (7, 14, 22 and 34 wt.% mKB) showed significantly improved OER performance. Particularly noteworthy, the Ni-MOF/mKB14 composite (14 wt.% mKB) demonstrated an overpotential of 294 mV at a benchmark current density of 10 mA cm^{-2} and a Tafel slope of 32 mV dec^{-1}, outperformed commercial RuO_2 and many Ni-Fe-based OER catalysts. Further enhancement in catalytic performance was achieved with the Ni(Fe)MOF/mKB14 composite (0.57 wt% Fe), showing an overpotential of 279 mV at a current density of 10 mA cm^{-2} and a low Tafel slope of 25 mV dec^{-1}, supported by electrochemical impedance spectroscopy (EIS) measurements. The Ni(Fe)MOF/mKB14 electrocatalyst on commercial nickel foam (NF) showed overpotentials of 247 mV at current densities of 10 mA cm^{-2}, maintained for 30 hours at a current density of 50 mA cm^{-2}. Importantly, this work elucidates the in situ transformation of Ni(Fe)MOF into OER-active α/β-$Ni(OH)_2$, β/γ-NiOOH, and FeOOH with residual porosity inherited from the MOF structure, as confirmed by powder X-ray diffractometry, FTIR and N_2 sorption analysis. The results consider MOF plays. a role as a precursor in the electrochemical reaction. In addition, the introduction of mKB as a conductive carbon additive in the MOF structure enables the construction of a homogeneous conductive network, improving the electronic conductivity of the MOF/mKB composites. This earth-abundant Ni and Fe-based electrocatalytic system holds promise for the development of efficient, practical and economical energy conversion materials for OER activity.

Author´s contribution to the publication:

- Planning of the research project and carrying out the literature review
- Synthesis and characterizations of NiDMOFs, modified Ketjenblack carbon (mKB), all NiDMOF/mKBx composite samples (x= 7, 14, 22, 34 wt.% mKB), Ni(Fe)DMOF and Ni(Fe)MOF/mKB14 composite (14 wt.% mKB)
- Investigation and evaluation for characterizations of PXRD, NMR, SEM, SEM-EDX, SEM mapping, and XPS measurements
- Investigations for electrochemical performance for the OER in an alkaline medium (1 mol L^{-1} KOH) of all materials with the support of Dr. Lars Rademacher
- Investigation of the transformation of the MOF materials before and after OER for PXRD, BET, and SEM
- Investigation and evaluation for BET measurement with the support of Mr. Robert Oestreich
- FTIR experiments by Mrs. Birgit Tommes and AAS measurements by Mrs. Annette Ricken
- Evaluation of all raw data and results as well as preparation of the manuscript and all figures, graphs, and tables contained in the manuscript
- Responses to reviewers of the manuscript with the comments of Herr. Lars Rademacher and Prof. Dr Christoph Janiak
- Submission of the publication to the international journal "*Molecules*" with Prof. Dr. Christoph Janiak

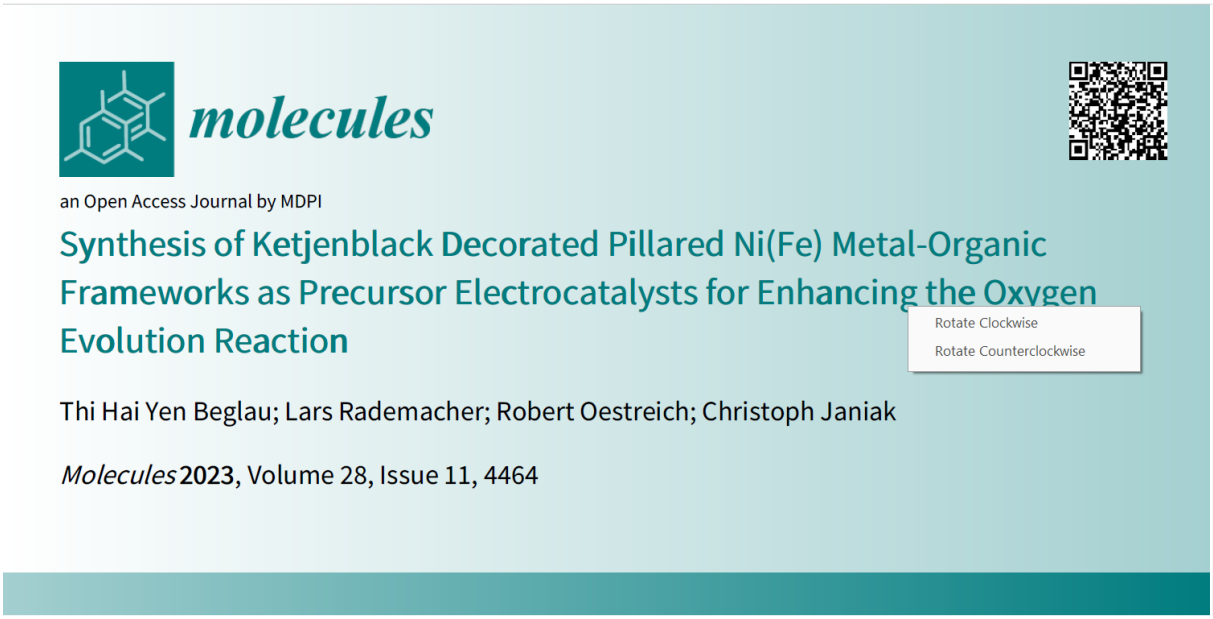

molecules

MDPI

Article

Synthesis of Ketjenblack Decorated Pillared Ni(Fe) Metal-Organic Frameworks as Precursor Electrocatalysts for Enhancing the Oxygen Evolution Reaction

Thi Hai Yen Beglau, Lars Rademacher, Robert Oestreich and Christoph Janiak *

Institut für Anorganische Chemie und Strukturchemie, Heinrich-Heine-Universität Düsseldorf, 40204 Düsseldorf, Germany; beglau@hhu.de (T.H.Y.B.); lars.rademacher@hhu.de (L.R.); robert.oestreich@hhu.de (R.O.)

* Correspondence: janiak@uni-duesseldorf.de; Tel.: +49-(21)-18112286

Abstract: Metal-organic frameworks (MOFs) have been investigated with regard to the oxygen evolution reaction (OER) due to their structure diversity, high specific surface area, adjustable pore size, and abundant active sites. However, the poor conductivity of most MOFs restricts this application. Herein, through a facile one-step solvothermal method, the Ni-based pillared metal-organic framework $[Ni_2(BDC)_2DABCO]$ (BDC = 1,4-benzenedicarboxylate, DABCO = 1,4-diazabicyclo[2.2.2]octane), its bimetallic nickel-iron form $[Ni(Fe)(BDC)_2DABCO]$, and their modified Ketjenblack (mKB) composites were synthesized and tested toward OER in an alkaline medium (KOH 1 mol L^{-1}). A synergistic effect of the bimetallic nickel-iron MOF and the conductive mKB additive enhanced the catalytic activity of the MOF/mKB composites. All MOF/mKB composite samples (7, 14, 22, and 34 wt.% mKB) indicated much higher OER performances than the MOFs and mKB alone. The Ni-MOF/mKB14 composite (14 wt.% of mKB) demonstrated an overpotential of 294 mV at a current density of 10 mA cm^{-2} and a Tafel slope of 32 mV dec^{-1}, which is comparable with commercial RuO_2, commonly used as a benchmark material for OER. The catalytic performance of Ni(Fe)MOF/mKB14 (0.57 wt.% Fe) was further improved to an overpotential of 279 mV at a current density of 10 mA cm^{-2}. The low Tafel slope of 25 mV dec^{-1} as well as a low reaction resistance due to the electrochemical impedance spectroscopy (EIS) measurement confirmed the excellent OER performance of the Ni(Fe)MOF/mKB14 composite. For practical applications, the Ni(Fe)MOF/mKB14 electrocatalyst was impregnated into commercial nickel foam (NF), where overpotentials of 247 and 291 mV at current densities of 10 and 50 mA cm^{-2}, respectively, were realized. The activity was maintained for 30 h at the applied current density of 50 mA cm^{-2}. More importantly, this work adds to the fundamental understanding of the in situ transformation of Ni(Fe)DMOF into OER-active α/β-$Ni(OH)_2$, β/γ-NiOOH, and FeOOH with residual porosity inherited from the MOF structure, as seen by powder X-ray diffractometry and N_2 sorption analysis. Benefitting from the porosity structure of the MOF precursor, the nickel-iron catalysts outperformed the solely Ni-based catalysts due to their synergistic effects and exhibited superior catalytic activity and long-term stability in OER. In addition, by introducing mKB as a conductive carbon additive in the MOF structure, a homogeneous conductive network was constructed to improve the electronic conductivity of the MOF/mKB composites. The electrocatalytic system consisting of earth-abundant Ni and Fe metals only is attractive for the development of efficient, practical, and economical energy conversion materials for efficient OER activity.

Keywords: metal-organic frameworks (MOFs); Ketjenblack; electrocatalysis; oxygen evolution reaction (OER); nickel; iron

Citation: Beglau, T.H.Y.; Rademacher, L.; Oestreich, R.; Janiak, C. Synthesis of Ketjenblack Decorated Pillared Ni(Fe) Metal-Organic Frameworks as Precursor Electrocatalysts for Enhancing the Oxygen Evolution Reaction. *Molecules* **2023**, *28*, 4464. https://doi.org/10.3390/molecules28114464

Academic Editor: Wen-Hua Zhang

Received: 14 April 2023
Revised: 20 May 2023
Accepted: 27 May 2023
Published: 31 May 2023

1. Introduction

In recent decades, issues caused by the burning of fossil fuels have become a global concern. Therefore, it is important to replace fossil fuels with clean, sustainable, and renewable resources [1,2].

In the past years, water splitting, with the use of renewable electricity for hydrogen generation, seems to be one of the most promising technologies of electrical energy conversion for storage and other uses of H_2 [3,4]. The electrolytic water-splitting process consists of two half-cell reactions: the hydrogen evolution at the cathode (HER) and the oxygen evolution at the anode (OER). The oxygen evolution reaction consists of three main processes: (i) the adsorption of H_2O/OH^- on the electrocatalyst surface; (ii) the formation of reaction intermediates; (iii) the release of O_2 molecules. OER passes through a four-electron transfer process coupled with the breaking of the O–H bond and the formation of the O–O bond, which is kinetically slow and requires a high overpotential to overcome the energy barrier. Noble metals such as Ru, Pt, and Ir are highly-active electrocatalysts for the water splitting process [5,6]. However, their commercialization on a large scale is hampered by their scarcity and high cost. Therefore, finding advanced low-cost electrocatalysts that also have long-term stability to replace noble metals for the OER is the primary requirement to enable large-scale electrocatalytic water splitting [7–9].

Numerous earth-abundant transition metal (e.g., Fe, Co, Ni, and Cu)-based materials including oxides, hydroxides, nitrides, phosphides, sulfides, and selenides are considered promising toward OER [10,11]. Nickel-based materials have received considerable attention [12]. The optimization of the morphology and porosity of nickel-based oxides and hydroxides [13,14], perovskites [15], nitrides [16], phosphides [17], sulfides [18,19], selenides [20,21], and mixed-metal oxides [22,23] have been published in various extensive works. Subbaraman et al. [24] ranked the electrocatalytic efficiency of 3d M^{2+} (M = Fe, Co, Ni and Mn) ions in the following order: Ni > Co > Fe > Mn. This order is inverse to the strength of the HO–M^{2+} bond [24]. $Ni(OH)_2$-based OER catalysts have been identified as good OER catalysts. Stern et al. reported enhanced activity in OER for β-$Ni(OH)_2$ nanoparticles with different morphologies, with the low overpotential of 299 mV for $Ni(OH)_2$ catalysts [25]. Because of their facile synthesis and excellent OER activities, amorphous metal (oxide) hydroxide materials have consistently outperformed crystalline metal oxides as the preferred catalyst in an alkaline medium [25]. However, it is still a challenge to overcome the low stability of $Ni(OH)_2$. Many strategies have been devoted to enhance the stability of $Ni(OH)_2$ such as forming the $Ni(OH)_2$/NiOOH pair with a small amount of iron [26–31] or using a ternary Ni–Co–Fe mixed-metal hydroxide [32–34]. The combination of iron into composite materials containing amorphous nickel- or cobalt-based catalysts can be beneficial for electrocatalytic water oxidation [32,33]. The presence of iron promotes the nickel oxidation from +2 to +3, which is an active state and leads to fast reaction kinetics and enhanced conductivity [32,33]. As reported by Yu et al. [30], the electrocatalyst with the optimal Ni/Fe composition of 32/1 performed with the highest activity due to the small reaction resistance and superior intrinsic activity. However, these materials usually have low surface areas and are multi-step synthesis procedures also involving high-temperature treatments. It is still necessary to develop a facile approach to synthesize highly porous and stable nickel hydroxide materials with simple and energy efficient synthesis procedures.

Metal-organic frameworks (MOFs) are porous and crystalline materials constructed from metal ions and multitopic bridging ligands and have been widely studied in many fields such as gas storage and isolation, energy conversion and storage devices as well as electro-catalysts in water splitting [35–38]. However, most MOFs have poor electrical conductivity and a lack of stability in a strongly acidic or basic aqueous electrolyte [39,40]. However, MOFs are promising precursor candidates toward OER catalysts based on their high surface area and porosity [41]. For example, Ni-MOFs decompose in an alkaline medium (e.g., 1 mol L^{-1} KOH) into a mixture of α/β-$Ni(OH)_2$, α/β-NiOOH, and γ-NiOOH, which appear to be mainly responsible for the observed OER activity [42–46]. MOFs are often mixed with conductive carbon materials such as graphene [47], graphene oxide (GO) [48], reduced graphene oxide (RGO) [49], or carbon nanotubes (CNT) [50,51] to overcome the low electrical conductivity of MOFs. These carbon materials not only elevate the electrical conductivity of MOFs, but also give a homogenous dispersion to enhance the electrocatalytic performances of the formed catalyst under highly alkaline

conditions. Ketjenblack carbon (KB) has a high surface area (~1300 m^2 g^{-1}), low cost, excellent charge-transport properties, and superior chemical stability. Currently, there are various reports on MOFs and nanoparticles with Ketjenblack carbon that were used as catalysts for OER [41,44,52–55]. For instance, Sondermann et al. [44] showed that the bimetallic $Ni_{10}Co$-BTC/KB composite gave an overpotential of 344 mV at a current density of 10 mA cm^{-2} and a Tafel slope of 47 mV dec^{-1} in 1 mol L^{-1} KOH. Öztürk et al. [55] reported Ni(Fe)-MOF-74 with KB for OER in an alkaline media. The required overpotential to achieve a current density of 10 mA cm^{-2} was only 274 mV and the Tafel slope was 40 mV dec^{-1}.

In this work, we report on the synthesis of the Ni-based pillared MOF [Ni_2(BDC)$_2$DABCO], (BDC = 1,4 benzenedicarbonxylate, DABCO = 1,4 diazabicyclo [2.2.2] octane), known as NiDMOF [56] as well as with the addition of iron as Ni(Fe)DMOF and as a composite with a modified Ketjenblack carbon (mKB) through a facile one-pot synthesis method (Scheme 1). NiDMOF consists of {$Ni_2(O_2C\text{-})_4$} paddle-wheel clusters connected by BDC linkers to form two dimensional layers that are pillared by DABCO ligands to a three-dimensional structure (Figure S1, Supplementary Materials). The pretreatment of KB with nitric acid adds hydrophilic oxygen-containing groups that are beneficial to improving the wettability and interfacial area, promoting electrolyte accessibility. Good wettability strengthens the ion-accessible surface area, promotes charge transportation between the electrolyte and electrode, and enables effective electrical integration to minimize the ohmic losses, leading to the improved OER activity [57,58]. The Ni(Fe)DMOF/mKB materials were employed as precursors to OER electrocatalysts in a KOH electrolyte. Stability tests of the MOF in KOH and post-mortem analyses showed the transformation of the precursor into α/β-$Ni(OH)_2$ and β/γ-NiOOH (Scheme 1), albeit with the retention of the MOF morphology.

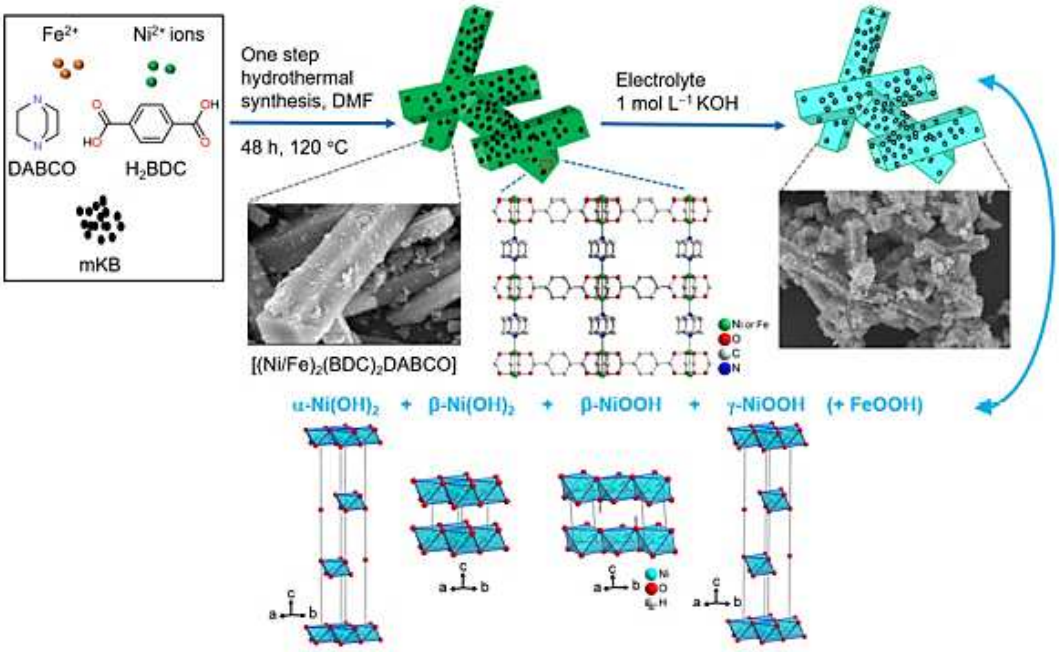

Scheme 1. Schematic illustration of the process used for the synthesis of the NiDMOF/mKB and Ni(Fe)DMOF/mKB composites and the transformation of the MOF into metal oxide-hydroxides with the retention of the MOF morphology. For the nickel (oxy)hydroxides, the unit cells of the crystal structures are given in polyhedral mode.

2. Results and Discussion

2.1. Characterization

Scheme 1 illustrates the procedure to prepare Ni(Fe)DMOF and its mKB composite. Nickel nitrate, together with iron acetate, benzene-1,4-dicarboxylic acid (H_2BDC), and 1,4 diazabicyclo[2.2.2]octane (DABCO), afford the products [$Ni_2(BDC)_2DABCO$] and [$(Ni/Fe)_2(BDC)_2DABCO$], abbreviated as NiDMOF and Ni(Fe)DMOF, respectively. In the presence of mKB, the composites NiDMOF/mKBx with different mKB fractions x = 7, 14, 22, and 34 wt.%. or Ni(Fe)DMOF)/mKB14 were obtained by using a one-step solvothermal reaction at 120 °C in DMF for 48 h. The synthesis of Ni(Fe)DMOF was carried out with a targeted molar Ni to Fe ratio of 32:1. A molar Ni to Fe ratio of 30:1 was achieved in the synthesized Ni(Fe)DMOF, as determined from atomic absorption spectroscopy (AAS) and SEM-EDX (Tables S2 and S3, Figure S9, Supplementary Materials). The weight fractions of mKB in the MOF/mKBx composites were about 7, 14, 22, and 34 wt.%, calculated from the MOF content, which was derived from the nickel amount by the atomic absorption spectroscopy (AAS) data (Table S2, Supplementary Materials).

As seen in the literature, the electric conductivity of the samples increases significantly by adding mKB (or another carbon material), thereby improving the excellent OER activities and cycling stability [59–64]. However, since mKB has almost no electrochemical activity, increasing the fraction of mKB would lead to lower energy density [65]. Only a small amount of mKB is needed to enhance the rate of OER performance as the electrons can also move due to incoherent jumps between neighboring locations. Furthermore, we will see later that the MOF is only the precursor. The active species are better conducting Ni–Fe oxide-hydroxides, for which the mKB then serves as a contact to the glassy carbon or nickel foam electrode. The experimental powder X-ray diffractogram (PXRD) of the MOF product was positively matched to the reported structure of $[Ni_2(BDC)_2DABCO]\cdot(DMF)_4\cdot(H_2O)_{1.5}$ (NiDMOF) (Figure 1a and Scheme S1) [56]. The PXRD also demonstrated that the presence of mKB influenced the crystallinity of the NiDMOF structure only at high mKB content in NiDMOF/mKB34, where peak broadening occurs (Figures 1 and S2, Supplementary Materials). This is due to the formation of a larger amount of smaller MOF crystallites, also evident from the scanning electron microscopy images (Figure S7, Supplementary Materials). In Figure 1, the main PXRD reflection of Ni(Fe)DMOF/mKB14 shifted to lower degrees compared with other counterparts, indicating an enlarged structural unit and the existence of a tensile strain. The crystal tensile strain will help to adsorb OH^- reactants to improve the OER performance [66,67]. The functional groups –OH, C–O, and –COOH of mKB can serve as crystallization points, leading to more crystal seeds, which subsequently do not grow into large crystals [68–70]. Furthermore, the ratio of the 001/100 reflex intensities increases in the NiDMOF/mKBx composites with mKB content, indicating that in the presence of mKB, the DMOF crystallites may become more oriented along the [001] direction of the NiDMOF structure (Figure S1, Supplementary Materials).

The electrochemical performance is strongly correlated to the surface area, porosity and pore size distribution of electrode materials [71]. To explore these properties, nitrogen sorption measurements were performed at 77 K and gave the expected Type I isotherms [72] for microporous NiDMOF and Ni(Fe)DMOF (Figures 2a and S6a). The specific BET surface area and total pore volume of NiDMOF was 2104 $m^2\ g^{-1}$ and 0.82 $cm^3\ g^{-1}$, respectively, in good agreement with the literature values (2050 $m^2\ g^{-1}$, 0.80 $cm^3\ g^{-1}$) (Table 1) [73]. Ni(Fe)DMOF also showed a similar high BET surface area and total pore volume with 1942 $m^2\ g^{-1}$ and 0.80 $cm^3\ g^{-1}$, respectively. The BET surface area and total pore volume of modified Ketjenblack (mKB) were 1234 $m^2\ g^{-1}$ and 1.50 $cm^3\ g^{-1}$, identical to the original Ketjenblack carbon (KB) (Table 1 and Figure S5a,b, Supplementary Materials). For the DMOF/mKBx composites, the desorption branch additionally displayed a Type H4 hysteresis [72], as seen in the isotherm of the mesoporous mKB carbon itself (Figures 2a and S5c,d). The experimental surface area and pore volume parameters of the composites NiDMOF/mKBx (x = 7, 14, 22, 34 wt.%) and Ni(Fe)DMOF/mKB14 were

somewhat lower than those estimated from the mass-weighted values of the neat MOF and mKB components (Table 1). This reduction in the BET value of composites was also observed for similar work and indicates that mutual pore blocking effects occur [55]. The NiDMOF can grow into the mKB pores or on the mKB surface, and therefore, access to the mKB and NiDMOF pores becomes restricted. The SEM images for NiDMOF/mKBx with a higher amount of mKB (x $\geq$ 22 wt.% mKB) illustrate the surface coverage of the NiDMOF rods with mKB particles (Figure S7, Supplementary Materials). At the same time, the combination of mKB with MOFs can increase the total (micro-meso)pore volume in the composites above the estimated value. The composite NiDMOF/mKB14 exhibited an experimental total pore volume of 1.18 $cm^3\ g^{-1}$, considerably higher than the estimate of 0.92 $cm^3\ g^{-1}$ for a physical mixture of 86 wt.% NiDMOF and 14 wt.% mKB. This pore volume of 1.18 $cm^3\ g^{-1}$ was also the maximum among the prepared DMOF/mKB composites.

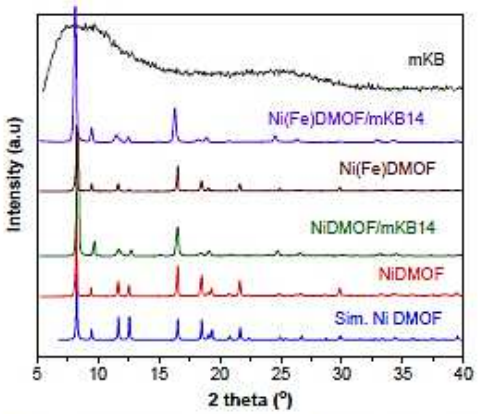

Figure 1. The PXRD patterns of NiDMOF, NiDMOF/mKB14, Ni(Fe)DMOF, Ni(Fe)DMOF/mKB14, and mKB. The simulated PXRD pattern of NiDMOF was obtained from CCDC no. 802892. The first five reflexes at 2θ = 8.2°, 9.4°, 11.7°, 12.4°, and 16.6° corresponded to the 100, 001, 110, 101 and 200 planes, respectively.

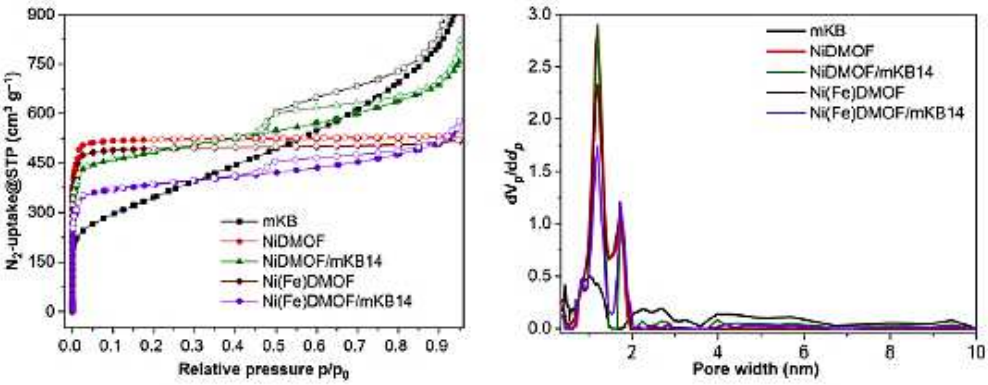

Figure 2. (**a**) Nitrogen sorption isotherms at 77 K (filled symbols adsorption; empty symbols desorption) and (**b**) the pore size distribution of NiDMOF, NiDMOF/mKB14, Ni(Fe)DMOF, Ni(Fe)DMOF/mKB14, and mKB.

Table 1. The BET surface area and total pore volume of the NiDMOF and DMOF/mKBx composites.

Material	BET Surface Area [a] (Estimated) [c] ($m^2\ g^{-1}$)	Total Pore Volume [b] (Estimated) [c] ($cm^3\ g^{-1}$)
NiDMOF-Literature [73]	2050	0.80
NiDMOF	2104	0.82
NiDMOF/mKB7	1897 (2043)	0.86 (0.87)
NiDMOF/mKB14	1773 (1982)	1.18 (0.92)
NiDMOF/mKB22	1106 (1913)	0.70 (0.97)
NiDMOF/mKB34	1087 (1808)	0.85 (1.05)
Ni(Fe)DMOF	1942	0.80
Ni(Fe)DMOF/mKB14	1486 (1843)	0.86 (0.90)
KB	1300	1.76
mKB	1234	1.50

[a] BET surface area calculated at $0.002 < p/p_0 < 0.15$ from the N_2 sorption isotherm 77 K with a standard deviation $\pm$ 20 $m^2 \cdot g^{-1}$. [b] The total pore volumes were determined at $p/p_0 = 0.95$ from the adsorption branch for pores $\leq$ 25 nm. [c] Estimated BET surface area as the sum of the mass-weighted surface areas of NiDMOF (2104 $m^2 \cdot g^{-1}$) and mKB (1234 $m^2 \cdot g^{-1}$) calculated from the following formula:

$$\text{BET (estimated)} = \frac{\text{wt.\% NiDMOF}}{100} \times 2104\ m^2 \cdot g^{-1} + \frac{\text{wt.\% mKB}}{100} \times 1234\ m^2 \cdot g^{-1} \quad (1)$$

The estimated total pore volume was calculated accordingly. NiDMOF/mKB7 stands for 93 wt.% NiDMOF and 7 wt.% mKB.

The synthesized NiDMOF and Ni(Fe)DMOF samples exhibited micropores with widths of about 1.2 and 1.7 nm (Figures 2b and S6d). In the NiDMOF/mKBx and Ni(Fe)DMOF/mKB14 composites, there were additional mesopores above 2 nm from the mKB component. The increased pore volume beyond the estimate could be traced to interparticle mesopores above 5 nm (Table 1 and Figure S6a). Open microporous channels can provide active sites for the electrochemical reaction and open mesoporous channels will improve the diffusion rate of electrolyte ions [74].

Scanning electron microscopy (SEM) of the MOFs and the composites showed rod or block microcrystals of the NiDMOF with an increasing amount of fine grains of mKB from NiDMOF/mKB7 to NiDMOF/mKB34 (Figures 3 and S6, Supplementary Materials). The observed NiDMOF morphology was in a good agreement with the reported one [75]. The element mapping from the SEM-energy-dispersive X-ray spectroscopy (SEM-EDX) (Figures 3c and S8, Supplementary Materials) demonstrated that in Ni(Fe)DMOF, the iron is homogeneously distributed in the MOF microcrystals.

The X-ray photoelectron spectroscopy (XPS) survey spectrum of Ni(Fe)DMOF/mKB14 confirmed the presence of all the elements (Ni, Fe, C, N, and O) of the synthesized material (Figure S10, Supplementary Materials for XPS of NiDMOF and Ni(Fe)DMOF). The high-resolution spectrum of Ni 2p (Figure 4a) showed two characteristic peaks at 855.7 and 873.2 eV, which were ascribed to Ni^{2+} $2p_{3/2}$ and Ni^{2+} $2p_{1/2}$, respectively, and two expected satellite peaks were located at 860.7 and 879 eV [25,76–78]. A spin-orbit coupling energy difference between the $2p_{3/2}$ and $2p_{1/2}$ binding energy of 17.6 eV supports the assignment of the +2 oxidation state [25,79]. Furthermore, in the Fe 2p spectrum, the peaks at 710 and 723 eV (Figure 4b) confirmed the +2 oxidation state of Fe [80,81]. The $2p^{3/2}$ spectrum range was 710 to 720 eV including a satellite peak at 715 eV, while the $2p_{1/2}$ spectrum range was from 721 to 735 eV with a satellite peak at 733 eV. It should be noted that the Fe 2p spectral

background had a contribution from a Ni_{LMM} Auger peak [82]. More detailed information on the high-resolution XPS of C 1s, O 1s, N 1s, and Fe 3p of Ni(Fe)DMOF/mKB14, Ni 2p and Fe 2p of Ni(Fe)DMOF, Ni 2p of NiDMOF is given in the Supplementary Materials (Figures S11 and S12).

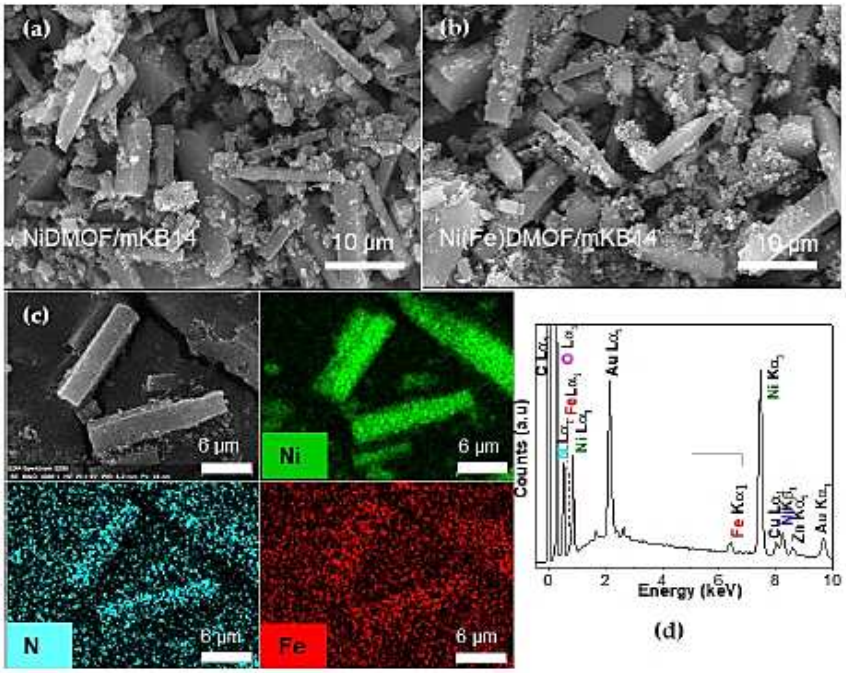

Figure 3. SEM images of (**a**) NiDMOF/mKB14, (**b**) Ni(Fe)DMOF/mKB14, (**c**) EDX scanning element mapping for nickel, nitrogen and iron for Ni(Fe)DMOF/mKB14, and (**d**) the EDX spectrum with the composition for the selected mapping area of Ni(Fe)DMOF/mKB14.

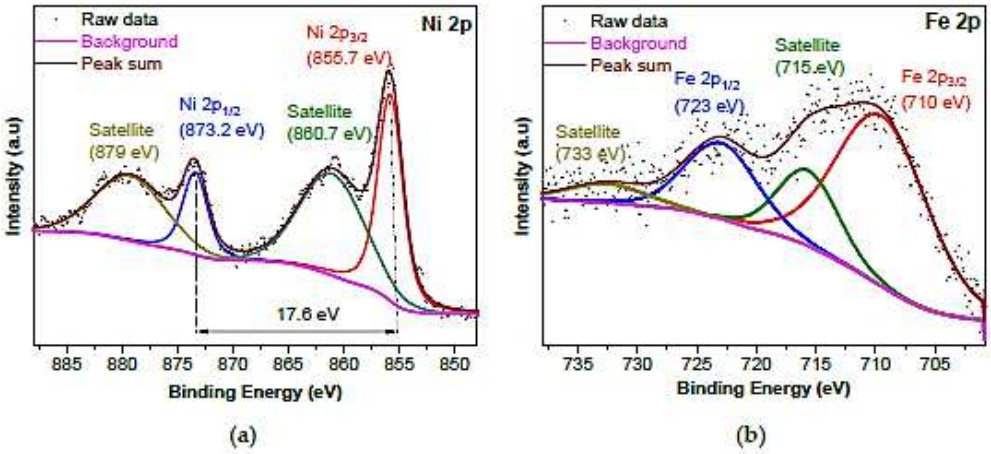

Figure 4. High-resolution XPS spectra of (**a**) Ni 2p and (**b**) Fe 2p of Ni(Fe)DMOF/mKB14.

2.2. *Electrochemical Properties*

The OER performance of different samples was evaluated by using a glassy carbon rotating disk electrode (GC-RDE) under alkaline conditions (1 mol L^{-1} KOH). OER polarization curves were collected from the linear sweep voltammetry (LSV) measurements at a sweep rate of 5 mV s^{-1}. As shown in the initial LSV curves (Figure 5a), the NiDMOF/mKBx

composites were more efficient for OER activity than pristine NiDMOF and mKB alone at a current density of 10 mA cm^{-2}. Thereby, it is worth noting that the OER activity of the NiDMOF sample is already as good as the commercial RuO_2 benchmark sample. Among all NiDMOF/mKBx composites (x = 7, 14, 22, 34 wt.% mKB), NiDMOF/mKB14 exhibited the best electrocatalytic activity with the smallest overpotential of 294 mV (vs. RHE at 1.23 V) to achieve a current density of 10 mA cm^{-2}, which was much lower than the overpotential of mKB (375 mV), NiDMOF (315 mV), NiDMOF/mKB7 (308 mV), NiDMOF/mKB22 (302 mV), and NiDMOF/mKB34 (304 mV), and competes with the performance of the benchmark material RuO_2 (317 mV). Thereby, the overpotential of RuO_2 is in good accordance with the literature [83]. A low overpotential means a lower demand of energy for the oxygen evolution reaction. The kinetics on the GCE toward NiDMOF and its DMOF/mKBx composites were described on the basis of the Tafel equation. The OER kinetic parameters of the samples were analyzed by the Tafel equation ($\eta = a + b \log(j)$), which is used to determine the reaction mechanism and the kinetics [84]. The Tafel slope indicates how much one has to increase the overpotential to increase the reaction rate by a factor of ten. It describes the influence of the overpotential on the steady-state current density and is an important parameter for the evaluation of OER kinetics. The Tafel slope was calculated from corresponding LSV plots to obtain a quantitative idea about the electrocatalytic performance. Krasil'shchikov's OER mechanism is one of the established mechanisms, which is described by Reactions (3)–(6) with the corresponding Tafel slopes b [44,85,86].

$$M + OH^- \leftrightarrows MOH + e^-, b = 120 \text{ mV dec}^{-1} \quad (2)$$

$$MOH + OH^- \leftrightarrows MO^- + H_2O, b = 60 \text{ mV dec}^{-1} \quad (3)$$

$$MO^- \rightarrow MO + e^-, b = 45 \text{ mV dec}^{-1} \quad (4)$$

$$2MO \rightarrow 2M + O_2, b = 19 \text{ mV dec}^{-1} \quad (5)$$

The value of the Tafel slope in NiDMOF (55 mV dec^{-1}) is in between Reactions (3) and (4), and indicates that the deprotonation of a metal hydroxide (3) and the oxidation of a metal oxide species (4) could occur together as rate-determining steps [86,87]. The corresponding Tafel curves derived from Figure 5b show the Tafel slopes for NiDMOF/mKBx composites (7, 14, 22, 34 wt.% mKB) with 53, 32, 45, and 51 mV dec^{-1}, respectively. Thus, integrating mKB with NiDMOF can enhance the kinetics of the catalyst. For the 14 and 22 wt.% composites, there was also a change in the rate-determining step toward Reaction (4) for 22 wt.% (slope of 45 mV dec^{-1}) and toward Reaction (5) of the evolution of O_2 for 14 wt.% (slope of 32 mV dec^{-1}). The NiDMOF/mKB14 composite had the smallest Tafel slope (32 mV dec^{-1}), confirming that the interaction between NiDMOF and 14 wt.% of mKB in the composite gives the most proficient material.

It is acknowledged that due to the surface structure reconstruction of Ni-based catalysts, an activation occurs during the water oxidation process [30,44]. In order to understand the electrocatalytic behavior and the activation process, 100 cyclic voltammetry (CV) scans were applied. With mKB present in the composites, the oxidation peak at 1.35–1.45 (V vs. RHE) became more noticeable and shifted into a positive direction, indicating the synergetic effect of mKB and NiDMOF on the oxidation of Ni^{+2} to Ni^{+3} (Figure S13, Supplementary Materials). As seen in Figure S14, the CV curves of all samples after 100 CVs showed that NiDMOF/mKB14 provided the most active catalyst, while mKB alone exhibited worse OER activity due to carbon corrosion in alkaline conditions [88]. The mKB additive led to the electrical conductivity between the active Ni sites and the GCE, and thereby enhanced the electrochemical activity [89,90]. However, an excessive amount of mKB lowered the carbon dispersion due to agglomeration from the π–π interaction between the carbon particles, which would lead to lower energy density for OER [65,91,92].

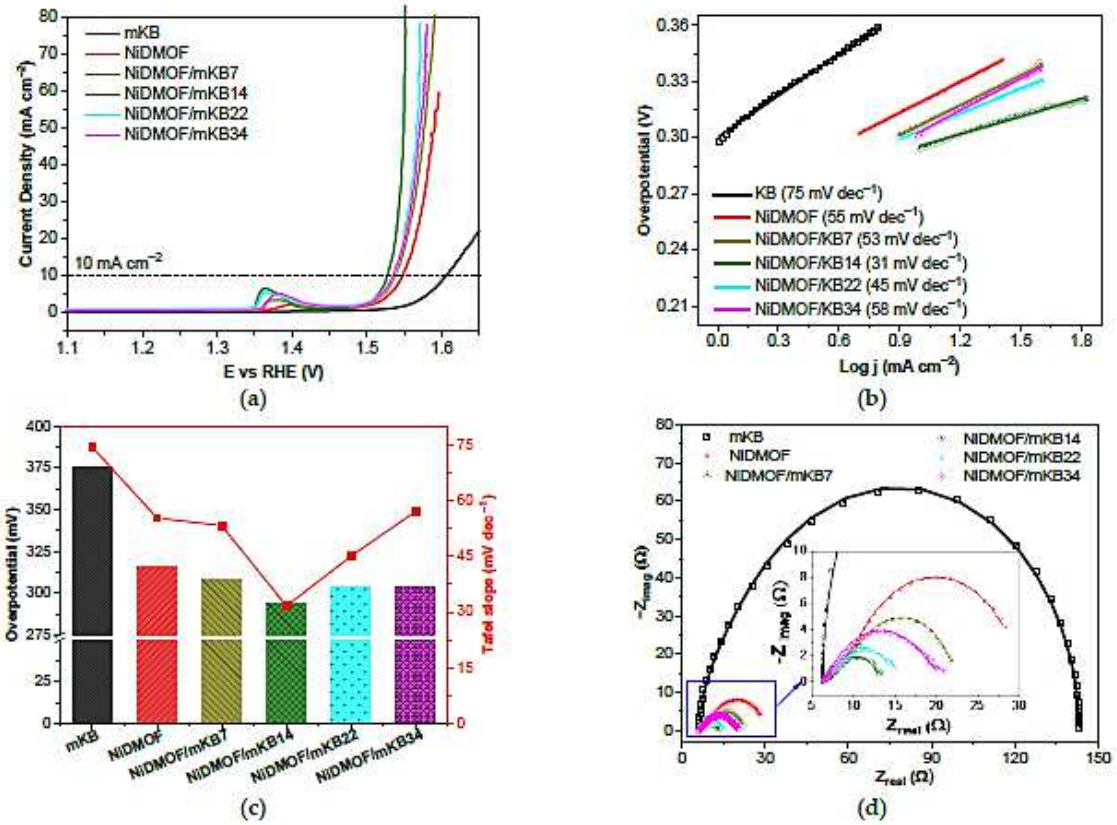

Figure 5. (a) Polarization curves (LSV) operated at a scan rate of 5 mV s^{-1} with the iR correction. (b) Tafel plots, (c) corresponding overpotentials (columns) and Tafel slopes (red dots) at 10 mA cm^{-2}, (d) raw data of Nyquist plots at 1.5 V vs. RHE (points) and fitting to an equivalent circuit model (Figure S16, Supplementary Materials) (solid line) from the EIS test of mKB, NiDMOF, NiDMOF/mKB7, NiDMOF/mKB14, NiDMOF/mKB22, and NiDMOF/mKB34.

Furthermore, electrochemical impedance spectroscopy (EIS) was carried out to assess the kinetics of the electrode reaction. The corresponding Nyquist plots (Figure 5d) obtained in a frequency range from 0.01 to 100 kHz with an AC potential amplitude of 5 mV at 1.5 V (RHE) were fitted to the simplified equivalent circuit by Doyle et al. for OER (Figure S16, Supplementary Materials) [30,93–95]. The kinetics of the interfacial charge transfer reaction corresponded to the resistive components R_s and R_p in terms of the electrocatalytic capabilities of the oxide layer. In particular, the polarization resistance (R_p) is considered as a total charge transfer resistance across multiple steps of OER, while R_s is related to the rate of production of one or more surface intermediates [30,93–95]. More detailed information concerning the circuit parameters is given in Figure S16. From the shape of the semicircles in the Nyquist plots, it can be seen that NiDMOF and the NiDMOF/mKBx composites follow a similar trend. Smaller semicircles are displayed by the NiDMOF/mKBx composites, which reflect smaller resistances at high frequency compared with both the pure NiDMOF and mKB, which illustrates that the kinetic performances of the neat MOF materials were improved by the integration of mKB. The low polarization resistance R_p (4Ω) and resistance adsorption components of the reaction intermediate R_s (2 Ω) for NiDMOF/mKB14 indicate a superior charge transfer rate and the easier formation of active species for OER, respectively, which contribute to its highest catalytic activity among the composites (Table S4, Supplementary Materials). Thus, mKB lowers the

overall resistances, which is considered to be a key factor in enhancing the electrochemical performance of MOF-based composites.

It has been intensively studied that Fe can be advantageously incorporated into Ni-based catalysts. With a small amount of Fe, the catalytic activity toward OER can be significantly improved [26,28,30,31,33,44,55]. In order to investigate the effect of Fe on the electrocatalytic NiDMOF performance, a bimetallic Ni(Fe)DMOF and the Ni(Fe)DMOF/mKB14 composite were prepared and measured under the same conditions. The presence of a small amount of Fe at a Ni:Fe ratio of ~30:1 can significantly enhance the OER performance. The Ni(Fe)DMOF without mKB already exhibited an enhanced OER performance with a much lower overpotential of 301 mV at the current density of 10 mA cm^{-2}, which was much smaller compared to the commercial RuO_2 benchmark (317 mV) and pristine NiDMOF (315 mV). The composite of Ni(Fe)DMOF with 14 wt.% mKB further enhanced the OER activity, giving the smallest overpotential of only 279 mV among the materials reported here (Figure 6a,c). These results strongly demonstrate that Fe plays a key role in improving the OER activities of pure NiDMOF and its composites. As shown in Figure 6b,c, the Tafel slope calculated from the corresponding LSV curve of bimetallic Ni(Fe)DMOF was 40 mV dec^{-1}, which is in agreement with a thin-film of Ni–Fe oxide [96] and outperformed the monometallic NiDMOF (55 mV dec^{-1}). Ni(Fe)DMOF/mKB14 presented the lowest Tafel slope (25 mV dec^{-1}) compared to RuO_2 (56 mV dec^{-1}) and all DMOFs and composites investigated here (Table S4, Supplementary Materials), reflecting the fastest kinetics. The results indicate a change in the mechanism where the rate-determining step becomes the evolution of O_2 (Reaction (5)). Furthermore, the Ni(Fe)DMOF/mKB14 composite stands out as one of the best in the recently reported most advanced Ni-based electrocatalysts with both its low overpotential (279 mV) and Tafel slope (25 mV dec^{-1}) (Table S4, Supplementary Materials). A lower overpotential was reported for Ni(Fe)-MOF-74/KB (48 wt.% KB) (274 mV) [55], Ni(Fe)$(OH)_2$/KB (47 wt.% KB) (265 mV) [55], and Fe-doped HXP@NC800 (266 mV) [97] (all at 10 mA cm^{-2}), albeit with larger Tafel slopes of 40, 55, and 49 mV dec^{-1}, respectively. From Figure S15, it can be seen that even after 1000 CVs, the overpotential of the catalysts only slightly changed from 301 mV to 318 mV for the Ni(Fe)DMOF precursor and from 279 mV to 285 mV for Ni(Fe)DMOF/mKB14 (at 10 mA cm^{-2}), indicating their long-term activity. Furthermore, electrochemical impedance spectrometry (EIS) measurements were carried out to understand the charge-transfer kinetics during the OER process among the different samples. As shown by the Nyquist plots (Figure 6d) and fitted data of the equivalent circuit model in Figure S16, the resistances of the charge-transfer and adsorption components of the reaction intermediates of Ni(Fe)DMOF/mKB14 (R_p 4 Ω and R_s 2 Ω) was as low as NiDMOF/mKB14 (R_p 4 Ω and R_s 2 Ω), that is, lower than that of RuO_2 (R_p 23 Ω and R_s 4 Ω), NiDMOF (R_p 21 Ω and R_s 7 Ω), and Ni(Fe)DMOF (R_p 6 Ω and R_s 4 Ω) (Table S4, Supplementary Materials). The polarization resistance (R_p) of Ni(Fe)DMOF/KB14 was much smaller than that of $Ni_{32}Fe$ oxide (17.1 Ω) [30], IrO_2 (~5 Ω) [86], $NiCo_2O_4$ (~8 Ω) [86], $Ni_{1.7}Co_{1.3}O_4$ (~6 Ω) [98], H-$SCF_{0.55}$ (~58 Ω) [99] (all data fitted with the same equivalent circuit model). The catalyst from the Ni(Fe)DMOF/mKB14 precursor presented the smallest charge-transfer resistance, which indicates its faster electron transport kinetics and intrinsic excellent electrical conductivity, well in accordance with its lowest overpotential. This result is in good agreement with the identified higher catalytic activity of Ni(Fe)-MOFs compared to analogous Ni-MOFs [30,55,100,101]. In particular, the presence of iron promotes the oxidation of nickel from +2 to +3, the latter seen as the active state of fast reaction kinetics and enhanced conductivity.

Loading a catalyst on a porous Ni foam (NF) electrode can further improve the reaction rate of OER [102]. Because of its metallic conductivity and 3D macroporous structure, NF provides a large surface area and facilitates mass transport during OER [30]. The catalyst ink was loaded by the drop-casting method on the surface of NF with a good distribution of the ink layer on the scaffold of the NF. The sample Ni(Fe)DMOF/mKB14, which showed the best OER activity on the glassy carbon RDE, was deposited on NF (1 cm^2) (Figure S17, Supplementary Materials). The LSV curves in Figure 7a showed

that the activity of Ni(Fe)DMOF/mKB14@NF was much higher than the pure NF substrate, reaching current densities of 10 and 50 mA cm^{-2} with overpotentials of 247 and 291 mV, respectively. A practical current density of 400 mA cm^{-2} could be delivered for Ni(Fe)DMOF/mKB14@NF at a low overpotential of 381 mV. This performance was better than the benchmark RuO_2@NF as an OER catalyst with overpotentials of 278 and 340 mV at current densities of 10 and 50 mA cm^{-2}, respectively (Figure 7a), the latter being in good accordance with the literature [103]. The pure NF electrode showed a much lower OER activity with an overpotential of 370 mV at 10 mA cm^{-2}, similar to the literature [103].

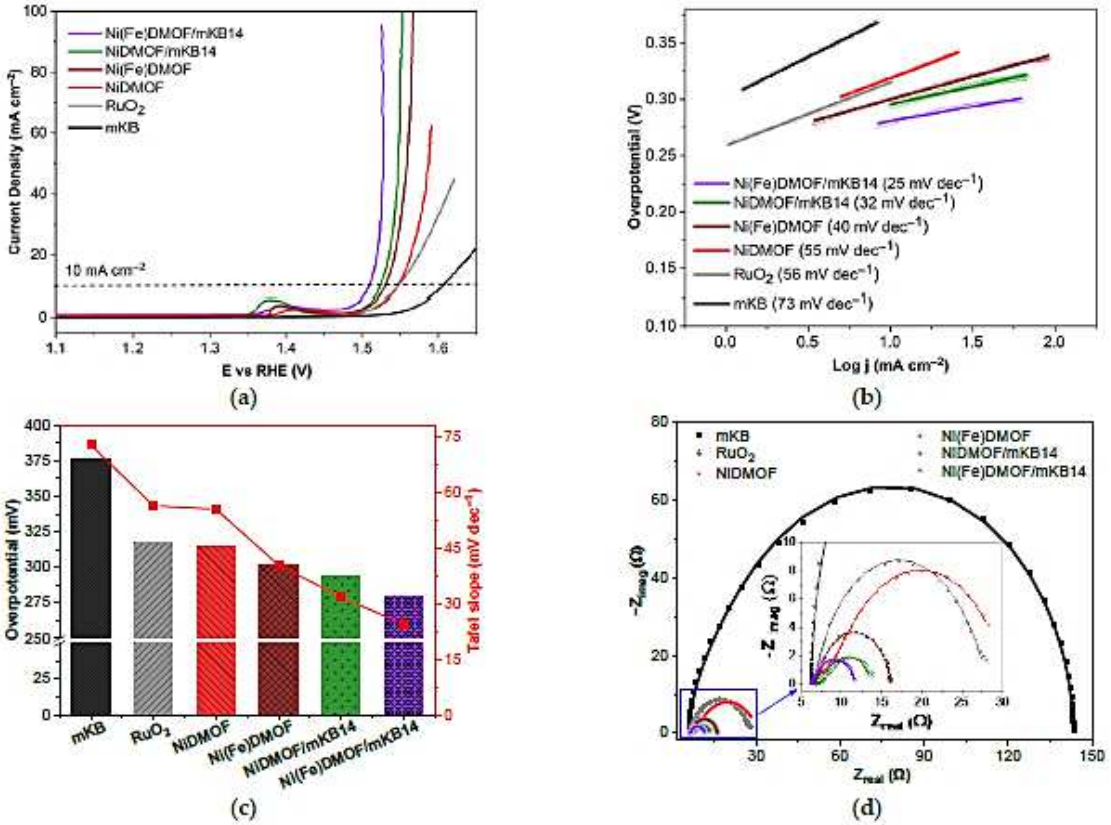

Figure 6. (**a**) Polarization curves (LSV) operated at a scan rate of 5 mV s^{-1} with iR correction, (**b**) Tafel plots, (**c**) corresponding overpotentials (columns) and Tafel slopes (red dots) at 10 mA cm^{-2}, (**d**) raw data of Nyquist plots at 1.5 V vs. RHE (points) and the fitting data of an equivalent circuit model (Figure S16, Supplementary Materials) (solid line) from the EIS test of mKB, RuO_2, NiDMOF, Ni(Fe)DMOF, NiDMOF/mKB14, and Ni(Fe)DMOF/mKB14.

The stability of an electrocatalyst determined by chronoamperometry is a key parameter to evaluate the practical application of a material. A long-term stability measurement was carried out by applying a potential to reach a constant current density of 50 mA cm^{-2} for 30 h (Figure 7b). The applied potential could be gradually decreased during the first 2.5 h, indicating that the Ni–Fe catalyst was activated under the anodic potential in 1 mol L^{-1} KOH electrolyte. After this time, the potential remained nearly unchanged during the rest of the 30 h measurement. In contrast, the bare NF electrode showed an increasing potential over time for delivering a current density of 50 mA cm^{-2} due to the oxidation of nickel, which occurs at the surface of the foam but can also reach its subsurface during electrolysis under a high current density [30,104]. Pure NF also necessitates a much higher potential at the current density of 50 mA cm^{-2} than Ni(Fe)DMOF/mKB14@NF during the 30 h of the chronoamperometry test. The catalyst derived from Ni(Fe)DMOF/mKB14 does

not only have a robust stability, but also an outstanding activity to deliver a high current density, which demonstrates that the Ni(Fe)DMOF/mKB14 precursor has the potential to serve as a good OER catalyst for practical applications.

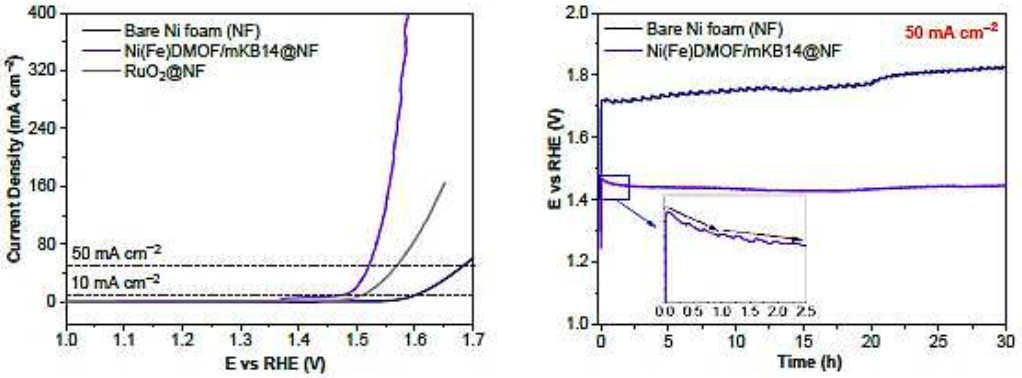

Figure 7. (a) Linear sweep voltammetry (LSV) curves at a scan rate of 5 mV s^{-1} with iR correction. (b) Chronopotentiometric curves for 30 h at a current density of 50 mA cm^{-2} of the NiFe-DMOF/mKB14 loaded on nickel foam (NF) and bare NF for comparison in a 1.0 mol L^{-1} KOH solution.

In order to understand the transformation of the precursors Ni(Fe)DMOF and Ni(Fe)DMOF/mKB14 in the alkaline electrolyte (1 mol L^{-1} KOH), we reacted macroscopic amounts of these samples in 1 mol L^{-1} KOH, followed by PXRD, FTIR, SEM, and N_2 sorption measurements to mimic post-mortem experiments of the minuscule electrode materials. The derived materials were collected by filtration after soaking Ni(Fe)DMOF and Ni(Fe)DMOF/mKB14 in 1 mol L^{-1} KOH electrolyte for 24 h and were dried for at least 12 h at 120 °C under vacuum (<10^{-2} mbar). The PXRD pattern of the derived-Ni(Fe)DMOF/mKB14 (Figure 8a) showed the disappearance of the crystalline MOF and suggests the formation of α/β–$Ni(OH)_2$, β–NiOOH, and γ–NiOOH from the reflections assigned in Figure 8a based on the patterns of nickel(II) hydroxides and nickel(III) oxide-hydroxides. This implies the transformation from Ni(Fe)DMOF/mKB14 to nickel and iron oxide-hydroxides under a strong alkaline environment (1 mol L^{-1} KOH) [105], which has also been observed by other researchers [106–110]. The FTIR of the derived-materials (Figure 8b and Table S1) showed two broad bands at ~3400 and ~3600 cm^{-1}, which corresponded to the stretching vibrations of the adsorbed water molecules and to the O–H stretching vibrations, as in $Ni(OH)_2$. At the same time, bands due to the asymmetric vibration $\nu_{asym}COO^-$ and the bending vibrations of the adsorbed water molecules of the δO–H hydroxyl groups of the BDC phenyl ring at ~1600 and ~1570 cm^{-1}, along with $\nu_{sym}COO^-$ at ~1350 cm^{-1}, decreased in intensity. New strong bands at 516 and 450 cm^{-1} were attributed to the Ni–OH bending vibrations in $Ni(OH)_2$ and the oxide-hydroxides [111]. Interestingly, the morphology of Ni(Fe)DMOF/mKB14, as seen with SEM (Figure 8c), did not change profoundly. The rod shape of Ni(Fe)DMOF was largely retained in the alkaline treatment. Accordingly, N_2 physisorption measurements at 77 K revealed a residual BET surface area and micro-mesoporosity in the derived-Ni(Fe)DMOF and derived-Ni(Fe)DMOF/mKB14 (Figure 8d). The derived-Ni(Fe)DMOF displayed a Type IV isotherm with H2(b) hysteresis (associated with pore blocking) [72] and a BET surface area of 222 m^2 g^{-1}. The adsorption isotherm of the derived-Ni(Fe)DMOF/mKB14 lacked the final saturation plateau of a Type IV isotherm and appeared like a Type II isotherm with an H_3 hysteresis, which would be given by a largely macroporous adsorbent. The pore size distribution curves showed mostly mesopores (>2 nm) for the derived-Ni(Fe)DMOF and the coexistence of micropores and mesopores for the derived-Ni(Fe)DMOF/mKB14 with micropores and small mesopores due to the mKB part (the macropore size is not given by N_2 sorption).

The BET surface area of the derived-Ni(Fe)DMOF/mKB14 was 352 $m^2\ g^{-1}$ with the increase over derived-Ni(Fe)DMOF coming from the mKB portion. Overall, a hierarchical porous nature of derived-Ni(Fe)DMOF/mKB14 was evidenced by its isotherm and hysteresis shape and the analysis of the pore size distribution. The decomposition of the Ni-MOF precursor and transformation to $Ni(OH)_2$/NiOOH was also observed in other work [112–114]. The OER activity of the Ni(Fe)DMOF precursor is due to the in situ formation of α/β-$Ni(OH)_2$/FeOOH, followed by β/γ–NiOOH under the oxidizing anodic potential, which favors the kinetics of OER [43,44,115–117]. Furthermore, the degradation of the micro-mesoporosity of Ni(Fe)DMOF in an alkaline environment provides a large number of accessible active Ni (and promoter Fe) sites in the still porous hydroxides, which show better electrochemical activities and longer cycle numbers than crystalline and dense metal oxide catalysts [42,43,118–121]. In addition, a suitable amount of mKB (14 wt.%) in the composites provides electrical conductivity with its small particle size, mixes well with the Ni active sites, and avoids the carbon corrosion effect of carbon materials [59–66].

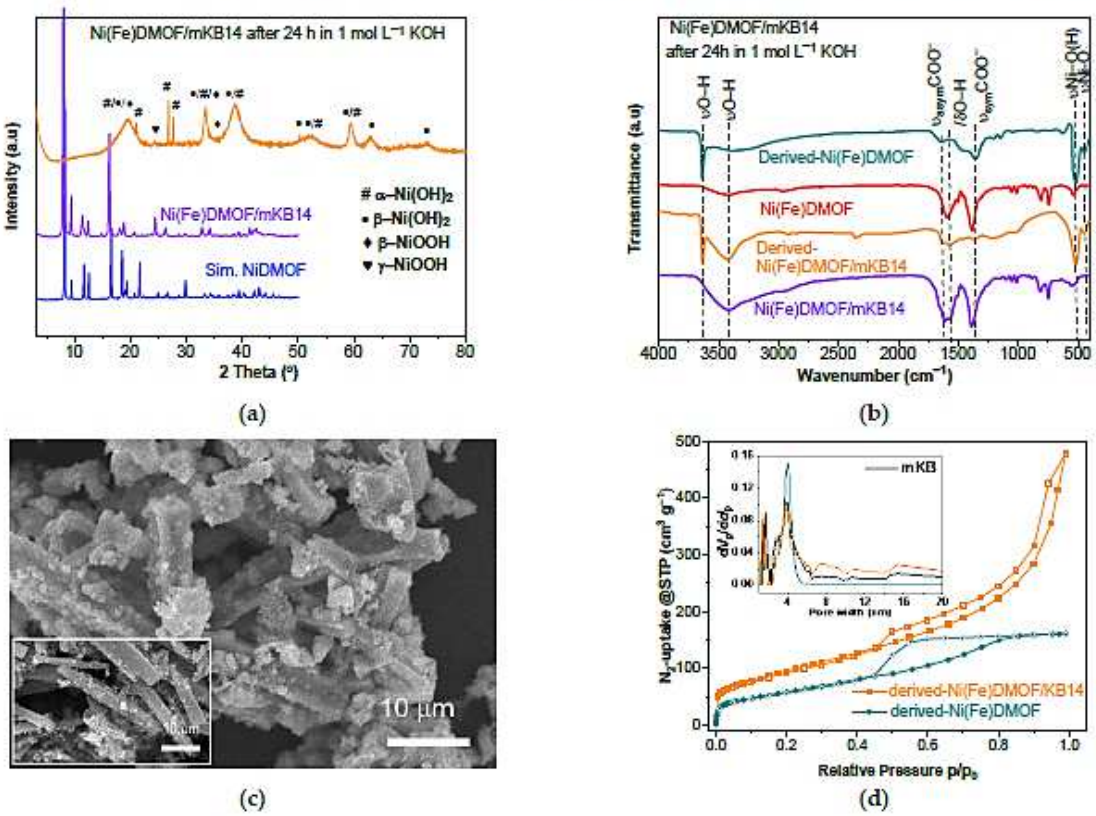

Figure 8. (**a**) PXRD patterns of the experimental Ni(Fe)DMOF/mKB14 and derived-Ni(Fe)DMOF/mKB14 after 24 h in 1 mol L^{-1} KOH and simulated NiDMOF (CCDC Nr. 802892). Reflections from β–$Ni(OH)_2$ (•, ICDD: 14-0117), α–$Ni(OH)_2$ (#, ICDD: 38-0715), β–NiOOH (◆, ICDD: 06-0141), and γ–NiOOH (▼, ICDD: 06-0075). (**b**) FTIR of Ni(Fe)DMOF and Ni(Fe)DMOF/mKB14 and its derived products in 1 mol L^{-1} KOH after 24 h. (**c**) SEM images of the derived-Ni(Fe)DMOF/mKB14 material (large image) and neat Ni(Fe)DMOF/mKB14 (small image). (**d**) Nitrogen sorption isotherms at 77 K (filled symbols adsorption, empty symbols desorption isotherm) and pore size distribution (small graph) of derived-Ni(Fe)DMOF and derived-Ni(Fe)DMOF/mKB14 after 24 h in 1 mol L^{-1} KOH.

3. Materials and Methods

3.1. Materials

Nickel(II) nitrate hexahydrate ($Ni(NO_3)_2{\cdot}6H_2O$, Merck, Darmstadt, Germany), iron(II) acetate ($Fe(OAc)_2$, 99.99%, Sigma-Aldrich, St. Loius, MO, USA), ruthenium(IV) oxide (RuO_2, 99.9%, Sigma-Aldrich, St. Loius, MO, USA), benzene-1,4-dicarboxylic acid (H_2BDC, 98%, Alfa Aesar, Karlsruhe, Deutschland), 1,4-diazabicyclo[2.2.2]octane (DABCO, 98%, Sigma-Aldrich, St. Loius, MO, USA), perfluorinated resin solution containing Nafion™ 1100W (5 wt.% in lower aliphatic alcohols and water, Sigma-Aldrich, St. Loius, MO, USA), potassium hydroxide solution (KOH, 1 mol L^{-1}, Carl Roth, Karlsruhe, Germany), nitric acid (HNO_3, 65%, Sigma-Aldrich, Darmstadt, Germany), *N*,*N*-dimethylformamide (DMF, 99.99 %, Fisher, Schwerte, Germany), Ketjenblack EC 600 JD (AkzoNobel, Amsterdam, The Netherlands), and methanol (MeOH, 99.98 %, Sigma-Aldrich, Darmstadt, Germany) were purchased and used without further purification. Nickel foam (NF) was obtained from Racemat BV (Dodewaard, The Netherlands), cleaned with 1 mol L^{-1} HCl solution in an ultrasound bath for 5 min to remove the surface nickel oxide layer of the NF and then rinsed with Millipore water (residual conductivity 18.2 MΩ·cm).

3.2. Synthesis of Modified Ketjenblack Carbon (mKB)

The amount of 10 g KB was dispersed into 1 L of HNO_3 (20 wt.%) to form a homogeneous black dispersion that was heated to 80 °C under continuous stirring. After 3 h, the product was separated by centrifugation (10,000 rpm, 10 min) and washed with deionized water (500 mL) until the pH value was 7. Yield: 9.58 mg. This modified Ketjenblack carbon was denoted as mKB. Elemental analysis for Ketjenblack carbon: C 97.91 (O 2.91)% and modified Ketjenblack carbon: C 87.93, H 0.79 (O 11.28)%. IR (ATR, cm^{-1}); 3435 (νOH), 1740 (νC=O), 1550 ($\nu_\delta OCO^-$), and 1181 (ν_sC–OO).

3.3. Synthesis of NiDMOF

NiDMOF was synthesized by a solvothermal reaction according to the literature with a slight modification [75]. $Ni(NO_3)_2{\cdot}6H_2O$ (183.12 mg, 0.63 mmol), H_2BDC (104.66 mg, 0.63 mmol), and DABCO (36.33 mg, 0.32 mmol) were added into 16 mL of *N*,*N*-dimethylformamide (DMF). The resulting slurry was stirred overnight at room temperature to obtain a homogeneous dispersion. The clear solution was collected and transferred into a Pyrex tube and then heated at 120 °C for 48 h. After cooling to room temperature, the green crystalline powder was separated by centrifugation (10,000 rpm, 10 min) and washed three times with DMF (20 mL each). The washing process was repeated three more times with MeOH (20 mL each) and the product collected by centrifugation (10,000 rpm, 10 min). The product was activated at 120 °C under vacuum (<10^{-2} mbar) for at least 12 h and finally stored under nitrogen.

Yield: 200 mg (57% based on H_2BDC). Elemental analysis for $[Ni_2(C_8H_4O_4)_2(C_6H_{12}N_2)]{\cdot}(H_2O)_{0.5}$ (MW 566.79 g mol^{-1}), calculated C 46.62, H 3.73, N 4.94, Ni 20.71 %; $[Ni_2(C_8H_4O_4)_2(C_6H_{12}N_2)]{\cdot}H_2O$ (MW 575.81 g mol^{-1}), calculated C 45.89, H 3.85, N 4.87, Ni 20.39%; found C 45.26, H 3.61, N 4.94, Ni 20.82%.

3.4. Synthesis of Ni(Fe)DMOF

The bimetallic Ni(Fe)DMOF was synthesized by a similar procedure to the monometallic NiDMOF. The amount of $Ni(NO_3)_2{\cdot}6H_2O$ (177.65 mg, 0.61 mmol), H_2BDC (104.66 mg, 0.63 mmol), and DABCO (36.33 mg, 0.32 mmol) were dispersed into 11 mL of DMF. The resulting slurry was stirred overnight at room temperature to obtain a homogeneous dispersion. To this solution, 0.02 mmol of $Fe(OAc)_2$ (3.32 mg) in 5 mL of DMF was added dropwise (for an intended molar Ni:Fe ratio of 32:1). After sonicating for 30 min, the mixture was sealed into a Pyrex tube and heated at 120 °C for 48 h. After cooling to room temperature, the palm-leaf crystalline powder was separated by centrifugation (10,000 rpm, 10 min) and washed three times with DMF (20 mL each). The washing process was repeated three more times with MeOH (20 mL each) and the product collected by centrifugation

(10,000 rpm, 10 min). The product was activated at 120 °C under vacuum (<10^{-2} mbar) for at least 12 h and stored under nitrogen.

Yield: 191 mg (54% based on H_2BDC). Elemental analysis for $[Ni_{1.94}Fe_{0.06}(C_8H_4O_4)_2(C_6H_{12}N_2)](H_2O)_{0.5}$ (MW 566.61 g mol^{-1}), calculated: C 46.63, H 3.74, N 4.94, Ni 20.10, Fe 0.59%; $[Ni_{1.94}Fe_{0.06}(C_8H_4O_4)_2(C_6H_{12}N_2)]\cdot(H_2O)$ (MW 573.88 g mol^{-1}), calculated: C 45.90, H 3.85, N 4.87, Ni 19.78, Fe 0.58%; found C 46.35, H 3.57, N 5.01, Ni 20.85, Fe 0.66%.

3.5. Synthesis of NiDMOF/mKBx and Ni(Fe)DMOF/mKB14

The composites NiDMOF/mKBx and Ni(Fe)DMOF/mKB14 were synthesized according to the above procedures described for NiDMOF and Ni(Fe)DMOF, except that the modified Ketjenblack carbon (mKB) powder (12, 24, 40 and 66 mg) was dispersed in 3 mL of DMF by sonication for 30 min in advance and then added into the metal salt/H_2BDC/DABCO/DMF solution. In order to determine the MOF and mKB content in the final composite, the metal wt.% in the NiDMOF/mKBx composites was determined by flame atomic absorption spectroscopy (AAS). From these metal wt.% of the AAS results, the mass fractions of the MOF were calculated from which the mKB wt.% in the composites was taken as the difference to 100% (Table S2, Supplementary Materials).

The NiDMOF/mKBx composites had mKB contents of x = 7, 14, 22, and 34 wt.%. For Ni(Fe)DMOF, the mKB content in the composite was 14 wt.%. NiDMOF is a green crystalline powder, but its mKB composites had an increasing darker color with increasing mKB content.

Yields: 61% NiDMOF/mKB7, 65% NiDMOF/mKB14, 70% NiDMOF/mKB22, 76% NiDMOF/mKB34, 62% Ni(Fe)DMOF/mKB14, based on H_2BDC.

3.6. Materials Characterization

Powder X-ray diffraction (PXRD) data were collected with a Rigaku Miniflex 600 powder diffractometer (Rigaku, Tokyo, Japan) using a low background silicon sample holder and Cu-Kα irradiation (λ = 1.54184 Å). The measurements were conducted over a 2θ = 2–100° range with a scan speed of 1.5 deg min^{-1} (600 W, 40 kV, 15 mA). The diffractograms were analyzed using the software Match 3.1.0.

The Fourier transform infrared (FTIR) spectra of all the samples were recorded on a Bruker FTIR Tensor 37 spectrometer (Bruker AXS, Karlsruhe, Germany) in attenuated total reflection (ATR) mode with a diamond crystal or as KBr pellets in the range of 400–4000 cm^{-1}.

^1H MNR measurements were performed with a Bruker Advance III-300 (Bruker, Karlsruhe, Germany) operating at 300 MHz. Before dissolution under digestion for the solution NMR measurement, the MOF samples were activated at 150 °C for at least 20 h under vacuum (<10^{-2} mbar) in order to remove the residual solvent molecules. Then, the amount of 5 mg of each activated sample was dissolved with decomposition in 0.8 mL DMSO-d_6 and 50 µL D_2SO_4.

Nitrogen sorption isotherms were obtained with a Belsorp MAXII (Microtrac MRB, Haan, Germany) high precision gas/vapor adsorption measurement instrument at 77 K and evaluated with the BELMaster MAXII software (version 7.3.2.0). Prior to the measurement, the materials were activated by degassing under vacuum (10^{-2} mbar) at 120 °C for 12 h. Brunauer–Emmett–Teller (BET) surface areas were determined from the nitrogen adsorption isotherms and the pore size distributions were derived by non-local density functional theory (NLDFT) calculations based on the "nitrogen at 77 K with slit pores" method. The total pore volumes were calculated from the adsorbed volume at $p/p_0 = 0.95$.

Elemental analysis (CHNS) was carried out using an Elementar Analysensysteme vario MICRO cube instrument (Elementar Analysensysteme, Langenselbold, Germany). The samples were dried at 150 °C under a vacuum (<10^{-2} mbar) for at least 20 h prior before the measurement.

Flame atomic absorption spectroscopy (AAS) was conducted with a PinAAcle 900T from PerkinElmer (Perkin Elmer LAS GmbH, Rodgau-Jügesheim, Germany). Exactly

weighted samples (15–20 mg) were heated and stirred with concentrated hydrochloric acid overnight. The solution was carefully filtered and diluted with Millipore water to a volume of 25 mL and again by a factor of 1:50 for the AAS measurements.

Scanning electron microscopy (SEM) images were collected with a Jeol JSM-65 10 LV QSEM (Jeol, Akishima, Japan) advanced electron microscope with a LaB_6 cathode at 20 kV equipped with a Bruker Xflash 410 (Bruker AXS, Karlsruhe, Germany) silicon drift detector for energy-dispersive X-ray spectrometric (EDX) elemental composition analysis. The signals of Cu, Zn, and Au in the EDX spectra originated from the sample holder and from the sputtering of the sample with gold prior to the investigation.

X-ray photoelectron spectroscopy (XPS) measurements were made using an ULVAC-PHI VersaProbe II microfocus X-ray photoelectron spectrometer (ULVAC-PHI, Chigasaki, Japan) equipped with a polychromatic aluminum Kα X-ray source (1486.8 eV). Experimental XP spectra were fitted by the CasaXPS, version 2.3.19PR1.0 from Casa Software Ltd. Program (Casa Software Ltd., Teignmouth, UK). A standard Shirley baseline with no offset was used for the background correction. Binding energies were calibrated to the carbon 1s orbital with a binding energy of 284.8 eV. In the case of the Fe 2p spectra, an additional correction was necessary due to the presence of a Ni-LMM Auger peak.

3.7. Electrochemical Measurements

Electrocatalytic measurements were carried out on an Interface 1010E potentiostat from Gamry Instruments with an RRDE-3A station from ALS Japan using a three-electrode configuration. The system consists of a coiled platinum wire as a counter electrode and a reversible hydrogen electrode (RHE) from Gaskatel (Kassel, Deutschland) as a reference electrode. Working electrodes were fabricated by depositing the prepared materials on a rotating disc electrode (RDE, 5 mm diameter, 0.196 cm^2 area), here, a rotating disc glassy carbon electrode (GCE, GC-RDE). The amount of 2.5 mg of MOF or MOF/mKB was dispersed in methanol (0.5 mL) with 25 µL of Nafion (around 5% in a mixture of water and lower aliphatic alcohols) as the binding agent. The suspension was sonicated for 30 min to form a homogeneous ink. Then, 10 µL of the prepared ink was dropped onto the rotating disc electrode (loading 0.25 mg cm^{-2}) and dried at room temperature. As an electrolyte, 1 mol L^{-1} KOH solution (pH: 14) was used and nitrogen was purged for 10 min through the cell to remove oxygen before the test. The working electrode was kept rotating at a rate of 1600 rpm during the measurements. The electrode was pre-cycled for at least 20 cycles at a sweep rate of 100 mV cm^{-1} between 1.0 and 1.7 V until reaching the steady state. All linear scanning voltammetry (LSV) curves were collected by sweeping the potential from 0.8 to 1.7 V vs RHE with a scan rate of 5 mV s^{-1}. Cyclic voltammetry (CV) measurements were carried out in the potential range between 1.0 and 1.7 V vs. RHE with a scan rate of 100 mV s^{-1}. iR compensation was completely applied to the recorded data afterward, as recommended in the literature [122]. In all measurements, R_u (uncompensated electrolyte resistance) was measured by electrochemical impedance spectroscopy (EIS) at the open circuit potential (OCP) and the iR_u drop was compensated automatically by the R_u value using the software Gamry Echem Analyst., Version 7.8.2.

The overpotential η was derived from the standard potential E vs. RHE using the formula:

$$\eta = \text{ERHE} - 1.23\ \text{V}. \quad (6)$$

The Tafel slope b was obtained by fitting the linear portion of the Tafel plots, which were derived from the LSV curves according to the Tafel equation:

$$\eta = a + b \times \log(j). \quad (7)$$

where a is a constant and j represents the current density. Electrochemical impedance spectroscopy (EIS) data were recorded with the frequency range of 0.1–10,000 Hz at the potential of 1.5 V. To check the long-term stability of the best catalyst material at a constant current by chronopotentiometry, a Ni(Fe)DMOF/mKB@NF electrode was fabricated by

drop-casting the catalyst ink on the surface of pre-treated nickel foam and drying at room temperature. The loading was around 1 mg cm^{-2} by weighing the electrode before and after material deposition. The chronopotentiometry at 50 mA cm^{-2} was carried out with 1 cm^2 of commercial nickel foam (NF) for 30 h in 1 mol L^{-1} KOH electrolyte.

4. Conclusions

In summary, we successfully fabricated a series of novel DMOF/mKB composites containing a bimetallic nickel-iron-based pillared MOF (DMOF) and modified Ketjenblack carbon using a simple one-step hydrothermal procedure, which can be directly used as efficient electrocatalysts in OER. The appropriate mass weight % of mKB in the composite DMOF/mKB is important for the fabrication of the optimum catalyst. Benefitting from enhanced conductivity, remarkably high surface areas, and the high intrinsic catalytic activity of mKB and the integration of Ni and Fe active sites from the MOF precursors, the Ni(Fe)DMOF/mKB14 with 14 wt.% mKB exhibited superior OER performance, which only needed a low overpotential of 279 mV and a Tafel slope of 25 mV dec^{-1} to reach the current density of 10 mA cm^{-2} in 1 mol L^{-1} of KOH electrolyte, outperforming the benchmark RuO_2 catalyst and many state-of-the art MOF-based and Ni-Fe-based OER catalysts. For the practical application, the working electrode was fabricated by depositing optimized Ni(Fe)DMOF/mKB14 electrocatalysts on commercial nickel foam, where the current density at 10 and 50 mA cm^{-2} was realized at 247 and 291 mV, respectively, and the activity was maintained for 30 h of applied bias. The superior OER performance is associated with the transformation of Ni(Fe)DMOF into highly functionalized α/β-$Ni(OH)_2$/β/γ-NiOOH and FeOOH inherited from the DMOF structure. The presented DMOF/mKB material preparation strategy is applicable to the development of high-performance electrode materials for other advanced energy storage systems.

Supplementary Materials: The following supporting information can be downloaded at: https://www.mdpi.com/article/10.3390/molecules28114464/s1, Section S1: 3D framework structure of NiDMOF; Section S2: Powder X-ray diffraction (PXRD) measurements; Section S3: Fourier-transform infrared (FT-IR) spectroscopy; Section S4: NMR spectroscopy; Section S5: Elemental analysis; Section S6: Nitrogen sorption experiments (T = 77 K); Section S7: Scanning electron microscopy (SEM); Section S8: X-ray photoelectron spectra (XPS); Section S9: Electrochemical measurements. References [123–131] are cited in the Supplementary Materials.

Author Contributions: Conceptualization, C.J. and T.H.Y.B.; Methodology, T.H.Y.B.; Validation, T.H.Y.B.; Formal analysis, T.H.Y.B.; Investigation, T.H.Y.B., L.R. and R.O.; Resources, C.J.; Data curation, T.H.Y.B.; Writing—original draft preparation, T.H.Y.B.; Writing—review and editing, C.J.; Visualization, T.H.Y.B.; Supervision, C.J.; Project administration, C.J.; Funding acquisition, C.J. All authors have read and agreed to the published version of the manuscript.

Funding: This research was funded by a joint National Natural Science Foundation of China–Deutsche Forschungsgemeinschaft (NSFC-DFG) project (DFG JA466/39-1).

Institutional Review Board Statement: Not applicable.

Informed Consent Statement: Not applicable.

Data Availability Statement: The data presented in this study are available on request from the corresponding author.

Acknowledgments: The authors also thank the Center for Molecular and Structural Analytics at Heinrich Heine University (CeMSA@HHU) for recording the NMR-spectrometric data. The authors thank Birgit Tommes for carrying out the FTIR experiments, Annette Ricken for the AAS measurements.

Conflicts of Interest: The authors declare no conflict of interest.

Sample Availability: Samples of the compounds will not be available.

References

1. Lianos, P. Review of recent trends in photoelectrocatalytic conversion of solar energy to electricity and hydrogen. *Appl. Catal. B* **2017**, *210*, 235–254. [CrossRef]
2. Chu, S.; Cui, Y.; Liu, N. Opportunities and challenges for a sustainable energy future. *Nat. Mater.* **2017**, *16*, 16–22. [CrossRef] [PubMed]
3. Wang, J.; Zhang, H.; Wang, X. Recent Methods for the Synthesis of Noble-Metal-Free Hydrogen-Evolution Electrocatalysts: From Nanoscale to Sub-nanoscale. *Small Methods* **2017**, *1*, 1700118. [CrossRef]
4. Shrivastav, V.; Sundriyal, S.; Goel, P.; Kaur, H.; Tuteja, S.K.; Vikrant, K.; Kim, K.-H.; Tiwari, U.K.; Deep, A. Metal-organic frameworks (MOFs) and their composites as electrodes for lithium battery applications: Novel means for alternative energy storage. *Coord. Chem. Rev.* **2019**, *393*, 48–78. [CrossRef]
5. Lee, Y.; Suntivich, J.; May, K.J.; Perry, E.E.; Shao-Horn, Y. Synthesis and Activities of Rutile IrO_2 and RuO_2 Nanoparticles for Oxygen Evolution in Acid and Alkaline Solutions. *J. Phys. Chem. Lett.* **2012**, *3*, 399–404. [CrossRef]
6. Pi, Y.; Zhang, N.; Guo, S.; Guo, J.; Huang, X. Ultrathin Laminar Ir Superstructure as Highly Efficient Oxygen Evolution Electrocatalyst in Broad pH Range. *Nano Lett.* **2016**, *16*, 4424–4430. [CrossRef]
7. Hu, C.; Zhang, L.; Gong, J. Recent progress made in the mechanism comprehension and design of electrocatalysts for alkaline water splitting. *Energy Environ. Sci.* **2019**, *12*, 2620–2645. [CrossRef]
8. Miao, X.; Wu, L.; Lin, Y.; Yuan, X.; Zhao, J.; Yan, W.; Zhou, S.; Shi, L. The Role of Oxygen Vacancies in Water Oxidation for Perovskite Cobalt Oxide Electrocatalysts: Are More Better? *Chem. Commun.* **2019**, *55*, 1442. [CrossRef]
9. Li, X.; Hao, X.; Wang, Z.; Abudula, A.; Guan, G. In-situ intercalation of NiFe LDH materials: An efficient approach to improve electrocatalytic activity and stability for water splitting. *J. Power Sources* **2017**, *347*, 193–200. [CrossRef]
10. Han, L.; Dong, S.; Wang, E. Transition-Metal (Co, Ni, and Fe)-Based Electrocatalysts for the Water Oxidation Reaction. *Adv. Mater.* **2016**, *28*, 9266–9291. [CrossRef]
11. Yu, M.; Budiyanto, E.; Tüysüz, H. Principles of water electrolysis and recent progress in cobalt-, nickel-, and iron-based oxides for the oxygen evolution reaction. *Angew. Chem. Int. Ed.* **2022**, *61*, e202103824. [CrossRef]
12. Vij, V.; Sultan, S.; Harzandi, A.M.; Meena, A.; Tiwari, J.N.; Lee, W.-G.; Yoon, T.; Kim, K.S. Nickel-based electrocatalysts for energy-related applications: Oxygen reduction, oxygen evolution, and hydrogen evolution reactions. *ACS Catal.* **2017**, *7*, 7196–7225. [CrossRef]
13. Hall, D.S.; Lockwood, D.J.; Bock, C.; MacDougall, B.R. Nickel hydroxides and related materials: A review of their structures, synthesis and properties. *Proc. Math. Phys. Eng. Sci.* **2015**, *471*, 20140792. [CrossRef]
14. Chen, Y.; Rui, K.; Zhu, J.; Dou, S.X.; Sun, W. Recent Progress on Nickel-Based Oxide/(Oxy) Hydroxide Electrocatalysts for the Oxygen Evolution Reaction. *Eur. J. Chem* **2019**, *25*, 703–713. [CrossRef]
15. Beall, C.E.; Fabbri, E.; Schmidt, T.J. Perovskite Oxide Based Electrodes for the Oxygen Reduction and Evolution Reactions: The Underlying Mechanism. *ACS Catal.* **2021**, *11*, 3094–3114. [CrossRef]
16. Tareen, A.K.; Priyanga, G.S.; Khan, K.; Pervaiz, E.; Thomas, T.; Yang, M. Nickel-Based Transition Metal Nitride Electrocatalysts for the Oxygen Evolution Reaction. *ChemSusChem* **2019**, *12*, 3941–3954. [CrossRef]
17. Wang, C.; Wu, Y.; Zhou, Z.; Wang, J.; Pei, S.; Liu, S. Electrodeposited amorphous nickel–iron phosphide and sulfide derived films for electrocatalytic oxygen evolution. *Int. J. Hydrog. Energy* **2022**, *47*, 40849–40859. [CrossRef]
18. Zhao, C.-X.; Liu, J.-N.; Wang, C.; Wang, J.; Song, L.; Li, B.-Q.; Zhang, Q. An anionic regulation mechanism for the structural reconstruction of sulfide electrocatalysts under oxygen evolution conditions. *Energy Environ. Sci.* **2022**, *15*, 3257–3264. [CrossRef]
19. Wan, K.; Luo, J.; Zhou, C.; Zhang, T.; Arbiol, J.; Lu, X.; Mao, B.-W.; Zhang, X.; Fransaer, J. Hierarchical Porous Ni_3S_4 with Enriched High-Valence Ni Sites as a Robust Electrocatalyst for Efficient Oxygen Evolution Reaction. *Adv. Funct. Mater.* **2019**, *29*, 1900315. [CrossRef]
20. Wan, K.; Luo, J.; Zhang, X.; Subramanian, P.; Fransaer, J. Sulfur-modified nickel selenide as an efficient electrocatalyst for the oxygen evolution reaction. *J. Energy Chem.* **2021**, *62*, 198–203. [CrossRef]
21. Wang, T.; Liu, X.; Yan, Z.; Teng, Y.; Li, R.; Zhang, J.; Peng, T. Facile Preparation Process of NiCoP–$NiCoSe_2$ Nano-Bilayer Films for Oxygen Evolution Reaction with High Efficiency and Long Duration. *ACS Sustain. Chem. Eng.* **2020**, *8*, 1240–1251. [CrossRef]
22. Saha, S.; Ganguli, A.K. FeCoNi Alloy as Noble Metal-Free Electrocatalyst for Oxygen Evolution Reaction (OER). *ChemistrySelect* **2017**, *2*, 1630–1636. [CrossRef]
23. Landon, J.; Demeter, E.; İnoğlu, N.; Keturakis, C.; Wachs, I.E.; Vasić, R.; Frenkel, A.I.; Kitchin, J.R. Spectroscopic Characterization of Mixed Fe–Ni Oxide Electrocatalysts for the Oxygen Evolution Reaction in Alkaline Electrolytes. *ACS Catal.* **2012**, *2*, 1793–1801. [CrossRef]
24. Subbaraman, R.; Tripkovic, D.; Chang, K.-C.; Strmcnik, D.; Paulikas, A.P.; Hirunsit, P.; Chan, M.; Greeley, J.; Stamenkovic, V.; Markovic, N.M. Trends in activity for the water electrolyser reactions on 3*d* M (Ni,Co,Fe,Mn) hydr(oxy)oxide catalysts. *Nat. Mater.* **2012**, *11*, 550–557. [CrossRef] [PubMed]
25. Stern, L.-A.; Hu, X. Enhanced oxygen evolution activity by NiO_x and $Ni(OH)_2$ nanoparticles. *Faraday Discuss.* **2014**, *176*, 363–379. [CrossRef]
26. Corrigan, D.A. The Catalysis of the Oxygen Evolution Reaction by Iron Impurities in Thin Film Nickel Oxide Electrodes. *J. Electrochem. Soc.* **1987**, *134*, 377–384. [CrossRef]

27. Louie, M.W.; Bell, A.T. An Investigation of Thin-Film Ni–Fe Oxide Catalysts for the Electrochemical Evolution of Oxygen. *J. Am. Chem. Soc.* **2013**, *135*, 12329–12337. [CrossRef]
28. Qi, J.; Zhang, W.; Xiang, R.; Liu, K.; Wang, H.-Y.; Chen, M.; Han, Y.; Cao, R. Porous Nickel–Iron Oxide as a Highly Efficient Electrocatalyst for Oxygen Evolution Reaction. *Adv. Sci.* **2015**, *2*, 1500199. [CrossRef]
29. Stevens, M.B.; Trang, C.D.M.; Enman, L.J.; Deng, J.; Boettcher, S.W. Reactive Fe-Sites in Ni/Fe (Oxy)hydroxide Are Responsible for Exceptional Oxygen Electrocatalysis Activity. *J. Electrochem. Soc.* **2017**, *139*, 11361–11364. [CrossRef]
30. Yu, M.; Moon, G.; Bill, E.; Tüysüz, H. Optimizing Ni–Fe Oxide Electrocatalysts for Oxygen Evolution Reaction by Using Hard Templating as a Toolbox. *ACS Appl. Energy Mater.* **2019**, *2*, 1199–1209. [CrossRef]
31. Fominykh, K.; Chernev, P.; Zaharieva, I.; Sicklinger, J.; Stefanic, G.; Döblinger, M.; Müller, A.; Pokharel, A.; Böcklein, S.; Scheu, C.; et al. Iron-Doped Nickel Oxide Nanocrystals as Highly Efficient Electrocatalysts for Alkaline Water Splitting. *ACS Nano* **2015**, *9*, 5180–5188. [CrossRef]
32. Burke, M.S.; Enman, L.J.; Batchellor, A.S.; Zou, S.; Boettcher, S.W. Oxygen Evolution Reaction Electrocatalysis on Transition Metal Oxides and (Oxy)hydroxides: Activity Trends and Design Principles. *Chem. Mater.* **2015**, *27*, 7549–7558. [CrossRef]
33. Burke, M.S.; Kast, M.G.; Trotochaud, L.; Smith, A.M.; Boettcher, S.W. Cobalt–Iron (Oxy)hydroxide Oxygen Evolution Electrocatalysts: The Role of Structure and Composition on Activity, Stability, and Mechanism. *J. Am. Chem. Soc.* **2015**, *137*, 3638–3648. [CrossRef]
34. Ray, C.; Lee, S.C.; Jin, B.; Kundu, A.; Park, J.H.; Jun, S.C. Stacked Porous Iron-Doped Nickel Cobalt Phosphide Nanoparticle: An Efficient and Stable Water Splitting Electrocatalyst. *ACS Sustain. Chem. Eng.* **2018**, *6*, 6146–6156. [CrossRef]
35. Li, B.; Wen, H.-M.; Zhou, W.; Chen, B. Porous metal–organic frameworks for gas storage and separation: What, how, and why? *J. Phys. Chem. Lett.* **2014**, *5*, 3468–3479. [CrossRef]
36. Ma, S.; Zhou, H.-C. Gas storage in porous metal–organic frameworks for clean energy applications. *Chem. Commun.* **2010**, *46*, 44–53. [CrossRef]
37. Yaghi, O.M.; Li, H. Hydrothermal Synthesis of a Metal-Organic Framework Containing Large Rectangular Channels. *J. Am. Chem. Soc.* **1995**, *117*, 10401–10402. [CrossRef]
38. Yaghi, O.M.; Li, G.; Li, H. Selective binding and removal of guests in a microporous metal–organic framework. *Nature* **1995**, *378*, 703–706. [CrossRef]
39. Scheurle, P.I.; Mähringer, A.; Jakowetz, A.C.; Hosseini, P.; Richter, A.F.; Wittstock, G.; Medina, D.D.; Bein, T. A highly crystalline anthracene-based MOF-74 series featuring electrical conductivity and luminescence. *Nanoscale* **2019**, *11*, 20949–20955. [CrossRef]
40. Allendorf, M.D.; Schwartzberg, A.; Stavila, V.; Talin, A.A. A roadmap to implementing metal–organic frameworks in electronic devices: Challenges and critical directions. *Chem. Eur. J.* **2011**, *17*, 11372–11388. [CrossRef]
41. Wu, H.B.; Lou, X.W. Metal-Organic Frameworks and Their Derived Materials for Electrochemical Energy Storage and Conversion: Promises and Challenges. *Sci. Adv.* **2017**, *3*, eaap9252. [CrossRef] [PubMed]
42. Zheng, W.; Lee, L.Y.S. Metal–organic frameworks for electrocatalysis: Catalyst or precatalyst? *ACS Energy Lett.* **2021**, *6*, 2838–2843. [CrossRef]
43. Singh, B.; Yadav, A.; Indra, A. Realizing electrochemical transformation of a metal–organic framework precatalyst into a metal hydroxide–oxy (hydroxide) active catalyst during alkaline water oxidation. *J. Mater. Chem. A* **2022**, *10*, 3843–3868. [CrossRef]
44. Sondermann, L.; Jiang, W.; Shviro, M.; Spieß, A.; Woschko, D.; Rademacher, L.; Janiak, C. Nickel-Based Metal-Organic Frameworks as Electrocatalysts for the Oxygen Evolution Reaction (OER). *Molecules* **2022**, *27*, 1241. [CrossRef] [PubMed]
45. Wang, J.; Kim, S.-J.; Liu, J.; Gao, Y.; Choi, S.; Han, J.; Shin, H.; Jo, S.; Kim, J.; Ciucci, F. Redirecting dynamic surface restructuring of a layered transition metal oxide catalyst for superior water oxidation. *Nat. Catal.* **2021**, *4*, 212–222. [CrossRef]
46. Gong, L.; Yang, H.; Wang, H.; Qi, R.; Wang, J.; Chen, S.; You, B.; Dong, Z.; Liu, H.; Xia, B.Y. Corrosion formation and phase transformation of nickel-iron hydroxide nanosheets array for efficient water oxidation. *Nano Res.* **2021**, *14*, 4528–4533. [CrossRef]
47. Hassan, M.H.; Soliman, A.B.; Elmehelmey, W.A.; Abugable, A.A.; Karakalos, S.G.; Elbahri, M.; Hassanien, A.; Alkordi, M.H. A Ni-loaded, metal–organic framework–graphene composite as a precursor for in situ electrochemical deposition of a highly active and durable water oxidation nanocatalyst. *Chem. Commun.* **2019**, *55*, 31–34. [CrossRef]
48. Meng, J.; Zhou, Y.; Chi, H.; Li, K.; Wan, J.; Hu, Z. Bimetallic porphyrin mof anchored onto rgo nanosheets as a highly efficient 2d electrocatalyst for oxygen evolution reaction in alkaline conditions. *ChemistrySelect* **2019**, *4*, 8661–8670. [CrossRef]
49. Zheng, X.; Cao, Y.; Liu, D.; Cai, M.; Ding, J.; Liu, X.; Wang, J.; Hu, W.; Zhong, C. Bimetallic metal–organic-framework/reduced graphene oxide composites as bifunctional electrocatalysts for rechargeable Zn–air batteries. *ACS Appl. Mater. Interfaces* **2019**, *11*, 15662–15669. [CrossRef]
50. Srinivas, K.; Chen, Y.; Wang, X.; Wang, B.; Karpuraranjith, M.; Wang, W.; Su, Z.; Zhang, W.; Yang, D. Constructing Ni/NiS heteronanoparticle-embedded metal–organic framework-derived nanosheets for enhanced water-splitting catalysis. *ACS Sustain. Chem. Eng.* **2021**, *9*, 1920–1931. [CrossRef]
51. Sohrabi, S.; Dehghanpour, S.; Ghalkhani, M. A cobalt porphyrin-based metal organic framework/multi-walled carbon nanotube composite electrocatalyst for oxygen reduction and evolution reactions. *J. Mater. Sci.* **2018**, *53*, 3624–3639. [CrossRef]
52. Wang, C.; Zhou, M.; Ma, Y.; Tan, H.; Wang, Y.; Li, Y. Hybridized Polyoxometalate-Based Metal–Organic Framework with Ketjenblack for the Nonenzymatic Detection of H_2O_2. *Chem. Asian J.* **2018**, *13*, 2054–2059. [CrossRef]
53. Peng, H.; Yang, X.; Ma, Y.; Liu, J.; Wang, Y.; Tan, H.; Li, Y. Polyoxometalate-based metal–organic framework loaded with an ultra-low amount of Pt as an efficient electrocatalyst for hydrogen production. *CrystEngComm* **2018**, *20*, 5387–5394. [CrossRef]

54. Huang, Z.-H.; Xie, N.-H.; Zhang, M.; Xu, B.-Q. Nonpyrolyzed Fe−N Coordination-Based Iron Triazolate Framework: An Efficient and Stable Electrocatalyst for Oxygen Reduction Reaction. *ChemSusChem* **2019**, *12*, 200–207. [CrossRef]
55. Öztürk, S.; Moon, G.-H.; Spieß, A.; Budiyanto, E.; Roitsch, S.; Tüysüz, H.; Janiak, C. A Highly-Efficient Oxygen Evolution Electrocatalyst Derived from a Metal-Organic Framework and Ketjenblack Carbon Material. *ChemPlusChem* **2021**, *86*, 1106–1115. [CrossRef]
56. Maniam, P.; Stock, N. Investigation of Porous Ni-Based Metal–Organic Frameworks Containing Paddle-Wheel Type Inorganic Building Units via High-Throughput Methods. *Inorg. Chem.* **2011**, *50*, 5085–5097. [CrossRef]
57. Zhang, Q.; Li, T.; Liang, J.; Wang, N.; Kong, X.; Wang, J.; Qian, H.; Zhou, Y.; Liu, F.; Wei, C. Highly wettable and metallic NiFe-phosphate/phosphide catalyst synthesized by plasma for highly efficient oxygen evolution reaction. *J. Mater. Chem. A* **2018**, *6*, 7509–7516. [CrossRef]
58. Qiu, Y.; Xin, L.; Li, W. Electrocatalytic oxygen evolution over supported small amorphous Ni–Fe nanoparticles in alkaline electrolyte. *Langmuir* **2014**, *30*, 7893–7901. [CrossRef]
59. Yaqoob, L.; Noor, T.; Iqbal, N.; Nasir, H.; Zaman, N.; Talha, K. Electrochemical synergies of Fe–Ni bimetallic MOF CNTs catalyst for OER in water splitting. *J. Alloys Compd.* **2021**, *850*, 156583. [CrossRef]
60. Abbasi, M.; Noor, T.; Iqbal, N.; Zaman, N. Electrocatalytic study of Cu/Ni MOF and its γ-C_3N_4 composites for methanol oxidation reaction. *Int. J. Energy Res.* **2022**, *46*, 13915–13930. [CrossRef]
61. Yaqoob, L.; Noor, T.; Iqbal, N.; Nasir, H.; Zaman, N. Development of Nickel-BTC-MOF-Derived Nanocomposites with rGO Towards Electrocatalytic Oxidation of Methanol and Its Product Analysis. *Catalysts* **2019**, *9*, 856. [CrossRef]
62. Fang, Y.; Li, X.; Li, F.; Lin, X.; Tian, M.; Long, X.; An, X.; Fu, Y.; Jin, J.; Ma, J. Self-assembly of cobalt-centered metal organic framework and multiwalled carbon nanotubes hybrids as a highly active and corrosion-resistant bifunctional oxygen catalyst. *J. Power Sources* **2016**, *326*, 50–59. [CrossRef]
63. Yu, S.; Wu, Y.; Xue, Q.; Zhu, J.-J.; Zhou, Y. A novel multi-walled carbon nanotube-coupled CoNi MOF composite enhances the oxygen evolution reaction through synergistic effects. *J. Mater. Chem. A* **2022**, *10*, 4936–4943. [CrossRef]
64. Jahan, M.; Liu, Z.; Loh, K.P. A Graphene oxide and copper-centered metal organic framework composite as a tri-functional catalyst for HER, OER, and ORR. *Adv. Funct. Mater.* **2013**, *23*, 5363–5372. [CrossRef]
65. Wang, H.; Han, J.; Li, L.; Peng, F.; Zheng, F.; Huang, D.; Lai, F.; Hu, S.; Pan, Q.; Li, Q. Effects of oxidized Ketjen Black as conductive additives on electrochemical performance of the LiMn2O4@Al2O3 cathode in lithium-ion batteries. *J. Alloys Compd.* **2021**, *860*, 158482. [CrossRef]
66. Guan, D.; Zhong, J.; Xu, H.; Huang, Y.-C.; Hu, Z.; Chen, B.; Zhang, Y.; Ni, M.; Xu, X.; Zhou, W.; et al. A universal chemical-induced tensile strain tuning strategy to boost oxygen-evolving electrocatalysis on perovskite oxides. *Appl. Phys. Rev.* **2022**, *9*, 011422. [CrossRef]
67. Guan, D.; Shi, C.; Xu, H.; Gu, Y.; Zhong, J.; Sha, Y.; Hu, Z.; Ni, M.; Shao, Z. Simultaneously mastering operando strain and reconstruction effects via phase-segregation strategy for enhanced oxygen-evolving electrocatalysis. *J. Energy Chem.* **2023**, *82*, 572–580. [CrossRef]
68. Li, D.-J.; Li, Q.-H.; Gu, Z.-G.; Zhang, J. A surface-mounted MOF thin film with oriented nanosheet arrays for enhancing the oxygen evolution reaction. *J. Mater. Chem. A* **2019**, *7*, 18519–18528. [CrossRef]
69. Henke, S.; Schneemann, A.; Wütscher, A.; Fischer, R.A. Directing the Breathing Behavior of Pillared-Layered Metal–Organic Frameworks via a Systematic Library of Functionalized Linkers Bearing Flexible Substituents. *J. Am. Chem. Soc.* **2012**, *134*, 9464–9474. [CrossRef]
70. Asgharnejad, L.; Abbasi, A.; Shakeri, A. Ni-based metal-organic framework/GO nanocomposites as selective adsorbent for CO_2 over N_2. *Microporous Mesoporous Mater.* **2018**, *262*, 227–234. [CrossRef]
71. Qi, J.; Zhang, W.; Cao, R. Porous Materials as Highly Efficient Electrocatalysts for the Oxygen Evolution Reaction. *ChemCatChem* **2018**, *10*, 1206–1220. [CrossRef]
72. Thommes, M.; Kaneko, K.; Neimark, A.V.; Olivier, J.P.; Rodriguez-Reinoso, F.; Rouquerol, J.; Sing, K.S.W. Physisorption of gases, with special reference to the evaluation of surface area and pore size distribution (IUPAC Technical Report). *Pure Appl. Chem.* **2015**, *87*, 1051–1069. [CrossRef]
73. Wang, X.; Niu, Z.; Al-Enizi, A.M.; Nafady, A.; Wu, Y.; Aguila, B.; Verma, G.; Wojtas, L.; Chen, Y.-S.; Li, Z.; et al. Pore environment engineering in metal–organic frameworks for efficient ethane/ethylene separation. *J. Mater. Chem. A* **2019**, *7*, 13585–13590. [CrossRef]
74. Jiang, X.; Deng, S.; Sun, L.; Liu, J.; Qi, N.; Chen, Z. Pillared nickel-based metal-organic frameworks as electrode material with high electrochemical performance. *J. Electroanal. Chem.* **2020**, *879*, 114802. [CrossRef]
75. Hungerford, J.; Bhattacharyya, S.; Tumuluri, U.; Nair, S.; Wu, Z.; Walton, K.S. DMOF-1 as a representative MOF for SO_2 adsorption in both humid and dry conditions. *J. Phys. Chem. C* **2018**, *122*, 23493–23500. [CrossRef]
76. McIntyre, N.S.; Cook, M.G. X-ray photoelectron studies on some oxides and hydroxides of cobalt, nickel, and copper. *Anal. Chem.* **1975**, *47*, 2208–2213. [CrossRef]
77. Jiang, H.; Guo, Y.; Wang, T.; Zhu, P.-L.; Yu, S.; Yu, Y.; Fu, X.-Z.; Sun, R.; Wong, C.-P. Electrochemical fabrication of $Ni(OH)_2$/Ni 3D porous composite films as integrated capacitive electrodes. *RSC Adv.* **2015**, *5*, 12931–12936. [CrossRef]
78. Lee, J.W.; Ahn, T.; Soundararajan, D.; Ko, J.M.; Kim, J.-D. Non-aqueous approach to the preparation of reduced graphene oxide/α-$Ni(OH)_2$ hybrid composites and their high capacitance behavior. *Chem. Commun.* **2011**, *47*, 6305–6307. [CrossRef]

79. Yan, J.; Fan, Z.; Sun, W.; Ning, G.; Wei, T.; Zhang, Q.; Zhang, R.; Zhi, L.; Wei, F. Advanced asymmetric supercapacitors based on $Ni(OH)_2$/graphene and porous graphene electrodes with high energy density. *Adv. Funct. Mater.* **2012**, *22*, 2632–2641. [CrossRef]
80. Yamashita, T.; Hayes, P. Analysis of XPS spectra of Fe^{2+} and Fe^{3+} ions in oxide materials. *Appl. Surf. Sci.* **2008**, *254*, 2441–2449. [CrossRef]
81. Biesinger, M.C.; Payne, B.P.; Grosvenor, A.P.; Lau, L.W.M.; Gerson, A.R.; Smart, R.S.C. Resolving surface chemical states in XPS analysis of first row transition metals, oxides and hydroxides: Cr, Mn, Fe, Co and Ni. *Appl. Surf. Sci.* **2011**, *257*, 2717–2730. [CrossRef]
82. Yin, L.I.; Yellin, E.; Adler, I. X-Ray Excited LMM Auger Spectra of Copper, Nickel, and Iron. *J. Appl. Phys.* **1971**, *42*, 3595–3600. [CrossRef]
83. Zhou, C.; Chen, X.; Liu, S.; Han, Y.; Meng, H.; Jiang, Q.; Zhao, S.; Wei, F.; Sun, J.; Tan, T.; et al. Superdurable Bifunctional Oxygen Electrocatalyst for High-Performance Zinc–Air Batteries. *J. Am. Chem. Soc.* **2022**, *144*, 2694–2704. [CrossRef] [PubMed]
84. Shinagawa, T.; Garcia-Esparza, A.T.; Takanabe, K. Insight on Tafel slopes from a microkinetic analysis of aqueous electrocatalysis for energy conversion. *Sci. Rep.* **2015**, *5*, 13801. [CrossRef] [PubMed]
85. Matsumoto, Y.; Sato, E. Electrocatalytic properties of transition metal oxides for oxygen evolution reaction. *Mater. Chem. Phys.* **1986**, *14*, 397–426. [CrossRef]
86. Li, G.; Anderson, L.; Chen, Y.; Pan, M.; Chuang, P.-Y.A. New insights into evaluating catalyst activity and stability for oxygen evolution reactions in alkaline media. *Sustain. Energy Fuels* **2018**, *2*, 237–251. [CrossRef]
87. Alobaid, A.; Wang, C.; Adomaitis, R.A. Mechanism and Kinetics of HER and OER on NiFe LDH Films in an Alkaline Electrolyte. *J. Electrochem. Soc.* **2018**, *165*, J3395. [CrossRef]
88. Möller, S.; Barwe, S.; Masa, J.; Wintrich, D.; Seisel, S.; Baltruschat, H.; Schuhmann, W. Online Monitoring of Electrochemical Carbon Corrosion in Alkaline Electrolytes by Differential Electrochemical Mass Spectrometry. *Angew. Chem. Int. Ed.* **2020**, *59*, 1585–1589. [CrossRef]
89. Li, J.; Zhou, N.; Song, J.; Fu, L.; Yan, J.; Tang, Y.; Wang, H. Cu–MOF-Derived Cu/Cu_2O Nanoparticles and CuN_xC_y Species to Boost Oxygen Reduction Activity of Ketjenblack Carbon in Al–Air Battery. *ACS Sustain. Chem. Eng.* **2018**, *6*, 413–421. [CrossRef]
90. Tee, S.Y.; Win, K.Y.; Teo, W.S.; Koh, L.-D.; Liu, S.; Teng, C.P.; Han, M.-Y. Recent Progress in Energy-Driven Water Splitting. *Adv. Sci.* **2017**, *4*, 1600337. [CrossRef]
91. Liu, Q.; Cong, H.; Deng, H. Deciphering the Spatial Arrangement of Metals and Correlation to Reactivity in Multivariate Metal–Organic Frameworks. *J. Am. Chem. Soc.* **2016**, *138*, 13822–13825. [CrossRef]
92. Gao, M.-R.; Xu, Y.-F.; Jiang, J.; Yu, S.-H. Nanostructured metal chalcogenides: Synthesis, modification, and applications in energy conversion and storage devices. *Chem. Soc. Rev.* **2013**, *42*, 2986–3017. [CrossRef]
93. Doyle, R.L.; Lyons, M.E.G. An electrochemical impedance study of the oxygen evolution reaction at hydrous iron oxide in base. *Phys. Chem. Chem. Phys.* **2013**, *15*, 5224–5237. [CrossRef]
94. Doyle, R.L.; Lyons, M.E.G. Kinetics and Mechanistic Aspects of the Oxygen Evolution Reaction at Hydrous Iron Oxide Films in Base. *J. Am. Chem. Soc.* **2013**, *160*, H142. [CrossRef]
95. Doyle, R.L.; Godwin, I.J.; Brandon, M.P.; Lyons, M.E.G. Redox and electrochemical water splitting catalytic properties of hydrated metal oxide modified electrodes. *Phys. Chem. Chem. Phys.* **2013**, *15*, 13737–13783. [CrossRef]
96. Miller, E.L.; Rocheleau, R.E. Electrochemical behavior of reactively sputtered iron-doped nickel oxide. *J. Electrochem. Soc.* **1997**, *144*, 3072. [CrossRef]
97. Lin, Y.; Wan, H.; Wu, D.; Chen, G.; Zhang, N.; Liu, X.; Li, J.; Cao, Y.; Qiu, G.; Ma, R. Metal–organic framework hexagonal nanoplates: Bottom-up synthesis, topotactic transformation, and efficient oxygen evolution reaction. *J. Am. Chem. Soc.* **2020**, *142*, 7317–7321. [CrossRef]
98. Negahdar, L.; Zeng, F.; Palkovits, S.; Broicher, C.; Palkovits, R. Mechanistic Aspects of the Electrocatalytic Oxygen Evolution Reaction over Ni−Co Oxides. *ChemElectroChem* **2019**, *6*, 5588–5595. [CrossRef]
99. Zhang, H.; Gao, Y.; Xu, H.; Guan, D.; Hu, Z.; Jing, C.; Sha, Y.; Gu, Y.; Huang, Y.-C.; Chang, Y.-C.; et al. Combined Corner-Sharing and Edge-Sharing Networks in Hybrid Nanocomposite with Unusual Lattice-Oxygen Activation for Efficient Water Oxidation. *Adv. Funct. Mater.* **2022**, *32*, 2207618. [CrossRef]
100. Feng, J.-X.; Xu, H.; Dong, Y.-T.; Ye, S.-H.; Tong, Y.-X.; Li, G.-R. FeOOH/Co/FeOOH hybrid nanotube arrays as high-performance electrocatalysts for the oxygen evolution reaction. *Angew. Chem. Int. Ed.* **2016**, *55*, 3694–3698. [CrossRef]
101. Lu, C.; Tranca, D.; Zhang, J.; Rodríguez Hernández, F.; Su, Y.; Zhuang, X.; Zhang, F.; Seifert, G.; Feng, X. Molybdenum carbide-embedded nitrogen-doped porous carbon nanosheets as electrocatalysts for water splitting in alkaline media. *ACS Nano* **2017**, *11*, 3933–3942. [CrossRef]
102. Luo, J.; Im, J.-H.; Mayer, M.T.; Schreier, M.; Nazeeruddin, M.K.; Park, N.-G.; Tilley, S.D.; Fan, H.J.; Grätzel, M. Water photolysis at 12.3% efficiency via perovskite photovoltaics and Earth-abundant catalysts. *Science* **2014**, *345*, 1593–1596. [CrossRef] [PubMed]
103. Dong, G.; Fang, M.; Zhang, J.; Wei, R.; Shu, L.; Liang, X.; Yip, S.; Wang, F.; Guan, L.; Zheng, Z.; et al. In situ formation of highly active Ni–Fe based oxygen-evolving electrocatalysts via simple reactive dip-coating. *J. Mater. Chem. A* **2017**, *5*, 11009–11015. [CrossRef]
104. Peugeot, A.; Creissen, C.E.; Karapinar, D.; Tran, H.N.; Schreiber, M.; Fontecave, M. Benchmarking of oxygen evolution catalysts on porous nickel supports. *Joule* **2021**, *5*, 1281–1300. [CrossRef]

105. Yuan, Y.; Xia, X.; Wu, J.; Yang, J.; Chen, Y.; Guo, S. Nickel foam-supported porous Ni(OH)$_2$/NiOOH composite film as advanced pseudocapacitor material. *Electrochim. Acta.* **2011**, *56*, 2627–2632. [CrossRef]
106. Lee, S.-Y.; Kim, I.-S.; Cho, H.-S.; Kim, C.-H.; Lee, Y.-K. Resolving Potential-Dependent Degradation of Electrodeposited Ni(OH)$_2$ Catalysts in Alkaline Oxygen Evolution Reaction (OER): In Situ XANES Studies. *Appl. Catal. B* **2021**, *284*, 119729. [CrossRef]
107. Klaus, S.; Cai, Y.; Louie, M.W.; Trotochaud, L.; Bell, A.T. Effects of Fe electrolyte impurities on Ni (OH)$_2$/NiOOH structure and oxygen evolution activity. *Open J. Phys. Chem. C* **2015**, *119*, 7243–7254. [CrossRef]
108. Nadesan, J.B.; Tseung, A.C. Oxygen evolution on nickel oxide electrodes. *J. Electrochem. Soc.* **1985**, *132*, 2957. [CrossRef]
109. Fominykh, K.; Feckl, J.M.; Sicklinger, J.; Döblinger, M.; Böcklein, S.; Ziegler, J.; Peter, L.; Rathousky, J.; Scheidt, E.-W.; Bein, T. Ultrasmall dispersible crystalline nickel oxide nanoparticles as high-performance catalysts for electrochemical water splitting. *Adv. Funct. Mater.* **2014**, *24*, 3123–3129. [CrossRef]
110. Ma, X.; Zheng, D.J.; Hou, S.; Mukherjee, S.; Khare, R.; Gao, G.; Ai, Q.; Garlyyev, B.; Li, W.; Koch, M.; et al. Structure–Activity Relationships in Ni- Carboxylate-Type Metal–Organic Frameworks' Metamorphosis for the Oxygen Evolution Reaction. *ACS Catal.* **2023**, *13*, 7587–7596. [CrossRef]
111. Xu, P.; Han, X.J.; Zhang, B.; Lv, Z.S.; Liu, X.R. Characterization of an ultrafine β-nickel hydroxide from supersonic co-precipitation method. *J. Alloys Compd.* **2007**, *436*, 369–374. [CrossRef]
112. Jiang, X.; Deng, S.; Liu, J.; Qi, N.; Chen, Z. Enhanced Electrochemical Performance of Bimetallic Doped Ni-Based Metal–Organic Frameworks by Redox Additives in an Alkaline Electrolyte. *ACS Appl. Energy Mater.* **2021**, *4*, 4610–4619. [CrossRef]
113. Qu, C.; Jiao, Y.; Zhao, B.; Chen, D.; Zou, R.; Walton, K.S.; Liu, M. Nickel-based pillared MOFs for high-performance supercapacitors: Design, synthesis and stability study. *Nano Energy* **2016**, *26*, 66–73. [CrossRef]
114. Jiao, Y.; Qu, C.; Zhao, B.; Liang, Z.; Chang, H.; Kumar, S.; Zou, R.; Liu, M.; Walton, K.S. High-Performance Electrodes for a Hybrid Supercapacitor Derived from a Metal–Organic Framework/Graphene Composite. *ACS Appl. Energy Mater.* **2019**, *2*, 5029–5038. [CrossRef]
115. Anantharaj, S.; Karthik, P.E.; Kundu, S. Petal-like hierarchical array of ultrathin Ni(OH)$_2$ nanosheets decorated with Ni(OH)$_2$ nanoburls: A highly efficient OER electrocatalyst. *Catal. Sci. Technol.* **2017**, *7*, 882–893. [CrossRef]
116. Gao, M.; Sheng, W.; Zhuang, Z.; Fang, Q.; Gu, S.; Jiang, J.; Yan, Y. Efficient Water Oxidation Using Nanostructured α-Nickel-Hydroxide as an Electrocatalyst. *J. Am. Chem. Soc.* **2014**, *136*, 7077–7084. [CrossRef]
117. Smith, R.D.L.; Prévot, M.S.; Fagan, R.D.; Trudel, S.; Berlinguette, C.P. Water Oxidation Catalysis: Electrocatalytic Response to Metal Stoichiometry in Amorphous Metal Oxide Films Containing Iron, Cobalt, and Nickel. *J. Am. Chem. Soc.* **2013**, *135*, 11580–11586. [CrossRef]
118. Tian, J.; Jiang, F.; Yuan, D.; Zhang, L.; Chen, Q.; Hong, M. Electric-field assisted in situ hydrolysis of bulk metal–organic frameworks (MOFs) into ultrathin metal oxyhydroxide nanosheets for efficient oxygen evolution. *Angew. Chem. Int. Ed.* **2020**, *59*, 13101–13108. [CrossRef]
119. Singh, B.; Prakash, O.; Maiti, P.; Menezes, P.W.; Indra, A. Electrochemical transformation of Prussian blue analogues into ultrathin layered double hydroxide nanosheets for water splitting. *Chem. Commun.* **2020**, *56*, 15036–15039. [CrossRef]
120. Kou, Z.; Li, X.; Zhang, L.; Zang, W.; Gao, X.; Wang, J. Dynamic surface chemistry of catalysts in oxygen evolution reaction. *Small Sci.* **2021**, *1*, 2100011. [CrossRef]
121. Li, J.; Huang, W.; Wang, M.; Xi, S.; Meng, J.; Zhao, K.; Jin, J.; Xu, W.; Wang, Z.; Liu, X. Low-crystalline bimetallic metal–organic framework electrocatalysts with rich active sites for oxygen evolution. *ACS Energy Lett.* **2018**, *4*, 285–292. [CrossRef]
122. Anantharaj, S.; Noda, S. iR drop correction in electrocatalysis: Everything one needs to know! *J. Mater. Chem. A* **2022**, *10*, 9348–9354. [CrossRef]
123. Brandenburg, K. *Diamond*; Version 4.6, Crystal and Molecular Structure Visualization, Crystal Impact; K. Brandenburg & H. Putz Gbr: Bonn, Germany, 2009–2022.
124. Zhang, C.; Liang, Y.; Wang, Y.; He, Y.; Majeed, A.; Yang, Z.; Yao, S.; Shen, X.; Li, T.; Qin, S. Polyamidoamine dendrimer modified Ketjen Black mixed sulfur coated cathode for enhancing polysulfides adsorbability in Li-S batteries. *Ionics* **2021**, *27*, 2997–3005. [CrossRef]
125. Xing, S.; Liang, J.; Brandt, P.; Schäfer, F.; Nuhnen, A.; Heinen, T.; Boldog, I.; Möllmer, J.; Lange, M.; Weingart, O. Capture and separation of SO_2 traces in metal–organic frameworks via pre-synthetic pore environment tailoring by methyl groups. *Angew. Chem. Int. Ed.* **2021**, *60*, 17998–18005. [CrossRef]
126. Wu, Y.; Song, X.; Xu, S.; Chen, Y.; Oderinde, O.; Gao, L.; Wei, R.; Xiao, G. Chemical fixation of CO_2 into cyclic carbonates catalyzed by bimetal mixed MOFs: The role of the interaction between Co and Zn. *Dalton Trans.* **2020**, *49*, 312–321. [CrossRef]
127. Grosvenor, A.P.; Kobe, B.A.; Biesinger, M.C.; McIntyre, N.S. Investigation of multiplet splitting of Fe 2p XPS spectra and bonding in iron compounds. *Surf. Interface Anal.* **2004**, *36*, 1564–1574. [CrossRef]
128. Paolella, A.; Bertoni, G.; Hovington, P.; Feng, Z.; Flacau, R.; Prato, M.; Colombo, M.; Marras, S.; Manna, L.; Turner, S. Cation exchange mediated elimination of the Fe-antisites in the hydrothermal synthesis of $LiFePO_4$. *Nano Energy* **2015**, *16*, 256–267. [CrossRef]
129. Pang, W.; Shao, B.; Tan, X.-Q.; Tang, C.; Zhang, Z.; Huang, J. Exfoliation of metal–organic frameworks into efficient single-layer metal–organic nanosheet electrocatalysts by the synergistic action of host–guest interactions and sonication. *Nanoscale* **2020**, *12*, 3623–3629. [CrossRef]

130. Zhao, X.; Ding, X.; Xia, Y.; Jiao, X.; Chen, D. Coupling-Effect-Induced Acceleration of Electron Transfer for α-$Ni(OH)_2$ with Enhanced Oxygen Evolution Reaction Activity. *ACS Appl. Nano Mater.* **2018**, *1*, 1476–1483. [CrossRef]
131. Biesinger, M.C. Accessing the robustness of adventitious carbon for charge referencing (correction) purposes in XPS analysis: Insights from a multi-user facility data review. *Appl. Surf. Sci.* **2022**, *597*, 153681. [CrossRef]

Supplementary Materials

Synthesis of Ketjenblack Decorated Pillared Ni(Fe) Metal-Organic Frameworks as Precursor Electrocatalysts for Enhancing the Oxygen Evolution Reaction

Thi Hai Yen Beglau[1], Lars Rademacher[1], Robert Oestreich[1] and Christoph Janiak*[1,§]

Address:
[1]Institut für Anorganische Chemie und Strukturchemie, Heinrich-Heine-Universität Düsseldorf, 40204 Düsseldorf, Germany,
E-Mail:
Christoph Janiak* - janiak@uni-duesseldorf.de
* Corresponding author
§ Fax: +49-211-81-12287; Tel: +49-211-81-12286
Emails: beglau@uni-duesseldorf.de; lars.rademacher@hhu.de; Robert.Oestreich@hhu.de

Section S1: 3D framework structure of NiDMOF

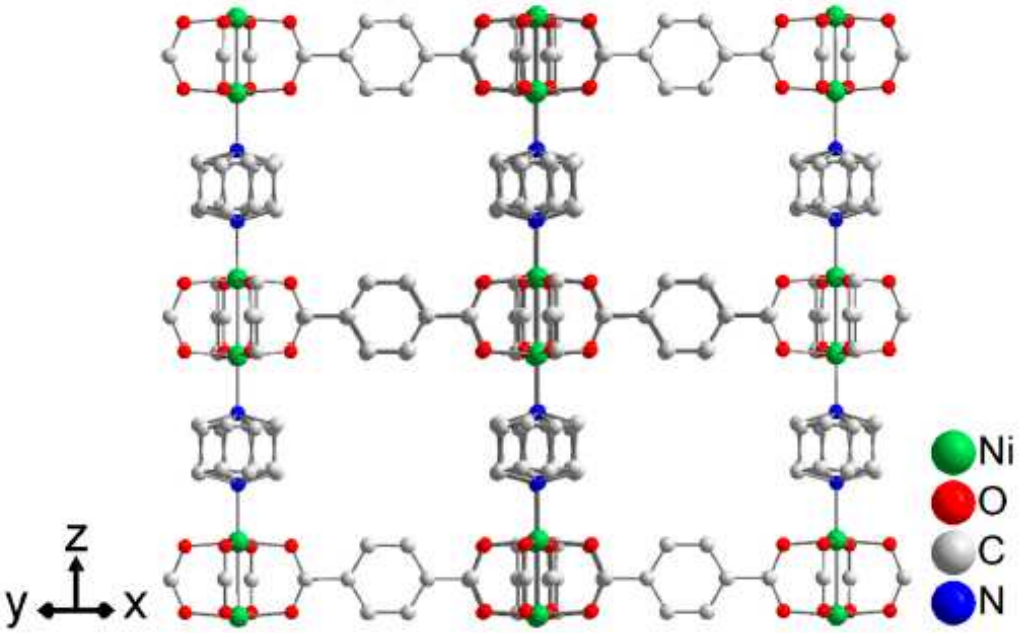

(a)

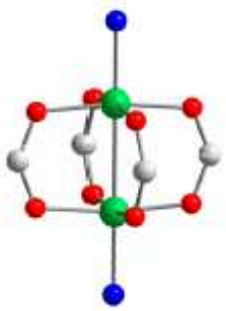

(b)

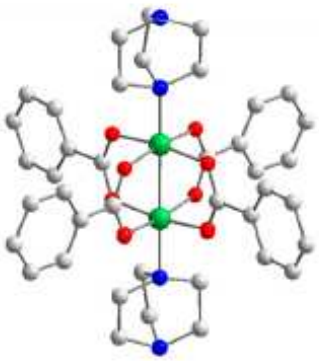

(c)

Figure S1. a) Secion of the 3D framework structure of $[Ni_2(BDC)_2DABCO]\cdot(DMF)_4\cdot(H_2O)_{1.5}$ (NiDMOF), b) and c) two presentations of the $\{Ni_2(O_2C\text{-})_4\}$ paddle-wheel cluster also showing the penta-coordination of the Ni centers by the nitrogen atoms from the DABCO ligand. Graphic produced with the software Diamond [1] from the deposited cif-file for NiDMOF with CCDC number 802892.[2]

Section S2: Powder X-ray diffraction (PXRD) measurements

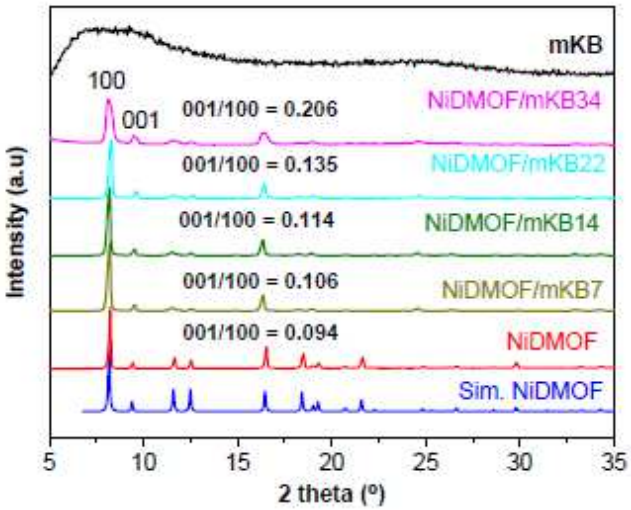

Figure S2. PXRD patterns of NiDMOF, its 7, 14, 22, 34 wt.% mKB composites and mKB. The simulated PXRD pattern of NiDMOF was obtained from the deposited cif-file for NiDMOF with CCDC number 802892.[2] The first five reflexes at 2θ = 8.2°, 9.4°, 11.7°, 12.4° and 16.6° correspond are the 100, 001, 110, 101 and 200 reflections.

Section S3: Fourier-transform infrared (FT-IR) spectroscopy

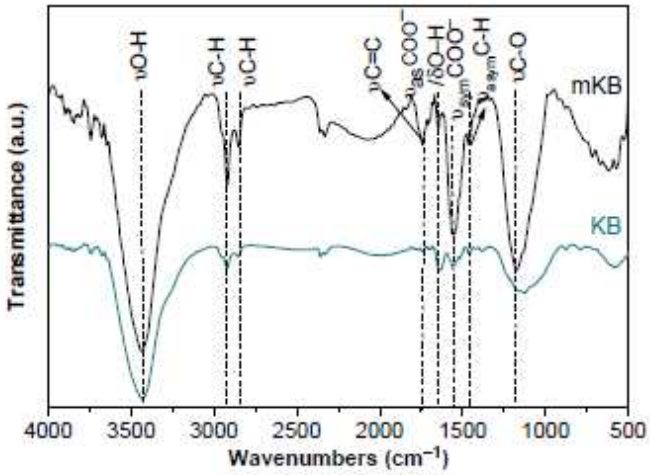

Figure S3. FTIR spectra of modified Ketjenblack carbon (mKB) and pristine Ketjenblack carbon (KB).

Fourier-transform infrared (FT-IR) spectroscopy was used to confirm the existence and increase of functional groups in mKB (Figure S3). The spectrum of mKB shows peaks at 3435, which could be attributed to the ν(O–H). The bands at 2921 and 2850 cm^{-1} are assigned to the ν_{asym}C–H and ν_{sym}C-H, respectively. After modification, the mKB has additional bands at 1640 ± 5, 1550 ± 5 and 1180 ± 5 cm^{-1},

attributed to the $\nu_{asym}COO^-$, δO–H, $\nu_{sym}COO^-$ and νC–O, respectively.[3] The oxygen containing groups –OH, -COO^- and -C-O can be obserbed in both KB and mKB, but the intensity in mKB is much stronger than in KB, indicating that oxidation with 20% HNO_3 increased the amount of oxygen containing functional groups.

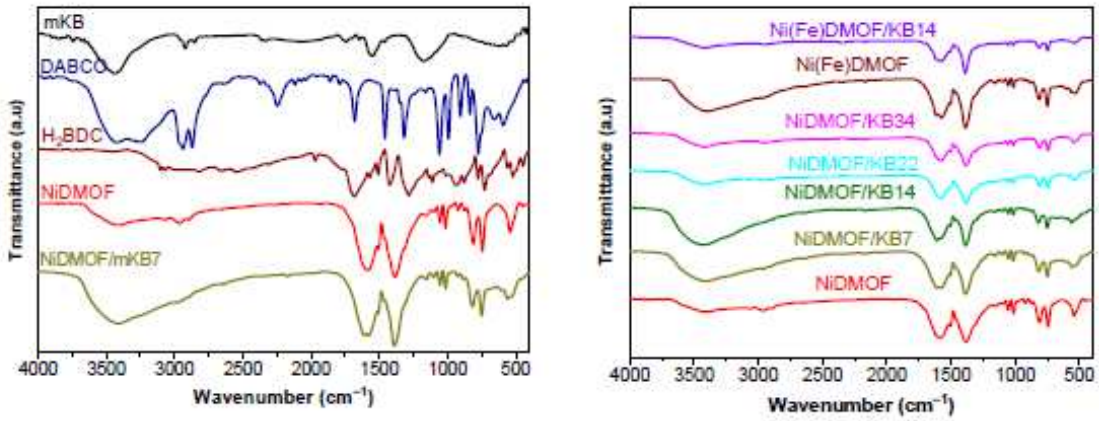

Figure S4. FT–IR spectra of a) mKB, H_2BDC, DABCO, NiDMOF and the Ni-DMOF/KB7 composite; b) NiDMOF and its 7, 14, 22, 34 wt.% mKB composites, Ni(Fe)DMOF and Ni(Fe)DMOF/mKB14.

As shown in Figure S4a, NiDMOF and NiDMOF/KB7 display the same characteristic bands in the fingerprint region which are in a good agreement with the literature.[2,4] The wide band at 2900–3400 cm^{-1} are attributed to ν_{asym}C–H and νO–H of uncoordinated water molecules. The strong bands at 1650-1580 cm^{-1} and 1400-1350 cm^{-1} were assigned to the $\nu_{asym}COO^-$ and $\nu_{sym}COO^-$ vibrations of the COO^- groups. The bands at 1100 ± 5 cm^{-1} and 1055 ± 5 cm^{-1} could be due to the ν_{as}C-N and ν_{as}C-N vibrations of DABCO. The absorbance bands at 810 ± 5 cm^{-1} and 750 ± 5 cm^{-1} correspond to the $\nu(C\text{-}C)_{Ar}$ and $\delta(C\text{-}H)_{Ar}$ vibrations, respectively, of the 1,4-BDC ligand. The composite series DMOF/mKBx exhibit similar bands as those in the parent DMOF, indicating that incorporation of mKB did not prevent the formation of DMOF units. The results confirmed that mKB could be smoothly mixed with the DMOFs, in agreement with the PXRD results.

Table S1. Assignment of IR-bands of KB, mKB, NiDMOF and NiDMOF/mKB analogs (cm^{-1}).

	νO–H	νC-H	$\nu_{asym}COO^-$/δO-H	$\nu_{sym}COO^-$	ν_sCO^-	ν_{as}C-N	νC-C_{Ar} / δ(C-H)$_{Ar}$	νNi-O/ νNi/Fe–O,
KB	3435	2918 2844	1641 1557	-	1174	-	879 722	-
mKB	3435	2918 2844	1645 1554	-	1181	-	875 782 722	-
NiDMOF	3406	2963 2887	1602 1573	1385	1147	1056 1010	813 737	540
NiDMOF/mKB	3430	2961 2895	1611 1573	1387	1144	1048 1005	817 715	560
Ni(Fe)DMOF	3408	2970	1615 1568	1390	1150	1055 1007	748 814	528
Ni(Fe)DMOF/mKB	3401	2918 2849	1618 1572	1390	1160	1053 1007	748 814	527
Derived- Ni(Fe)DMOF[b]	3637 3425	-	1633	1347	-	-	-	517 439
Derived- Ni(Fe)DMOF/mKB[b]	3634 3430	-	1641 1570	1367	-		-	516 450

[a] ν = stretching vibration (ν_{asym}= asymmetric vibration, ν_{sym}=symmetric stretching vibration); δ =bending vibration (ρ = in plane, γ= out of plane vibration); $_{Ar}$ = aromatic vibration.

[b] All major IR bands are listed for the decomposition product of Ni(Fe)DMOF and Ni(Fe)DMOF/mKB after 24 h in 1 mol L^{-1} KOH.

Section S4: NMR spectroscopy

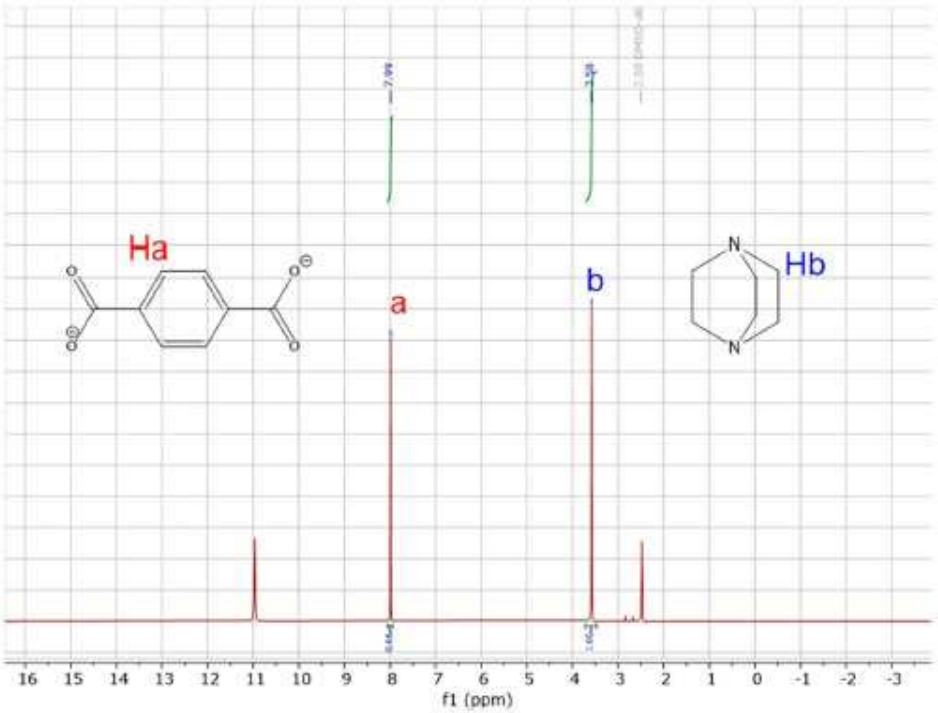

Figure S5. Solution ^{1}H NMR spectra of digested NiDMOF [$Ni_2(BDC)_2DABCO$] in DMSO-d_6 (2.50 ppm). The intergration ratio of H on 1 DABCO ($C_6H_{12}N_2$) to H on 2 BDC (2 $C_6H_4(CO_2^-)_2$) matches the expected 1.5:1 ratio.

Section S5: Elemental analysis

Table S2. Elemental analysis of DMOF samples and their composite series with mKB.[a]

Material	C (wt.%)	H (wt.%)	N (wt.%)	Ni (wt.%)	Fe (wt.%)	mKB from AAS (wt.%)
NiDMOF found	45.26	3.61	4.94	20.82	-	-
NiDMOF = $[Ni_2(C_8H_4O_4)_2(C_6H_{12}N_2)]\cdot(H_2O)_{0.5}$ calculated	46.62	3.73	4.94	20.71	-	-
$[Ni_2(C_8H_4O_4)_2(C_6H_{12}N_2)]\cdot H_2O$ calculated	45.89	3.85	4.87	20.39		
NiDMOF/mKB7	46.28	3.36	4.24	19.49	-	7
NiDMOF/mKB14	48.84	3.19	4.18	18.13	-	14
NiDMOF/mKB22	50.20	3.11	3.88	16.44	-	22
NiDMOF/mKB34	51.86	3.00	3.69	13.98	-	34
Ni(Fe)DMOF	46.35	3.57	5.01	20.85 3.55 at.%	0.66 0.118 at.%	-
			molar ratio Ni:Fe 30:1			
Ni(Fe)DMOF= $[Ni_{1.94}Fe_{0.06}(C_8H_4O_4)_2(C_6H_{12}N_2)]\cdot(H_2O)_{0.5}$ calc.	46.63	3.74	4.94	20.10	0.59	-
$[Ni_{1.94}Fe_{0.06}(C_8H_4O_4)_2(C_6H_{12}N_2)]\cdot(H_2O)$ calc.	45.90	3.85	4.87	19.78	0.58	
Ni(Fe)DMOF/mKB14	49.17	3.28	4.27	18.11 3.086 at.%	0.57 0.102 at.%	14
			molar ratio Ni:Fe 30:1			

[a] The samples were dried at 150 °C for at least 20 h under vacuum condition (< 10^{-2} mbar) before using for the element analysis, in order to avoid the residual solvent molecules or re-adsorbed moisture during storage and handling.

[b] MOF wt. % in composite $= \frac{\text{Ni wt.\% (composite)}}{20.71\ x\ \text{Ni wt.\% (pure MOF)}} \cdot 100\%$; mKB wt.% = 100% – MOF wt.%

Section S6: Nitrogen sorption experiments (T = 77 K)

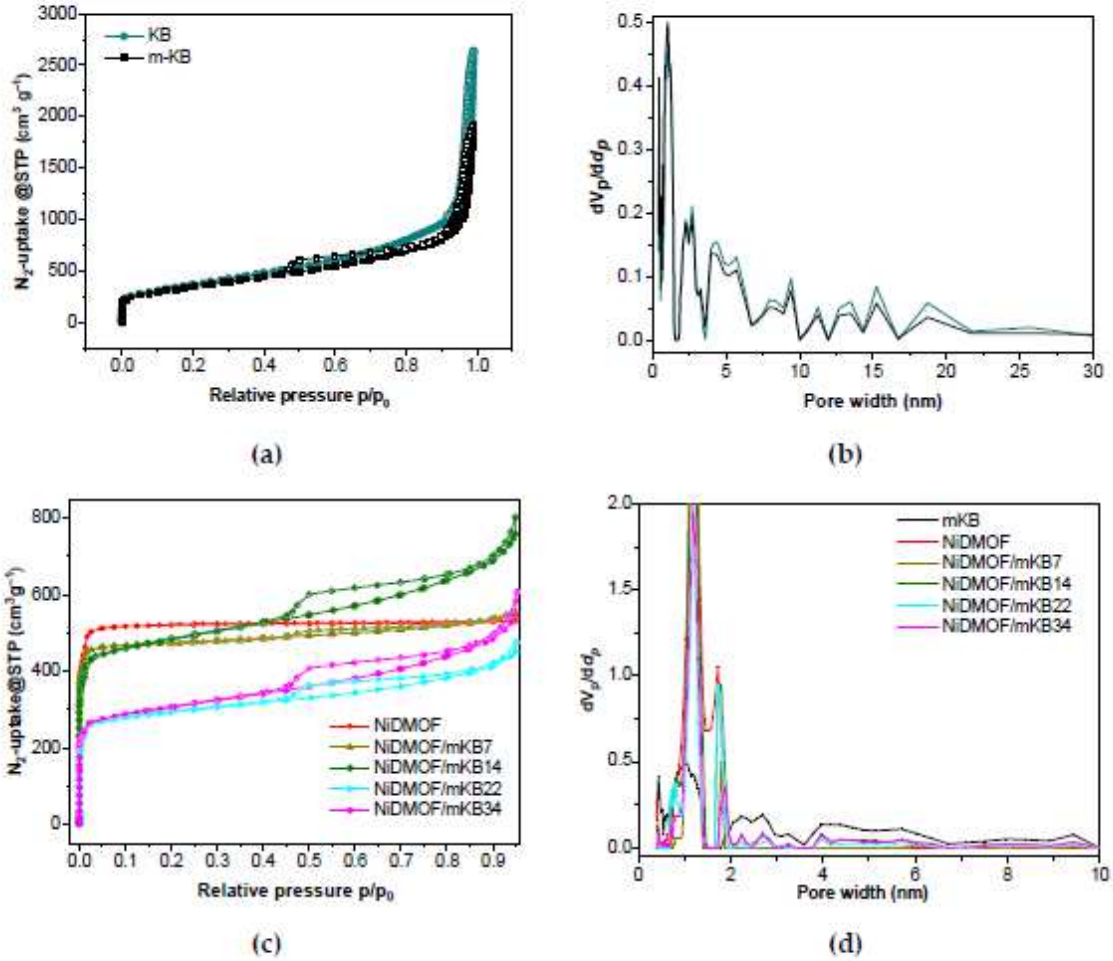

Figure S6. a) Nitrogen sorption isotherms at 77 K (filled symbols adsorption; empty symbols desorption) and b) pore size distribution of modified Ketjenblack carbon (mKB) and neat Ketjenblack carbon (KB). c) Nitrogen sorption isotherms at 77 K (filled symbols adsorption; empty symbols desorption) and d) pore size distribution of NiDMOF, its 7, 14, 22, 34 wt.% mKB composites and mKB.

Section S7: Scanning electron microscopy (SEM)

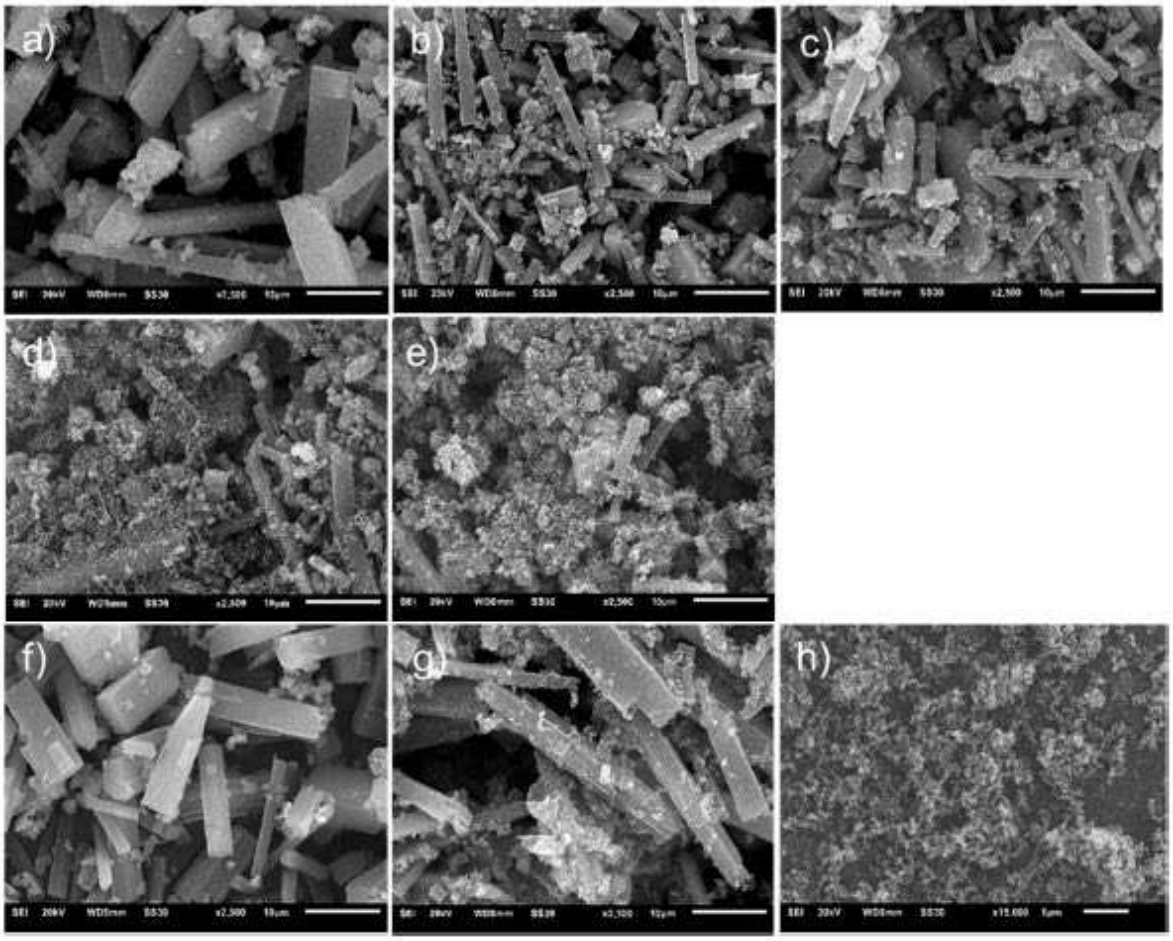

Figure S7. SEM images of a) NiDMOF, b) NiDMOF/mKB7 c) NiDMOF/mKB14 d) NiDMOF/mKB22, e) NiDMOF/mKB34, f) Ni(Fe)DMOF, g) Ni(Fe)DMOF/mKB14 and h) mKB. The scale bar is 10 µm except for h) where it is 1 µm.

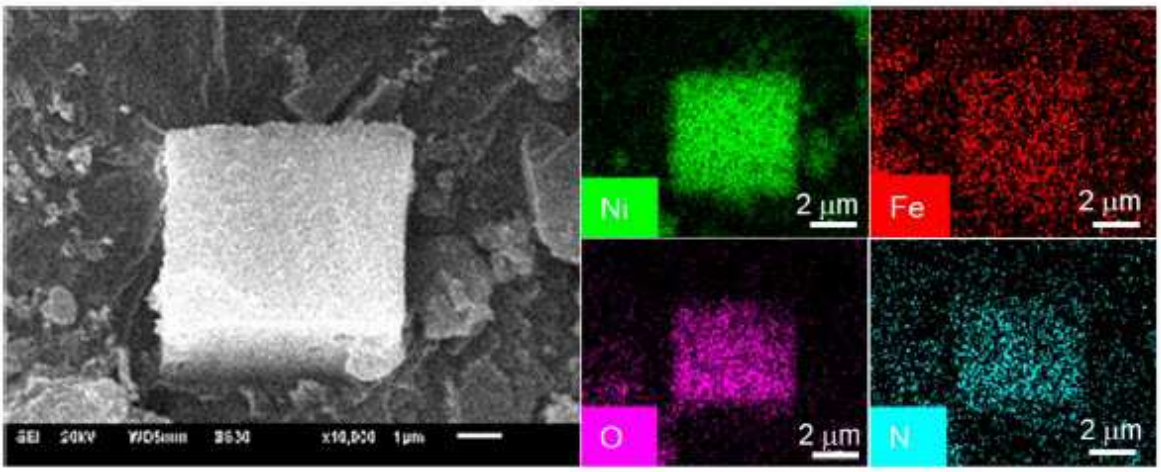

Figure S8. EDX element mapping for nickel, iron, nitrogen and oxygen of Ni(Fe)DMOF.

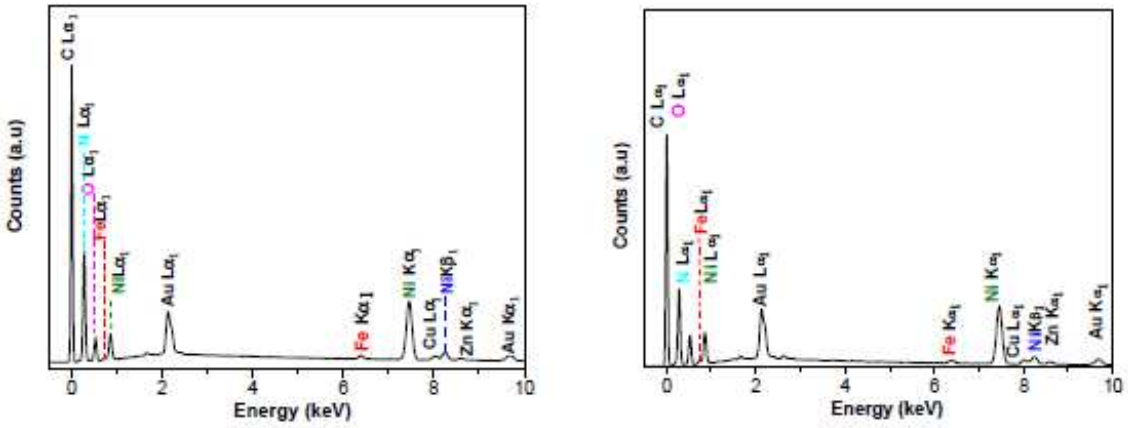

(a) (b)

Figure S9. EDX spectra with the composition for a) Ni(Fe)DMOF in the selected area in Figure S8, b) for Ni(Fe)DMOF/mKB14 in the selected area in Figure 3 in the main text.

Table S3. SEM-EDX and AAS Ni:Fe ratios of Ni(Fe)DMOF and Ni(Fe)DMOF/mKB14.

Material	SEM-EDX	AAS	Synthesis
	Molar Ni:Fe ratio		
Ni(Fe)DMOF	31.5:1	30:1	32:1
Ni(Fe)DMOF/mKB14	31:1	30:1	32:1

Section S8: X-ray photoelectron spectra (XPS)

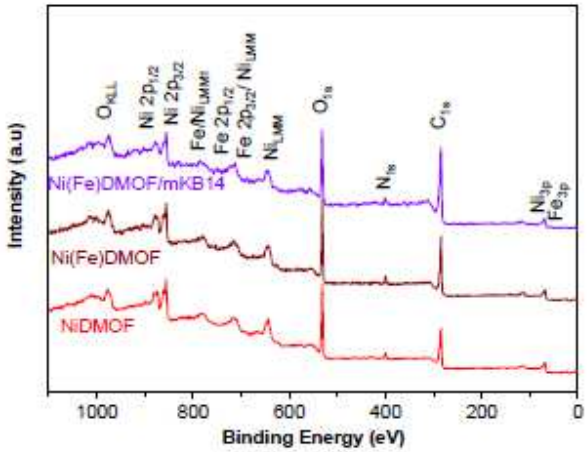

Figure S10. Full X-ray photoelectron spectra (XPS) of NiDMOF, Ni(Fe)DMOF and Ni(Fe)DMOF/mKB14.

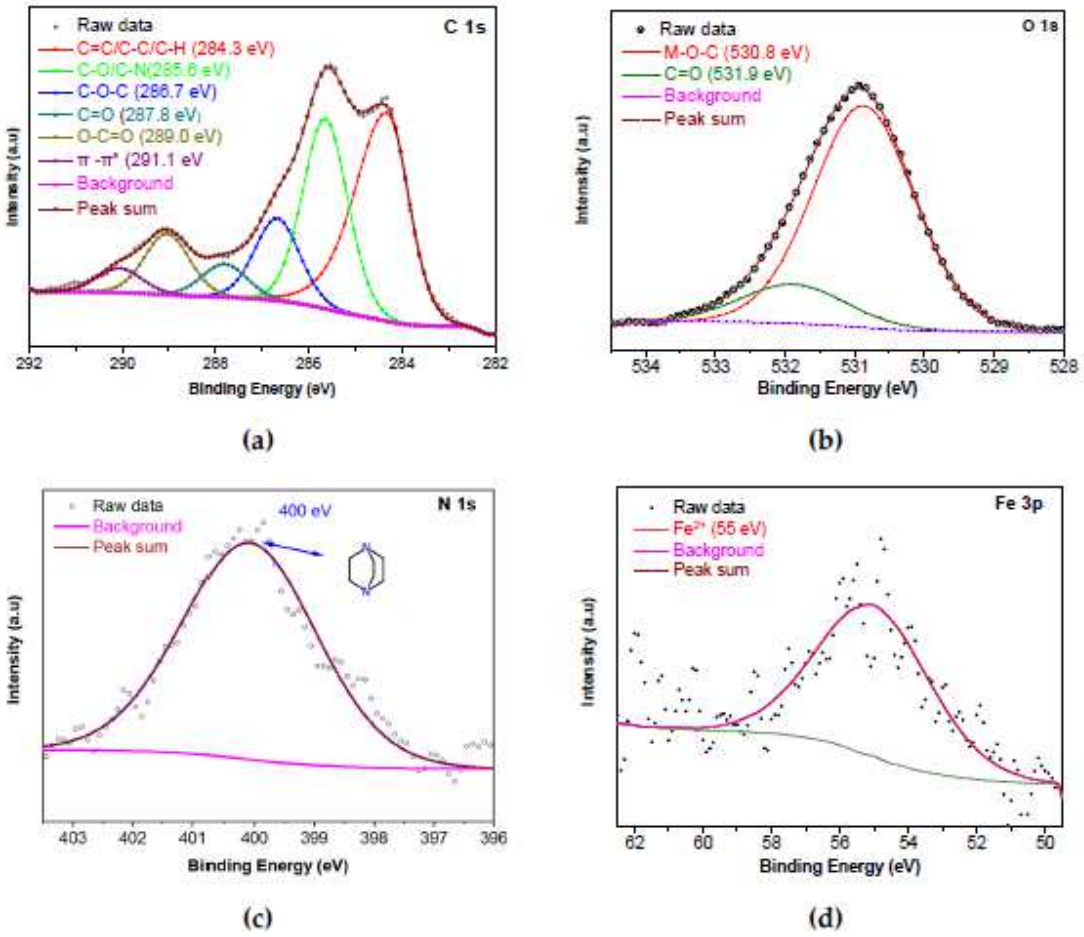

Figure S11. High-resolution X-ray photoelectron spectra (XPS) of a) C 1s, b) O 1s, c) N 1s and d) Fe 3p of Ni(Fe)DMOF/mKB14 composite.

The deconvolution of the carbon 1s spectrum (C 1s) can be fitted into five peaks with binding energies of 284.3, 285.6, 286.7, 287.8 and 289.0 eV, which indicate the presence of C-C/C=C/C-H, C-O/C-N, C-O-C, C=O and O-C=O, respectively. The shallow broad peak at 291.1 eV is a π to π^* shake-up satellite.[5] This implies the presence of terephthalate and the functional groups of modified Ketjenblack carbon (mKB). Similarly, the oxygen spectrum (O 1s) can be deconvoluted into two peaks positioned at 530.8 and 531.9 eV, which are related to typical M-O-C bonds and C=O, respectively. The N 1s spectrum consists of one peaks with a binding energy of 400 eV which corresponds to the presence of tertiary N bonded to carbon ($N\text{-}C_3$),[6,7] as in DABCO. It should be noted that the Fe 2p peaks have a contribution from a Ni LMM Auger peak (Figure S11).[8] Therefore, the weaker Fe 3p peak was used, instead, for the Ni:Fe ratio quantification. The Fe 3p XPS region of Ni(Fe)DMOF/mKB shows one peak at 55 eV, which confirms of the presence of Fe(II) (Figure S11d).[9,10]

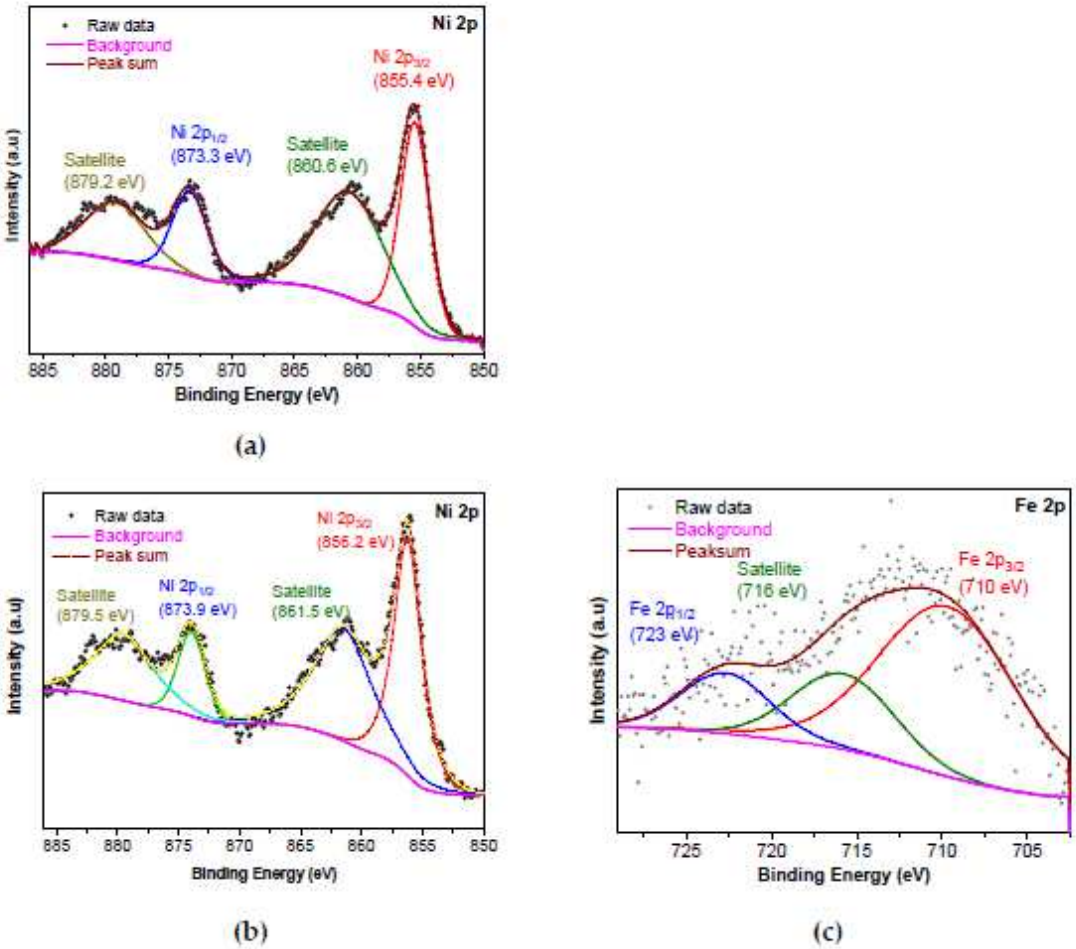

Figure S12. High-resolution X-ray photoelectron spectra (XPS) of a) Ni 2p of NiDMOF, b) Ni 2p and c) Fe 2p of Ni(Fe)DMOF. In c) the Ni LMM Auger peak occurs at the same positions as the Fe 2p signals.[8]

Section S9: Electrochemical measurements

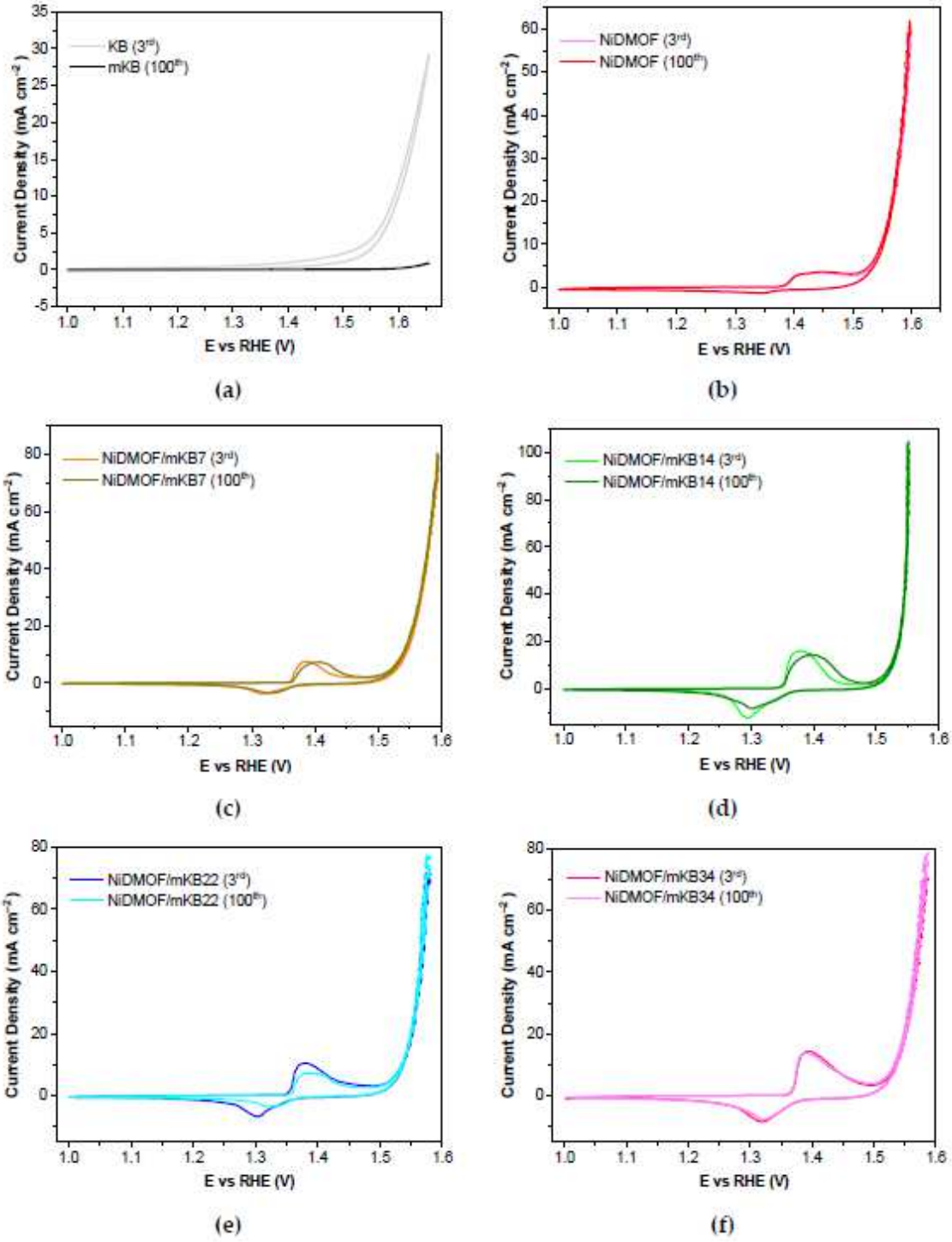

Figure S13. Comparison of CV curves collected after the 3rd and 100th cycle for a) mKB, b) NiDMOF, c) NiDMOF/mKB7, d) NiDMOF/mKB14, e) NiDMOF/mKB22 and f) NiDMOF/mKB34.

100 cyclic voltammetry (CV) scans were applied to explore the electrocatalytic behaviors and their activation/deactivation profiles due to surface reconstruction. As shown in Figure S13,

with mKB present in the composites, the Ni^{2+} to Ni^{3+} oxidation peak (at 1.35–1.45 V vs RHE) became more noticeable and shifted into positive direction, indicating the synergetic effect of mKB and NiDMOF on the oxidation of $Ni^{+2}(OH)_2$ to $Ni^{+3}OOH$. Oxidation currents at higher potentials are then due to the evolution of oxygen according to $4OH^- \rightarrow O_2 + 2H_2O + 4e^-$.

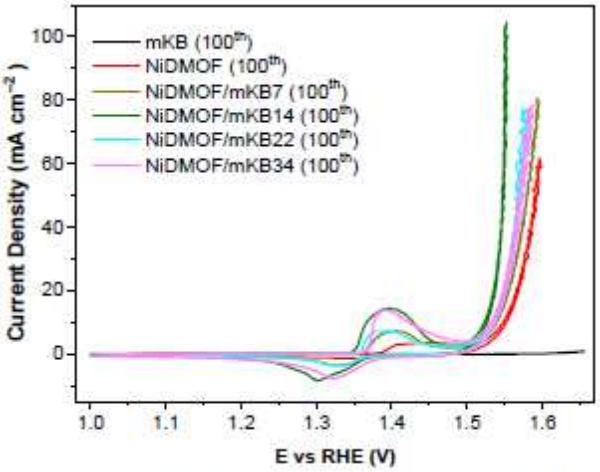

Figure S14. Comparison of CV curves collected after 100th cycle for mKB, NiDMOF and its 7, 14, 22, 34 wt.% mKB composites.

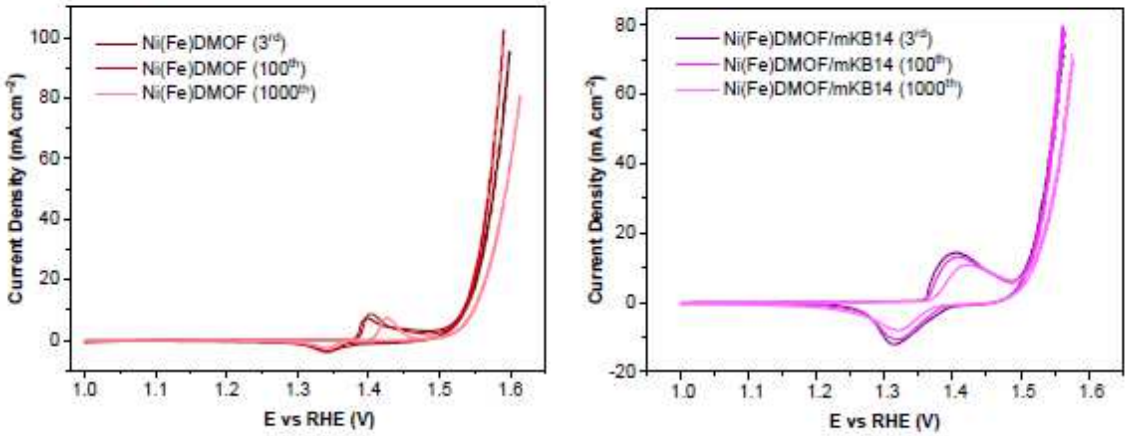

(a) (b)

Figure S15. Comparison of CV curves collected after 3rd, 100th and 1000th cycle for a) Ni(Fe)DMOF and b) Ni(Fe)DMOF/mKB14.

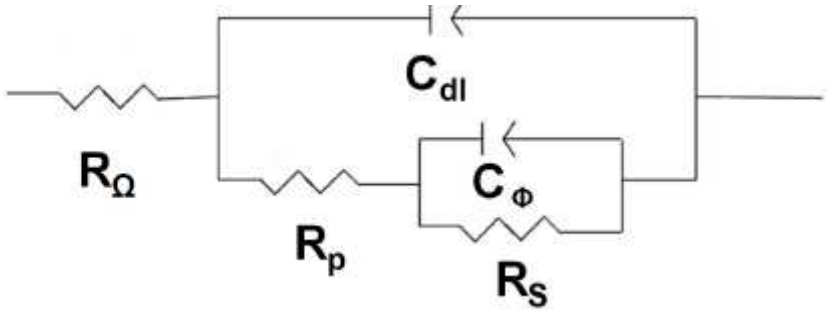

Figure S16. Equivalent circuit for the metal oxides catalyzing OER.

The R_Ω presents an electrolyte resistance, while C_{dl} is an element model, which represents the double layer capacitance of a solid electrode. The kinetic of Faradaic OER is determined by these circuit parameters: R_p, R_s and C_Φ. The polarization resistance (R_P) presents the total charge transfer resistance of the multiple steps in OER, while R_s is related to the rate of production of surface intermediates during OER. In general, C_Φ is related to the changes in charged surface species during the process of OER.[11,12,13]

Table S4. Overpotentials at 10 mA cm^{-2} and Tafel slopes of NiDMOF, Ni(Fe)DMOF and their mKB composite series materials at 1.5 V vs. RHE.

Material	Overpotential at 10 mA cm^{-2} (mV)	Tafel slope ($mV\ dec^{-1}$)	R_p (Ω)	R_s (Ω)
Ketjenblack (mKB)	375	73	62	75
RuO_2	317	56	23	4
NiDMOF	315	55	21	7
NiDMOF/mKB7	308	53	8	3
NiDMOF/mKB14	294	32	4	2
NiDMOF/mKB22	303	45	5	3
NiDMOF/mKB34	304	51	11	4
Ni(Fe)DMOF	301	40	6	4
Ni(Fe)DMOF/mKB14	279	24	4	2

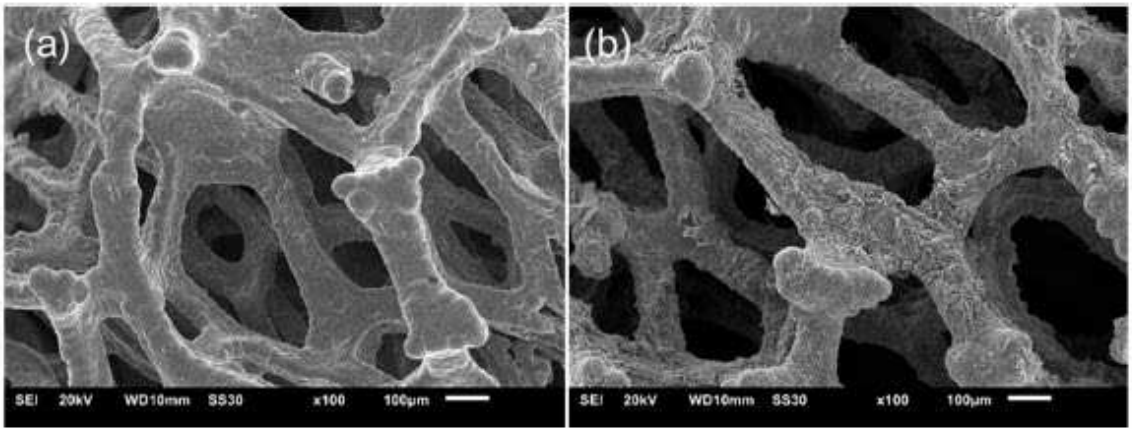

Figure S17. SEM images of (a) bare Ni foam (NF) and (b) Ni(Fe)DMOF/mKB14 loaded on nickel foam for the chronopotentiometry (CP) test for 30 h.

Table S5. Comparison of OER performance of published materials and in this work.

Material [a]	Electrolyte [b]	Substrate	Overpotential @ 10 mA cm^{-2} (mV)	Tafel slope (mV dec^{-1})	Ref.
NiDMOF/mKB14	KOH [b]	GCE	294	32	This work
Ni(Fe)DMOF/mKB14 (14 wt.% mKB)	KOH	GCE	279	25	This work
Ni(Fe)DMOF/mKB14 (14 wt.% mKB)	KOH	NF	247		This work
Ni(Fe)-MOF-74/KB (48 wt.% KB)	KOH	GCE	274	40	[14]
Ni(Fe)$(OH)_2$/KB (47 wt.%)	KOH	GCE	265	55	[14]
Ni10CoBTC/KB (33 wt.% KB)	KOH	GCE	347	70	[15]
Ni10FeBTC	KOH	GCE	344	47	[15]
2D-Ni-single-layer (Ni_2 BDC_2 DABCO)	PB, pH = 7.0 (0.2 mol L^{-1})	Carbon cloth	749	182	[16]
2D-CoNi-single-layer (NiCoBDC$_2$DABCO)	PB, pH = 7.0 (0.2 mol L^{-1})	Carbon cloth	527	171	[16]
HXP@NC800	KOH	GCE	307	48	17
Fe-doped HXP@NC800	KOH	GCE	266	49	[17]
Ni_{32}Fe oxide	KOH	NF	291	58	[18]
β-Ni$(OH)_2$ nanoburls	KOH	GCE	303	43	[19]
α-Ni$(OH)_2$	KOH	GCE	387	53	[20]
α-Ni$(OH)_2$-GO	KOH	GCE	356	50	[20]

[a] mKB: modified Ketjenblack carbon, KB: Ketjenblack carbon; NF: nickel foam, BDC: 1-4-bezene dicarboxylate, TED = DABCO: triethylenediamine, HXP: hexagonal 2D $Ni_2(BDC)_2(DABCO)\cdot(DMF)_4(H_2O)_4$, rGO: reduced graphene oxide and PB: Sodium Phosphate Buffer 0.2 mol L^{-1} electrolyte, pH 7.0. – [b] 1 mol L^{-1} KOH electrolyte.

References

1 Brandenburg, K. Diamond, Version 4.6, Crystal and Molecular Structure Visualization, Crystal Impact; K. Brandenburg & H. Putz Gbr: Bonn, Germany, 2009–2022.

2 Maniam, P.; Stock, N. Investigation of Porous Ni-Based Metal–Organic Frameworks Containing Paddle-Wheel Type Inorganic Building Units via High-Throughput Methods. *Inorg. Chem.* **2011**, *50*, 5085–5097, doi:10.1021/ic200381f.

3 Zhang, C.; Liang, Y.; Wang, Y.; He, Y.; Majeed, A.; Yang, Z.; Yao, S.; Shen, X.; Li, T.; Qin, S. Polyamidoamine dendrimer modified Ketjen Black mixed sulfur coated cathode for enhancing polysulfides adsorbability in Li-S batteries. *Ionics* **2021**, *27*, 2997–3005, doi:10.1007/s11581-021-04100-2.

4 Xing, S.; Liang, J.; Brandt, P.; Schäfer, F.; Nuhnen, A.; Heinen, T.; Boldog, I.; Möllmer, J.; Lange, M.; Weingart, O. Capture and separation of SO_2 traces in metal–organic frameworks via pre-synthetic pore environment tailoring by methyl groups. *Angew. Chem. Int. Ed.* **2021**, *60*, 17998–18005, doi:10.1002/anie.202105229.

5 Biesinger, M.C. Accessing the robustness of adventitious carbon for charge referencing (correction) purposes in XPS analysis: Insights from a multi-user facility data review. *Appl. Surf. Sci.* **2022**, *597*, 153681, doi:10.1016/j.apsusc.2022.153681.

6 Jiao, Y.; Qu, C.; Zhao, B.; Liang, Z.; Chang, H.; Kumar, S.; Zou, R.; Liu, M.; Walton, K.S. High-Performance Electrodes for a Hybrid Supercapacitor Derived from a Metal–Organic Framework/Graphene Composite. *ACS Appl. Energy Mater.* **2019**, *2*, 5029–5038, doi:10.1021/acsaem.9b00700.

7 Wu, Y.; Song, X.; Xu, S.; Chen, Y.; Oderinde, O.; Gao, L.; Wei, R.; Xiao, G. Chemical fixation of CO_2 into cyclic carbonates catalyzed by bimetal mixed MOFs: the role of the interaction between Co and Zn. *Dalton Trans.* **2020**, *49*, 312–321, doi:10.1039/C9DT04027G.

[8] Yin, L.I.; Yellin, E.; Adler, I. X-Ray Excited LMM Auger Spectra of Copper, Nickel, and Iron. *J. Appl. Phys.* **1971**, *42*, 3595–3600, doi:10.1063/1.1660775.

[9] Grosvenor, A.P.; Kobe, B.A.; Biesinger, M.C.; McIntyre, N.S. Investigation of multiplet splitting of Fe 2p XPS spectra and bonding in iron compounds. *Surf. Interface Anal.* **2004**, *36*, 1564–1574, doi:10.1002/sia.1984.

[10] Paolella, A.; Bertoni, G.; Hovington, P.; Feng, Z.; Flacau, R.; Prato, M.; Colombo, M.; Marras, S.; Manna, L.; Turner, S. Cation exchange mediated elimination of the Fe-antisites in the hydrothermal synthesis of $LiFePO_4$. *Nano Energy* **2015**, *16*, 256–267, doi:10.1016/j.nanoen.2015.06.005.

[11] Doyle, R.L.; Lyons, M.E.G. An electrochemical impedance study of the oxygen evolution reaction at hydrous iron oxide in base. *Phys. Chem. Chem. Phys.* **2013**, *15*, 5224–5237, doi:10.1039/C3CP43464H.

[12] Doyle, R.L.; Lyons, M.E.G. Kinetics and Mechanistic Aspects of the Oxygen Evolution Reaction at Hydrous Iron Oxide Films in Base. *J. Am. Chem. Soc.* **2013**, *160*, H142, doi:10.1149/2.015303jes.

[13] Doyle, R.L.; Godwin, I.J.; Brandon, M.P.; Lyons, M.E.G. Redox and electrochemical water splitting catalytic properties of hydrated metal oxide modified electrodes. *Phys. Chem. Chem. Phys.* **2013**, *15*, 13737–13783, doi:10.1039/C3CP51213D.

[14] Öztürk, S.; Moon, G.-H.; Spieß, A.; Budiyanto, E.; Roitsch, S.; Tüysüz, H.; Janiak, C. A Highly-Efficient Oxygen Evolution Electrocatalyst Derived from a Metal-Organic Framework and Ketjenblack Carbon Material. *ChemPlusChem* **2021**, *86*, 1106–1115, doi:10.1002/cplu.202100278.

[15] Sondermann, L.; Jiang, W.; Shviro, M.; Spieß, A.; Woschko, D.; Rademacher, L.; Janiak, C. Nickel-Based Metal-Organic Frameworks as Electrocatalysts for the Oxygen Evolution Reaction (OER). *Molecules* **2022**, *27*, 1241, doi:10.3390/molecules27041241.

[16] Pang, W.; Shao, B.; Tan, X.-Q.; Tang, C.; Zhang, Z.; Huang, J. Exfoliation of metal–organic frameworks into efficient single-layer metal–organic nanosheet electrocatalysts by the synergistic action of host–guest interactions and sonication. *Nanoscale* **2020**, *12*, 3623–3629, doi:10.1039/C9NR09742B.

[17] Lin, Y.; Wan, H.; Wu, D.; Chen, G.; Zhang, N.; Liu, X.; Li, J.; Cao, Y.; Qiu, G.; Ma, R. Metal–organic framework hexagonal nanoplates: bottom-up synthesis, topotactic transformation, and efficient oxygen evolution reaction. *J. Am. Chem. Soc.* **2020**, *142*, 7317–7321, doi:10.1021/jacs.0c01916.

[18] Yu, M.; Moon, G.; Bill, E.; Tüysüz, H. Optimizing Ni–Fe Oxide Electrocatalysts for Oxygen Evolution Reaction by Using Hard Templating as a Toolbox. *ACS Appl. Energy Mater.* **2019**, *2*, 1199–1209, doi:10.1021/acsaem.8b01769.

[19] Anantharaj, S.; Karthik, P.E.; Kundu, S. Petal-like hierarchical array of ultrathin Ni(OH)2 nanosheets decorated with Ni(OH)2 nanoburls: a highly efficient OER electrocatalyst. *Catal. Sci. Technol.* **2017**, *7*, 882–893, doi:10.1039/C6CY02282K.

[20] Zhao, X.; Ding, X.; Xia, Y.; Jiao, X.; Chen, D. Coupling-Effect-Induced Acceleration of Electron Transfer for α-$Ni(OH)_2$ with Enhanced Oxygen Evolution Reaction Activity. *ACS Appl. Nano Mater.* **2018**, *1*, 1476–1483, doi:10.1021/acsanm.7b00360.

3.2. Exceptionally Stable and Super-Efficient Electrocatalysts Derived from Semiconducting Metal Phosphonate Frameworks

Thi Hai Yen Beglau[+], Marcus N. A. Fetzer[+], Istvan Boldog, Tobias Heinen, Markus Suta, Christoph Janiak, Gündoğ Yücesan

Chem. Eur. J. ***2024***, *30 (1), e202302765.* DOI: 10.1002/chem.202302765.

[+]These authors contributed equally to this work.

(License Number: 5819040157556)

Abstract:

In this study, we introduce two new semiconductive metal phosphonate frameworks, Co_2[1,4-NDPA] and Zn_2[1,4-NDPA] (where 1,4-$NDPA^{4-}$ represents 1,4-naphthalenediphosphonate). These frameworks exhibit optical bandgaps of 1.7 eV and 2.5 eV, respectively, falling within the semiconductive range. The electrocatalyst derived from Co_2[1,4-NDPA] as a precursor demonstrated a lower overpotential of 374 mV in the OER, with a Tafel slope of 43 mV dec^{-1} at a current density of 10 mA cm^{-2} in an alkaline electrolyte (1 mol L^{-1} KOH), indicative of notably superior reaction kinetics. The OER performance of Co_2[1,4-NDPA] materials as precatalysts coupled with nickel foam (NF) revealed exceptional long-term stability at a current density of 50 mA cm^{-2} for water splitting compared to the state-of-the-art Pt/C/RuO_2@NF after 30 hours in 1 mol L^{-1} KOH. Furthermore, to gain insights into the OER mechanism, the transformation of Co_2[1,4-NDPA] into its electrocatalytical active species was investigated.

Author´s contribution to the publication:

- Planning of the research project and carrying out the literature review with support from Dr. Gündoğ Yücesan
- Synthese and characterizations of 1,4-naphthalenediphosphonate as well as Co_2[1,4-NDPA] and Zn_2[1,4-NDPA] Metal Phosphonate Frameworks by Mr. Marcus N. A. Fetzer
- Investigations and evaluation of crystal structure description by Mr. Tobias Heinen and Dr. Istvan Boldog
- Investigations and evaluation of optical measurements by Jun. Prof. Dr. Markus Suta
- Investigations and evaluation for all electrochemical performance of the OER and overall water splitting in an alkaline medium (1 mol L^{-1} KOH) of Co_2[1,4-NDPA] and Zn_2[1,4-NDPA] Metal Phosphonate Frameworks
- Synthesis, characterization, and evaluation of the electrochemical performance of the OER and overall water splitting of β-$Co(OH)_2$, physical mixing of β-$Co(OH)_2$ and ligand [1,4-$NDPAH_4$] and commercial RuO_2 as the reference materials
- Investigation and evaluation for characterization of PXRD, SEM, SEM-EDX, and SEM mapping measurements before and after OER

- TGA measurements by Mr. Till Strothmann, FTIR measurements by Mrs. Birgit Tommes
- Preparation of the manuscript and all figures, graphs, and tables contained in the manuscript with support from Dr. Gündoğ Yücesan
- Revision of the manuscript with the comments of Mr. Marcus N. A. Fetzer, Dr. Istvan Boldog, Dr. Gündoğ Yücesan, Jun. Prof. Dr. Markus Suta and Prof. Dr Christoph Janiak
- Submission of the publication to the international journal " Chemistry: A European Journal" with Dr. Gündoğ Yücesan

Check for updates

Chemistry–A European Journal

Research Article
doi.org/10.1002/chem.202302765

Chemistry Europe
European Chemical Societies Publishing

www.chemeurj.org

Exceptionally Stable And Super-Efficient Electrocatalysts Derived From Semiconducting Metal Phosphonate Frameworks

Thi Hai Yen Beglau[+],[a] Marcus N. A. Fetzer[+],[a] Istvan Boldog,[a] Tobias Heinen,[a] Markus Suta,[b] Christoph Janiak,*[a] and Gündoğ Yücesan*[a]

Two new isostructural semiconducting metal-phosphonate frameworks are reported. Co_2[1,4-NDPA] and Zn_2[1,4-NDPA] (1,4-NDPA^{4-} is 1,4-naphthalenediphosphonate) have optical bandgaps of 1.7 eV and 2.5 eV, respectively. The electrocatalyst derived from Co_2[1,4-NDPA] as a precatalyst generated a low overpotential of 374 mV in the oxygen evolution reaction (OER) with a Tafel slope of 43 mV dec^{-1} at a current density of 10 mA cm^{-2} in alkaline electrolyte (1 mol L^{-1} KOH), which is indicative of remarkably superior reaction kinetics. Benchmarking of the OER of Co_2[1,4-NPDA] material as a precatalyst coupled with nickel foam (NF) showed exceptional long-term stability at a current density of 50 mA cm^{-2} for water splitting compared to the state-of-the-art Pt/C/RuO_2@NF after 30 h in 1 mol L^{-1} KOH. In order to further understand the OER mechanism, the transformation of Co_2[1,4-NPDA] into its electrocatalytically active species was investigated.

Introduction

During the last two decades, metal organic frameworks (MOFs) have been one of the most active research areas.[1,2] MOFs provide rich structural diversity and reticular chemistry to optimize pore sizes and surface areas in porous materials.[3–6] Furthermore, MOF surface areas can be decorated with a large variety of organic functional groups via linker design as well as post-synthetic modifications.[7–11] The rich structural diversity of MOFs has been well reflected in their potential application areas such as small molecule capture,[12–14] small molecule storage,[15] electrode materials,[16,17] electrochemical energy storage,[18] magnetism,[19,20] drug delivery,[21–23] heterogeneous catalysis,[24–27] electrocatalysis,[28] etc. Among these applications, electrocatalysis of the oxygen evolution reaction (OER) is one of the fundamental steps in electrochemical systems such as water splitting or zinc-air batteries.[29–31] Design and synthesis of novel OER electrocatalysts with fast kinetics, excellent catalytic activity and stability has been extensively studied during the last years. Metal-based oxides such as IrO_2 and RuO_2 are the current bench-mark materials for OER due to their low overpotential and large current density.[32] However, high cost, poor durability, and low earth reserves of IrO_2 and RuO_2 hinder the feasibility of these compounds for industrial applications.[33] As an alternative to IrO_2 and RuO_2, MOFs are recently emerging as precatalysts for electrocatalysis of the hydrogen evolution (HER), oxygen evolution (OER), and oxygen reduction reactions (ORR).[34–37] Such compounds could potentially provide more feasible and environmentally friendlier options towards industrialization of OERs.[38] In the current state of the art, MOFs generally function as precatalysts, undergoing a sequence of structural reconfigurations, such as hydrolysis, metal ion leaching, and oxidation of the metal ions in the alkaline medium to generate an active catalyst such as [$M(OH)_2$-$M(O)_x(OH)_y$].[39]

One of the unexplored material types in electrocatalysis is the use of recently emerging semiconducting metal-phosphonate frameworks. Hypothetically, the use of narrow band gap or semiconducting MOFs might help improve OER kinetics, and currently there is a limited number of narrow band gap MOFs in the literature.[40] Our research group has recently reported on the electrical conductivity of microporous phosphonate MOFs and layered metal phosphonates.[17,20,41–44] The reported semiconducting phosphonate MOFs by our group have narrow band gaps between 1.4 and 2.5 eV. We have previously shown that changing the identity and coordination environment of the metal ions in isostructural MOFs and hydrogen-bonded organic framework (HOFs) are important tools for fine band-gap tuning of the framework.[43,45] The band gap of a compound might be an indicator for the ease of an electron transfer step in electrocatalytic reactions.[46,47] For example, the Co^{3+}/Co^{2+} couple is currently intensely investigated for photocatalytic water splitting because the respective reduction potential at

[a] T. H. Y. Beglau,[+] M. N. A. Fetzer,[+] I. Boldog, T. Heinen, C. Janiak, G. Yücesan
Institute of Inorganic and Structural Chemistry
Heinrich Heine Universität Düsseldorf
Universitätstr. 1, 40225, Düsseldorf (Germany)
E-mail: janiak@uni-duesseldorf.de
guendog.yuecesan@hhu.de

[b] M. Suta
Inorganic Photoactive Materials, Institute for Inorganic Chemistry and Structural Chemistry
Heinrich Heine University Düsseldorf
Universitätsstr. 1, 40225 Düsseldorf (Germany)

[+] These authors contributed equally to this work.

Supporting information for this article is available on the WWW under https://doi.org/10.1002/chem.202302765

pH = 7 is E^0 ~ + 1.41 V > + 1.23 V for the OER of pure water.[48] Furthermore, phosphonate-MOFs could exhibit exceptional thermal stabilities above 400 °C and chemical stabilities between pH = 0 and 12.[49–54]

In this work, we successfully synthesized two new dense isostructural semiconducting metal phosphonate frameworks namely Co_2[1,4-NDPA] and Zn_2[1,4-NDPA] (where 1,4-$NDPA^{4-}$ is 1,4-naphthalenediphosphonate) by hydrothermal methods in pure water. The structures were characterized by single crystal X-ray diffraction (XRD), powder-XRD, infrared (IR) and scanning electron microscopy (SEM) with energy dispersive X-ray analysis (EDX). Optical measurements were carried out to determine the absorption onset of the materials. The Co_2[1,4-NDPA] and Zn_2[1,4-NDPA] materials were used for OER on a glassy carbon electrode. Furthermore, the materials were used as cathode and anode on nickel foam (NF) and compared with commercial platinum on carbon (Pt/C) (cathode catalyst) and RuO_2 (anode catalyst) couple for water splitting. The formation of the active species derived from Co_2[1,4-NPDA] was investigated to understand the OER mechanism.

Results and Discussion

Synthesis

Chemicals were purchased from Aldrich, Alfa Aesar and TCI chemicals, and used without further purification. 1,4-naphthalenediphosphonic acid, 1,4-$NDPAH_4$ was synthesized according to the literature.[17,55] A detailed description of the linker synthesis can be found in the Supporting Information. Co_2[1,4-NDPA] and Zn_2[1,4-NDPA] were synthesized under the same hydrothermal reaction conditions. $Co(NO_3)_2 \cdot 6H_2O$ (273 mg, 0.93 mmol) or $Zn(NO_3)_2 \cdot 6H_2O$ (276 mg, 0.93 mmol), 1,4-naphthalenediphosphonic acid (100 mg, 0.34 mmol) and 4,4′-bipyridine as a modulator (40 mg, 0.25 mmol) and 10 mL of ultrapure water were placed in a Parr Teflon-lined autoclave. After brief mixing of the reaction mixture, the autoclave was closed and heated to 200 °C for 72 hours. Afterwards, the product was washed three times with 10 mL of ultrapure water and one time with 10 mL acetone prior to drying. The product was dried in air at room temperature, yielding dark blue crystal plates of Co_2[1,4-NDPA] and white crystal plates of Zn_2[1,4-NDPA].

Crystal structure description

The structures of Co_2[1,4-NDPA] and Zn_2[1,4-NDPA] were determined and refined using single crystal X-ray diffraction methods. As depicted in Figure 1a, the two isostructural compounds Co_2[1,4-NDPA] and Zn_2[1,4-NDPA] exhibit a pillared layered metal phosphonate network. The layered secondary building unit (SBU) is constructed from tetrahedrally coordinated Co^{2+} or Zn^{2+} atoms and phosphonate groups ($-PO_3^{2-}$) from the fully deprotonated 1,4-$NDPA^{4-}$ linkers, forming isolated four-membered M–O–M–O rings (M = Co or Zn), surrounded by six eight-membered M–O–P–O-M–O-P–O rings to give a layered network of Co_2[1,4-NDPA] and Zn_2[1,4-NDPA] (Figure 1a and 1b). The actual topology of the layered SBU of Co_2[1,4-NDPA] and Zn_2[1,4-NDPA] is unprecedented among other layered metal phosphonate frameworks with a 3,3,4 L25 net type (see Supporting Information for topological characterization). The layered SBUs are connected by aromatic naphthalene units of 1,4-$NDPA^{4-}$ to form the three-dimensional framework (see Figure 1a and Supporting Information). The analysis for purity of the single-crystalline phase was done by PXRD. As shown in the PXRD (Figure 2), both Co_2[1,4-NDPA] and Zn_2[1,4-NDPA] show good agreement with simulation and were synthesized as single crystalline phases. As depicted in Figures S1 to S3, the intercentroid distances between the naphthalene moieties for Co_2[1,4-NDPA] and Zn_2[1,4-NDPA] are, respectively, 3.91 Å and 3.97 Å and shortest C···C distances

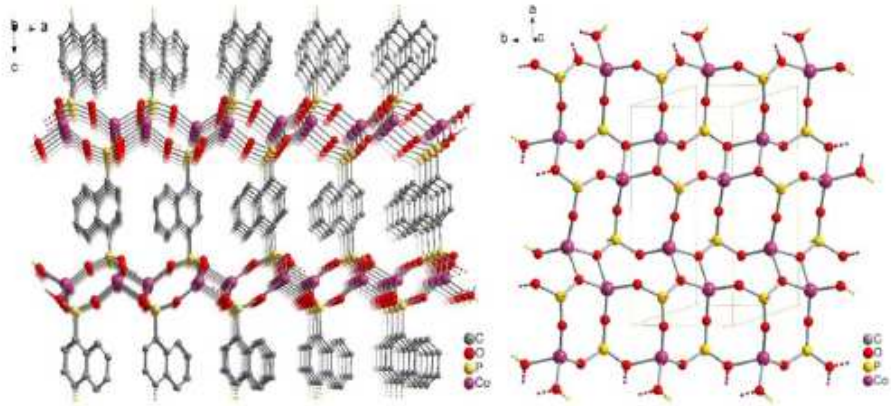

Figure 1. (a) Section of the packing diagram of the three-dimensional structure of Co_2[1,4-NDPA]. (b) Structure of the layered inorganic building unit of Co_2[1,4-NDPA] (isostructural to Zn_2[1,4-NDPA]).

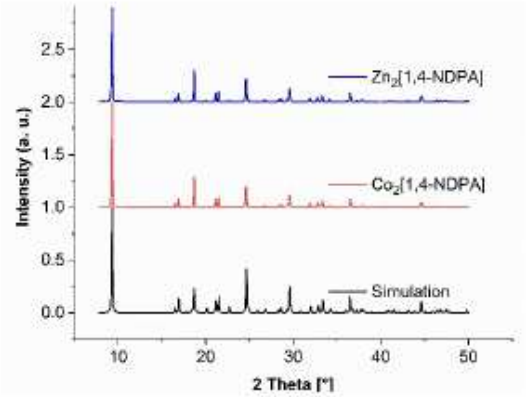

Figure 2. PXRD of the single-crystalline phase in agreement with the simulation from the structure of Zn_2[1,4-NDPA].

3.40–3.48 Å and 3.35–3.44 Å, which are similar to interlayer distances of graphite (for a more detailed description of the crystal structure see Supporting Information).

Optical measurements

Based on the marked color difference of Co_2[1,4-NDPA] and Zn_2[1,4-NDPA], diffuse reflectance spectra were measured on powdered samples of these two compounds in an integrating sphere setup (Ulbricht sphere). If the thickness of the powder slab is sufficiently high such that transmittance along the layer is negligible, the absorbance A of the powder scales with the Kubelka-Munk function K/S given by Equation (1):

$$\frac{K}{S} = f(R_\infty) = \frac{(1-R_\infty)^2}{2R_\infty} \propto A \quad (1)$$

with R_∞ as the diffuse reflectance of the powder layer. The Kubelka-Munk spectra of Co_2[1,4-NDPA] and Zn_2[1,4-NDPA] are depicted in Figure 3. Both spectra show a strong increase around 500 nm (~2.5 eV) and are very similar in that wavelength range. This absorption is assigned to an interband transition, which is expectedly strongly localized at the naphthalene moieties. The low onset energy (< 3 eV) for strong absorption indicates a semiconducting behavior of the two compounds. The strong increase in absorption below 400 nm in the ultraviolet (UV) range of Zn_2[1,4-NDPA] explains why the related powdered compound appears colorless under daylight. The Kubelka-Munk spectrum of Co_2[1,4-NDPA] reveals additional low-energetic broad absorption bands in the range between 500 nm and 700 nm (onset of ~1.7 eV in the energy domain), which are absent in the Zn analogue and thus have to be identified as localized transitions due to the presence of tetrahedrally coordinated Co(II) in Co_2[1,4-NDPA]. The electronic transitions of the tetrahedrally coordinated $3d^7$ ion Co^{2+} can be in principle interpreted by means of the Tanabe-Sugano diagram of an octahedrally coordinated $d^{10-7}=d^3$ ion. Comparison to other literature-reported examples of Co^{2+}-doped purely inorganic oxides such as spinel-type $MAl_2O_4:Co^{2+}$ (M = Zn, Mg),[56,57] willemite-type[58] $Zn_2SiO_4:Co^{2+}$ or wurtzite-type[59] binary compounds $MX:Co^{2+}$ (M = Zn, X = O, S) offering tetrahedrally coordinated sites for Co^{2+} allows the assignment to a $^4A_2(^4F) \rightarrow {}^4T_1(^4P)$ ligand field transition of the observed absorption bands in that wavelength range (see Figure 3). The dark blue color of Co_2[1,4-NDPA] can be related to both the absorption in the deep red to near infrared range ($\lambda > 650$ nm) on the one hand and the strong reflection of light in the blue range of the

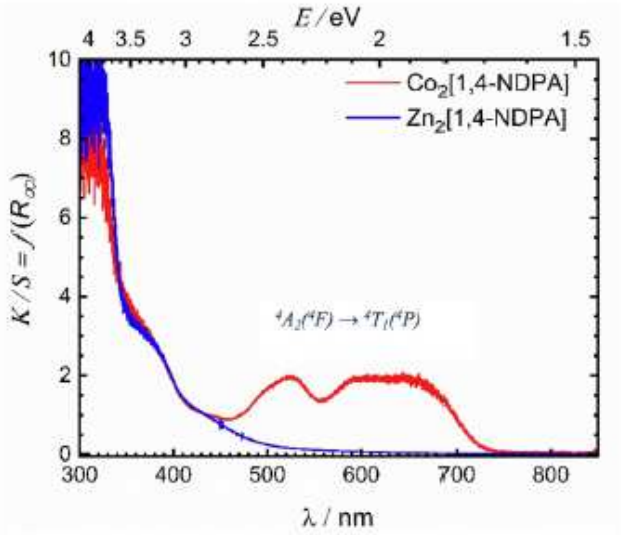

Figure 3. Optical Kubelka-Munk spectra of powdered Co_2[1,4-NDPA] (red) and Zn_2[1,4-NDPA] (dark blue) obtained from diffuse reflectance spectra at room temperature. The localized Co(II)-based ligand field transition is denoted

visible spectrum. Similar colors are known from the pigment Thénard blue ($CoAl_2O_4$) with high concentrations of Co^{2+}, which crystallizes in a spinel-type structure and in which the Co^{2+} ions also occupy tetrahedrally coordinated sites.

Electrocatalytic performance of the OER

The electrochemical OER is an anodic half-cell reaction and produces O_2 at a theoretical input of 1.23 V (vs. reversible hydrogen electrode (RHE)). We investigated the OER using Co_2[1,4-NDPA] and Zn_2[1,4-NDPA] as precatalysts in a 1 mol L^{-1} KOH electrolyte (pH = 14) and the obtained results were compared with commercial RuO_2. We used a glassy carbon rotating disk electrode (GC-RDE) with a geometric area of 0.196 cm^{-2} at a rotating velocity of 1600 rpm in a standard three-electrode system. The mass loading of electrocatalysts on the GC-RDE was quantified at 0.23 mg cm^{-2} (see Supporting Information for details). The polarization curves were generated by the linear sweep voltammogram (LSV) of Co_2[1,4-NDPA] and Zn_2[1,4-NDPA] and are compared to β-$Co(OH)_2$, a physical mixture of β-$Co(OH)_2$ and the ligand 1,4-$NDPAH_4$ and commercial RuO_2 in the same Nafion ink (see Supporting Information about how the ink for the electrode was prepared). The synthesized β-$Co(OH)_2$ and physical mixture of β-$Co(OH)_2$ and the ligand 1,4-$NDPAH_4$ were used as reference catalysts. Figure 4a presents the polarization curves of the samples after 20 cyclic voltammetry (CV) cycles of activation at a scan rate 50 mV s^{-1}, in order to get a stable state of the catalysts on the GC-RDE surface. The overpotentials of the various working electrodes are determined to be 374 mV for Co_2[1,4-NDPA], 380 mV for β-$Co(OH)_2$, 392 mV for the physical mixture of β-$Co(OH)_2$ and the ligand 1,4-$NDPAH_4$, 408 mV for Zn_2[1,4-NDPA] and 318 mV for RuO_2 at the current density of 10 mA cm^{-2} (see Figure 4a).

The Tafel plots are usually obtained in a potential range where the current is predominantly controlled by catalysis kinetics (non-mass-transfer restriction).[60] Therefore, we evaluated electrocatalytic kinetics for the OER of the precatalysts Co_2[1,4-NDPA] and Zn_2[1,4-NDPA] by generating their corresponding Tafel slopes. As seen in Figure 4b, the linear portion of the Tafel plot was fitted using the equation $\eta = a + b \times \log j$, where η and j represent the overpotential and the current density, respectively; b is the Tafel slope and a represents the cathodic intercept that is related to the exchange current density.[60] The smaller Tafel slope often refers to more favorable OER kinetics and a better electrocatalytic activity. The OER is a four-electron transfer reaction with a sequence of steps and intermediates, such as MO, MOOH or physisorbed peroxide species.[60] One of the most accepted OER mechanisms is the Krasil'shchikov's pathway, given in Reactions (1)–(4) with their corresponding Tafel slopes (b).[61–63]

$$M + OH^- \leftrightarrows MOH + e^-,\ b = 120\ mV\,dec^{-1} \quad (1)$$

$$MOH + OH^- \leftrightarrows MO^- + H_2O,\ b = 60\ mV\,dec^{-1} \quad (2)$$

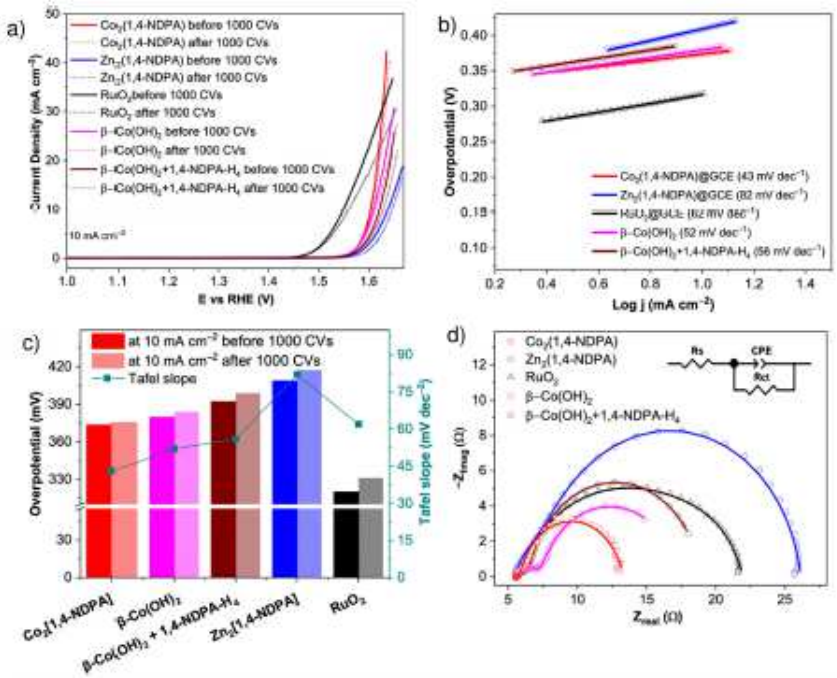

Figure 4. a) OER polarization curves before and after 1000 CVs in 1.0 mol L^{-1} KOH (pH = 14) b) OER Tafel plots obtained from the OER polarization curves c) corresponding overpotentials (columns) before and after 1000 CVs at 10 mA cm^{-2} and Tafel slopes (dark cyan dots). (d) raw data Nyquist plots at 1.6 V vs. RHE (symbol) and fitting to an equivalent model (solid line) from EIS test of Co_2[1,4-NDPA], Zn_2[1,4-NDPA], β -$Co(OH)_2$, physical mixture of β -$Co(OH)_2$ and ligand 1,4-$NDPAH_4$ and RuO_2 and benchmark material RuO_2 on GC-RDE.

$$MO^{-} \rightarrow MO + e^{-},\ b = 45\ mV\,dec^{-1} \quad (3)$$

$$2MO \rightarrow 2M + O_2,\ b = 19\ mV\,dec^{-1} \quad (4)$$

Based on the Krasil'shchikov's pathway, a Tafel slope of $b = 43\ mV\,dec^{-1}$ to the OER involving Co_2[1,4-NDPA] corresponds to reaction (3) as a rate determining step. The Tafel slope of Zn_2[1,4-NDPA] ($b = 82\ mV\,dec^{-1}$) falls in between the values of the reaction (1) and (2). This can be attributed to stronger OH^- binding to Zn^{2+} ions that accelerates the rate of electron transfer in Reaction (1) (Figure 4b). As presented in Table S6, the Tafel slope of the electrocatalysts derived from Co_2[1,4-NDPA] and Zn_2[1,4-NDPA] is much lower than RuO_2 ($62\ mV\,dec^{-1}$), β-$Co(OH)_2$ ($52\ mV\,dec^{-1}$, the physical mixture of β-$Co(OH)_2$ and the ligand 1,4-$NDPAH_4$ ($56\ mV\,dec^{-1}$) and other Co-based catalysts in the literature,[38] which suggest its superior reaction kinetics. In addition, the stability of the electrocatalysts derived from Co_2[1,4-NDPA] and Zn_2[1,4-NDPA] was investigated and compared with the commercial benchmark RuO_2 after 1000 continuous CVs. The electrocatalysts derived from Co_2[1,4-NDPA] and Zn_2[1,4-NDPA] showed stronger durability compared to β-$Co(OH)_2$, the physical mixture of β-$Co(OH)_2$ and the ligand 1,4-$NDPAH_4$, and RuO_2, as they exhibited only minor positive shifts of 2 and 8 mV, respectively. RuO_2, β-$Co(OH)_2$, and the physical mixture of β-$Co(OH)_2$ and the ligand 1,4-$NDPAH_4$ showed an increase of the overpotential by 14, 4 and 6 mV, respectively, at the current density of $10\ mA\,cm^{-2}$ after 1000 CVs (see Figure 4c).

To better understand the OER kinetics, an electrochemical impedance spectroscopy (EIS) measurements were carried out at 1.6 V in a frequency range of 0.1 Hz to 100 kHz in $1\ mol\,L^{-1}$ KOH. The semicircles in the high-frequency range of the Nyquist plots are attributed to charge-transfer resistance, which is equivalent for all catalysts. The Nyquist plots of catalysts Co_2[1,4-NDPA], Zn_2[1,4-NDPA], β-$Co(OH)_2$ and the physical mixture of β-$Co(OH)_2$ and ligand 1,4-$NDPAH_4$ and RuO_2 were curve-fitted to the model to evaluate the charge transfer resistance (R_{ct}) (see Figure 4d). The small R_{ct} value indicates the efficient electron transfer between the active sites of catalysts derived from Co_2[1,4-NDPA] and Zn_2[1,4-NDPA] and the electrolyte ion during OER. Co_2[1,4-NDPA] has the smallest R_{ct} value of 8 Ω, which is obviously smaller than that of β-$Co(OH)_2$ (10 Ω), the physical mixture of β-$Co(OH)_2$ and the ligand 1,4-$NDPAH_4$ (13 Ω), RuO_2 (16 Ω) and Zn_2[1,4-NDPA] (21 Ω).

Overall electrochemical water splitting

The overall water splitting contains two half reactions, which are the hydrogen evolution reaction (HER) and the oxygen evolution reaction (OER). The Co_2[1,4-NDPA] and Zn_2[1,4-NDPA] materials were coated on the surface of NF with a uniform thin layer (see SI for experimental details). Both the anode and cathode was constructed by employing the Co_2[1,4-NDPA] or Zn_2[1,4-NDPA] materials in the alkaline electrolyzer with $1\ mol\,L^{-1}$ KOH. The integrated commercial platinum on carbon (Pt/C) (cathode catalyst) and RuO_2 (anode catalyst) couple (Pt/C@NF/RuO_2@NF) was also tested for comparison. As expected, the LSV curves in Figure 5a show that the Pt/C@NF/RuO_2@NF couple catalysed the water electrolysis with an overpotential of 278 and 340 mV at a current density of 10 and $50\ mA\,cm^{-1}$, respectively. Therefore, the catalysts derived from Co_2[1,4-NDPA]@NF (312 mV) and Zn_2[1,4-NDPA]@NF (371 mV) show a lower overpotential compared to the performance of the glassy carbon electrode. Additionally, the activity of Co_2[1,4-NDPA]@NF is higher than the benchmark RuO_2@NF, reaching a practical current density of $200\ mA\,cm^{-2}$ at 1.63 V. The long-term stability plays an important role to evaluate electrocatalysts for practical water electrolysis.

The long-term stabilities of the catalysts derived from Co_2[1,4-NDPA] and Zn_2[1,4-NDPA] and the commercial Pt/C/RuO_2 couple in $1\ mol\,L^{-1}$ KOH was further checked by a chronopotentiometric test applying a constant current density at $50\ mA\,cm^{-2}$ continuously for 30 h. The potential of the catalysts derived from Co_2[1,4-NDPA]@NF and Zn_2[1,4-NDPA]-

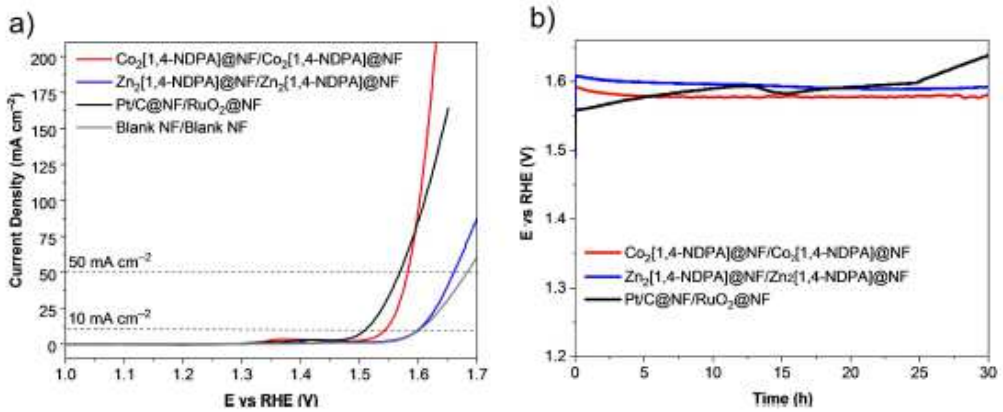

Figure 5. (a) Polarization curves and (b) the long-term stabilities in the electrolysis at a current density of $\eta = 50\ mA\,cm^{-2}$ by chronopotentiometric measurements of Co_2[1,4-NDPA], Zn_2[1,4-NDPA], Pt/C/RuO_2 on NF for overall water splitting in $1\ mol\,L^{-1}$ KOH.

@NF remained nearly unchanged during the whole measurement. In contrast, the commercial benchmark Pt/C/RuO_2@NF couple showed an increasing working potential at the current density of 50 mA cm^{-2} over 30 h. Consequently, the electrocatalysts derived from Co_2[1,4-NDPA] and Zn_2[1,4-NDPA] adhered well on the surface of NF after the stability test, as proven by SEM and element mapping (Figure S10 and Figure S11).

Zheng *et al.* point out that the metal-organic-framework based catalysts are precatalysts, and change to active phases during the electrochemical treatment under alkaline condition (1 mol L^{-1} KOH).[37] Therefore, we tested the chemical stability of Co_2[1,4-NDPA] by soaking the material in the alkaline electrolyte (1 mol L^{-1} KOH) for 30 min and 24 h, in order to gain a better understanding of the activation mechanism. The PXRD pattern of Co_2[1,4-NDPA] after 24 h in 1 mol L^{-1} KOH revealed the presence of cobalt hydroxide species (Figure 6). in the form of α-$Co(OH)_2$ (ICDD: 74-1057) and β-$Co(OH)_2$ (ICDD: 30-0443). It was indicated that the active sites in α/β-$Co(OH)_2$ are responsible for the excellent electrocatalyst performance.[64-66]

Thermal stability

The thermal stability of the Co_2[1,4-NDPA] and Zn_2[1,4-NDPA] was investigated by thermogravimetric analysis (TGA) measurements under a nitrogen atmosphere. Co_2[1,4-NDPA] and Zn_2[1,4-NDPA] show exceptional thermal stability where the organic components start to decompose at ca. 650 °C with 29.1 % experimental weight loss (theoretical 30.9 %) for Zn_2[1,4-NDPA]. The TGA curve of Co_2[1,4-NDPA] indicates a more gradual weight loss with a sharp mass decrease above 650 °C (see Figure S7).

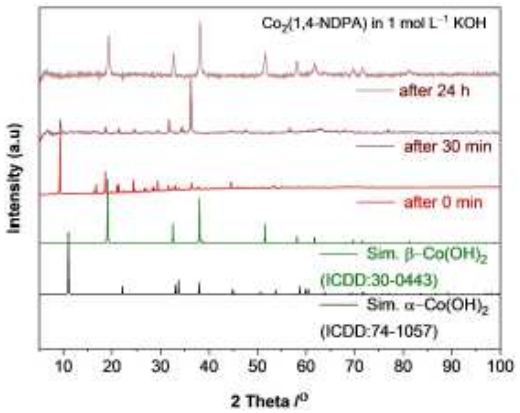

Figure 6. PXRD patterns of Co_2[1,4-NDPA], after 30 min and 24 h in 1 mol L^{-1} KOH; reflections from β-$Co(OH)_2$ (ICDD:30-0443) and α-$Co(OH)_2$ (ICDD: 74-1057).

Conclusions

Herein, we report the hydrothermal synthesis of the two new semiconducting metal-phosphonate frameworks Co_2[1,4-NDPA] and Zn_2[1,4-NDPA], and we have shown that changing the metal ions in isostructural semiconducting metal-phosphonate frameworks can be used to tune band gap and semiconducting properties. Both powdered compounds have absorption onsets at around 500 nm (2.5 eV), derived from photoluminescence optical Kubelka-Munk spectra data, which are strongly localized at the naphthalene moieties. Furthermore, Co_2[1,4-NDPA] shows a second onset at 700 nm (1.7 eV) which has to be identified as ligand-field transitions localized at the Co center with its low energetic $^4A_2(^4F) \rightarrow {}^4T_1(^4P)$ ligand field transition of tetrahedrally coordinated d^7-Co(II). We have furthermore used the new semiconducting metal-phosphonate frameworks as precatalysts for the OER reaction. We have shown that both Co_2[1,4-NDPA] and Zn_2[1,4-NDPA] are remarkable precatalysts for the OER reaction in water splitting with overpotentials of 374 mV for Co_2[1,4-NDPA] and 408 mV for Zn_2[1,4-NDPA] for a glassy carbon rotating electrode system and 312 mV and 371 mV on NF at a current density 10 mA cm^{-2}. The Tafel slope of 43 mV dec^{-1} in 1 mol L^{-1} KOH at a current density of 10 mA cm^{-2} of the Co_2[1,4-NDPA] precatalyst indicates its superior reaction kinetics compared to the commercial benchmark material RuO_2 or other compound families like metal phosphides and some reported MOFs in the literature. Besides, its good reaction kinetics, electrocatalyst derived from Co_2[1,4-NDPA] also shows remarkably improved activity, compared to RuO_2 on NF for water splitting reaching a current density of 200 mA cm^{-2} at 1.63 V. This work also demonstrated the exceptionally high stability of the derived active species of β-$Co(OH)_2$ and β-CoOOH catalysts by using Co_2[1,4-NDPA] as a precatalyst in 1 mol L^{-1} KOH for 30 h at a constant current density of 50 mA cm^{-2}. Several features may contribute to the excellent OER performance of the catalyst derived from Co_2[1,4-NDPA] when compared to the concurrently studied RuO_2, β-$Co(OH)_2$ and physically mixed β-$Co(OH)_2$ with the ligand 1,4-NDPAH_4. For example, the Co_2[1,4-NDPA] precatalyst might hypothetically generate a more uniform distribution of α/β-$Co(OH)_2$ and 1,4-NDPA-H_4 ligand on the surface of the glassy carbon electrode creating superior OER activities compared to the concurrently studied systems. All these results demonstrate that both materials, but especially the Co_2[1,4-NDPA] are potential candidates for industrial applications as precatalysts for OER in water electrolysis.

Supporting Information

Additional detailed experimental and characterization methods; synthesis progress; crystallography information; FTIR measurement; thermogravimetric analysis; electrochemical measurement; SEM and SEM-EDX before and after electrolysis; OER performance comparison; and topological analysis.

Deposition Numbers 2235305 (for Co_2[1,4-NDPA]), 2212088 (for Zn_2[1,4-NDPA]) contain the supplementary crystallographic

data for this paper. These data are provided free of charge by the joint Cambridge Crystallographic Data Centre and Fachinformationszentrum Karlsruhe Access Structures service.

Acknowledgements

G.Y. acknowledges financial support from DFG through grant YU-267/2-1. M.S. gratefully acknowledges funding from a materials cost allowance of the Fonds der Chemischen Industrie e.V. and a scholarship from the "Young College" of the North-Rhine Westphalian Academy of Sciences and Arts. C.J. thanks the DFG for funding within the Priority Program SPP 1928/2 COORNETs (grant Ja466/43-1). Open Access funding enabled and organized by Projekt DEAL.

Conflict of Interests

The authors declare no competing financial interest.

Data Availability Statement

The data that support the findings of this study are available in the supplementary material of this article.

Keywords: electrocatalysis · phosphonates · semiconducting materials

[1] J. D. Evans, B. Garai, H. Reinsch, W. Li, S. Dissegna, V. Bon, I. Senkovska, R. A. Fischer, S. Kaskel, C. Janiak, et al., *Coord. Chem. Rev.* **2019**, *380*, 378–418.
[2] H. Furukawa, K. E. Cordova, M. O'Keeffe, O. M. Yaghi, *Science* **2013**, *341*, 1230444.
[3] Z. Chen, H. Jiang, M. Li, M. O'Keeffe, M. Eddaoudi, *Chem. Rev.* **2020**, *120*, 8039.
[4] O. M. Yaghi, M. O'Keeffe, N. W. Ockwig, H. K. Chae, M. Eddaoudi, J. Kim, *Nature* **2003**, *423*, 705.
[5] S. Canossa, Z. Ji, C. Gropp, Z. Rong, E. Ploetz, S. Wuttke, O. M. Yaghi, *Nat. Rev. Mater.* **2023**, *8*, 331.
[6] P. Tholen, Y. Zorlu, J. Beckmann, G. Yücesan, *Eur. J. Inorg. Chem.* **2020**, 1542.
[7] M. Kalaj, M. S. Denny, K. C. Bentz, J. M. Palomba, S. M. Cohen, *Angew. Chem. Int. Ed.* **2019**, *58*, 2336.
[8] Z. Wang, S. M. Cohen, *J. Am. Chem. Soc.* **2007**, *129*, 12368.
[9] S. M. Cohen, *Chem. Rev.* **2012**, *112*, 970.
[10] S. M. Cohen, *J. Am. Chem. Soc.* **2017**, *139*, 2855.
[11] X. Kong, H. Deng, F. Yan, J. Kim, J. A. Swisher, B. Smit, O. M. Yaghi, J. A. Reimer, *Science* **2013**, *341*, 882.
[12] J.-B. Lin, T. T. Nguyen Tai, R. Vaidhyanathan, J. Burner, M. Taylor Jared, H. Durekova, F. Akhtar, K. Mah Roger, O. Ghaffari-Nik, S. Marx, et al., *Science* **2021**, *374* (6574), 1464.
[13] H. A. Evans, D. Mullangi, Z. Deng, Y. Wang, S. B. Peh, F. Wei, J. Wang, C. M. Brown, D. Zhao, P. Canepa, et al., *Sci. Adv.* **2022**, *8*, eade1473.
[14] B. E. R. Snyder, A. B. Turkiewicz, H. Furukawa, M. V. Paley, E. O. Velasquez, M. N. Dods, J. R. Long, *Nature* **2023**, *613* (7943), 287.
[15] M. P. Suh, H. J. Park, T. K. Prasad, D. W. Lim, *Chem. Rev.* **2012**, *112*, 782.
[16] D. Sheberla, *Nat. Mater.* **2017**, *16*, 220.
[17] K. Siemensmeyer, C. A. Peeples, P. Tholen, F. J. Schmitt, B. Çoşut, G. Hanna, G. Yücesan, *Adv. Mater.* **2020**, *32*, e2000474.
[18] J. Liu, X. Song, T. Zhang, S. Liu, H. Wen, L. Chen, *Angew. Chem. Int. Ed.* **2021**, *60*, 5612.
[19] E. Coronado, G. Mínguez Espallargas, *Chem. Soc. Rev.* **2013**, *42*, 1525.
[20] C. A. Peeples, D. Kober, F.-J. Schmitt, P. Tholen, K. Siemensmeyer, Q. Halldorson, B. Çoşut, A. Gurlo, A. O. Yazaydin, G. Hanna, et al., *Adv. Funct. Mater.* **2021**, *31*, 2007294.
[21] S. Rojas, A. Arenas-Vivo, P. Horcajada, *Coord. Chem. Rev.* **2019**, *388*, 202.
[22] P. Horcajada, R. Gref, T. Baati, P. K. Allan, G. Maurin, P. Couvreur, G. Férey, R. E. Morris, C. Serre, *Chem. Rev.* **2012**, *112*, 1232.
[23] P. Horcajada, T. Chalati, C. Serre, B. Gillet, C. Sebrie, T. Baati, J. F. Eubank, D. Heurtaux, P. Clayette, C. Kreuz, et al., *Nat. Mater.* **2010**, *9*, 172.
[24] A. Corma, H. García, F. X. Llabrés i Xamena, *Chem. Rev.* **2010**, *110*, 4606.
[25] X. Wang, X. Han, J. Zhang, X. Wu, Y. Liu, Y. Cui, *J. Am. Chem. Soc.* **2016**, *138*, 12332.
[26] D. Dang, P. Wu, C. He, Z. Xie, C. Duan, *J. Am. Chem. Soc.* **2010**, *132*, 14321.
[27] L. Zhu, X. Q. Liu, H. L. Jiang, L. B. Sun, *Chem. Rev.* **2017**, *117*, 8129.
[28] S. Jin, *ACS Energy Lett.* **2019**, *4* (6), 1443.
[29] H.-F. Wang, L. Chen, H. Pang, S. Kaskel, Q. Xu, *Chem. Soc. Rev.* **2020**, *49*, 1414.
[30] J. Suntivich, K. J. May, H. A. Gasteiger, J. B. Goodenough, Y. Shao-Horn, *Science* **2011**, *334* (6061), 1383.
[31] A. Mahmood, W. Guo, H. Tabassum, R. Zou, *Adv. Energy Mater.* **2016**, *6*, 1600423.
[32] C. C. L. McCrory, S. Jung, J. C. Peters, T. F. Jaramillo, *J. Am. Chem. Soc.* **2013**, *135*, 16977.
[33] S. Dou, C.-L. Dong, Z. Hu, Y.-C. Huang, J.-l. Chen, L. Tao, D. Yan, D. Chen, S. Shen, S. Chou, et al., *Adv. Funct. Mater.* **2017**, *27*, 1702546.
[34] Y. Yang, Y. Yang, Y. Liu, S. Zhao, Z. Tang, *Small Science* **2021**, *1*, 2100015.
[35] F. Sun, Q. Li, H. Xue, H. Pang, *ChemElectroChem* **2019**, *6*, 1273.
[36] B. R. Wygant, K. Kawashima, C. B. Mullins, *ACS Energy Lett.* **2018**, *3*, 2956.
[37] W. Zheng, L. Y. S. Lee, *ACS Energy Lett.* **2021**, *6*, 2838–2843.
[38] C. Zhang, Q. Qi, Y. Mei, J. Hu, M. Sun, Y. Zhang, B. Huang, L. Zhang, S. Yang, *Adv. Mater.* **2023**, *35*, 2208904.
[39] B. Singh, A. Yadav, A. Indra, *J. Mater. Chem. A* **2022**, *10*, 3843.
[40] L. S. Xie, G. Skorupskii, M. Dincă, *Chem. Rev.* **2020**, *120*, 8536.
[41] Y. Zorlu, L. Wagner, P. Tholen, M. M. Ayhan, C. Bayraktar, G. Hanna, A. O. Yazaydin, Ö. Yavuzçetin, G. Yücesan, *Adv. Opt. Mater.* **2022**, *10*, 2200213.
[42] M. M. Ayhan, C. Bayraktar, K. B. Yu, G. Hanna, A. O. Yazaydin, Y. Zorlu, G. Yücesan, *Chem. Eur. J.* **2020**, *26*, 14813.
[43] C. A. Peeples, A. Çetinkaya, P. Tholen, F.-J. Schmitt, Y. Zorlu, K. Bin Yu, O. Yazaydin, J. Beckmann, G. Hanna, G. Yücesan, *Chem. Eur. J.* **2022**, *28*, e202104041.
[44] P. Tholen, L. Wagner, J. G. A. Ruthes, K. Siemensmeyer, T. H. Y. Beglau, D. Muth, Y. Zorlu, M. Okutan, J. C. Goldschmidt, C. Janiak, et al., *Small* **2023**, 2304057.
[45] P. Tholen, C. A. Peeples, M. M. Ayhan, L. Wagner, H. Thomas, P. Imbrasas, Y. Zorlu, C. Baretzky, S. Reineke, G. Hanna, et al., *Small* **2022**, *18*, 2204578.
[46] H.-J. Liu, C.-Y. Chiang, Y.-S. Wu, L.-R. Lin, Y.-C. Ye, Y.-H. Huang, J.-L. Tsai, Y.-C. Lai, R. Munprom, *ACS Catal.* **2022**, *12*, 6132.
[47] L.-C. Wang, B.-H. Liu, C.-Y. Su, W.-S. Liu, C.-C. Kei, K.-W. Wang, T.-P. Perng, *ACS Appl. Nano Mater.* **2018**, *1*, 3673.
[48] S. Chen, T. Takata, K. Domen, *Nat. Rev. Mater.* **2017**, *2*, 17050.
[49] P. Salcedo-Abraira, S. M. F. Vilela, A. A. Babaryk, M. Cabrero-Antonino, P. Gregorio, F. Salles, S. Navalón, H. García, P. Horcajada, *Nano Res.* **2021**, *14*, 450.
[50] M.-F. Qin, Q.-Q. Mu, S.-S. Bao, X. Liang, Y. Peng, L.-M. Zheng, *ACS Appl. Energ. Mater.* **2021**, *4*, 4319.
[51] C. Healy, K. M. Patil, B. H. Wilson, L. Hermanspahn, N. C. Harvey-Reid, B. I. Howard, C. Kleinjan, J. Kolien, F. Payet, S. G. Telfer, et al., *Coord. Chem. Rev.* **2020**, *419*, 213388.
[52] K. J. Gagnon, H. P. Perry, A. Clearfield, *Chem. Rev.* **2012**, *112*, 1034.
[53] G. Yücesan, Y. Zorlu, M. Stricker, J. Beckmann, *Coord. Chem. Rev.* **2018**, *369*, 105.
[54] A. Bulut, M. Wörle, Y. Zorlu, E. Kirpi, H. Kurt, J. Zubieta, S. Grabowsky, J. Beckmann, G. Yücesan, *Acta Crystallogr. Sect. B* **2017**, *73*, 296.
[55] T. Rhauderwiek, K. Wolkersdorfer, S. Oien-Odegaard, K. P. Lillerud, M. Wark, N. Stock, *Chem. Commun.* **2018**, *54*, 389.
[56] J. Ferguson, D. L. Wood, L. G. Van Uitert, *J. Chem. Phys.* **1969**, *51*, 2904.
[57] P. J. Dereń, W. Strék, U. Oetliker, H. U. Güdel, *Phys. Status Solidi B* **1994**, *182*, 241.
[58] T. C. Brunold, H. U. Güdel, E. Cavalli, *Chem. Phys. Lett.* **1996**, *252*, 112.
[59] H. A. Weakliem, *J. Chem. Phys.* **1962**, *36*, 2117.
[60] T. Shinagawa, A. T. Garcia-Esparza, K. Takanabe, *Sci. Rep.* **2015**, *5*, 13801.
[61] G. Li, L. Anderson, Y. Chen, M. Pan, P.-Y. Abel Chuang, *Sustain. Energy Fuels* **2018**, *2*, 237.

[62] L. Sondermann, W. Jiang, M. Shviro, A. Spieß, D. Woschko, L. Rademacher, C. Janiak, *Molecules* **2022**, *27*, 1241.
[63] Y. Matsumoto, E. Sato, *Mater. Chem. Phys.* **1986**, *14*, 397.
[64] A. Bergmann, T. E. Jones, E. Martinez Moreno, D. Teschner, P. Chernev, M. Gliech, T. Reier, H. Dau, P. Strasser, *Nat. Catal.* **2018**, *1*, 711.
[65] X. Bu, C. Chiang, R. Wei, Z. Li, Y. Meng, C. Peng, Y. Lin, Y. Li, Y. Lin, K. S. Chan, et al., *ACS Appl. Mater. Interfaces* **2019**, *11*, 38633.
[66] P. W. Menezes, C. Panda, C. Walter, M. Schwarze, M. Driess, *Adv. Funct. Mater.* **2019**, *29*, 1808632.

Manuscript received: August 25, 2023
Accepted manuscript online: September 15, 2023
Version of record online: November 8, 2023

Chemistry–A European Journal

Supporting Information

Exceptionally Stable And Super-Efficient Electrocatalysts Derived From Semiconducting Metal Phosphonate Frameworks

Thi Hai Yen Beglau, Marcus N. A. Fetzer, Istvan Boldog, Tobias Heinen, Markus Suta, Christoph Janiak,* and Gündoğ Yücesan*

Table of Contents

1. Synthesis

1.1. Synthesis of tetraethyl naphthalene-1,4-diylbis(phosphonate)

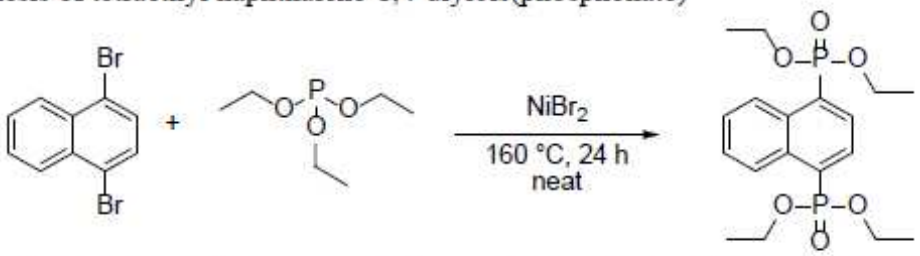

Under a nitrogen flow, 1,4-dibromonaphthalene (5,1 g, 17.8 mmol) was placed in a three-neck round-bottom flask equipped with a stirring bar. The flask was heated to 160 °C to melt the 1,4-dibromonaphthalene. To the melted 1,4-dibromonaphthalene $NiBr_2$ (0.5 g, 2.2 mmol) was added. Finally, triethyl phosphite (7.8 g, 46.9 mmol) was added dropwise over a period of 7 h. The reaction was stirred at the same temperature for 24 h. The crude product, a dark brown to orange oil, was purified by column chromatography using a mixture of EtOAc and EtOH (9:1 v:v). The product was isolated as a colorless oil with a yield of 3.8 g (9.5 mmol, 53.3 %).

^{1}H NMR (300 MHz, $CDCl_3$) δ 8.63-8.59 (m, 2H), 8.29-8.22 (m, 2H), 7.68-7.64 (m, 2H), 4.27-4.07 (m, 8H), 1.32 (t, J = 7.1 Hz, 12H); ^{31}P{^{1}H} NMR (121 MHz, $CDCl_3$) δ 17.4 (s); ^{13}C{^{1}H} NMR (75 MHz, $CDCl_3$) δ 132.9-132.4, 131.6 (d, J = 3.6 Hz), 129.2 (d, J = 3.5 Hz), 127.6, 127.3, 62.5 (d, J = 3.0 Hz), 16.3.

1.2. Synthesis of naphthalene-1,4-diphosphonic acid (1,4-NDPA-H_4)

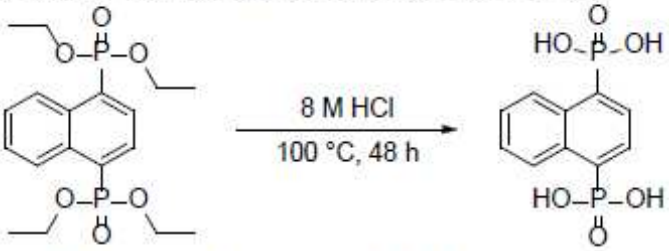

Tetraethyl naphthalene-1,4-diylbis(phosphonate) (3.8 g, 9.5 mmol) was mixed with 100 mL of 8 M hydrochloric acid and refluxed for 24 h. The white precipitate was filtered off and dried at 60 °C under reduced pressure to obtain 2.5 g (yield: 95 %) of pure acid.

^{1}H NMR (300 MHz, DMSO-d_6) δ 8.69-8.65 (m, 2H), 8.08-8.01 (m, 2H), 7.64 (dd, J=6.5, 3.4 Hz, 2H); ^{31}P{^{1}H} NMR (121 MHz, DMSO-d_6) δ 11.0 (s);
^{13}C{^{1}H} NMR (75 MHz, DMSO-d_6)δ 135.6 (d), 132.4 (d), 130.3-129.9 (m), 127.8 (s), 126.4 (s).

2. Crystallography

A suitable dark blue crystal of Co_2[1,4-NDPA], or white in the case of Zn_2[1,4-NDPA] was mounted on a microloop in a drop of immersion oil. The measurement was performed using a XtaLAB Synergy (Rigaku) single crystal diffractometer equipped with a PhotonJet microfocus sealed tube X-ray source (Cu-Kα, λ = 1.54184 Å) at 100 K under a nitrogen gas stream (Oxford Cryostream liquid nitrogen cooling system). The data collection calculation, data reduction and adsorption correction were performed using CrysAlis PRO.[1] The structure was solved by SHELX-2018,[2] and refined using Olex.[3]

The structures were refined as inversion twins. The hydrogen atoms were placed geometrically and refined with Uiso(H) = 1.2 Ueq(C) thermal displacement parameters. The relevant crystal and structure refinement data is collected in Table S1.

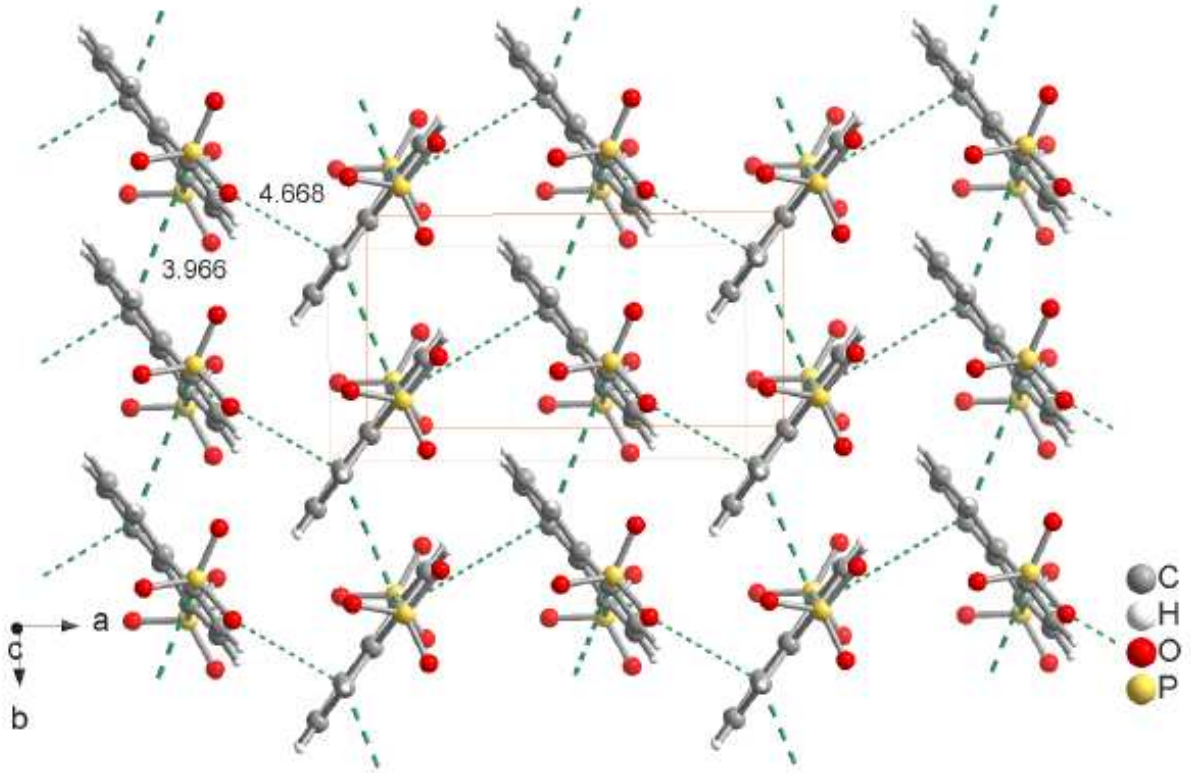

Figure S1. Presentation of π··· π interactions between the naphthalene moieties in Co_2[1,4-NDPA], **1**. The longer-dash lines show the intercentroid distances between the face-to-face interacting naphthalene moieties (3.97 Å), while the shorter-dash lines the edge-to-face ones (4.67 Å, note the presence of contiguous chains sustained by either type of the interactions.).

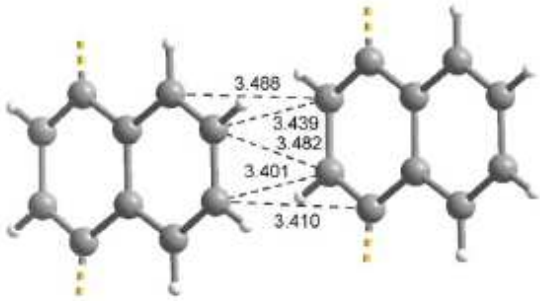

Figure S2. The shortest C···C contacts between the naphthalene moieties in Co_2[1,4-NDPA]

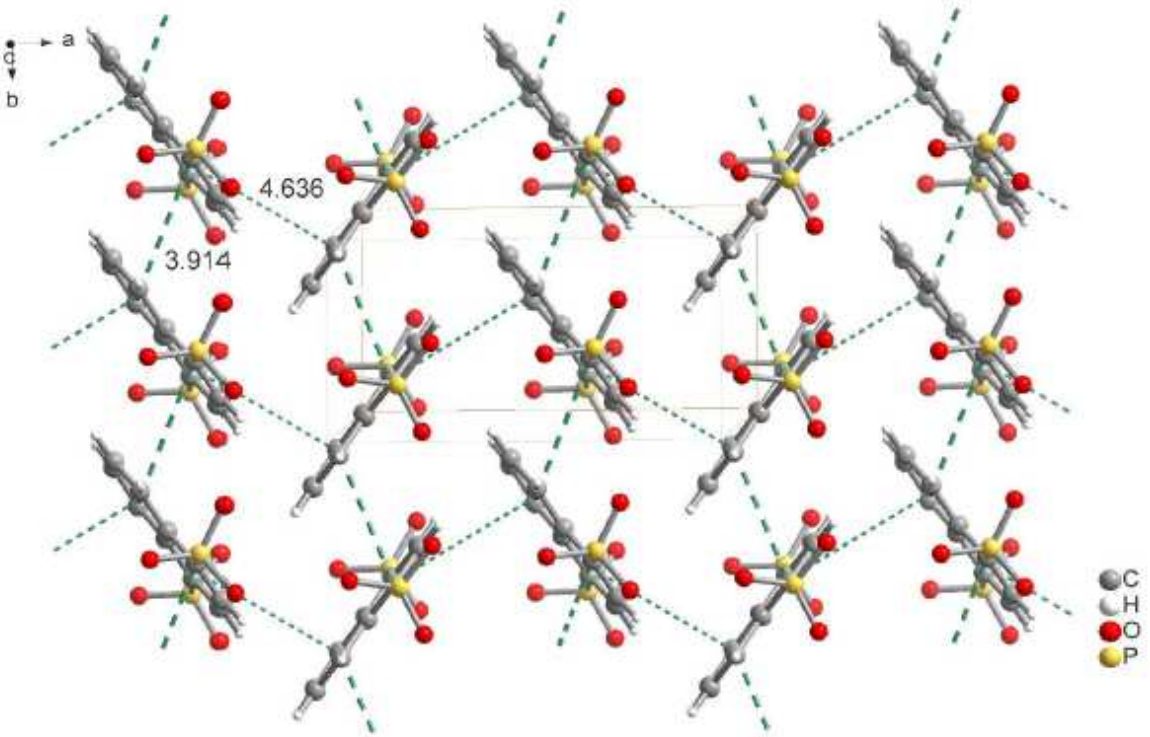

Figure S3. Presentation of π··· π interactions between the naphthalene moieties in Zn_2[1,4-NDPA]. The longer-dash lines shows the intercentroid distances between the face-to-face interacting naphthalene moieties (3.91 Å), while the shorter-dash lines the edge-to-face ones (4.64 Å, note the presence of contiguous chains sustained by either type of the interactions.).

Table S1 Crystal data and structure refinement for Co_2[1,4-NDPA] and Zn_2[1,4-NDPA]

	Co_2[1,4-NDPA]	**Zn_2[1,4-NDPA]**
Empirical formula	$C_{10}H_6O_6P_2Co_2$	$C_{10}H_6O_6P_2Zn_2$
M_r /g mol^{-1}	401.95	414.83
T /K	100(1)	100(1)
Wavelength / Å	1.54184	1.54184
Crystal system	Orthorhombic	Orthorhombic
Space group	$Pna2_1$ (no. 33)	$Pna2_1$ (no. 33)
a /Å	10.99806(17)	10.8927(4)
b /Å	5.63586(9)	5.5934(2)
c /Å	19.0334(3)	19.0195(6)
V /Å^3	1179.76(3)	1158.81(7)
Z	4	4
Calc. density / g cm^{-3}	2.263	2.378
μ / mm-1	24.848	7.962
F(000)	792	816
Crystal size /mm^3	0.1 × 0.07 × 0.02	0.06×0.03×0.02
θ range /°	4.646 to 78.575	4.65 to 79.00
Index ranges (hkl)	[-13, 11]; [-6, 6]; [-23, 22]	[-13, 13], [-7, 6], [-24, 22]
Reflections collected	7548	11741
Independent refl. (R_{int})	2150 (0.0302)	2227 (0.068)
Completeness / % to θ /°	67.684	99.9
Data / restraints / parameters	2150 / 1 / 182	2227 / 115 / 182
Goodness-of-fit (GooF)	1.060	1.069
$R[F^2 > 2\sigma(F^2)]$, $wR2$ [a)]	0.0264, 0.0718	0.0522, 0.1401
$R1$, $wR2$ (all data)	0.0274, 0.0722	0.0545, 0.1432

Inversion twin component sizes	0.336(6)	0.56(8)/0.44(8)
Largest diff. peak and hole	0.538, -0.428	2.283, -1.073
CCDC deposition number	**2235305**	**2212088**

[a)]Full-matrix least-square refinement on F^2 as implemented in SHELX. $R1 = \Sigma||F_o| - |F_c||/\Sigma|F_o|$; $wR2 = \{\Sigma[w(F_o^2-F_c^2)]^2/\Sigma[w(F_o^2)^2]\}^{1/2}$ where $w^{-1} = [\sigma^2(F_o^2) + (aP)^2 + bP]$, $P = [2F_c^2 + \text{Max}(F_o^2, 0)] / 3$, a and b are refined parameters; GooF = $\{\Sigma[w(F_o^2-F_c^2)^2] / (n-p)\}^{1/2}$.

PXRD pattern comparison and LeBail fitting for Co_2[1,4-NDPA].

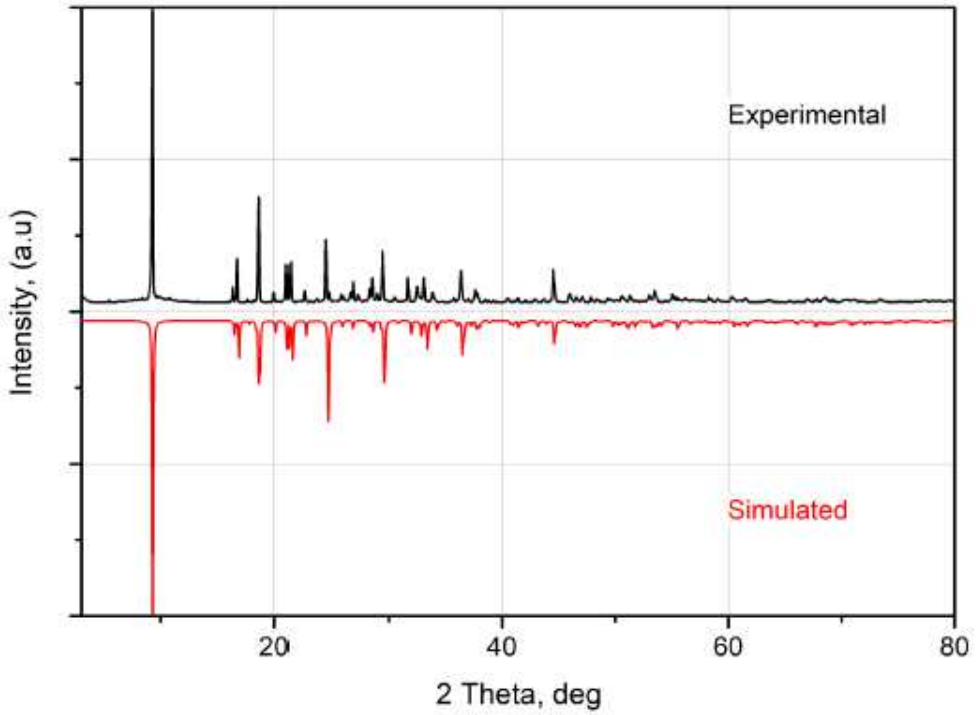

Figure S4. Comparison of the background-subtracted experimental and simulated PXRD patterns shown in a mirror-image like arrangement for Co_2[1,4-NDPA].

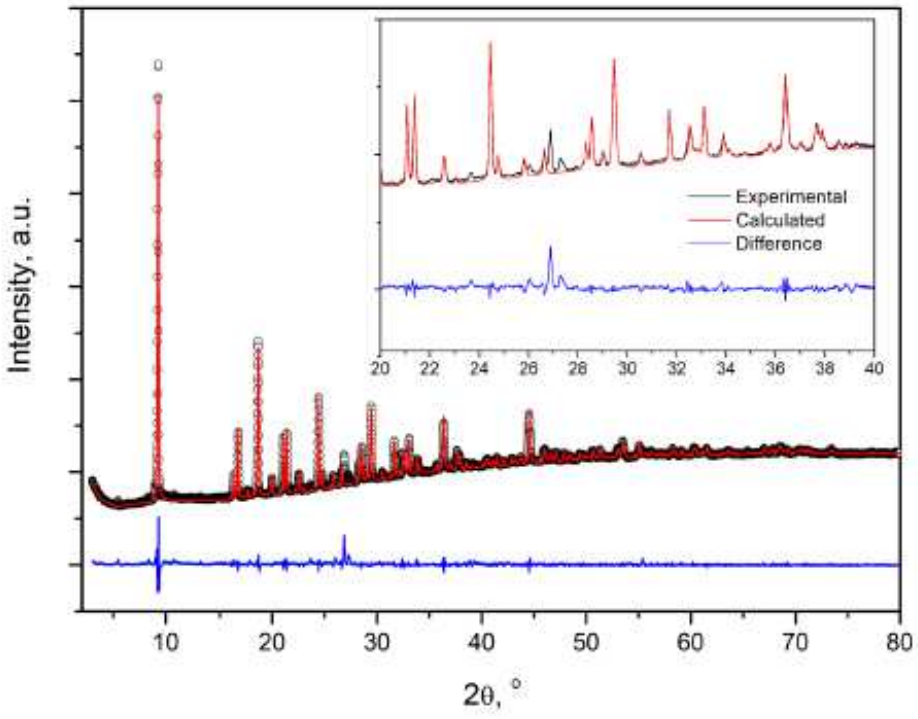

Figure S5. LeBail fitting of the experimental pattern of Co_2[1,4-NDPA], performed by the software Jana-2006; the experimental pattern was collected at 295 K (LeBail fit refines the cell parameter and tests the correctness of the chosen symmetry).[4] The results of the fitting: *P*na2_1; a = 11.00904 Å, b = 5.643041 Å, c = 18.98074. R_p = 1.21, GoF = 3.03. Only a minor amount of impurities present.

3. FT-IR spectroscopy

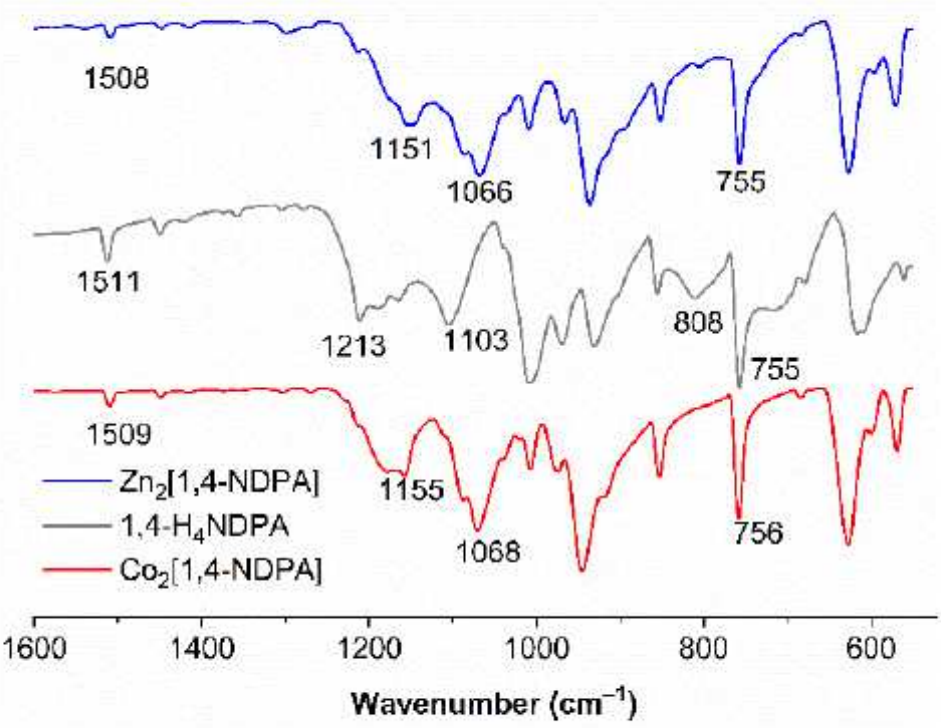

Figure S6.

The ATR-IR spectra of Co_2(1,4-NDPA) and Zn_2(1,4-NDPA) together with the pure linker. Spectrum of the linker 1,4-NDPA-H_4 corresponds to M. J. Bialek, J. Janczak, J. Zon, CrystEngComm, 2013, 15, 390.

4. Thermogravimetric analysis

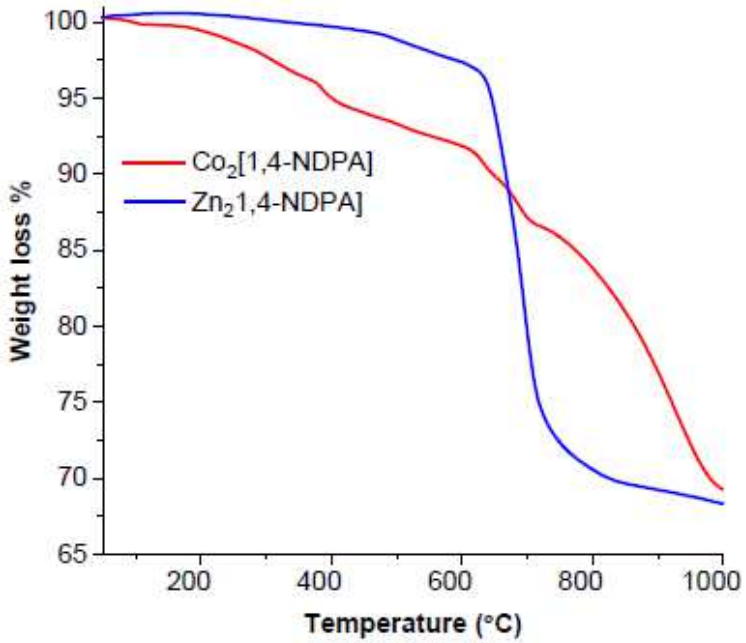

Figure S7. TGA curves of Co_2[1,4-NDPA] and Zn_2[1,4-NDPA] under N_2 atmosphere with a heating rate of 5 K/min.

The thermal stability of the Co_2[1,4-NDPA] and Zn_2[1,4-NDPA] were investigated by thermogravimetric analysis (TGA) measurements under a nitrogen atmosphere. Co_2[1,4-NDPA] and Zn_2[1,4-NDPA] show exceptional thermal stability where the organic components start to decompose at ca. 650 °C with 29% experimental weight loss (theoretical 30.9 %) for Zn_2[1,4-NDPA]. TGA curve of Co_2[1,4-NDPA] indicates a more gradual and broad weight loss until 1000 °C (See Figure S7).

5. Electrochemical measurement

All electrochemical experiments were performed by a Gamry Interace 1000 instrument in a three-electrode cell system at room temperature using a rotating disk glassy-carbo electrode (RD-GCE, 5 mm in diameter) at a rotation of 1600 rpm. 1.0 mol L^{-1} KOH (pH=14) solution was used as electrolyte and nitrogen was purged through the cell to remove oxygen for 30 min before the measurements. Samples were tested with the RD-GCE as working electrode, a reversible hydrogen electrode (RHE) as a reference electrode and a Pt plate as a counter electrode. 2.5 mg of pre-catalysts were dispersed in 250 μL ethanol + 250 μL DI water + 50 μL 5 wt.% Nafion solution by sonication for 30 min. Then, 10 μL of the well–dispersed pre-catalysts (0.23 mg cm^{-2}) were covered on the RD-GCE with drying at room temperature before testing. All linear sweep voltammetry (LSV) curves were recorded by sweeping the potential from 0.9 – 1.7 V vs RHE with scan rate 5 mV s^{-1}. Cyclic voltammetry (CV) measurements were carried out in the potential range between 1.0 – 1.7 V (vs RHE) with a scan rate of 10 mV s^{-1}. Each measurement was repeated 5 times in order to avoid any incidental error. The accelerated stability tests of the Co_2[1,4-NDPA] and Zn_2[1,4-NDPA] precatalysts for OER were performaned at room temperature by potential cycling for 1000 cycles at 100 mV s^{-1}. At the end of the cycling, the final catalyst formed on the working electrode was again subjected to polarization measurements at the scan rate 5 mV s^{-1}. In all measurements, the iR drop was compensated by the ohmic resistance arising from the electrolyte/contact resistance of the setup, and measured by electrochemical impedance spectroscopy (EIS).

For overall water splitting (both HER and OER) tests, the pre-catalysts were coated on commercial nickel foam (NF) which was used as both anode and cathode. The catalyst@NF electrode was fabricated by drop–casting the catalyst ink on the surface of pre–treated Ni foam which was dried at 60 °C under vacuum atmosphere. The loading was around 1 mg cm^{-2} by weighing the electrode before and after the catalyst deposition. The potential scan range was from 0.8 –1.8 V. The stability tests were carried out using a controlled current electrolysis where the potential was recorded at a constant current density of 50 mA cm^{-2} over a period of 30 h in 1.0 mol L^{-1} KOH electrolyte.

6. SEM and SEM-EDX before and after electrolysis

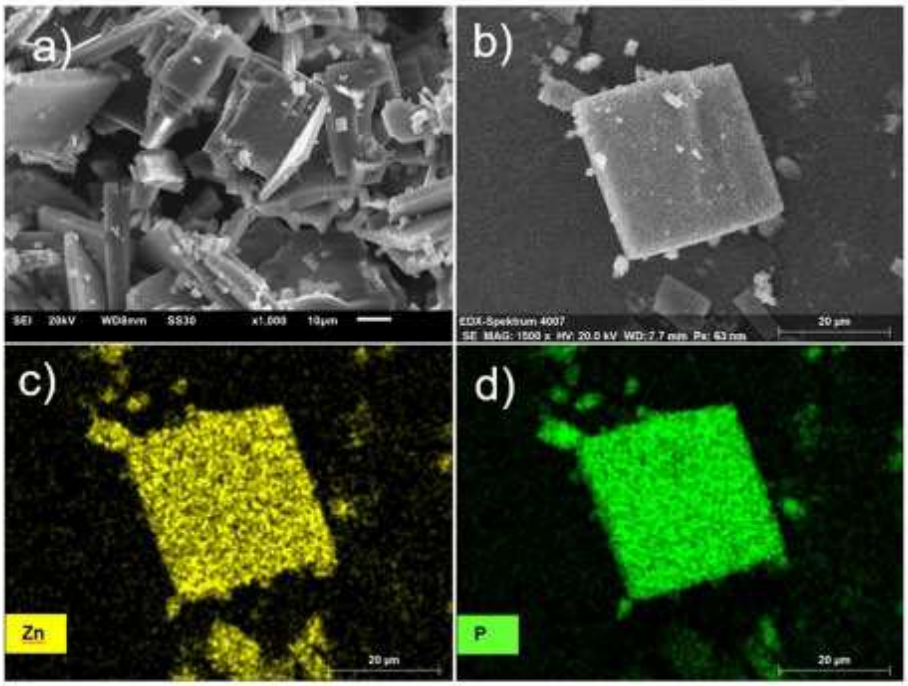

Figure S8. a) and b) SEM images of Zn_2[1,4-NDPA] and the corresponding elemental mapping of c) Co and d) P.

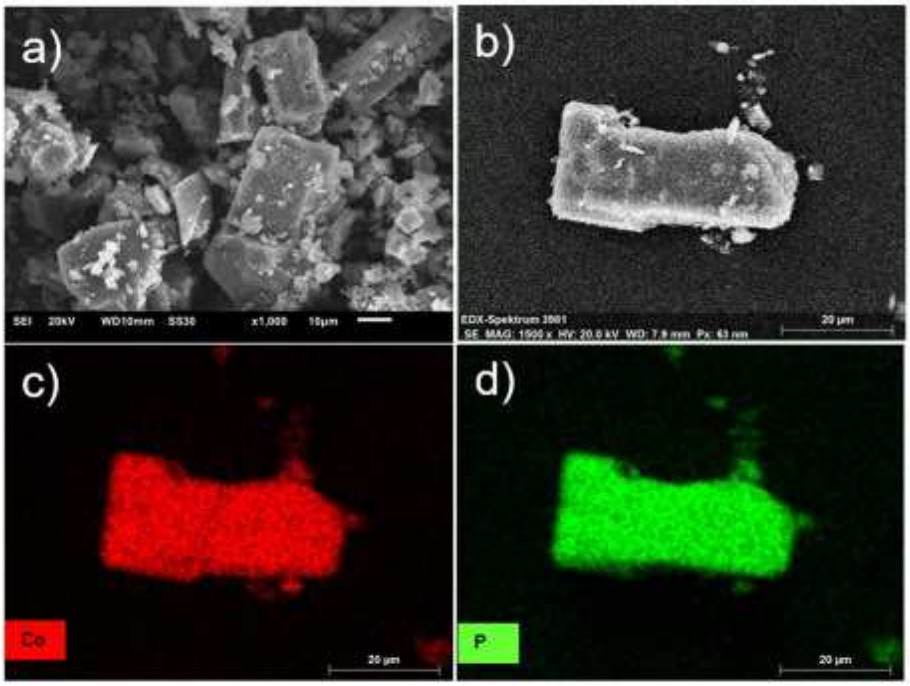

Figure S9. a) and b) SEM images of Co_2[1,4-NDPA] and the corresponding elemental mapping of c) Zn and d) P.

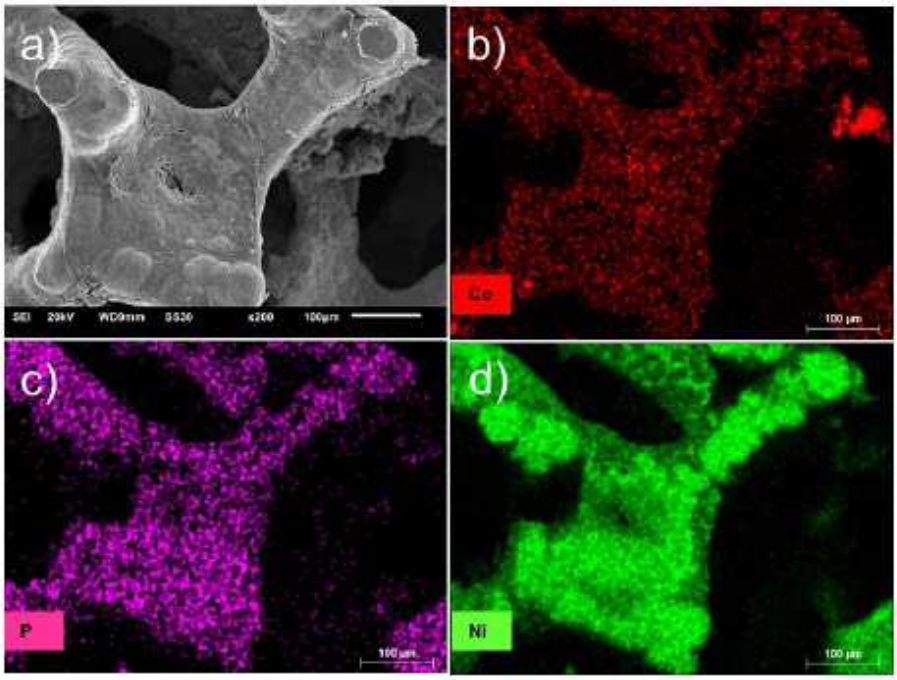

Figure S10. a) SEM images of the Co_2[1,4-NDPA]@NF electrode after 30 h of OER and corresponding elemental mapping of b) Co, c) P and d) Ni.

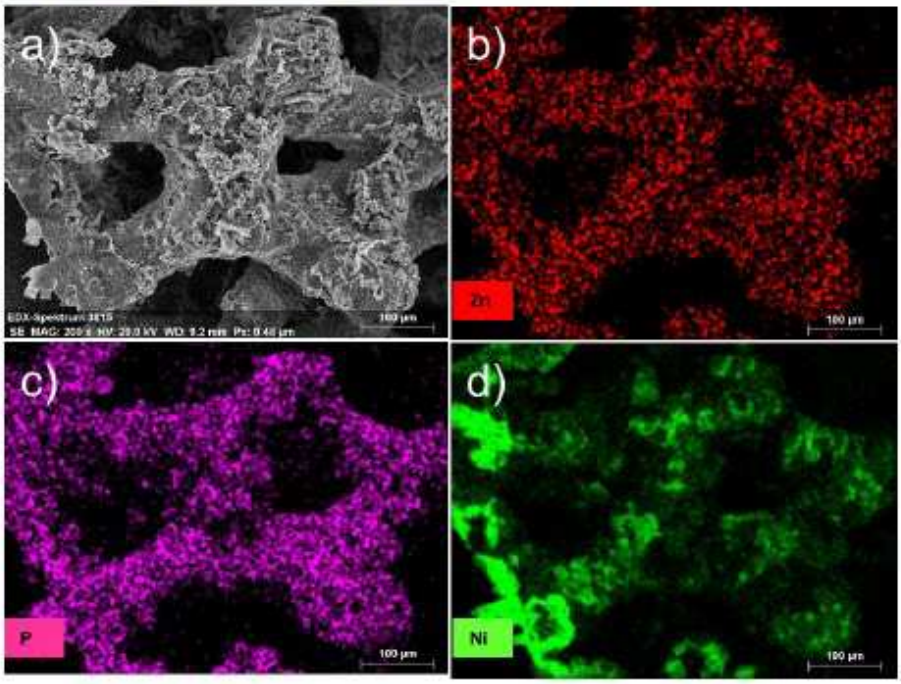

Figure S11. a) SEM image of Zn_2[1,4-NDPA]@NF electrode after 30 h of OER and corresponding elemental mapping of b) Zn, c) P and d) Ni

Table S5. SEM-EDX analysis of the ratio between metal and phosphorus of Co_2[1,4-NDPA] and Zn_2[1,4-NDPA] (theor. 1:1) before and after 30 h of electrolysis in 1 mol L^{-1} KOH electrolyte.

Sample	Molar ratio		Before OER		After OER	
	Metal	P	Metal	P	Metal	P
Co_2[1,4-NDPA]	1.3	1	1.1	1	99	1
Zn_2[1,4-NDPA]	1.3	1	1.1	1	5	1

Moreover, to further evaluate the OER activity of the Co_2[1,4-NDPA] and Zn_2[1,4-NDPA] precatalyst Table S6 compares the overpotentials and Tafel slopes at s current density of 10 mA cm^{-2} with previously reported Co- and Zn- catalysts. The Co_2[1,4-NDPA] and Zn_2[1,4-NDPA] precatalysts exhibit smaller or similar overpotentials and Tafel slopes at a current density of 10 mA cm^{-2}, in line with their good OER catalytic activity.

7. PXRD of synthesised β–$Co(OH)_2$ and physical mixing of β–$Co(OH)_2$ and the ligand 1,4-NDPA–H_4.

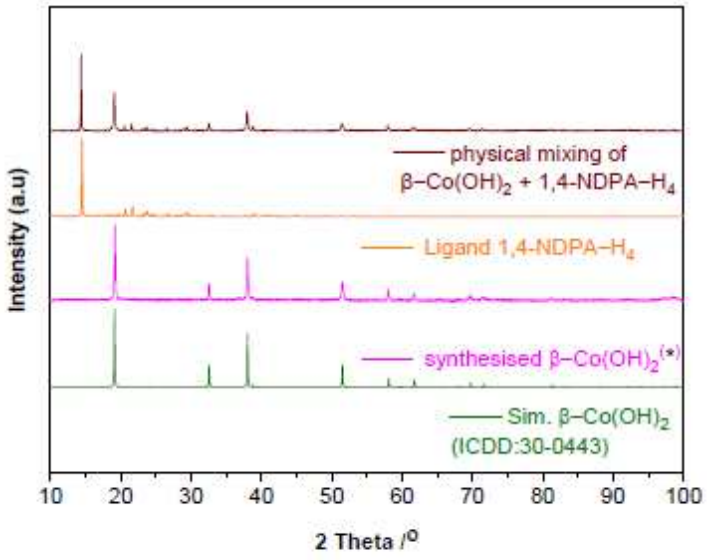

Figure S12. PXRD of the β–$Co(OH)_2$, ligand 1,4-NDPA–H_4 and physical mixing of β–$Co(OH)_2$ and ligand 1,4-NDPA–H_4 and simulation of β–$Co(OH)_2$ (ICDD: 30-0443)

(*) The β–$Co(OH)_2$ was used as a reference material for Co_2[1,4-NDPA]. 653 mg $Co(NO_3)_2 \cdot 6H_2O$ and 200 mg NaOH were added in 20 mL H_2O and ultrasonicated to homogenize. The solution was transferred into 50 mL Teflon line stainless-steel autoclave and put in oven at temperature of 180 °C in 12 h, followed by cooling to room temperature. The final products were obtained after washed

several time with DI water and ethanol via centrifugation (10,000 rpm, 10 min), followed by drying at 60 °C. The as-obtained powder was confirmed the structure by PXRD and denoted as β–$Co(OH)_2$.

8. OER performance comparison.

Table S6. Comparison of OER performance for several Co/Zn-based electrocatalysts.

Catalyst	Electrolyte (mol L^{-1} KOH)	Substrate	Overpotential η (mV) at 10 mA cm^{-2}	Tafel slope (mV dec^{-2}) at 10 mA cm^{-2}	Reference
Co_2[1,4-NDPA]	1	GCE	374	43	This work
Zn_2[1,4-NDPA]	1	GCE	408	82	This work
Co_2[1,4-NDPA]	1	NF	312	-	This work
Zn_2[1,4-NDPA]	1	NF	371	-	This work
RuO_2	1	GCE	318	62	This work
Co-MOF-74	1	GCE	377	193	5
Co-ZIF 67	0.1 mol L^{-1} NaOH	GCE	420	78	6
Co-BTC	1	NF	540	86	7
CoP	1	NF	390	65	8
Co_3O_4	1	GCE	530	47	9
CoP	1	GCE	390	50	10

NF: Nickel Foam, GCE: Glassy Carbon Electrode

9. Topological Analysis

The nearly planar 2D inorganic SBU, $\{M(RPO_3)\}$, (M = Co or Zn) is represented by a 3,3,4L25 topology (short symbol: $\{4.5.6\}\{4.5^2.6.7.8\}\{5^2.6\}$), which is essentially a relatively simple tiling of 4-, 5-,6- gons in a ratio of 1:2:1. As the tiling could not be achieved using regular n-gons, it is not particularly important. Yet, the Topos database lists more app. 50 occurrences of different compounds with this topology. There are no strictly similar metal phosphonate layers.

References

1. Rigaku, OD, *CrysAlis PRO*. Rigaku Oxford Diffraction Ltd, 2020, Yarnton, England
2. G. M. Sheldrick, *Acta Cryst. Sect. C*, 2015, 71, 3–8.
3. O. V Dolomanov, L. J. Bourhis, R. J. Gildea, J. A. K. Howard, and H. Puschmann, J. Appl. Crystallogr., 2009, 42, 339–341.
4. V. Petříček, M. Dušek, and L. Palatinus, Crystallographic Computing System JANA2006: General features. *Zeitschrift Für Kristallographie - Crystalline Materials*, 2014, 229(5), 345–352.
5. Z. Gao *et al.*, Synthesis, Characterization, and Electrocatalytic Activity Exploration of MOF-74: A Research-Style Laboratory Experiment. *Journal of Chemical Education*, 2021, 98, 3341-3347
6. S. Ghoshal *et al.*, ZIF-67 Based Highly Active Electrocatalysts as Oxygen Electrodes in Water Electrolyzer. 2018, *ACS Appl. Energy Mater.* 2, 5568
7. D. H. Taffa, D. Balkenhohl, M. Amiri, M. Wark, Minireview: Ni–Fe and Ni–Co Metal–Organic Frameworks for Electrocatalytic Water-Splitting Reactions. *Small Structures* 2022, 2200263
8. Z. Li *et al.*, Fe–Co–Ni trimetallic organic framework chrysanthemum-like nanoflowers: efficient and durable oxygen evolution electrocatalysts. *Journal of Materials Chemistry A*, 2022, 10, 4230-4241
9. A. J. Esswein, D. G. Nocera, Hydrogen production by molecular photocatalysis. *Chem. Rev.* 2007, 107, 4022
10. A. Dutta, A. K. Samantara, S. K. Dutta, B. K. Jena, N. Pradhan, Surface-Oxidized Dicobalt Phosphide Nanoneedles as a Nonprecious, Durable, and Efficient OER Catalyst. *ACS Energy Letters* 2016, 1, 169-174

3.3. Microwave-Assisted ultrafast Synthesis of Bimetallic Nickel-Cobalt Metal-Organic Frameworks for Application in the Oxygen Evolution Reaction

Thi Hai Yen Beglau, Yanyan Fei, and Christoph Janiak*

Chem. Eur. J. 2024, e202401644.
DOI: 10.1002/chem.202401644

Abstract:

Bimetallic MOFs present enhanced opportunities for tailoring the properties of MOFs, generating significant interest between pristine bimetallic MOFs and their derived metal hydroxide electrocatalysts. Herein, a series of monometallic and bimetallic MOFs (M, M': Ni, Co, Zn) with tunable pillar linkers were prepared through a novel ultrafast microwave-assisted thermal (MW) conversion synthesis method within only 12 min, which are selected systematically to explore the catalytic-activity for OER. Remarkably, among all the bimetallic MOF-derived catalysts, the NiCoMOF exhibits superior catalytic activity for the OER with the lowest overpotentials of 301 mV and Tafel slopes of 42 mV dec^{-1} on a glassy carbon electrode (GCE) at a current density of 10 mA cm^{-2}, attributed to its unique structure and high valence state of nickel. Electrochemical evaluations demonstrate that the pristine structure of MOFs influences OER performance during extended alkali treatment, affecting the kinetics of transformation from disordered α-Ni/Co$(OH)_2$ to ordered β-Ni/Co$(OH)_2$ under alkaline conditions Compared to the TOF from β-M$(OH)_2$ (0.002 s^{-1}), our study demonstrates that a bimetallic MOF improves the electrocatalytic performance of the derived catalyst by giving an intimate and uniform mixture of the involved metals at the nanoscale. In addition, employing the microwave (MW) synthesis method, NiCoMOF was grown on nickel foam (NF) via a growth approach, which provides more accessible active sites for electrocatalytic OER performance. The optimized NiCoMOF grown on NF in just 25 min exhibits superior OER activity, requiring overpotentials of 313 and 328 mV to achieve current densities of 50 and 300 mA cm^{-2} which surpasses the state-of-the-art RuO_2 and catalysts derived from MOFs for the OER. More importantly, this newly developed bimetallic MOF family, characterized by its two kinds of organic ligands, is anticipated to function as a versatile assembly platform, providing extensive opportunities for the practical use of MOFs in various energy storage applications.

Author´s contribution to the publication:

- Planning of the research project and carrying out the literature review
- Synthesis and characterizations of monometallic MMOFs with the support of Mr. Yanyan Fei as his bachelor thesis
- Synthesis and characterizations of powder monometallic Ni-, Co-, Zn-MOFs and bimetallic MM'MOFs (NiCoMOF, NiZnMOF, CoZnMOF), in situ grown NiCoMOF on NF (NiCoMOF/NF), and NiCoMOF-derived in KOH (1 mol L^{-1})
- Investigation and evaluation for characterization of PXRD, SEM, SEM-EDX, SEM mapping, BET measurement and XPS measurements
- Investigations for the electrochemical performance of the OER in an alkaline medium (1 mol L^{-1} KOH) of all materials
- FTIR experiments by Mrs. Birgit Tommes and AAS measurements by Mrs. Annette Ricken
- Evaluation of all raw data and results as well as preparation of the manuscript and all figures, graphs, and tables contained in the manuscript
- Revision of the manuscript with the comments of Prof. Dr Christoph Janiak
- Submission of the publication to the international journal "Chemistry: A European Journal" with and Prof. Dr Christoph Janiak

Check for updates

Chemistry–A European Journal | Research Article
doi.org/10.1002/chem.202401644

Chemistry Europe
European Chemical Societies Publishing

www.chemeurj.org

Hot Paper

Microwave-Assisted Ultrafast Synthesis of Bimetallic Nickel-Cobalt Metal-Organic Frameworks for Application in the Oxygen Evolution Reaction

Thi Hai Yen Beglau,[a] Yanyan Fei,[a] and Christoph Janiak*[a]

Herein, a series of monometallic Ni-, Co- and Zn-MOFs and bimetallic NiCo-, NiZn- and CoZn-MOFs of formula $M_2(BDC)_2DABCO$ and $(M,M')_2(BDC)_2DABCO$, respectively, (M, M' = metal) with the same pillar and layer linkers 1,4-diazabicyclo[2.2.2]octane (DABCO) and benzene-1,4-dicarboxylate (BDC) were prepared through a fast microwave-assisted thermal conversion synthesis method (MW) within only 12 min. In the bimetallic MOFs the ratio M:M' was 4:1. The mono- and bimetallic MOFs were selected to systematically explore the catalytic-activity of their derived metal oxide/hydroxides for the oxygen evolution reaction (OER). Among all tested bimetallic MOF-derived catalysts, the NiCoMOF exhibits superior catalytic activity for the OER with the lowest overpotentials of 301 mV and Tafel slopes of 42 mV dec^{-1} on a rotating disk glassy carbon electrode (RD-GCE) in 1 mol L^{-1} KOH electrolyte at a current density of 10 mA cm^{-2}. In addition, NiCoMOF was *in situ* grown in just 25 min by the MW synthesis on the surface of nickel foam (NF) with, for example, a mass loading of 16.6 mg_{MOF}/g_{NF}, where overpotentials of 313 and 328 mV at current densities of 50 and 300 mA cm^{-2}, respectively, were delivered and superior long-term stability for practical OER application. The low Tafel slope of 27 mV dec^{-1}, as well as a low reaction resistance from electrochemical impedance spectroscopy (EIS) measurement ($R_{tot} = 2\ \Omega$), confirm the excellent OER performance of this NiCoMOF/NF composite. During the electrocatalytic processes or even before upon KOH pre-treatment, the MOFs are transformed to the mixed-metal hydroxide phase α-/β-$M(OH)_2$ which presents the active species in the reactions (turnover frequency TOF = 0.252 s^{-1} at an overpotential of 320 mV). Compared to the TOF from β-$M(OH)_2$ (0.002 s^{-1}), our study demonstrates that a bimetallic MOF improves the electrocatalytic performance of the derived catalyst by giving an intimate and uniform mixture of the involved metals at the nanoscale.

Introduction

The burning of fossil fuels, with its inherent problems such as air pollution, CO_2 emission and global warming, provoke the development and investigation of environmentally friendly and renewable energy systems.[1,2] The imminent shift towards environmentally friendly and renewable energy sources, like wind, solar, and hydroelectric power, has put significant attention on hydrogen produced through water electrolysis as a promising energy carrier and storage medium.[3,4] Overall water splitting consists of two half-reactions, the hydrogen evolution reaction (HER) at the cathode and the oxygen evolution reaction (OER) at the anode.[5] It is crucial to note that the OER is a four-electron-proton coupled process, while the HER involves only a two-electron transfer. Consequently, OER demands a higher energy input (higher overpotential) to surmount its kinetic barrier.[6] In the past several decades, the electrocatalytic OER has been extensively studied and various catalysts have been designed to improve electrode kinetics and stability under different electrolyte environments. For instance, state-of-the-art catalysts such as Ru-based or Ir-based oxides demonstrate exceptional OER performance across a wide pH range.[7] However, the scarcity and high-cost of noble metals greatly restrict their large-scale commercial application. Therefore, electrocatalysts need to be developed that are mainly composed of earth-abundant elements and are also easily scalable, thereby promoting OER in water electrolysis with an alkaline electrolyte and at a lower cost.[8,9]

Electrocatalysts obtained from bimetallic, mixed-metal or multivariate metal-organic frameworks (MOFs) are of interest because the synergy of uniformly distributed two or more metal ion types at the nanoscale can avoid noble metals.[10] MOFs are organic-inorganic hybrid materials with compositional tunability, large nanoporosity and surface area, which are also investigated as (precursors to) electrocatalytic materials.[11,12,13] Compared with monometallic MOFs, bimetallic MOFs like NiCo-MOFs,[14,15] NiZn-MOFs,[16,17] and CoZn-MOFs[18,19] generally show superior electrocatalytic activity for the OER due to the synergistic effects exerted by the two metals. The MOF $(Ni,Fe)_2(BDC)_2DABCO$ has been reported by us and was demonstrated as a promising OER pre-electrocatalyst (BDC = 1,4-benzenedicarboxylate, DABCO = 1,4-diazabicyclo[2.2.2]octane).[20] It is important to note that MOFs are usually not the actual electrocatalysts but precursor materials to the catalytic species that form in the aqueous

[a] T. H. Y. Beglau, Y. Fei, C. Janiak
Institut für Anorganische Chemie und Strukturchemie, Heinrich-Heine-Universität Düsseldorf, 40204 Düsseldorf, Germany
E-mail: janiak@uni-duesseldorf.de

Supporting information for this article is available on the WWW under https://doi.org/10.1002/chem.202401644

acidic or alkaline medium where many MOFs are of low stability.[21] The decomposition of MOFs, for example, in an alkaline aqueous medium transforms them into metal oxides/hydroxides.[10,20,22,23] Directly applied pristine MOFs in electrocatalysis undergo dynamic reconstruction under the given conditions to form mostly amorphous, yet active metal oxide/hydroxides without other pre-treatments (e.g. pyrolysis or calcination).[24,25] Carboxylate-based MOFs are relatively unstable under strongly alkaline conditions, since OH^- ions can split the coordination bonds that hold the carboxylate ligands to the metal sites, leading to the formation of metal hydroxides.[26,27,28] In addition to the KOH pre-treatment, recently Fischer and co-workers systematically studied the transformation process from Ni-carboxylate-type MOFs into distinct nickel hydroxide phases.[29] The PXRD and Raman spectroscopic results demonstrated that the linker controls the transformation of NiMOFs to α-$Ni(OH)_2$ and β-$Ni(OH)_2$ which occurs gradually during the alkaline treatment. Lee and co-workers studied the transformation process of ZIF-67 under an alkaline condition during both cyclic voltammetry and amperometry.[30] Their *in situ* spectroelectrochemistry results demonstrated that the strong transformation of tetrahedral Co sites in ZIF-67 to tetrahedral α-$Co(OH)_2$ and octahedral β-$Co(OH)_2$ occurs gradually during the electrochemical treatment. These two studies indicate only the formation of metal(II) hydroxides but gave no evidence for the oxidation to metal(III) oxide/hydroxide under the alkaline treatment. The active center for the OER then lies in CoOOH species, generated by the electrochemical oxidation of α/β-$Co(OH)_2$. MOFs are seen as good precursor materials to active mixed-metal oxide/hydroxide electrocatalysts as they allow to achieve a defined mixed-metal composition with a uniform distribution of the metals on the nano-level.[31–34] Due to these advantages, MOFs provide unique design approaches for electrocatalyst development. This is a different approach than the energy-intensive carbonization (pyrolysis) pre-treatment of MOFs.[35–37]

It is known that glassy carbon electrodes can only work under a low current density (usually $\leq 100\ mA\ cm^{-2}$) and are unable to meet the requirements for practical applications, which are often operated under high current densities (usually $\geq 300\ mA\ cm^{-2}$).[38,39] The electrode materials grown directly on conductive supports (e.g., Ni foam, Cu foam, carbon cloth, metal plates …) have been effective in preventing catalyst aggregation and shedding, and can also expose more active species and reduce the resistance to charge transfer, which is beneficial for improving electrochemical performance.[40–42] Due to its metallic conductivity, high electrochemical accessible surface area and excellent mechanical strength, nickel foam (NF) has been widely used as an electrode support for OER.[43,44] Therefore, *insitu* growth of MOFs on NF presents an effective strategy for an electrocatalyst design of highly efficient and durable electrodes for practical applications.

There are various methods for synthesizing MOFs, including hydrothermal, room temperature, ultrasonic, microwave-assisted heating (MW), mechanochemical, sonochemical, and electrochemical methods.[45] The MW synthesis has the advantages of fast reaction, homogeneous nucleation, a substantial reduction in time, good reproducibility, morphology/size tuning, and facile evaluation of reaction parameters.[46–49] MW synthesis is based on the interaction of electromagnetic radiation with electric charges, such as polar ions, solvent molecules, or electrons.[50] In the liquid phase, as the temperature increases, the kinetic energy of the molecules increases, leading to increased collisions between polar molecules when frequency is utilized in the electromagnetic field.[51,52] Maniam et al.[53] successfully synthesized $Ni_2(BDC)_2DABCO$, from $Ni(NO_3)_2 \cdot 6H_2O$, H_2BDC and DABCO in dimethylformamide (DMF) solution, by using microwave heating at a temperature of 110°C. The method reduced the synthesis time from 48 h for the traditional solvothermal method, to a mere 2 h. However, the synthesis scale was very small (1–10 mL). Zou et al. described the MW method at a larger batch scale (35 mL) and an efficient approach for producing $Ni_2(BDC)_2DABCO$ within only 12 min.[54] The synthesis of *insitu* grown nanomaterials (but no MOFs) on the surface of NF by the MW heating method has been reported[55–58] and an insight into the growth mechanism has been provided.[59] Therefore, the binder-free and homogenous formation of MOFs on a NF electrode using microwave irradiation may effectively improve its OER performance for electrocatalytic applications.

Herein, the mono- bimetallic MOFs $M_2(BDC)_2DABCO$ and $(M,M')_2(BDC)_2DABCO$ (M, M' = Ni, Co, Zn; molar ratio M:M' = 4:1) were prepared through a facile and effective microwave synthesis method in a short time (12 min), as pristine powders and on NF. This work will be divided into (i) bulk MOFs as precursors, and (ii) MOF pre-electrocatalysts directly grown on the conductive substrate NF. The pristine MOFs serve as precursors for the formation of active mixed-metal hydroxide species. The catalytic properties of derived materials from monometallic Ni-, Co- and Zn-MOFs and bimetallic NiCo-, NiZn- and CoZn-MOFs were investigated systematically in direct comparison. To demonstrate the advantages of bimetallic MOFs as OER precatalysts, the comparison of NiCoMOFs with β-$(Ni,Co)(OH)_2$ nanoparticles and the physical mixture of NiMOF and CoMOF (metal molar ratio 4:1) was investigated. A MOF precatalyst nanosheet was for the first time obtained on Ni foam through the microwave-assisted heating growth approach. Our study demonstrated that mixed-metal MOFs offer a way to form OER catalysts with uniformly distributed two or more metal ion types at the nano-level.

Results and Discussion

Characterization of MM'MOFs

The metal nitrate salts and a mixture of the organic linkers H_2BDC and DABCO were reacted in DMF under microwave-induced heating to form homogeneous bimetallic 3D MOFs of formula $(M,M')_2(BDC)_2DABCO$ (M, M' = Ni, Co, Zn), hereafter abbreviated as MM'MOF, as indicated in Scheme 1. The set M:M' ratio was 4:1. For comparison the monometallic $M_2(BDC)_2DABCO$ analogues, abbreviated as MMOF were prepared by the same processes. The bimetallic MM'MOFs were

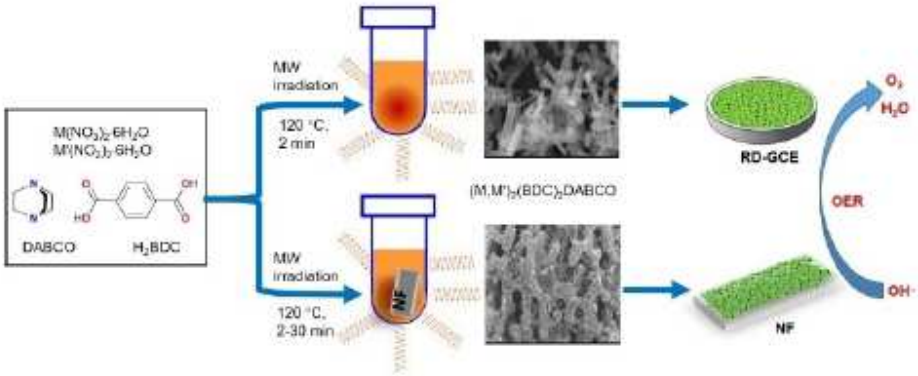

Scheme 1. Schematic illustration of the microwave-heating process for the synthesis of bimetallic $(M,M')_2(BDC)_2DABCO$ and its application in an ink on a rotating disk glassy carbon electrode (RD-GCE) or *in situ* grown on nickel foam (NF) for use in the OER

also grown on NF by the microwave technique and used directly as a working electrode for OER. With the microwave synthesis method, the deposited MOF mass loading on the NF electrode could be optimized by adjusting the synthesis time. To reveal the influence of the second metal in the bimetallic MOF precursors under an alkaline electrolyte, the transformation of the MOFs in KOH (1 mol L^{-1}) and under OER conditions was investigated over time. This study aims to understand the synergistic effect of two metals in bimetallic MOF-derived electrocatalysts on OER using either a rotating disk glassy carbon electrode (RD-GCE) or a NF electrode as the anode.

In addition, the monometallic MMOFs $M_2(BDC)_2DABCO$ (M: Ni, Co, Zn), were synthesized for comparison. The powder X-ray diffractograms (PXRDs) of the monometallic MMOFs and bimetallic MM'MOFs matched the simulated pattern of the reported structure of $Ni_2(BDC)_2DABCO\cdot(DMF)_4\cdot(H_2O)_{1.5}$ (CCDC: No. 802892) (Figure 1, Figure S1 and Scheme S1),[34] confirming the isostructural nature of the monometallic and bimetallic MOF series. Slight shifts in the position of the reflections are attributed to the effect of the different metal atom radius, the lattice distortion from the coordination of two metal ions whereby the crystal structures of MOFs undergo subtle changes.[60] The very similar FTIR spectra of the M- and MM'MOFs in Figure S3, where NiMOF, CoMOF, ZnMOF, NiCo-MOF, NiZnMOF and CoZnMOF display the same characteristic bands in the fingerprint region, are in good agreement with the literature.[61] ^1H NMR spectra of digested monometallic and bimetallic MOFs confirmed a molar ratio near 2:1 of BDC to DABCO ligands, which matched well with the formula of $M_2(BDC)_2DABCO$ (Figure S4). The metal contents and metal ratios of the samples were analyzed by energy-dispersive X-ray spectroscopy (EDX), atomic absorption spectroscopy (AAS) and X-ray photoelectron spectroscopy (XPS) (Figure 1b and Table S4). The content of two metals was very close to the intended molar ratio of 4:1 set by the stoichiometric amounts in the synthesis. The results confirmed that the two metals could be smoothly mixed within the MOFs and according to the above results, the monometallic $M_2(BDC)_2DABCO$ and the bimetallic $(M,M')_2(BDC)_2DABCO$ MOF structures were successfully obtained by a simple MW heating synthesis.

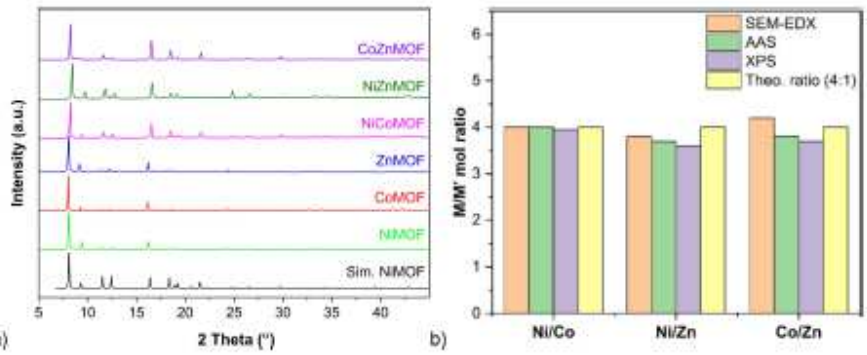

Figure 1. PXRD patterns of as-synthesized monometallic $M_2(BDC)_2DABCO$ (MMOF) and bimetallic $(M,M')_2(BDC)_2DABCO$ (MM'MOF). The simulated PXRD pattern of $Ni_2(BDC)_2DABCO$ was obtained from CCDC No. 802892. b) Metal composition of the bimetallic MM'MOF materials according to SEM-EDX, AAS, XPS and stoichiometric (theoretical) ratio (see Table S4, SI for specific values).

The monometallic MMOFs exhibit the expected type I isotherm based on the IUPAC classification for MOFs with microporous structures (pore size < 2 nm).[62] For the bimetallic MM'MOFs, the isotherms are a composite of type I and probably type II with an H4 hysteresis loop. The pronounced uptake at low relative pressure stems from the filling of the micropores. The type II branch is given by non- or macroporous adsorbents and derives here from the texture effect of the physisorption in the meso- and macroporous voids of the aggregated crystallites. The bimetallic MM'MOFs give significantly smaller crystallites than the monometallic MMOFs (Figure 3a–f). A comparison of BET surface areas and pore volumes for the MMOF and MM'MOF materials is summarized in Table S3. The BET surface areas of monometallic NiMOF, CoMOF, and ZnMOF were 1856, 1838, and 1547 $m^2 g^{-1}$, respectively, in good agreement with the literature values (also given in Table S3).[53,63,64] In addition, the pore widths of all were evaluated to be around ~1.2 nm micropores (Figure 2b).

Scanning electron microscopy (SEM) of the monometallic and bimetallic MMOFs and MM'MOFs showed rectangular block-shaped microcrystals with smooth surfaces and block lengths ranging from ~3 to 10 μm for the MM'MOFs and from ~5 to 20 μm for the MMOFs (Figure 3a–f). The observed block-shaped morphologies of MMOFs and MM'MOFs (Figure 3 and S2) were in good agreement with the reported ones.[60,65] Furthermore, according to the element mapping from SEM-EDX

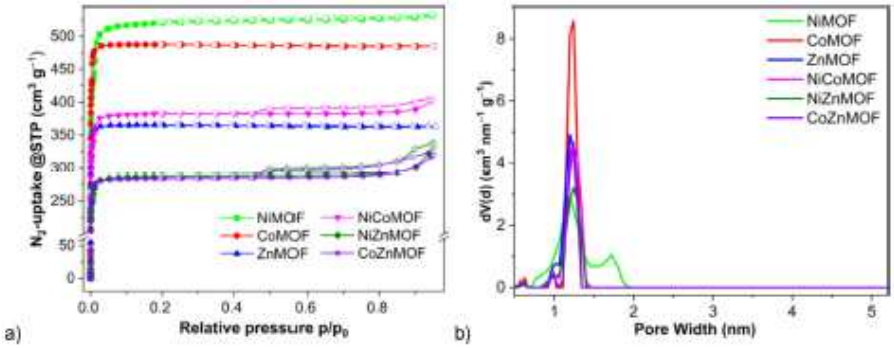

Figure 2. a) Nitrogen sorption isotherms (adsorption: filled symbols; desorption: empty symbols) and b) pore size distribution curves of the MMOF and MM'MOF samples. BET surface areas and total pore volumes are given in Table S3.

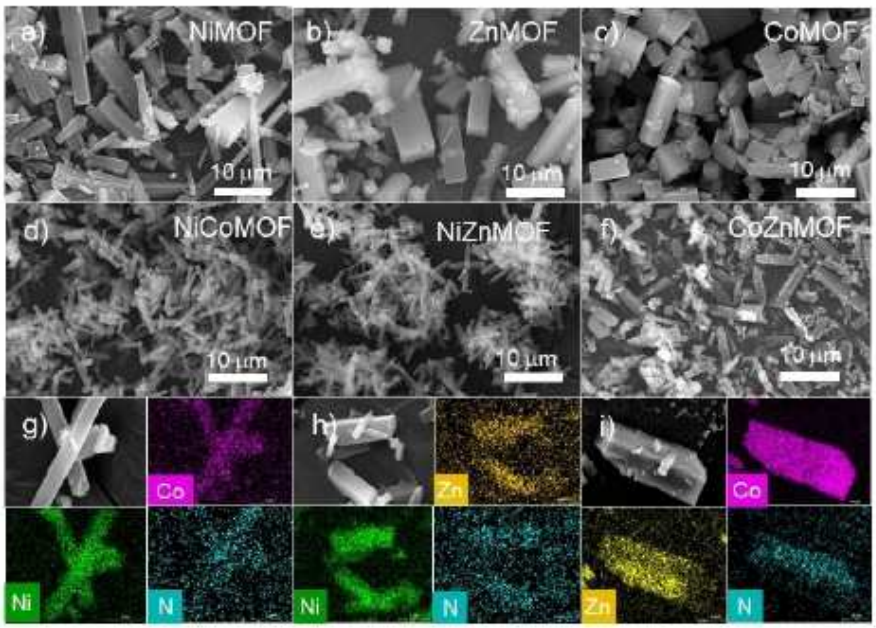

Figure 3. SEM images of a) NiMOF, b) ZnMOF, c) CoMOF, d) NiCoMOF, e) NiZnMOF and f) CoZnMOF and SEM-EDX scanning element mappings of nickel, cobalt, zinc and nitrogen of g) NiCoMOF, h) NiZnMOF and i) CoZnMOF.

in Figure 3g–i and Figure S5, both metals in the MM'MOFs are homogeneously distributed in the microcrystals.

The element species and chemical states in the bimetallic MM'MOFs and for comparison also in the monometallic MMOFs are further confirmed by X-ray photoelectron spectroscopy (XPS) measurement.[66,67] As shown in Figure 4a, the corresponding elements of Ni, Co, Zn, C, O, and N were detected in the survey XPS spectra. The Zn $2p_{3/2}$ binding energy in the monometallic and bimetallic MOFs is almost the same, and has a characteristic peak at around 1022 eV corresponding to the Zn $2p_{3/2}$ of Zn^{2+}.[68,69] The Co 2p spectrum displayed the contributions of Co $2p_{3/2}$ (~781 eV) and Co $2p_{1/2}$ (~796 eV) each with shake-up satellite peaks (~786 and ~801 eV). The oxidation state of cobalt cannot be unequivocally determined from the binding energies of the peaks as the fitting of the main Co $2p_{3/2}$ contribution between 779–782 eV to two or three peaks does not correlate with the oxidation states.[70–72] Instead, cobalt(III) oxides were distinguished from cobalt(II) oxides by the absence of the multielectron excitation satellite at 785–786 eV to the Co $2p_{3/2}$ line in the former. In Figure 4c the areas of the satellites for NiCoMOF, CoZnMOF and CoMOF (blue curves) are between 32–34% of the total Co $2p_{3/2}$ line indicating the presence of mainly Co^{2+}.[71] The peak of Ni^{2+} at about 856 eV for Ni $2p_{3/2}$ and 873–874 eV for Ni $2p_{1/2}$, together with two corresponding satellite peaks originates from Ni^{2+}.[73] The results show that metal ions remain in their divalent form in both the monometallic and bimetallic MOFs and that the introduction of a second metal does not alter the chemical state of the metal ions.[60] Figure S6 in the Supporting Information (SI) presents the high-resolution XPS of C 1s, O 1s and N 1s of the MOFs.

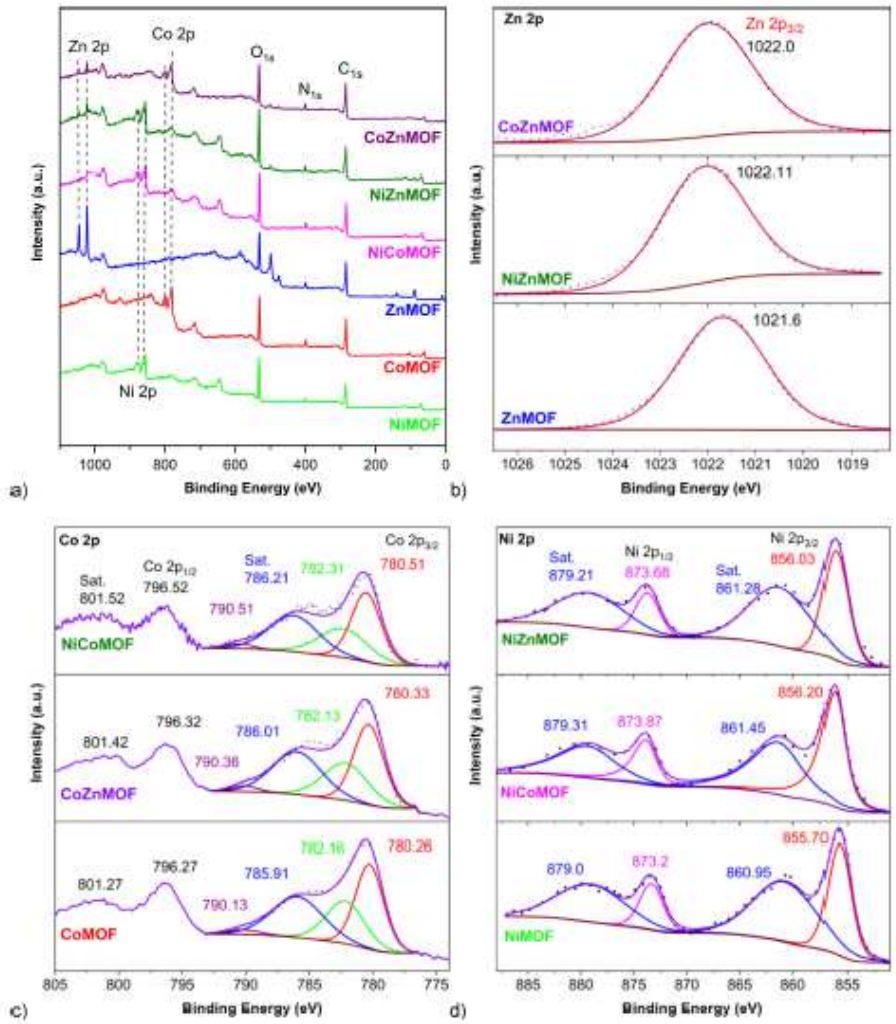

Figure 4. a) Survey XPS spectra of MMOF and MM'MOF samples. Comparison of the high-resolution XPS spectra of b) Zn $2p_{3/2}$, c) Co 2p and d) Ni 2p of the MMOF and MM'MOF samples.

Characterization of NiCoMOF/NF

The NF-supported bimetallic MOF was synthesized by immersing NF (1 cm×2 cm; thickness: 1.6 mm) in the mixture of $Ni(NO_3)_2 \cdot 6H_2O$, $Co(NO_3)_2 \cdot 6H_2O$ (molar ratio 4:1), H_2BDC and DABCO in DMF in a microwave tube through the MW synthesis method (see details in SI). To measure the PXRD of the MOF from the NiCoMOF/NF sample, the MOF particles were carefully scratched from the surface of the NF, collected and transferred to the sample holder. The PXRD of NiCoMOF/NF matched the simulated pattern of $Ni_2(BDC)_2DABCO \cdot (DMF)_4 \cdot (H_2O)_{1.5}$ (CCDC: No. 802892) (Figure 5a, cf. Figure 1) indicating a well-crystallized $(Ni,Co)_2(BDC)_2DABCO$ structure which was successfully grown on NF in the MW synthesis. Additional diffraction reflexes at 45.3°, 52.9° and 77.2° (Figure 5a) are caused by elemental nickel (ICDD: 04–0850) which was scraped off together with the MOF. The homogeneous growth of NiCoMOF on NF can be seen optically and by SEM compared with bare NF (Figure S7 and Figure 6). The element mapping by SEM-EDX (Figure 5b) of NiCoMOF/NF demonstrated that Ni, Co, and N were homogeneously distributed on the surface of the NF substrates.

The NiCoMOF/NF crystallites, depicted in Figure 6 (and enlarged in Figure S7b–g), are of much smaller size and with no clearly seen rod-shape morphology compared to NiCoMOF powder (given in Figure 3). This can be attributed to the microwave synthesis time. The NiCoMOF powder was obtained

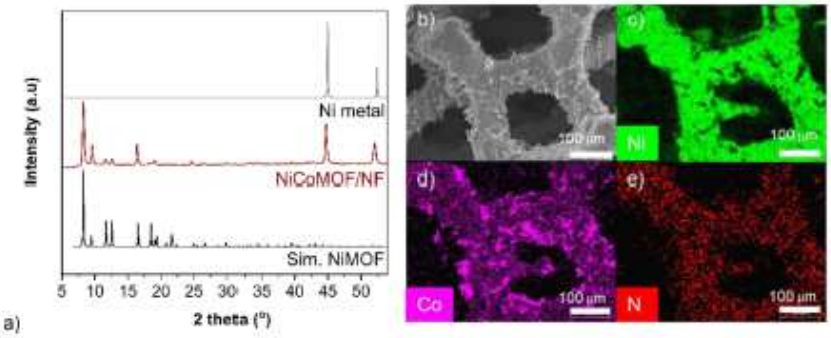

Figure 5. a) PXRD of scratched-off $(Ni,Co)_2(BDC)_2DABCO$ from the NF substrate and simulation of NiMOF and Ni metal. b) SEM image and elemental mappings of NiCoMOF/NF after 12 min under MW heating synthesis.

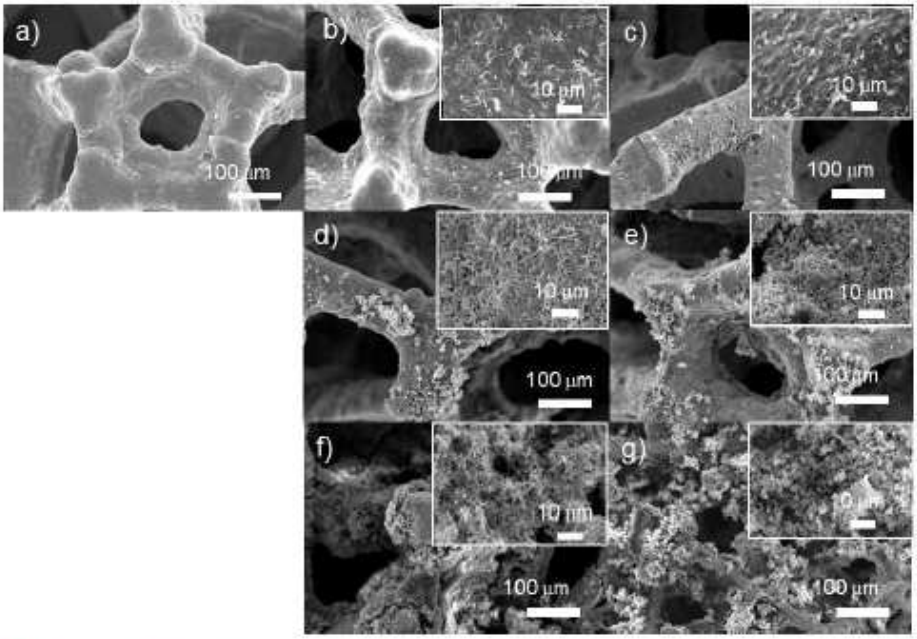

Figure 6. SEM image of a) bare NF, b) NiCoMOF/NF-4.5, c) NiCoMOF/NF-12.6, d) NiCoMOF/NF-15.0, e) NiCoMOF/NF-16.6, f) NiCoMOF/NF-18.7 and g) NiCoMOF/NF-28.6. The number denotes the loading in mg_{MOF}/g_{NF} and the sequence b) to g) correlates with 12, 15, 20, 25, 30 and 40 min, respectively, of synthesis time.

after 70 min of microwave synthesis with a well-defined morphology. The NiCoMOF/NF size and morphology were evaluated with a synthesis time, ranging from 12 to 40 minutes.

To determine if an interaction between the ligands with NF during the microwave synthesis reaction can occur, that is, if the synthesis of the NiCoMOF/NF can originate from the NF without metal salts, the synthesis of NiCoMOF/NF was carried out according to the procedures described, except without adding any metal salt. The NF was immersed in the mixture of H_2BDC and DABCO in 15 mL of DMF in a 30 mL microwave tube. The reaction ran at 120 °C for 40 min of heating time at a microwave power of ~25–30 W. The product was denoted as BDC-DABCO/NF. SEM and SEM-EDX did neither indicate the formation of any MOF nano-seeds on the surface of NF nor the presence of nitrogen (from DABCO) (Figure S25b and d). As Figure S25, the SEM image of the obtained product shows that a very small number of crystal seeds was distributed on the surface NF to compare with bare NF.

Since the catalytic activity for OER can also be influenced by the mass loading of the MOF on the NF substrate,[74] the microwave-assisted synthesis method was used to control the mass loading through the reaction time. The NiCoMOF samples were grown on NF with different synthesis times of 12, 15, 20, 25, 30 and 40 min to investigate the OER activity at different amounts of NiCoMOF precursor on NF. The SEM images in Figure 6 indicate that the MOF thickness on NF increased with increased synthesis time. After 12 min, a small number of nanorods appeared on the NF and the MOF did not cover the NF completely. After 15 to 20 min of MW synthesis time, the MOF crystallites with a larger size and better coverage could be observed on the NF substrate. The mass loading of NiCoMOF increased with synthesis time from 4.5 mg/g (NF) at 12 min to 28.6 mg/g (NF) at 40 min as determined by the weighted mass gain (Table S2 and Figure S8).[75]

Electrochemical OER Performance of MMOF- and MM'MOF-Derived Electrocatalysts

MOF/RD-GCE Systems

The electrochemical OER performance was tested across the series of monometallic MMOF and bimetallic MM'MOF (M, M' = Ni, Co, Zn). Synthesized MOF materials were coated on a rotating disk glassy carbon electrode (RD-GCE) (mass loading ~ 0.23 mg cm^{-2}) as a working electrode following a standard drop-casting technique (Electrochemical measurements, SI). All electrochemical measurements were referred to a reversible hydrogen electrode (RHE) in KOH (1 mol L^{-1}), using Pt wire as a counter electrode. Typically, to obtain a stable activated state for the OER, the samples were conditioned by cyclic voltammetry (CV) from 1.0 to 1.6 V vs RHE over 100 cycles with a scan speed of 100 mV s^{-1}, corresponding to ~ 20–22 min of conditioning time. In these polarization CV curves in Figure S11, the anodic peaks in the potential region around 1.25 to 1.45 V (vs RHE) of the Ni-containing MOFs are due to the pre-OER Ni^{2+} to Ni^{3+} redox transition of the Ni centers.[76,77] The intensity of this pre-OER redox peak increased substantially, indicating that the Ni species were activated during long-term CV measurement.[78] After obtaining a stable activation CV state, the OER performance was investigated by recording linear sweep voltammetry (LSV) under a scan speed of 5 mV s^{-1} (Figure 7a). The potential at a current density of 10 mA cm^{-2} was deducted from 1.23 V to give the overpotential. Whereas the native RD-GCE had no OER activity, the bimetallic CoZnMOF showed a better OER activity judged by the lower overpotential compared to the monometallic CoMOF and ZnMOF. On the RD-GCE the overpotential of NiCoMOF (301 mV) is significantly smaller than that of NiZnMOF (306 mV), CoZnMOF (342 mV), NiMOF (315 mV), CoMOF (356 mV), ZnMOF (365 mV) and commercial RuO_2 (317 mV), to reach a typical benchmarking current density of 10 mA cm^{-2} (Figure 7c).

The catalytic OER activity by tuning the Ni:Co molar ratio was investigated. Among all precatalysts with different molar Ni:Co ratios from (Ni:Co) 4:1 to 1:4, NiCoMOF with a molar metal ratio of 4:1 showed the highest OER activity (Figure S13). The same phenomenon was also found in other NiCoMOFs and NiCo nanoparticles[79–82] Accordingly, the molar metal ratio of 4:1 was selected for further experiments.

Additionally, the kinetics of the derived catalysts on the RD-GCE were investigated using Tafel plots which were calculated from the LSV curves. A smaller Tafel slope indicates a faster increase in current density and a smaller variation in overpotential, suggesting a faster reaction rate constant and a better electrocatalytic performance.[83] On the RD-GCE the Tafel slope of NiCoMOF is 42 mV dec^{-2}, which is significantly smaller than that of NiZnMOF (46 mV dec^{-2}), and CoZnMOF (50 mV dec^{-2}), NiMOF (55 mV dec^{-2}), CoMOF (57 mV dec^{-2}), ZnMOF (61 mV dec^{-2}) and RuO_2 (91 mV dec^{-2}), which demonstrates superior reaction kinetics for the catalyst derived from NiCoMOF compared to the other samples (Figure 7b). The results are consistent with the corresponding LSV curves for the excellent OER activity of the NiCoMOF-derived catalyst.

The Tafel slope provides crucial information on the rate-determining step (RDS).[6,84] It is generally accepted that the first step of the OER involves oxidation of the active metal site with the binding of a hydroxide anion, that is, the formation of adsorbed metal hydroxide species with the release of an electron ($M + OH^- \rightarrow M^+\text{-}OH + e^-$) which if it would be the rate-determining step (RDS) would correspond to a Tafel slope of 120 mV dec^{-1}. In the second step of the OER, this metal hydroxide species reacts with a hydroxide anion to produce a water molecule and a metal oxide species with the release of a second-electron ($M^+\text{-}OH + OH^- \rightarrow M^+\text{-}O + H_2O + e^-$), which as RDS would give a Tafel slope of 60 mV dec^{-1}. The third step of the OER involves the reaction of a hydroxide anion with the metal oxide species to produce a metal hydroperoxide with the third-electron transfer ($M^+\text{-}O + OH^- \rightarrow M\text{-}OOH + e^-$), with a corresponding Tafel slope of 40 mV dec^{-1} as RDS. In the last step of the OER, this metal hydroperoxide species reacts with an additional hydroxide anion which leads to the regeneration of the active metal site (M), dioxygen and water and the release of a fourth electron ($M\text{-}OOH + OH^- \rightarrow M + O_2 + H_2O + e^-$), and is indicated as RDS with a Tafel slope of 15 mV dec^{-1}.[85,86] There-

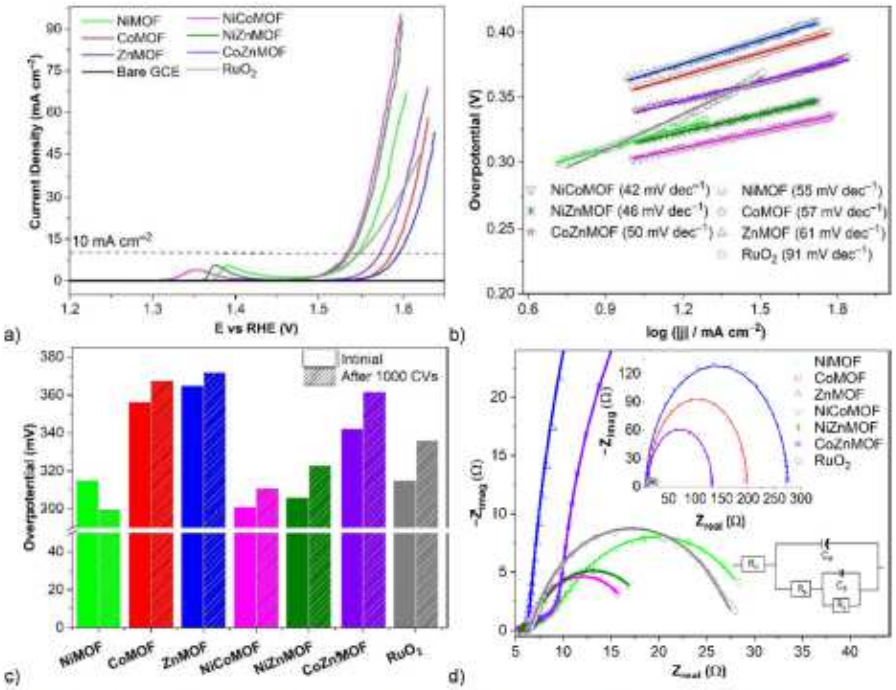

Figure 7. Electrocatalytic OER performance of the monometallic MMOFs and bimetallic MM'MOFs on RD-GCE in 1 mol L^{-1} KOH (each GC electrode contains a mass loading of ~0.23 mg_{MOF} cm^{-2}): a) LSV polarization curves of as-synthesized monometallic and bimetallic MOFs on RD-GCE at a scan rate of 5 mV s^{-1}, b) corresponding Tafel plots, c) comparison of overpotential before and after 1000 CVs at 10 mA cm^{-2}, d) EIS of OER at constant potential of 1.53 V (vs RHE) and fitting to an equivalent circuit model.

fore, the Tafel slope from 61 to 42 mV dec^{-1} for the MOF-derived catalysts suggests that the RDS involves the second and the third electron transfer steps. At the same time, the overpotential and Tafel slope of RuO_2 for the OER, which was measured here, is in good accordance with the literature.[87]

Electrochemical impedance spectroscopy (EIS) was employed to understand the electrode kinetics of the MOF/RD-GCE systems during the OER electrocatalysis. The EIS data was fitted by the equivalent electrical circuit model for OER catalysts (Figure 7d).[88,89] C_{dl} and R_Ω are the double-layer capacitance and electrolyte resistance, respectively. The polarization resistance (R_p) presents the total charge transfer resistance of the multiple steps in the OER, while R_s is related to the production rate of surface intermediates during the OER. Together the two give the Faradaic resistance of the catalyst, which is simply defined as $R_{far} = R_s + R_p$.[90] C_Φ is related to the changes in charged surface species during the process of OER.[88,91,92] The determined parameters from the EIS fitting are listed in Table S5 and present a comparable trend to overpotentials and Tafel slopes. Among the tested catalysts, NiCoMOF has the smallest value of R_{far} (12.2 Ω) and the smallest semicircle diameter in the Nyquist plot, indicating the faster electron transport kinetics of this NiCoMOF-derived catalyst which leads to the superior OER electrocatalysis.[93]

To comprehensively assess the intrinsic catalytic activity of bimetallic MOFs on RD-GCE towards the OER, the turnover frequency (TOF) was used as a quantitative parameter to indicate the amount of oxygen gas produced per unit of time at a defined overpotential.[94,95] As can be seen in Table S5, the NiCoMOF has the highest TOF value (0.074 s^{-1}), higher than the other bimetallic MOF-derived catalysts NiZnMOF (0.062 s^{-1}) and CoZnMOF (0.009 s^{-1}), at an overpotential of 320 mV. It is worth mentioning, that the TOF value of NiCoMOF is 2 times and 26 times higher than in the monometallic NiMOF and CoMOF, respectively. This again demonstrated the strong effect of introducing a second metal on optimizing the catalytic performance for OER.

Finally, the durability of the bimetallic MM'MOF-derived catalysts was investigated by CV curves for 1000 cycles from 1.0 to 1.7 V vs RHE at a scan rate of 100 mV s^{-1} in 1 mol L^{-1} KOH (Figure S12). The recorded polarization LSV curves of the MOF series before and after 1000 CVs show a slight increase in the overpotential of 10 mV for NiCoMOF, 17 mV for NiZnMOF and 19 mV for CoZnMOF. Interestingly, the overpotential of NiMOF after 1000 CVs decreased by 16 mV, indicating the reorganization of NiMOF at their interface to the electrolyte, while the overpotential of CoMOF and ZnMOF increased 11 and 7 mV, respectively. These observations indicate that each metal

reconstructs differently to active species under OER conditions (Figure 7c and Figure S12).

KOH Treatment and Transformation Investigation

A facile alkaline hydrolysis strategy is used to fabricate MOF-derived OER electrocatalysts.[26,96,97] The NiCoMOF transformation through the inherent reaction with KOH during the electrochemical measurements was investigated in a separate KOH treatment. The MOF materials were dispersed in 1 mol L^{-1} KOH over a defined time (t = 15, 30, 60 and 120 min). After centrifuging, the materials were collected and washed three times with 20 mL of doubly-ionized (DI) water and dried at 80 °C overnight. The NiCoMOF reflections already disappeared within 15 min of KOH treatment (Figure 8a). At 15 min new sharp reflexes appeared at 9.3°, 13.0°, 26.0°, 32.8° and 39.2° 2theta which also became weaker over time and almost disappeared again at 120 min. These new reflexes are assigned to the initial but also intermediate formation of a variant of 2D–Ni-BDC (9.3°) and α-$(Ni,Co)(OH)_2$ (13.0°, 26.0°, 32.8° and 39.2°) (Figure 8b). It is noted that the reflection at 13.0° and 26.0° of α-$(Ni,Co)(OH)_2$ are shifted to higher 2theta values than the standard patterns ICDD 38–0715 and ICDD 46–0605 (Figure 8b), indicating a decrease in the *c*-unit cell parameter due to differences in the incorporated interlayer spacing species.[76,98,99] Also new broad reflexes are present after 15 min at 19.2°, 32.8°, 38.7°, 51.5°, 59.1° and 63.0°, which grow in intensity, sharpen and remain as dominant reflexes after 120 min of KOH treatment time. These reflexes are assigned to β-$(Ni,Co)(OH)_2$ (Figure 8b and Figure S14) and indicate the conversion of the MOF to the α-/β-phases of mixed-metal-hydroxide. The results are in good agreement with the literature.[29]

Notably, a higher abundance of α-$Ni(OH)_2$ results in a higher catalytic activity in the OER.[29,100] The reconstruction of NiCoMOF in KOH starts with the formation of α-$(Ni,Co)(OH)_2$, hence, after 15 min the best OER performance is seen (see below). The metal oxidation state of the product after 120 min of KOH treatment time was determined via XPS measurement and confirmed to be predominantly Ni^{2+} and Co^{2+} with only a small contribution of Ni^{3+} (about 18%) and Co^{3+} (see details in Figure S16 and accompanying text). The morphology of NiCoMOF after 120 min of KOH treatment time, as seen with the SEM (Figure S10), did not change profoundly from the pristine NiCoMOF morphology.

The reconstruction of NiCoMOF with KOH over time was followed by the electrochemical measurements, that is, NiCo-MOF and also NiMOF and CoMOF on the RD-GCE were pre-treated with KOH (1 mol L^{-1}) for 15, 30, 60 and 120 min without

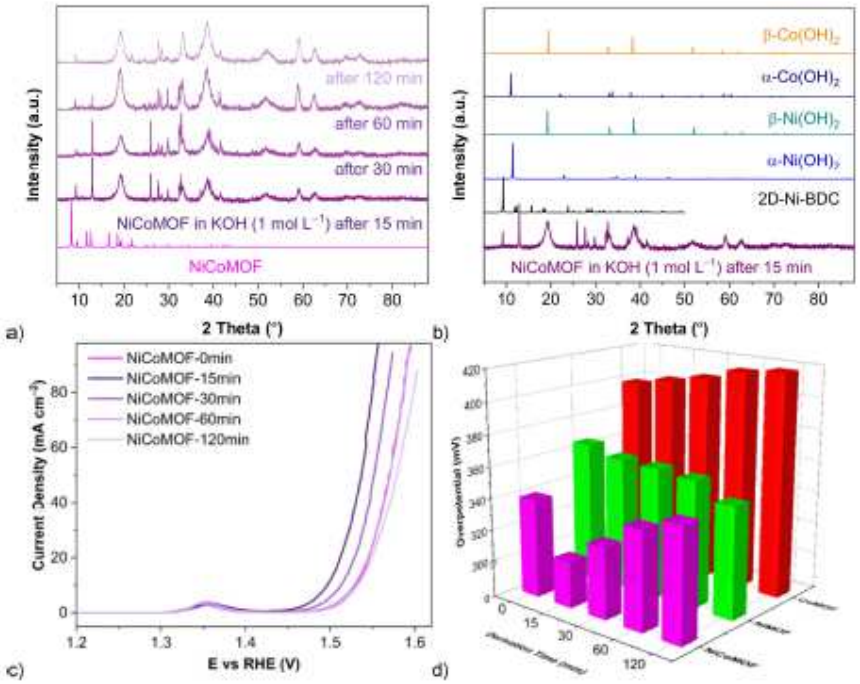

Figure 8. PXRD pattern a) of monitoring structural transformation of NiCoMOF under alkaline electrolyte KOH (1 mol L^{-1}) (KOH pre-treatment time: t = 0, 15, 30, 60 and 120 min), b) of NiCoMOF after 15 min in 1 mol L^{-1} KOH and simulated reflections from 2D-NIBDC (CCDC Nr. 638866),[106] α-$Ni(OH)_2$ (ICDD: 38-0715), β-$Ni(OH)_2$ (ICDD: 14-0117), α-$Co(OH)_2$ (ICDD: 46-0605) and β-$Co(OH)_2$ (ICDD: 30-0443). c) Electrochemical evaluation of polarization curves of the pristine NiCoMOF-coated electrodes (RD-GCE) in electrolyte KOH (1 mol L^{-1}) (derivation time: t_D = 0, 15, 30, 60 and 120 min) without applying potential and d) comparison of overpotentials of derived-NiMOFs, -CoMOFs and -NiCoMOFs at 50 mA cm^{-2} with different derivation times.

applying a potential. Afterwards, the OER testing was done similarly to the series of OER measurements described above, which refers to a soaking time $t_0 = 0$ min. The NiCoMOF/RD-GCE system was chosen over NiCoMOF/NF (discussed below) as the RD-GCE reduces the uncertainty in specific surface area determination which is a commonly experienced disadvantage when using nickel foam or carbon paper as the substrate.[29]

The influence of the KOH pre-treatment on the OER performance is well reflected by the LSV curves in Figure 8c, where the change in OER properties is given in correlation with the pre-treatment time. Particularly, the overpotential at 50 mA cm^{-2} decreases for NiCoMOF over the pre-treatment time from 339 mV (0 min) to 306 mV (15 min) and increases again to 322 mV (30 min), 339 mV (60 min) and 348 mV (120 min) (Figure 8d). Additionally, the TOF values at an overpotential of 320 mV followed a similar trend, as for NiCoMOF after 15 min of KOH pre-treatment the value (0.252 s^{-1}) is higher than that of pristine NiCoMOF (0.074 s^{-1}) and decreases again with extended soaking time (0.145–0.052 s^{-1}) (Figure S19). The results underscore that the pristine MOFs are not the true catalysts but merely precatalysts, due to the reorganization of MOFs at their interface with the electrolyte.[101]

Notably, the TOF value of NiCoMOF after 15 min of KOH pre-treatment is much higher as compared to previously reported NiCo electrocatalysts: $CoNi_{40}$ – MOFNs (TOF = 0.118 s^{-1}, η = 350 mV);[102] NiCo-MOF/NF (TOF = 0.0112 s^{-1}, η = 350 mV);[15] NiCo-LDH (TOF = 0.002 s^{-1}, η = 419 mV);[103] Ni_3Co_3-MOF (TOF = 0.0045 s^{-1}, η = 400 mV);[104] NiCoDH/NiCoS (TOF = 0.1 s^{-1}, η = 320 mV).[105]

Additionally, as shown in Figure S17, derived-NiMOF shows the highest OER activity after a KOH-pre-treatment time of 120 min with a low overpotential of 347 mV at 50 mA cm^{-1}, which is in good agreement with other literature (Figure 8d).[107,113] In contrast to NiMOF, the electrocatalytic activity of CoMOF after KOH pre-treatment for different periods was decreased significantly (Figure S17), consistent with previous reports.[108]

The data show the selection of metal ion nodes of MOFs is a crucial determinant for the metal hydroxide species which are obtained under alkaline treatment, and which affects the OER activity of the derived materials. The impact of introducing Co anodes in bimetallic NiCoMOF is generally categorized as (1) a synergetic effect of the mixed metal complex at the nanoscale and (2) while Co promotes the formation of high-valence Ni oxide/hydroxide in bimetallic MOFs, the transformation of both Ni and Co nodes from hydroxide to oxide/hydroxide then leads to the best OER activity.[109–112]

After 120 min the β-(Ni,Co)$(OH)_2$, which is formed from the MOF decomposition or reconstruction, appears still largely amorphous. A much more crystalline and phase-pure β-(Ni,Co)$(OH)_2$ sample could be obtained by immersing 30 mg of the NiCoMOF in 30 mL of KOH solution at a temperature of 120 °C for 24 h, which is denoted here as (NiCo)$(OH)_2$-120 °C.[111] The PXRD pattern of the obtained product in Figure S9a (after washing, centrifugation and drying) shows only the hexagonal phase of β-Ni$(OH)_2$ (ICDD: 14–0117) and/or β-Co$(OH)_2$ (ICDD: 30–0443) with sharp reflections. (NiCo)$(OH)_2$-120 °C has an irregular shard-like morphology (Figure S10c), different from the rod shape of the pristine NiCoMOF and the material derived after alkaline treatment at room temperature (cf. Figure S10a). The metal contents and Ni:Co ratios (~4:1) of the samples were analyzed by energy-dispersive X-ray spectroscopy (EDX) and atomic absorption spectroscopy (AAS) (Figure S10).

In order to assess the effect of the second metal at the nanoscale on the OER performance of bimetallic NiCoMOF, we also compared the activity for the electrocatalyst derived from a physical mixture of NiMOF and CoMOF (molar Ni:Co ratio 4:1).

The electrocatalytic OER activity of (NiCo)$(OH)_2$-120 °C and of the physical mixture of NiMOF + CoMOF was evaluated, as shown in Figure S18. Both (NiCo)$(OH)_2$-120 °C and the physical mixture NiMOF + CoMOF exhibited poorer electrocatalytic activity, manifested by high overpotentials of 376 and 342 mV as well as by TOFs of 0.002 and 0.016 s^{-1}, respectively (Figure S19). The amorphous phase of α/β-(Ni,Co)$(OH)_2$ which is formed in KOH at room temperature, without applying a potential, has a higher number of randomly oriented unsaturated species, which facilitates the adsorption of reactants, in comparison to the crystalline form of β-(Ni,Co)$(OH)_2$ in (NiCo)$(OH)_2$-120 °C. Furthermore, the amorphous phase comprises numerous local structures that can be flexibly altered, thereby accelerating the charge transfer between the active site and the intermediate.[114] The cyclic and reversible conversion of α- into β-Ni$(OH)_2$ to β- and then γ-NiOOH during an OER process was described by Bode (Figure S20).[115]

The advantages of bimetallic NiCoMOFs for electrocatalysis could be summarized as follows: (1) they can provide rich catalytically active centers by promoting the transformation from α-/β-NiCo$(OH)_2$ to β-/γ-NiCoOOH during the electrochemical reaction; (2) the synergistic effect among two metals at the nanoscale can improve OER performance; (3) the introduction of two metal centers tunes the properties of the bimetallic MOFs concerning crystal size, crystallinity, surface area and pore volume.[19,56]

NiCoMOF/NF System

NiCoMOF samples were grown on NF with different microwave heating times of 12, 15, 20, 25, 30 and 40 min to achieve a different mass loading of 4.5, 12.6, 15.0, 16.6, 18.7 and 28.6 mg_{MOF}/g_{NF}, respectively (Table S2). Based on the LSV curves in 1 mol L^{-1} KOH (Figure 9a), the overpotential decreased from 450 to 313 mV (at 50 mA cm^{-2}) and the Tafel slope from 88 to 27 mV dec^{-1} when the loading increased from 4.5 to 16.6 mg_{MOF}/g_{NF} (Figure 9b and c). Upon further increase of the MOF loading up to 28.6 mg_{MOF}/g_{NF} the overpotential and the Tafel slope increased again. The optimal sample of NiCoMOF/NF with a loading of 16.6 mg_{MOF}/g_{NF} (named as NiCoMOF/NF-16.6) with its overpotential of 313 mV at 50 mA cm^{-1} or 328 mV at 300 mA cm^{-2} is comparable with the best performing NiCo-based OER catalysts (Table S7). A higher loading of the MOF up to 16.6 mg_{MOF}/g_{NF} leads to an increase in the number of active species, which in turn enhanced the OER performance.[116] Further extending the loading then leads to aggregation of the

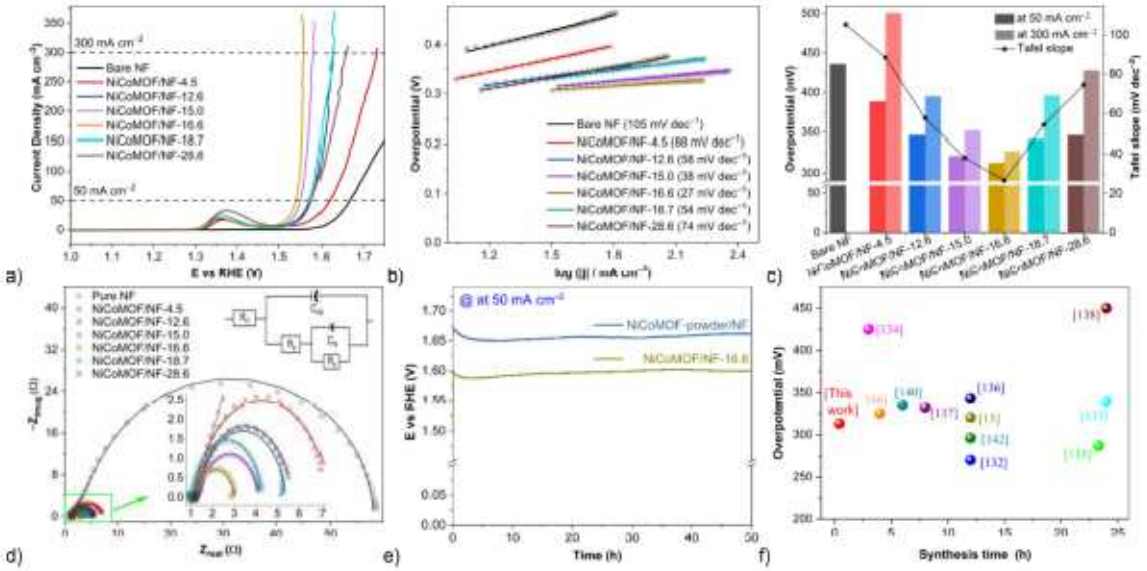

Figure 9. The electrochemical OER performance for NiCoMOF/NF with different mass loading of 4.5, 12.6, 15.0, 16.6, 18.7 and 28.6 mg of MOF per gram of NF based on a) the LSV polarization curves at a scan rate 5 $mV\,s^{-1}$; b) the corresponding Tafel plots; c) comparison of overpotential at current density of 50 and 300 $mA\,cm^{-2}$ and Tafel slope of the samples; d) the electrochemical impedance spectroscopy (EIS) and its fitted curves based on the circuit model in 1 $mol\,L^{-1}$ KOH solution. e) Chronoamperometry curves at a constant applied current density of 50 $mA\,cm^{-2}$ in 1 $mol\,L^{-1}$ KOH solution over 50 h of NiCoMOF/NF-16.6 and NiCoMOF-powder/NF and f) overpotential at 50 $mA\,cm^{-2}$ and synthesis time comparison for different NiCo-based catalysts described in the noted references.

MOF nanorods and an enhanced thickness (Figure 6f,g and Figure S7), which both reduce the gas diffusion rate and increase the electrode resistance which decreases the OER activity.[117]

Electrochemical impedance spectroscopy (EIS) and the semicircle diameter of the fitted curves also show that NiCoMOF/NF-16.6 had the best electrocatalytic performance for the OER with the smallest semicircle diameter (R_{ct} = 2 Ω) (Figure 9d and Figure S21), indicating the superior charge transfer rate and easier formation of active species which contribute to its highest catalytic activity among the NiCoMOF/NF electrodes.

A faradaic efficiency (FE, %) of oxygen generation is crucial for assessing the OER activity of carbon-containing catalysts to rule out carbon instead of water oxidation. The value for the FE is obtained by comparing the experimentally evolved quantity of O_2 with the theoretically calculated O_2 amount.[118] The anodic oxygen evolution of the optimal sample NiCoMOF/NF-16.6 was performed under the chronopotentiometry test at a constant current density of 50 $mA\,cm^{-2}$ The quantitative measurement of the generated O_2 shows that the faradaic efficiency for O_2 formation was nearly 94%, ruling out any significant other oxidation processes (Figure S23).

To assess the effect of *in situ* grown NiCoMOF on NF versus the separately prepared and deposited MOF on NF, an ink of NiCoMOF in Nafion was drop-casted on NF to give a mass loading of 16.6 mg_{MOF}/g_{NF}. Also, commercial RuO_2 was coated on NF. The samples were named as NiCoMOF-powder/NF and RuO_2/NF, respectively, and were evaluated under the same conditions as the *in situ* grown NiCoMOF/NF (Figure S22).

At a current density of 50 $mA\,cm^{-2}$, the *in situ* grown NiCoMOF/NF-16.6 had a lower overpotential of 313 mV compared to NiCoMOF-powder/NF and RuO_2/NF with an overpotential of 341 and 360 mV, respectively (Figure S22). Such increase is generally due to chemical binders such as Nafion or polymeric binders which are required to glue the catalysts to a substrate electrode. Consequently, the insulating binders can reduce the contact area between the electrolyte and catalytic active species and reduce the overall conductivity of the working electrode.[119] Therefore, the high catalytic OER activity of NiCoMOF/NF-16.6 is also achieved due to the intimate substrate contact on a binder-free working electrode.

Additionally, the durability tests of NiCoMOF/NF-16.6 and NiCoMOF-powder/NF through a 50-h chronoamperometry test at a current density of 50 $mA\,cm^{-2}$ (Figure 9e) indicate negligible changes and thus a high OER stability for both derived catalysts.

The NiCoMOF/NF-16.6 sample was analyzed by PXRD, FTIR and SEM-EDX (Figure S24) which shows that the MOF is degraded as noted above but the MOF-derived material still adheres to NF after the OER process (from the Co and N element mapping).

Remarkably, from the comparison of the overpotential values and synthesis times reported in the recent literature (Figure 9f and Table S7) our use of microwave heating demonstrates a significant reduction in synthesis time for MOF/NF precatalysts with low overpotentials.

Conclusions

In summary, a series of bimetallic NiCo-, NiZn- and CoZn-MOFs was successfully prepared using a rapid microwave-heating synthesis method with reaction times as low as 12 min. These bimetallic MOFs have the same NiMOF structure with dinuclear (M_2) handles as metal nodes which allows for the proximity of the two different metals at the atomic scale. As expected, the introduction of a second metal ion allows for the modification of the intrinsic characteristics of the monometallic MOFs, preserving their initial morphology and pore structure. Notably, among the tested systems the bimetallic NiCoMOF demonstrates superior catalytic activity for the oxygen evolution reaction (OER) in aqueous alkaline solution. The pristine structure of the MOFs is clearly degraded through aqueous alkali treatment, which yielded for NiCoMOF a transformation from disordered α- to ordered β-$(NiCo)(OH)_2$ over the time period of 2 hours. Moreover, taking advantage of the MW synthesis method, the NiCoMOFs were *insitu* grown on the surface of nickel foam, NF. The OER efficiency can be optimized effectively by tuning the loading of the MOF on NF employing different MW synthesis times. The NiCoMOF/NF with its loading of 16.6 mg of MOF per gram of NF which was obtained within only 25 min of synthesis time showed superior OER activity with required overpotentials of only 313 and 328 mV to achieve current densities of 50 and 300 mA cm^{-2}, respectively, and excellent stability after 50 h, which surpasses the state-of-the-art RuO_2 and other MOF-derived catalysts for the OER. These promising results not only prove that the properties of MOFs can be tailored by the incorporation of a second metal into the MOF structure but also that microwave heating presents a new strategy for developing promising highly efficient electrocatalysts in practical applications. Further, this bimetallic MOF family, characterized by its two kinds of organic linkers (BDC and DABCO), is anticipated to function as a versatile assembly platform, where also the DABCO pillars are customizable, so as to provide extensive opportunities for MOF pre-catalysts in electrocatalytic applications.

Experimental Section

Materials

Nickel(II) nitrate hexahydrate ($Ni(NO_3)_2 \cdot 6H_2O$), cobalt (II) nitrate hexahydrate ($Co(NO_3)_2 \cdot 6H_2O$), zinc (II) nitrate hexahydrate ($Zn(NO_3)_2 \cdot 6H_2O$), ruthenium(IV) oxide (RuO_2), benzene-1,4-dicarboxylic acid (H_2BDC), 1,4-diazabicyclo[2.2.2]octane (DABCO), perfluorinated resin solution containing Nafion™ 1100 W (5 wt. % in lower aliphatic alcohols and water), potassium hydroxide solution (KOH, 1 mol L^{-1}), N,N-dimethylformamide (DMF, 99.99%), and methanol (MeOH, 99.98%) were purchased from Merck GmbH and used without further purification. Nickel foam (NF) (thickness, 1.6 mm; average surface area density: 0.43 g cm^{-2}) was obtained from Racemat BV and rinsed with doubly-ionized, DI water (residual conductivity 18.2 MΩ cm).

Doubly-ionized, DI water with a residual conductivity of 0.05 µS cm^{-1} (at 25 °C) was obtained from a MILLIPORE Synergy® water treatment system.

Methods

A Monowave 400 microwave reactor (Anton Paar GmbH, Graz, Austria), with a maximum power of 850 W, attained temperatures up to 300 °C and pressures up to 30 bar was used for all microwave reactions.

Powder X-ray diffraction (PXRD) data were collected with a Rigaku Miniflex 600 powder diffractometer using a low background silicon sample holder and Cu–Kα irradiation (λ = 1.54184 Å). The measurements were conducted over a 2θ = 2–100° range with a scan speed of 1.5 deg min^{-1} (600 W, 40 kV, 15 mA). The diffractograms were analyzed using the software Match 3.1.0.

N_2 sorption isotherms were obtained with a Belsorp MAXII high-precision gas/vapor adsorption measurement instrument at 77 K and evaluated with the BELMaster MAXII software (version 7.3.2.0). The materials were activated by degassing under a vacuum (~ 10^{-5} mbar) at 150 °C for 5 h. Brunauer–Emmett–Teller (BET) surface areas were determined from the nitrogen adsorption isotherms and the pore size distributions were derived by non-local density functional theory (NLDFT) calculations based on the "N_2 at 77 K with slit pores" method. The total pore volumes were calculated from the adsorbed volume at $p/p_0 = 0.95$.

^{1}H NMR measurements in solution were performed with a Bruker Advance III-300, operating at 300 MHz. Before dissolution under digestion, the MOF samples were activated at 150 °C for at least 20 h under vacuum (< 10^{-2} mbar) to remove the residual solvent content. Then,10 mg of each activated MOF sample was suspended in 0.7 mL of DMSO-d_6 and digested by the addition of 20 µL of D_2SO_4 (98 wt.% in D_2O).

The Fourier transform infrared (FTIR) spectra of all the samples were recorded on a Bruker FTIR Tensor 37 spectrometer (Bruker AXS, Karlsruhe, Germany) in attenuated total reflection (ATR) mode with a diamond crystal or as KBr pellets in the range of 400—4000 cm^{-1}.

Flame atomic absorption spectroscopy (AAS) was done with a PinAAcle 900 T from PerkinElmer. For the AAS sample preparation, the precisely weighted samples (in the range of 15–20 mg) were heated and stirred with concentrated HCl (36%) overnight. The solution was carefully filtered and diluted with Millipore water to a volume of 50 mL in a volumetric flask and diluted again by a factor of 1:50 for the AAS measurements.

Scanning electron microscopy (SEM) images were collected with a Jeol JSM-65 10 LV QSEM advanced electron microscope with a LaB_6 cathode at 20 kV equipped with a Bruker Xflash 410 silicon drift detector for energy-dispersive X-ray spectrometric (EDX) elemental composition analysis.

X-ray photoelectron spectroscopy (XPS) measurements were made on a ULVAC-PHI VersaProbe II TM with a small minimum beam size of 100 µm and a spectral resolution of 0.5 eV. The spectra were calibrated by the C 1s signal (at 284.80 eV).

Electrochemical Measurements

All electrochemical measurements were carried out on a three-electrode system on an RRDE-3 A station from ALS Japan, which included a platinum counter electrode, a rotating disk glassy carbon electrode (RD-GCE) as working electrode with a geometric area of 0.196 cm^2 and a Gamry Interface 1010 E potentiostat (Gamry Instrument, Warminster, PA, USA). The system consists of a coiled platinum wire as a counter electrode and a reversible hydrogen electrode (RHE) as a reference electrode. The oxygen concentration during electrocatalysis was measured *insitu* by using an Ocean

Optics NeoFOX sensing system equipped with a FOSPOR probe (see below for further details).

Working electrodes were fabricated by depositing the prepared MOF materials on a rotating disc electrode (RD-GCE, 5 mm diameter, 0.196 cm^2 area) or on nickel foam, NF (~1 cm×2 cm, thickness: 1.6 mm). The piece of NF is larger than the actual tested area of ~1 cm×1 cm used for the measurement because a part of the NF is connected with a copper wire of the Gamry Instruments, such that the connection does not come into contact with the KOH electrolyte to avoid any damage.

For the deposition on the RD-GCE, the amount of 2.5 mg of catalyst was dispersed in 0.5 mL of a 1:1 (v:v) mixture of DI water and methanol with 50 µL of Nafion (around 5% in a mixture of water and lower aliphatic alcohols) as the binding agent. The suspension was sonicated for 30 min to form a homogeneous ink. Then, 10 µL of the prepared ink was dropped onto the rotating disc electrode (mass loading 0.23 mg cm^{-2}) and dried at room temperature. As an electrolyte 1 mol L^{-1} KOH solution (pH: 14) was used and nitrogen was purged for 10 min through the cell to remove oxygen before the electrochemical tests. The working electrode was kept rotating at a rate of 1600 rpm during the measurements. The electrode films were pre-cycled for at least 100 cyclic voltammetry (CV) cycles at a sweep rate of 100 mV cm^{-1} between 1.0 and 1.7 V (which lasted about 20–22 min) to ensure a stable electrochemical performance as an activation process. All linear sweep voltammetry (LSV) curves were collected by sweeping the potential from 0.8 to 1.7 V vs RHE with a scan rate of 5 mV s^{-1}. All current densities were calculated based on the geometrical surface area of the electrodes. All LSV curves were iR-corrected to compensate for the influence of the solution resistance by the following Equation (1):

$$E_{iR-corrected} = E - iR \quad (1)$$

where i is the current (A) and R (Ω) is the electrolyte resistance measured by electrochemical impedance spectroscopy (EIS).

The overpotential η was derived from the standard potential E vs RHE using Equation (2):

$$\eta = E_{RHE} - 1.23\ V \quad (2)$$

The Tafel slope b was obtained by fitting the linear portion of the Tafel plots, which were derived from the LSV curves according to the Tafel Equation (3):

$$\eta = a + b\ \log(j) \quad (3)$$

where a is a constant and j represents the current density.

Electrochemical impedance spectroscopy (EIS) data were recorded with the frequency range of 0.1–100 kHz at the potential of 1.53 V after activation. Chronopotentiometry tests were carried out at a fixed current density of 50 mA cm^{-2}.

The turnover frequency (TOF) per mol of metal was calculated using Equation (4):

$$TOF = \frac{j \times A}{4 \times n \times F} \quad (4)$$

where j is the current density (mA cm^{-2}) at an overpotential of 320 mV, A is the surface area of the RD-GCE electrode (0.196 cm^{-2}), F is the Faraday constant (96485 s A mol^{-1}), n represents the number of moles of all metal ions deposited on the RD-GCE electrode (mmol). The method has also been used in the literature.[29]

Faradaic Efficiency (FE%)

The literature has been followed to evaluate the faradaic efficiency (FE%) towards oxygen production.[118] The chronopotentiometry test was carried out by applying a fixed current (50 mA cm^{-2}) while the oxygen concentration in the headspace was measured *insitu* by using an Ocean Optics NeoFOX sensing system equipped with an FOSPOR probe. The FOSPOR probe underwent calibration through a two-point calibration process, fixing 0% O_2 under N_2 flow and 20.9% O_2 in air. To ensure optimal conditions, the solution underwent thorough de-aeration by purging with N_2 for a minimum of 1 hour before initiating the experiment. After the purging with N_2 was stopped, a baseline for the molar O_2 background content (blind value) was recorded for 30 min before starting the chronoamperometry measurement.

The moles of O_2 generated during the electrochemical experiment were calculated via the following Equation (5):

$$nO_{2,exp} = \%\ O_{2g} \times P_{total} \times V_{gas\ space} \times R^{-1} \times T^{-1}/100 \quad (5)$$

where % O_2 is given by the FOSPOR probe, P_{total} is 1 atm, $V_{gas\ space}$ (L) is measured for each experiment, R is the universal gas constant in 0.082 atm L K^{-1} mol^{-1} and T is 293 K. The faradaic oxygen production was calculated using the charge data from the chronoamperometry experiment, as described in the following Equation (6):

$$nO_{2,far} = Q \times n_e^{-1} \times F^{-1} \quad (6)$$

where Q (C) is the charge passed through the system, n_e is the number of mols of electrons in the water oxidation reaction to generate one mol of oxygen ($n_e = 4$) and F is the Faraday constant (96 485 C mol^{-1}).

Then the faradaic efficiency (FE%) is calculated as follows from Equation (7):

$$FE = \frac{100 \times nO_{2,exp}}{nO_{2,far}} \quad (7)$$

Supporting Information Summary

The authors have cited additional references within the Supporting Information.[120–145]

Acknowledgements

The authors also thank the Center for Molecular and Structural Analytics at Heinrich-Heine University (CeMSA@HHU) for recording the NMR-spectrometric data. The authors thank Dr. Ulrich Hagemann at the University of Duisburg-Essen for supporting XPS measurement. The authors thank Mrs. Birgit Tommes for carrying out the FTIR experiments, Mrs. Annette Ricken for the AAS measurements, Ms. Annette Vollrath for supporting the experimental part during revision, Mr. Robert Oestreich for the BET measurements. The research was funded by the Deutsche Forschungsgemeinschaft (DFG) within the Priority Program SPP

1928/2 COORNETs (grant Ja466/43-1). Open Access funding enabled and organized by Projekt DEAL.

Conflict of Interests

The authors declare no conflict of interest.

Data Availability Statement

The data that support the findings of this study are available in the supplementary material of this article.

Keywords: Metal-organic frameworks (MOFs) · Oxygen evolution reaction (OER) · Microwave-assisted synthesis · Bimetallic MOF · Electrocatalysis

[1] M. S. Faber, S. Jin, *Energy Environ. Sci.* **2014**, *7*, 3519–3542.
[2] C. Tan, X. Cao, X.-J. Wu, Q. He, J. Yang, X. Zhang, J. Chen, W. Zhao, S. Han, G.-H. Nam, M. Sindoro, H. Zhang, *Chem. Rev.* **2017**, *117*, 6225–6331.
[3] C. G. Morales-Guio, L.-A. Stern, X. Hu, *Chem. Soc. Rev.* **2014**, *43*, 6555–6569.
[4] T. F. Jaramillo, K. P. Jørgensen, J. Bonde, J. H. Nielsen, S. Horch, I. Chorkendorff, *Science* **2007**, *317*, 100–102.
[5] L. Rademacher, T. H. Y. Beglau, B. Ali, L. Sondermann, T. Strothmann, I. Boldog, J. Barthel, C. Janiak, *J. Mater. Chem. A* **2024**, *12*, 2093–2109.
[6] N.-T. Suen, S.-F. Hung, Q. Quan, N. Zhang, Y.-J. Xu, H. M. Chen, *Chem. Soc. Rev.* **2017**, *46*, 337–365.
[7] T. Reier, M. Oezaslan, P. Strasser, *ACS Catal.* **2012**, *2*, 1765–1772.
[8] N. Zhang, Y. Chai, *Energy Environ. Sci.* **2021**, *14*, 4647–4671.
[9] D. Zhu, M. Qiao, J. Liu, T. Tao, C. Guo, *J. Mater. Chem. A* **2020**, *8*, 8143–8170.
[10] S. Abdpour, M. N. A. Fetzer, R. Oestreich, T. H. Y. Beglau, I. Boldog, C. Janiak, *Dalton Trans.* **2024**, *53*, 4937–4951.
[11] X. Z. Song, N. Zhang, X. F. Wang, Z. Tan, *Mater. Today Energy* **2021**, *19*, 100597.
[12] J. Du, F. Li, L. Sun, *Chem. Soc. Rev.* **2021**, *50*, 2663–2695.
[13] Y. Yang, Y. Yang, Y. Liu, S. Zhao, Z. Tang, *Small Sci.* **2021**, *1*, 2100015.
[14] Z. Gao, Y. Lai, L. Zhang, Y. Lin, L. Xiao, Y. Luo, F. Luo, *J. Chem. Educ.* **2021**, *98*, 3341–3347.
[15] M. Jothi, P. Gnanasekar, J. Kulandaivel, *Energy Fuels* **2022**, *36*, 13713–13721.
[16] M. Liu, H. Su, W. Cheng, F. Yu, Y. Li, W. Zhou, H. Zhang, X. Sun, X. Zhang, S. Wei, Q. Liu, *Small* **2022**, *18*, 2202248.
[17] Y. Wang, W. Wu, Y. Rao, Z. Li, N. Tsubaki, M. Wu, *J. Mater. Chem. A* **2017**, *5*, 6170–6177.
[18] J. Li, S. Gadipelli, *Chem. Eur. J.* **2020**, *26*, 14167–14172.
[19] S. Li, Y. Gao, N. Li, L. Ge, X. Bu, P. Feng, *Energy Environ. Sci.* **2021**, *14*, 1897–1927.
[20] T. H. Beglau, L. Rademacher, R. Oestreich, C. Janiak, *Molecules* **2023**, *28*, 4464.
[21] J. Huo, Y. Wang, L. Yan, Y. Xue, S. Li, M. Hu, Y. Jiang, Q.-G. Zhai, *Nanoscale* **2020**, *12*, 14514–14523.
[22] S. Öztürk, G. Moon, A. Spieß, E. Budiyanto, S. Roitsch, H. Tüysüz, C. Janiak, *ChemPlusChem* **2021**, *86*, 1106–1115.
[23] L. Sondermann, W. Jiang, M. Shviro, A. Spieß, D. Woschko, L. Rademacher, C. Janiak, *Molecules* **2022**, *27*, 1241.
[24] N. Hales, T. J. Schmidt, E. Fabbri, *Curr. Opin. Electrochem.* **2023**, *38*, 101231.
[25] B. Singh, A. Yadav, A. Indra, *J. Mater. Chem. A* **2022**, *10*, 3843–3868.
[26] M. Liu, L. Kong, X. Wang, J. He, J. Zhang, J. Zhu, X.-H. Bu, *Nano Res.* **2021**, *14*, 4680–4688.
[27] Q. Qian, Y. Li, Y. Liu, L. Yu, G. Zhang, *Adv. Mater.* **2019**, *31*, 1901139.
[28] K. Rui, G. Zhao, Y. Chen, Y. Lin, Q. Zhou, J. Chen, J. Zhu, W. Sun, W. Huang, S. X. Dou, *Adv. Funct. Mater.* **2018**, *28*, 1801554.
[29] X. Ma, D. J. Zheng, S. Hou, S. Mukherjee, R. Khare, G. Gao, Q. Al, B. Garlyyev, W. Li, M. Koch, J. Mink, Y. Shao-Horn, J. Warnan, A. S. Bandarenka, R. A. Fischer, *ACS Catal.* **2023**, *13*, 7587–7596.
[30] W. Zheng, M. Liu, L. Y. S. Lee, *ACS. Catal.* **2020**, *10*, 81–92.
[31] L. Yang, G. Zhu, H. Wen, X. Guan, X. Sun, H. Feng, W. Tian, D. Zheng, X. Cheng, Y. Yao, *J. Mater. Chem. A* **2019**, *7*, 8771–8776.
[32] E. A. Dolgopolova, A. J. Brandt, O. A. Ejegbavwo, A. S. Duke, T. D. Maddumapatabandi, R. P. Galhenage, B. W. Larson, O. G. Reid, S. C. Ammal, A. Heyden, M. Chandrashekhar, V. Stavila, D. A. Chen, N. B. Shustova, *J. Am. Chem. Soc.* **2017**, *139*, 5201–5209.
[33] S. Zhao, Y. Wang, J. Dong, C.-T. He, H. Yin, P. An, K. Zhao, X. Zhang, C. Gao, L. Zhang, J. Lv, J. Wang, J. Zhang, A. M. Khattak, N. A. Khan, Z. Wei, J. Zhang, S. Liu, H. Zhao, Z. Tang, *Nat. Energy* **2016**, *1*, 16184.
[34] D. Senthil Raja, H.-W. Lin, S.-Y. Lu, *Nano Energy* **2019**, *57*, 1–13.
[35] S. Mukherjee, S. Hou, S. A. Watzele, B. Garlyyev, W. Li, A. S. Bandarenka, R. A. Fischer, *ChemElectroChem* **2022**, *9*, e202101476.
[36] W. Hu, M. Zheng, B. Xu, Y. Wei, W. Zhu, Q. Li, H. Pang, *J. Mater. Chem. A* **2021**, *9*, 3880–3917.
[37] Y.-Z. Chen, C. Wang, Z.-Y. Wu, Y. Xiong, Q. Xu, S.-H. Yu, H.-L. Jiang, *Adv. Mater.* **2015**, *27*, 5010–5016.
[38] D. Senthil Raja, X.-F. Chuah, S.-Y. Lu, *Adv. Energy Mater.* **2018**, *8*, 1801065.
[39] H. Sun, Z. Yan, F. Liu, W. Xu, F. Cheng, J. Chen, *Adv. Mater.* **2020**, *32*, 1806326.
[40] J. Duan, S. Chen, C. Zhao, *Nat. Commun.* **2017**, *8*, 15341.
[41] L.-L. Feng, G. Yu, Y. Wu, G.-D. Li, H. Li, Y. Sun, T. Asefa, W. Chen, X. Zou, *J. Am. Chem. Soc.* **2015**, *137*, 14023–14026.
[42] Y. Li, B. Thomas, C. Tang, T. Asefa, *Dalton Trans.* **2023**, *52*, 17834–17845.
[43] F. Sun, G. Wang, Y. Ding, C. Wang, B. Yuan, Y. Lin, *Adv. Energy Mater.* **2018**, *8*, 1800584.
[44] N. K. Chaudhari, H. Jin, B. Kim, K. Lee, *Nanoscale* **2017**, *9*, 12231–12247.
[45] N. Stock, S. Biswas, *Chem. Rev.* **2012**, *112*, 933–969.
[46] A. L. Buchachenko, E. L. Frankevich, *Chemical Generation and Reception of Radio-and Microwaves*, Wiley-VCH, Weinheim/VCH Publishers, New York **1994**.
[47] V. K. Ahluwulia, *Alternative energy processes in chemical synthesis*, Alpha Science International LTD, Oxford, United Kingdom **2008**.
[48] L. Perreux, A. Loupy, *Tetrahedron* **2001**, *57*, 9199–9223.
[49] Q. Li, Y. Liu, S. Niu, C. Li, C. Chen, Q. Liu, J. Huo, *J. Colloid Interface Sci.* **2021**, *603*, 148–156.
[50] A. A. Vodyashkin, A. V. Sergorodceva, P. Kezimana, Y. M. Stanishevskiy, *Int. J. Mol. Sci.* **2023**, *24*.
[51] C. Vollmer, E. Redel, K. Abu-Shandi, R. Thomann, H. Manyar, C. Hardacre, C. Janiak, *Chem. Eur. J.* **2010**, *16*, 3849–3858.
[52] L. Rademacher, T. H. Y. Beglau, T. Heinen, J. Barthel, C. Janiak, *Front. Chem.* **2022**, *10*, 945261.
[53] P. Maniam, N. Stock, *Inorg. Chem.* **2011**, *50*, 5085–5097.
[54] F. Zou, S. L. Chao, Y. X. Wang, Y. L. Wang, Q. X. Guan, W. Li, *Environ. Sci. Nano* **2017**, *4*, 46–51.
[55] S. Wang, X. Du, S. Liu, Y. Fu, N. Huang, *Nanomater.* **2023**, *13*.
[56] E. Ruiz-Trejo, A. K. Azad, J. T. S. Irvine, *J. Electrochem. Soc.* **2015**, *162*, F273.
[57] Q. Liu, Q. Yan, S. Wu, J. Wang, H. Liu, *Electrochem.* **2016**, *84*, 219–223.
[58] S. Khamlich, T. Mokrani, M. S. Dhlamini, B. M. Mothudi, M. Maaza, *Energy Procedia* **2016**, *88*, 614–618.
[59] A. Kumar, E. E. Wolf, A. S. Mukasyan, *AIChE J.* **2011**, *57*, 2207–2214.
[60] R. Li, X. Han, Q. Liu, A. Qian, F. Zhu, J. Hu, J. Fan, H. Shen, J. Liu, X. Pu, H. Xu, B. Mu, *ACS Omega* **2022**, *7*, 20081–20091.
[61] S. Xing, J. Liang, P. Brandt, F. Schäfer, A. Nuhnen, T. Heinen, I. Boldog, J. Möllmer, M. Lange, O. Weingart, C. Janiak, *Angew. Chem. Int. Ed.* **2021**, *60*, 17998–18005.
[62] M. Thommes, K. Kaneko, A. V. Neimark, J. P. Olivier, F. Rodriguez-Reinoso, J. Rouquerol, K. S. Sing, *Pure Appl. Chem.* **2015**, *87*, 1051–1069.
[63] J. Long, K. Shen, L. Chen, Y. Li, *J. Mater. Chem. A* **2016**, *4*, 10254–10262.
[64] J. Guerrero-Medina, G. Mass-González, L. Pacheco-Londoño, S. P. Hernández-Rivera, R. Fu, A. J. Hernández-Maldonado, *Microporous Mesoporous Mat.* **2015**, *212*, 8–17.
[65] B. Mousavi, S. Chaemchuen, B. Moosavi, K. Zhou, M. Yusubov, F. Verpoort, *ChemistryOpen* **2017**, *6*, 674–680.
[66] J. Wu, Z. Yu, Y. Zhang, S. Niu, J. Zhao, S. Li, P. Xu, *Small* **2021**, *17*, 2105150.

[67] J. Zhou, Z. Han, X. Wang, H. Gai, Z. Chen, T. Guo, X. Hou, L. Xu, X. Hu, M. Huang, S. V. Levchenko, H. Jiang, *Adv. Funct. Mater.* **2021**, *31*, 2102066.
[68] S. Menzel, T. Heinen, I. Boldog, T. H. Y. Beglau, S. Xing, A. Spieß, D. Woschko, C. Janiak, *CrystEngComm* **2022**, *24*, 3675–3691.
[69] S. Bera, S. Dhara, S. Velmurugan and A. K. Tyagi, *Int. J. Spectrosc.* **2012**, 1–4; http://www.xpsfitting.com/search/label/Zinc.
[70] J. Yang, H. Liu, W. N. Martens, R. L. Frost, *J. Phys. Chem. C* **2010**, *114*, 111–119.
[71] M. C. Biesinger, B. P. Payne, A. P. Grosvenor, L. W. Lau, A. R. Gerson, R. S. Smart, *Appl. Surf. Sci.* **2011**, *257*, 2717–2730.
[72] R. Lontio Fomekong, P. Kammi Yontchoum, T. J. Matemb Ma Ntep, H. M. Tedjieukeng Kamta, P. Kenfack Tsobnang, S. Krüger, J. Sturala, Z. Sofer, C. Janiak, B. Saruhan, A. Delcorte, J. N. Lambi, *Adv. Energy Sustain. Res.* **2024**, *5*, 2300232.
[73] L. Marchetti, F. Miserque, S. Perrin, M. Pijolat, *Surf. Interface Anal.* **2015**, *47*, 632–642.
[74] W. Jiang, W. Lehnert, M. Shviro, *ChemElectroChem* **2023**, *10*, e202200991.
[75] A. Spieß, J. Wiebe, E. Iwaschko, D. Woschko, C. Janiak, *Mol. Syst. Des.* **2022**, *7*, 1682–1696.
[76] J. Yan, L. Kong, Y. Ji, J. White, Y. Li, J. Zhang, P. An, S. Liu, S.-T. Lee, T. Ma, *Nat. Commun.* **2019**, *10*, 2149.
[77] O. Díaz-Morales, D. Ferrus-Suspedra, M. T. M. Koper, *Chem. Sci.* **2016**, *7*, 2639–2645.
[78] S. Hou, W. Li, S. Watzele, R. M. Kluge, S. Xue, S. Yin, X. Jiang, M. Döblinger, A. Welle, B. Garlyyev, M. Koch, P. Müller-Buschbaum, C. Wöll, A. S. Bandarenka, R. A. Fischer, *Adv. Mater.* **2021**, *33*, 2103218.
[79] H. Shooshtari Gugtapeh, M. Rezaei, *ACS Appl. Mater. Interfaces.* **2023**, *15*, 34682–34697.
[80] R. Yu, C. Wang, D. Liu, Z. Wu, J. Li, Y. Du, *Inorg. Chem. Front.* **2022**, *9*, 3130–3137.
[81] S. Huang, X.-R. Shi, C. Sun, X. Zhang, M. Huang, R. Liu, H. Wang, S. Xu, *Appl. Surf. Sci.* **2022**, *572*, 151344.
[82] H. Liu, H. Guo, N. Wu, W. Yao, R. Xue, M. Wang, W. Yang, *J. Alloys Compd.* **2021**, *856*, 156535.
[83] A. Raveendran, M. Chandran, R. Dhanusuraman, *RSC Adv.* **2023**, *13*, 3843–3876.
[84] Y. Wang, Y. Zhang, Z. Liu, C. Xie, S. Feng, D. Liu, M. Shao, S. Wang, *Angew. Chem. Int. Ed.* **2017**, *56*, 5867–5871.
[85] G. Li, L. Anderson, Y. Chen, M. Pan, P.-Y. Abel Chuang, *Sustain. Energy Fuels.* **2018**, *2*, 237–251.
[86] Y. Lin, M. Zhang, L. Zhao, L. Wang, D. Cao, Y. Gong, *Appl. Surf. Sci.* **2021**, *536*, 147952.
[87] Y. Qin, T. Yu, S. Deng, X.-Y. Zhou, D. Lin, Q. Zhang, Z. Jin, D. Zhang, Y.-B. He, H.-J. Qiu, L. He, F. Kang, K. Li, T.-Y. Zhang, *Nat. Commun.* **2022**, *13*, 3784.
[88] R. L. Doyle, I. J. Godwin, M. P. Brandon, M. E. G. Lyons, *Phys. Chem. Chem. Phys.* **2013**, *15*, 13737–13783.
[89] M. Yu, G. Moon, E. Bill, H. Tüysüz, *ACS Appl. Energy Mater.* **2019**, *2*, 1199–1209.
[90] J. R. Swierk, S. Klaus, L. Trotochaud, A. T. Bell, T. D. Tilley, *J. Phys. Chem. C* **2015**, *119*, 19022–19029.
[91] R. L. Doyle, M. E. G. Lyons, *Phys. Chem. Chem. Phys.* **2013**, *15*, 5224–5237.
[92] R. L. Doyle, M. E. G. Lyons, *J. Electrochem. Soc.* **2013**, *160*, H142.
[93] M. E. Lyons, R. L. Doyle, M. P. Browne, I. J. Godwin, A. A. Rovetta, *Curr. Opin. Electrochem.* **2017**, *1*, 40–45.
[94] S. Anantharaj, P. E. Karthik, S. Noda, *Angew. Chem. Int. Ed.* **2021**, *60*, 23051–23067.
[95] M. Ma, F. Qu, X. Ji, D. Liu, S. Hao, G. Du, A. M. Asiri, Y. Yao, L. Chen, X. Sun, *Small* **2017**, *13*, 1700394.
[96] C. Qu, B. Zhao, Y. Jiao, D. Chen, S. Dai, B. M. Deglee, Y. Chen, K. S. Walton, R. Zou, M. Liu, *ACS Energy Lett.* **2017**, *2*, 1263–1269.
[97] X. Liu, F. Xia, R. Guo, M. Huang, J. Meng, J. Wu, L. Mai, *Adv. Funct. Mater.* **2021**, *31*, 2101792.
[98] M. Gao, W. Sheng, Z. Zhuang, Q. Fang, S. Gu, J. Jiang, Y. Yan, *J. Am. Chem. Soc.* **2014**, *136*, 7077–7084.
[99] X. Yi, V. Celorrio, H. Zhang, N. Robertson, C. Kirk, *J. Mater. Chem. A* **2023**, *11*, 22275–22287.
[100] S. Anantharaj, K. Karthick, S. Kundu, *Mater. Today Energy* **2017**, *6*, 1–26.
[101] Y. Mousazade, M. R. Mohammadi, P. Chernev, R. Bagheri, Z. Song, H. Dau, M. M. Najafpour, *Inorg. Chem.* **2020**, *59*, 15335–15342.
[102] C.-F. Du, Q. Song, Q. Liang, X. Zhao, J. Wang, R. Zhi, Y. Wang, H. Yu, *ChemNanoMat* **2021**, *7*, 539–544.
[103] J. Jiang, A. Zhang, L. Li, L. Ai, *J. Power Sources.* **2015**, *278*, 445–451.
[104] Y. Chen, H. Jin, Y. Gao, T. Xiao, M. Bi, S. Li, Y. Liang, *Ion.* **2023**, *29*, 1285–1300.
[105] H. Zhao, Y. Yang, X. Dai, H. Qiao, J. Yong, X. Luan, L. Yu, C. Luan, Y. Wang, X. Zhang, *Electrochim. Acta* **2019**, *295*, 1085–1092.
[106] A. Carton, A. Mesbah, T. Mazet, F. Porcher, M. François, *Solid State Sci.* **2007**, *9*, 465–471.
[107] J. Zhou, Y. Dou, X.-Q. Wu, A. Zhou, L. Shu, J.-R. Li, *Small* **2020**, *16*, 1906564.
[108] Q. Zha, F. Yuan, G. Qin, Y. Ni, *Inorg. Chem.* **2020**, *59*, 1295–1305.
[109] S. Zhao, C. Tan, C.-T. He, P. An, F. Xie, S. Jiang, Y. Zhu, K.-H. Wu, B. Zhang, H. Li, J. Zhang, Y. Chen, S. Liu, J. Dong, Z. Tang, *Nat. Energy* **2020**, *5*, 881–890.
[110] B. Qiu, L. Cai, Y. Wang, Z. Lin, Y. Zuo, M. Wang, Y. Chai, *Adv. Funct. Mater.* **2018**, *28*, 1706008.
[111] X. Xiao, C.-T. He, S. Zhao, J. Li, W. Lin, Z. Yuan, Q. Zhang, S. Wang, L. Dai, D. Yu, *Energy Environ. Sci.* **2017**, *10*, 893–899.
[112] K. Zhang, R. Zou, *Small* **2021**, *17*, 2100129.
[113] M. Rinawati, Y.-X. Wang, K.-Y. Chen, M.-H. Yeh, *J. Chem. Eng.* **2021**, *423*, 130204.
[114] H. Han, H. Choi, S. Mhin, Y.-R. Hong, K. M. Kim, J. Kwon, G. Ali, K. Y. Chung, M. Je, H. N. Umh, D.-H. Lim, K. Davey, S.-Z. Qiao, U. Paik, T. Song, *Energy Environ. Sci.* **2019**, *12*, 2443–2454.
[115] H. Bode, K. Dehmelt, J. Witte, *Electrochim. Acta.* **1966**, *11*, 1079–1087.
[116] S. S. Jeon, J. Lim, P. W. Kang, J. W. Lee, G. Kang, H. Lee, *ACS Appl. Mater. Interfaces.* **2021**, *13*, 37179–37186.
[117] D.-J. Li, Q.-H. Li, Z.-G. Gu, J. Zhang, *J. Mater. Chem. A* **2019**, *7*, 18519–18528.
[118] J. Yu, S. Giancola, B. Khezri, D. Nieto-Castro, J. Redondo, F. Schiller, S. Barja, M. C. Spadaro, J. Arbiol, F. A. Garcés-Pineda, J. R. Galán-Mascarós, *EES catal.* **2023**, *1*, 765–773.
[119] N. K. Chaudhari, H. Jin, B. Kim, K. Lee, *Nanoscale* **2017**, *9*, 12231–12247.
[120] K. Brandenburg, *Diamond 4.6, Crystal and Molecular Structure Visualization*. Copyright 1997–2022 Crystal Impact GbR, Bonn, Germany. Available online: https://www.crystalimpact.com/diamond/ (accessed on 10 August 2022).
[121] Y. Jiao, C. Qu, B. Zhao, Z. Liang, H. Chang, S. Kumar, R. Zou, M. Liu, K. S. Walton, *ACS Appl. Energy Mater.* **2019**, *2*, 5029–5038.
[122] Y. Wu, X. Song, S. Xu, Y. Chen, O. Oderinde, L. Gao, R. Wei, G. Xiao, *Dalton Trans.* **2020**, *49*, 312–321.
[123] P. Xu, X. J. Han, B. Zhang, Z. S. Lv, X. R. Liu, *J. Alloys Compd.* **2007**, *436*, 369–374.
[124] S. Palmas, F. Ferrara, A. Vacca, M. Mascia, A. M. Polcaro, *Electrochim. Acta* **2007**, *53*, 400–406.
[125] E. Castro, C. Gervasi, *Int. J. Hydrogen Energy.* **2000**, *25*, 1163–1170.
[126] X. Liu, Z. Chang, L. Luo, T. Xu, X. Lei, J. Liu, X. Sun, *Chem. Mater.* **2014**, *26*, 1889–1895.
[127] N. Song, S. Hong, M. Xiao, Y. Zuo, E. Jiang, C. Li, H. Dong, *J. Colloid Interface Sci.* **2021**, *582*, 535–542.
[128] Y. Yang, M. Zhou, W. Guo, X. Cui, Y. Li, F. Liu, P. Xiao, Y. Zhang, *Electrochim. Acta* **2015**, *174*, 246–253.
[129] X. Yu, J. Zhao, L.-R. Zheng, Y. Tong, M. Zhang, G. Xu, C. Li, J. Ma, G. Shi, *ACS Energy Lett.* **2018**, *3*, 237–244.
[130] J. Han, S. Hao, Z. Liu, A. M. Asiri, X. Sun, Y. Xu, *Chem. Commun.* **2018**, *54*, 1077–1080.
[131] G. Nagaraju, S. Chandra Sekhar, L. Krishna Bharat, J. S. Yu, *ACS Nano* **2017**, *11*, 10860–10874.
[132] Q. Chen, Z. Xue, F. Wei, Q. Cheng, R. Wang, T. Hu, C. Guan, B. Ouyang, S. Xu, B. Fan, X. Li, *Int. J. Hydrogen Energy.* **2024**, *51*, 1327–1336.
[133] W. Li, H. Zhang, K. Zhang, Z. Cheng, H. Chen, G. Tan, X. Feng, L. Wang, S. Mu, *Chem. Commun.* **2023**, *59*, 4750–4753.
[134] P. Thangasamy, S. Shanmuganathan, V. Subramanian, *Nanoscale Adv.* **2020**, *2*, 2073–2079.
[135] T. Sun, S. Lin, Z. Xu, L. Li, *CrystEngComm* **2021**, *23*, 7650–7657.
[136] D. Liu, H. Xu, C. Wang, H. Shang, R. Yu, Y. Wang, J. Li, X. Li, Y. Du, *Inorg. Chem.* **2021**, *60*, 5882–5889.
[137] M. Zong, K. Wang, Z. Lin, Z. Tang, *Int. J. Electrochem. Sci.* **2021**, *16*, 21094.
[138] D. Xiong, M. Gu, C. Chen, C. Lu, F.-Y. Yi, X. Ma, *J. Chem. Eng.* **2021**, *404*, 127111.
[139] H. Chen, S. Qiao, J. Yang, X. Du, *Mol. Catal.* **2022**, *518*, 112086.
[140] E. Sadeghi, N. S. Pelghambardoust, S. Chamani, U. Aydemir, *ACS Mater. Au.* **2023**, *3*, 143–163.

[141] S. Sk, R. Madhu, D. S. Gavali, V. Bhasin, R. Thapa, S. N. Jha, D. Bhattacharyya, S. Kundu, U. Pal, *J. Mater. Chem. A* **2023**, *11*, 10309–10318.
[142] S. Abdpour, L. Rademacher, M. N. A. Fetzer, T. H. Beglau, C. Janiak, *Solids* **2023**, *4*, 181–200.
[143] D. Chen, J. Luo, Q. Sun, C. Han, Q. Li, J. Qian, *Int. J. Hydrogen Energy.* **2022**, *47*, 18700–18707.
[144] S. Zhang, D. Lv, A. Zhou, D. Di Wang, Cai, *J. Alloys Compd.* **2023**, *943*, 169091.
[145] M. C. Biesinger, B. P. Payne, L. W. M. Lau, A. Gerson, R. C. St, *Surf. Interface Anal.* **2009**, *41*, 324–332.

Manuscript received: April 26, 2024
Accepted manuscript online: June 13, 2024
Version of record online: ■■, ■■

RESEARCH ARTICLE

MOFs are good precursors for active mixed-metal oxide/hydroxide electrocatalysts, with a uniform distribution of metals at the nanoscale. The catalytic properties of materials from monometallic Ni-, Co- and Zn-MOFs and bimetallic NiCo-, NiZn- and CoZn-MOFs with benzene-1,4-dicarboxylate (BDC) and 1,4-diazabicyclo[2.2.2]octane (DABCO) are investigated in direct comparison. A MOF nanosheet was for the first time obtained on Ni foam through microwave-heating.

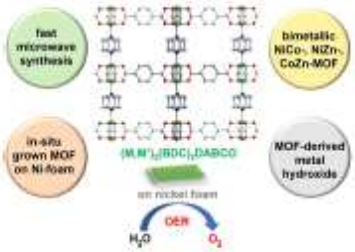

*T. H. Y. Beglau, Y. Fei, C. Janiak**

Supporting Information

Microwave-Assisted ultrafast Synthesis of Bimetallic Nickel-Cobalt Metal-Organic Frameworks for Application in the Oxygen Evolution Reaction

Thi Hai Yen Beglau[1], Yanyan Fei [1], and Christoph Janiak*[1]

Address:

[1]*Institut für Anorganische Chemie und Strukturchemie, Heinrich-Heine-Universität Düsseldorf, 40204 Düsseldorf, Germany*

E-Mail:

Christoph Janiak* - janiak@uni-duesseldorf.de

* Corresponding author

Fax: +49-211-81-12287; Tel: +49-211-81-12286

Emails: Thi Hai Yen Beglau - beglau@uni-duesseldorf.de; Yanyan Fei- yafei100@hhu.de

Characterization of monometallic M_2BDC_2DABCO and bimetallic $(M,M')_2BDC_2DABCO$

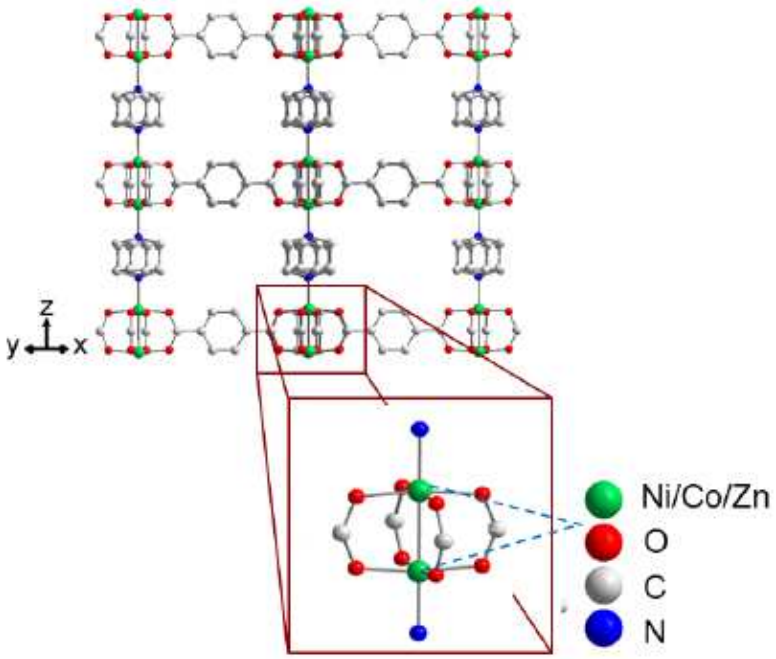

Scheme S1. Illustration of the 3D framework structure of $Ni_2(BDC)_2DABCO$ (abbreviated here as NiMOF). Graphic produced with the software Diamond [1] from the deposited cif-file with CCDC number 802892.[2]

Synthesis of monometallic $M_2(BDC)_2DABCO$ (MMOF) and bimetallic $(M,M')_2(BDC)_2DABCO$ (MM'MOF) (M,M' = Ni, Co, Zn)

The $M_2(BDC)_2DABCO$ was synthesized *via* a microwave irradiation synthesis method (MW), similar to the literature.[3] The bimetallic MOFs were synthesized by a similar procedure to the monometallic MOFs. The two metal nitrate salts (combined 0.63 mmol), benzene-1,4-dicarboxylic acid (H_2BDC) (104.7 mg, 0.63 mmol) and 4-diazabicyclo[2.2.2]octane (DABCO) (35.9 mg, 0.32 mmol) were dispersed into 20 mL of DMF. After stirring at room temperature, the solutions were placed into a microwave vessel (30 mL). The reaction was carried out without stirring at 120 °C with preheating for 10 min and holding at this temperature for 2 h. After cooling to room temperature, the crystalline powder was separated by centrifugation (10,000 rpm, 10 min) and washed three times with DMF (20 mL each for 24 h). The washing process was continued thrice with MeOH (20 mL each for 24 h) and the product was collected by centrifugation (10,000 rpm, 10 min). The product was activated at 120 °C under vacuum ($<10^{-2}$ mbar) for at least 12 h and stored under vacuum. The yields are summarized in Table S1.

Table S1. Summary of the synthetic conditions and yields for the monometallic and bimetallic MOFs.

Sample	$M(NO_3)_2 \cdot 6H_2O$ (mg)	$M'(NO_3)_2 \cdot 6H_2O$ (mg)	Molar ratio M: M':BDC: DABCO	Yield (%) after 2 h
NiMOF	$Ni(NO_3)_2 \cdot 6H_2O$ (183.2)	-	1.6:0.4:2:1	48
CoMOF	$Co(NO_3)_2 \cdot 6H_2O$ (183.4)	-	1.6:0.4:2:1	64
ZnMOF	$Zn(NO_3)_2 \cdot 6H_2O$ (187.7)	-	1.6:0.4:2:1	68
NiCoMOF	$Ni(NO_3)_2 \cdot 6H_2O$ (146.6)	$Co(NO_3)_2 \cdot 6H_2O$ (36.4)	1.6:0.4:2:1	65
NiZnMOF	$Ni(NO_3)_2 \cdot 6H_2O$ (146.6)	$Zn(NO_3)_2 \cdot 6H_2O$ (34.4)	1.6:0.4:2:1	59
CoZnMOF	$Co(NO_3)_2 \cdot 6H_2O$ (146.7)	$Zn(NO_3)_2 \cdot 6H_2O$ (34.5)	1.6:0.4:2:1	72

Synthesis of NiCoMOF/NF

Before preparation of NiCoMOF/NF, a piece of nickel foam, NF, of about 1 cm x 2 cm (thickness 1.6 mm; surface area density, 0.43 g cm^{-3}) was cut from a larger part, cleaned first with acetone and Millipore water in an ultrasonic bath to remove residual metal powder on the surface of the NF. The NF-supported bimetallic MOF was synthesized by immersing NF in the mixture of $Ni(NO_3)_2 \cdot 6H_2O$, $Co(NO_3)_2 \cdot 6H_2O$ (molar ratio 4:1), H_2BDC and DABCO in 15 mL of DMF in a 30 mL microwave tube through the MW synthesis method. The reaction was carried out at 120 °C for 12, 15, 20, 25, 30 or 40 min of heating time at a power of ~25-30 W. The NiCoMOF/NF samples were dipped afterwards in DMF for a few seconds five times, repeatedly washed with MeOH five times to remove residual NiCoMOF powder on the surface of NF and dried at 120 °C under vacuum($<10^{-2}$ mbar) for at least 12 h.

Table S2. Loading of the bimetallic NiCoMOF materials on nickel foam (NF) after different synthesis times, determined by mass gain and from AAS.

Sample [a]	Synthesis time (min)	Mass loading of MOF on NF from weight gain (mg)[a]	Mass loading of MOF on NF by AAS (mg) [b]	mass NiCoMOF/mass (NF) (mg_{MOF}/g_{NF}) [c]
NiCoMOF/NF-4.5	12	0.94	0.62	4.5
NiCoMOF/NF-12.6	15	2.31	2.05	12.6
NiCoMOF/NF-15.0	20	3.12	2.68	15.0
NiCoMOF/NF-16.6	25	3.38	3.42	16.6
NiCoMOF/NF-18.7	30	3.84	4.07	18.7
NiCoMOF/NF-28.6	40	6.09	6.44	28.6

[a] The mass of each piece of NF was slightly different. The mass of the ~1 cm x 2 cm NF piece was in the range of 0.18-0.21 g. Here only the mass difference is given as determined by the weighted mass gain of NF before and after the synthesis.

[b] For AAS, the exactly weighted NiCoMOF/NF composites were heated, stirred, and digested with concentrated HCl (36 %) for 48 h. The mass loading of the MOF on NF was calculated using the determined Co mass (as Ni is present both in the MOF and in the NF).

[c] The value of mg_{MOF}/g_{NF} is derived from the value of the weighted mass gain in column 3.

Pre-treatment of NiCoMOF in KOH

The sample of pristine bimetallic NiCoMOF (30 mg) was immersed in 1 mol L^{-1} KOH solution (30 mL) and stirred at different times (15, 30, 60, 120 min) dried at 80 °C overnight, to obtain homogeneous products. The solid products were collected after washing several times with doubly-ionized (DI) water (10 mL) by centrifugation (10,000 rpm, 10 min) and were dried at room temperature. The products were noted as NiCoMOF-xmin (where x = 15, 30, 60, 120).

Synthesis of $(NiCo)(OH)_2$ at 120 °C

A mixture of NiCoMOF (30 mg) and 30 mL of 1 mol L^{-1} KOH solution was transferred into a 100 mL Teflon-lined stainless-steel autoclave and put in an oven at a temperature of 120 °C for 24h. The products were obtained after washing several times with DI water (10 mL) by centrifugation (10,000 rpm, 10 min). The final products were dried at 60 °C. The product was noted as $(NiCo)(OH)_2$-120 °C and was used as a reference material for electrocatalysis performance comparison.

Fabrication of NiCoMOF-powder and commercial RuO_2 powder on NF

3.38 mg of NiCoMOF powder, 0.5 mL of a 1:1 (v:v) mixture of DI water and methanol (0.5 mL) with 50 µL of Nafion (around 5% in a mixture of water and lower aliphatic alcohols) as the binding agent was dispersed under 30 min sonication to form a homogeneous suspension ink. Afterwards, the ink was coated on NF (the mass of the ~1 cm x 2 cm NF piece was about 0.2 g) using a drop-casting method. After the solution was evaporated at room temperature, the NiCoMOF powder was loaded on NF with the prepared ink and named as NiCoMOF-powder/NF. The mass loading of the NiCoMOF-powder/NF was about 16.6 mg_{MOF}/g_{NF}. The preparation method of commercial RuO_2-loaded NF was similar to the fabrication of NiCoMOF powder on NF, named RuO_2/NF.

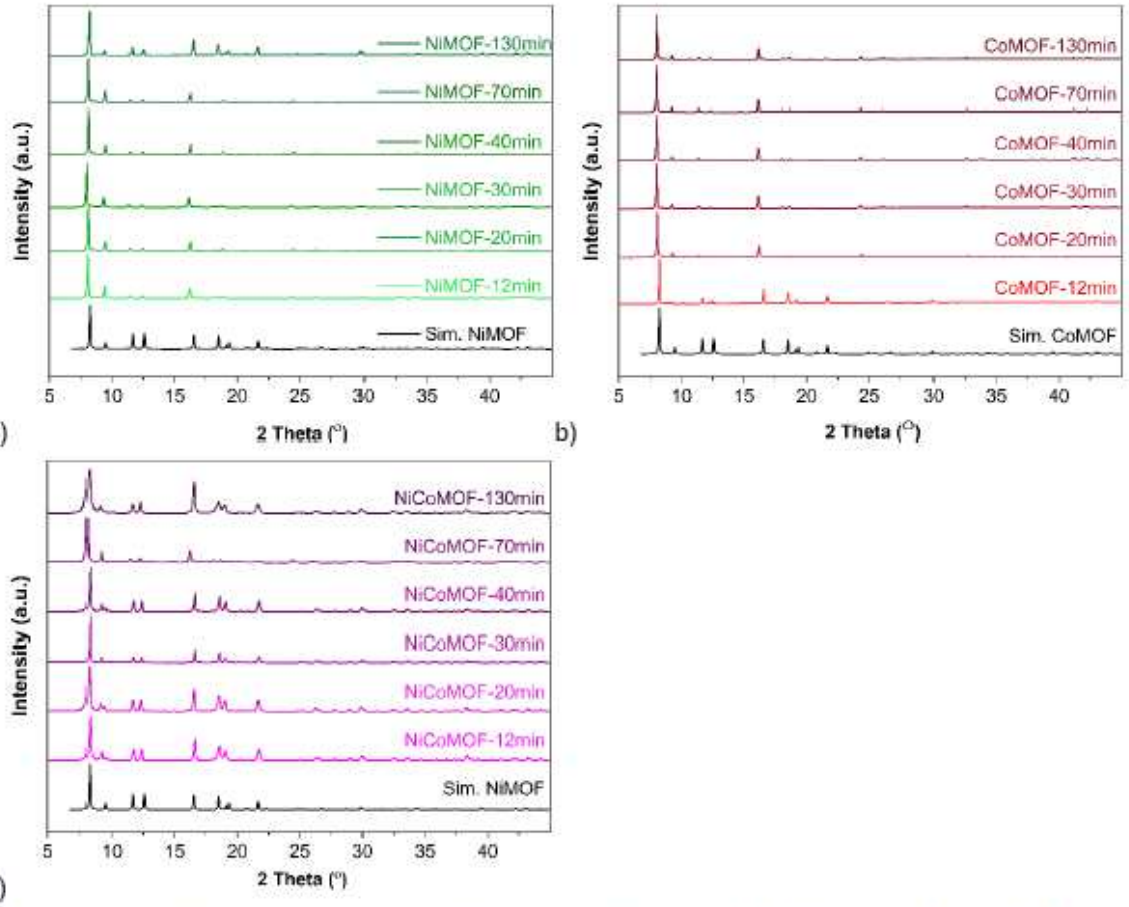

Figure S1. Powder X-ray diffraction (PXRD) patterns of the of a) NiMOF, b) CoMOF, c) NiCoMOF under different synthesis times such as 12, 20, 30, 40, 70 and 130 min. The simulated PXRD pattern of NiMOF was obtained from the deposited cif-file for NiMOF with CCDC number 802892. The first five reflexes at 2θ = 8.2°, 9.4°, 11.7°, 12.4° and 16.6° correspond to the 100, 001, 110, 101 and 200 reflections, respectively.

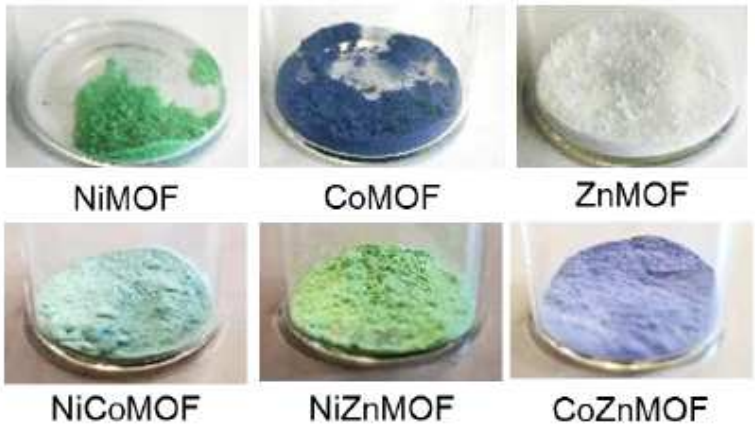

Figure S2. The visual appearance of the various M- and MM'MOFs.

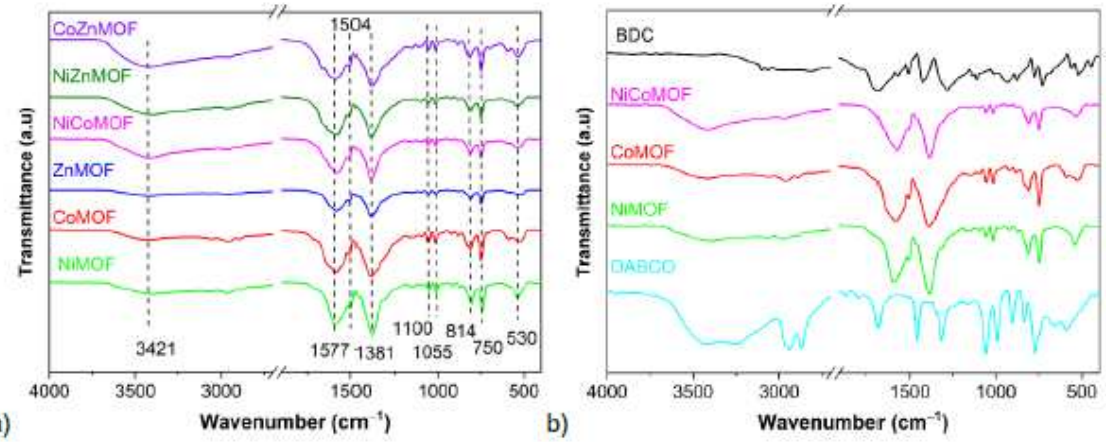

Figure S3. FTIR spectra of a) monometallic and bimetallic MOFs, b) of H_2BDC, DABCO, NiMOF, CoMOF and NiCoMOF.

For the stretching vibration of –OH groups from adsorbed water, the absorption bands appear at 3400 cm^{-1}. A stronger absorption band appears at 1577 and 1381 cm^{-1} which is assigned to the asymmetric and symmetric vibration modes of the –COOH group; respectively. In addition, an absorption band at 1504 cm^{-1} is assigned to the phenyl modes. The weaker bands at 1100 cm^{-1} and 1055 cm^{-1} could be due to the ν_{as}C-N and ν_{as}C-N vibrations of DABCO. The absorbance bands at 814 cm^{-1} and 750 cm^{-1} correspond to the $\nu(C\text{-}C)_{Ar}$ and $\delta(C\text{-}H)_{Ar}$ vibrations, respectively, of the BDC ligand. Absorption bands at 530 cm^{-1} are assigned to the M–O stretching vibration for the $\{M_2O_8\}$ unit in SBU of $M_2(BDC)_2DABCO$.

Digestion ^{1}H NMR spectra

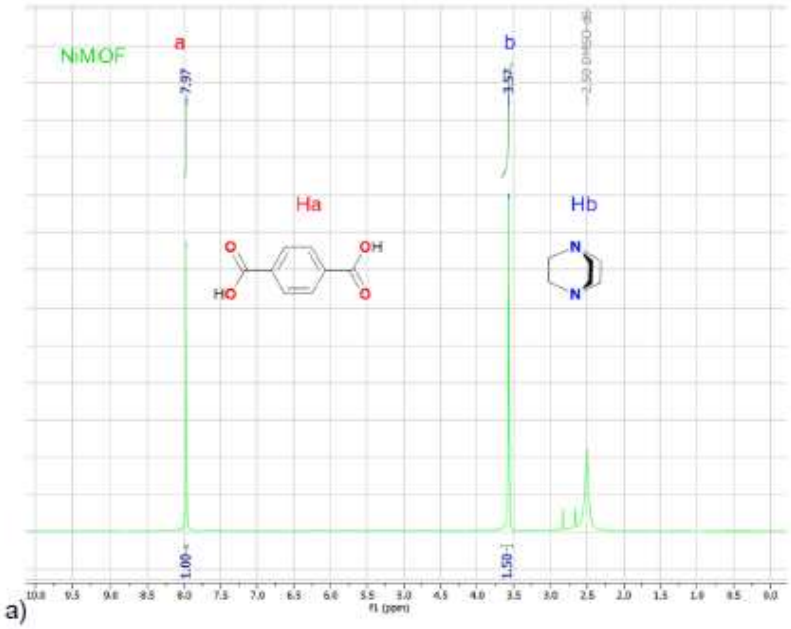

a)

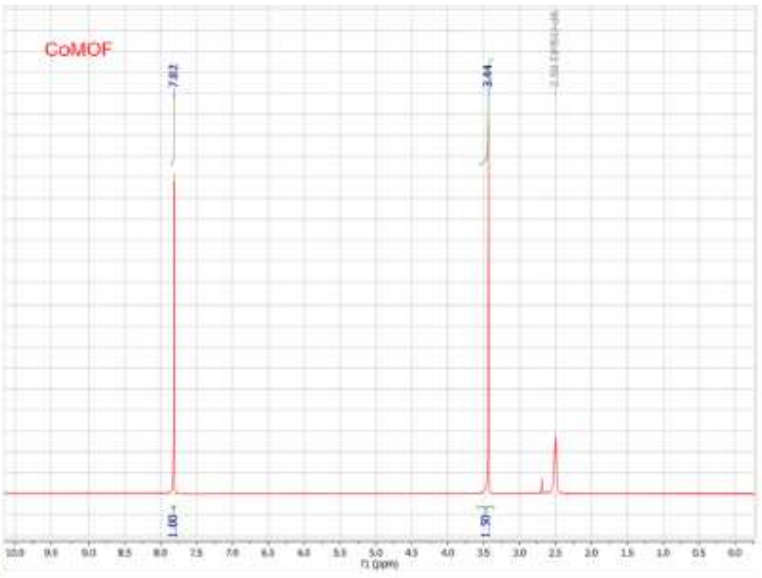

b)

Figure S4a,b. Solution ^{1}H NMR spectra (300 MHz) of digested a) NiMOF and b) CoMOF in DMSO-d_6 (2.50 ppm). The integration ratio of the H atoms on 1 DABCO ($C_6H_{12}N_2$) to the H atoms on 2 BDC (2 $C_6H_4(CO_2^-)_2$) of 12:8 matches the expected ratio of 1.5:1. For the ^{1}H-NMR experiments, 10 mg of the MOF samples were suspended in 0.7 mL DMSO-d_6 and digested by the addition of 20 µL of D_2SO_4 (98 wt.% in D_2O).

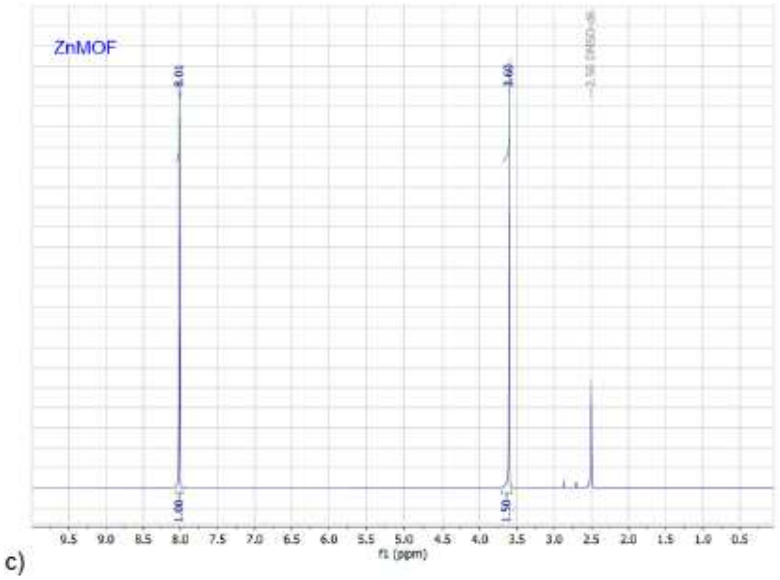

c)

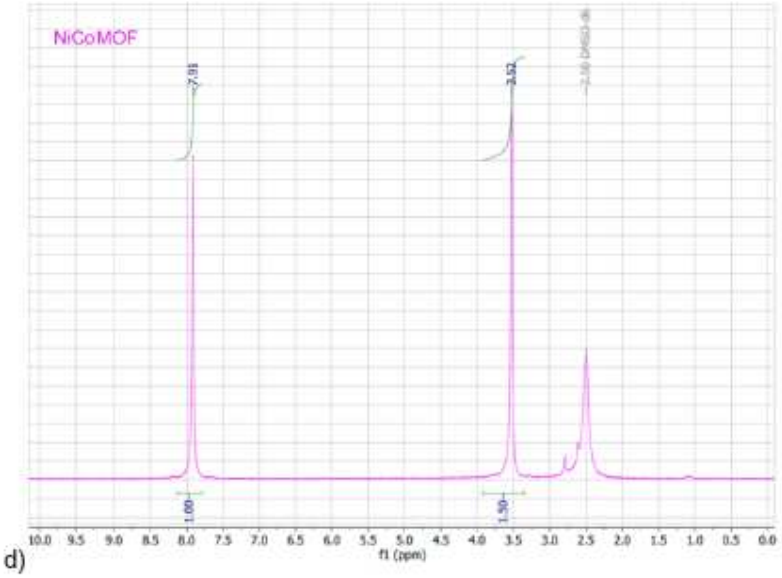

d)

Figure S4c,d. Solution ^{1}H NMR spectra (300 MHz) of digested c) ZnMOF and d) NiCoMOF in DMSO-d_6 (2.50 ppm). The integration ratio of the H atoms on 1 DABCO ($C_6H_{12}N_2$) to the H atoms on 2 BDC (2 $C_6H_4(CO_2^-)_2$) of 12:8 matches the expected ratio of 1.5:1. For the ^{1}H-NMR experiments 10 mg of the MOF samples were suspended in 0.7 mL DMSO-d_6 and digested by the addition of 20 µL of D_2SO_4 (98 wt.% in D_2O).

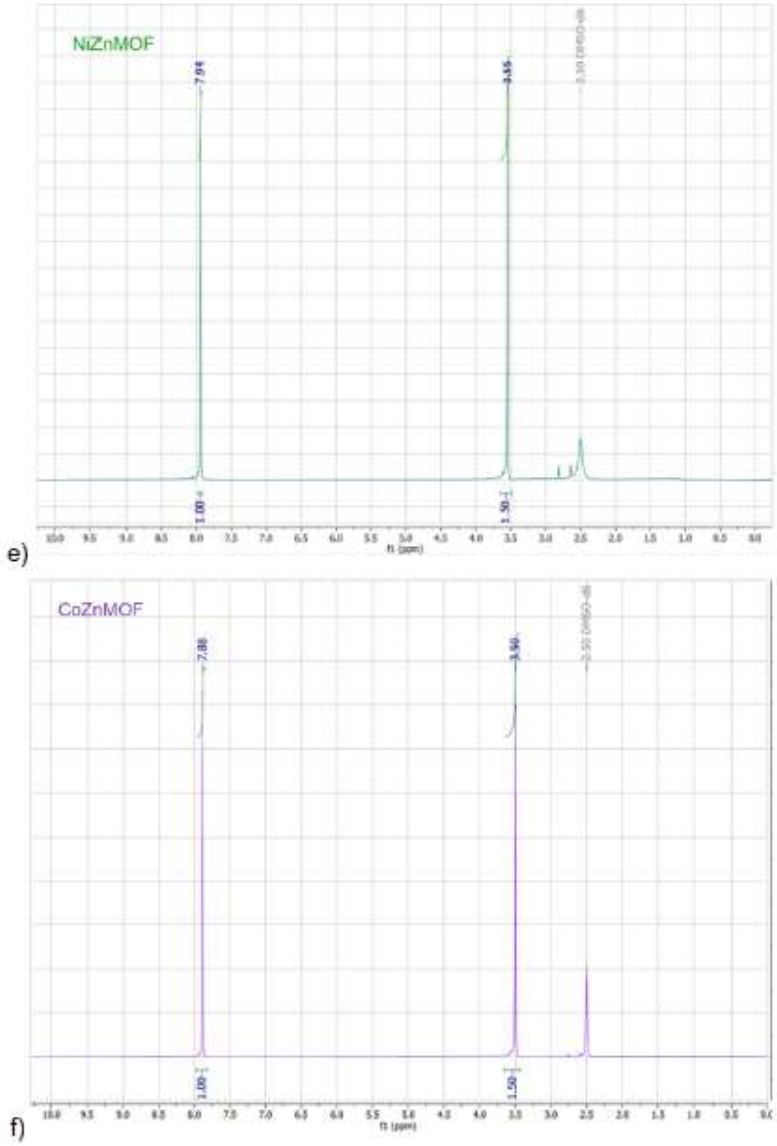

Figure S4e,f. Solution ^{1}H NMR spectra (300 MHz) of digested e) NiZnMOF and f) CoZnMOF in DMSO-d_6 (2.50 ppm). The integration ratio of the H atoms on 1 DABCO ($C_6H_{12}N_2$) to the H atoms on 2 BDC (2 $C_6H_4(CO_2^-)_2$) of 12:8 matches the expected ratio of 1.5:1. For the ^{1}H-NMR experiments 10 mg of the MOF samples were suspended in 0.7 mL DMSO-d_6 and digested by the addition of 20 µL of D_2SO_4 (98 wt.% in D_2O).

Table S3. BET-surface areas and total pore volumes of the M- and MM'MOF samples.

Material	BET surface area [a] ($m^2 g^{-2}$)	Total pore volume [b] ($cm^3 g^{-1}$)
NiMOF	1856	0.85
NiMOF-Literature[2]	1807	0.66
CoMOF	1838	0.76
CoMOF-Literature[4]	1501	0.70
ZnMOF	1547	0.57
ZnMOF-Literature[5]	1523	0.56
NiCoMOF	1611	0.66
NiZnMOF	1213	0.53
CoZnMOF	1223	0.52

[a] BET surface area calculated at $0.002 < p/p_0 < 0.15$ from the N_2 sorption isotherm 77 K with a standard deviation ± 20 $m^2 \cdot g^{-1}$. [b] The total pore volumes were determined at $p/p_0 = 0.95$ from the adsorption branch for the pores ≤ 25 nm.

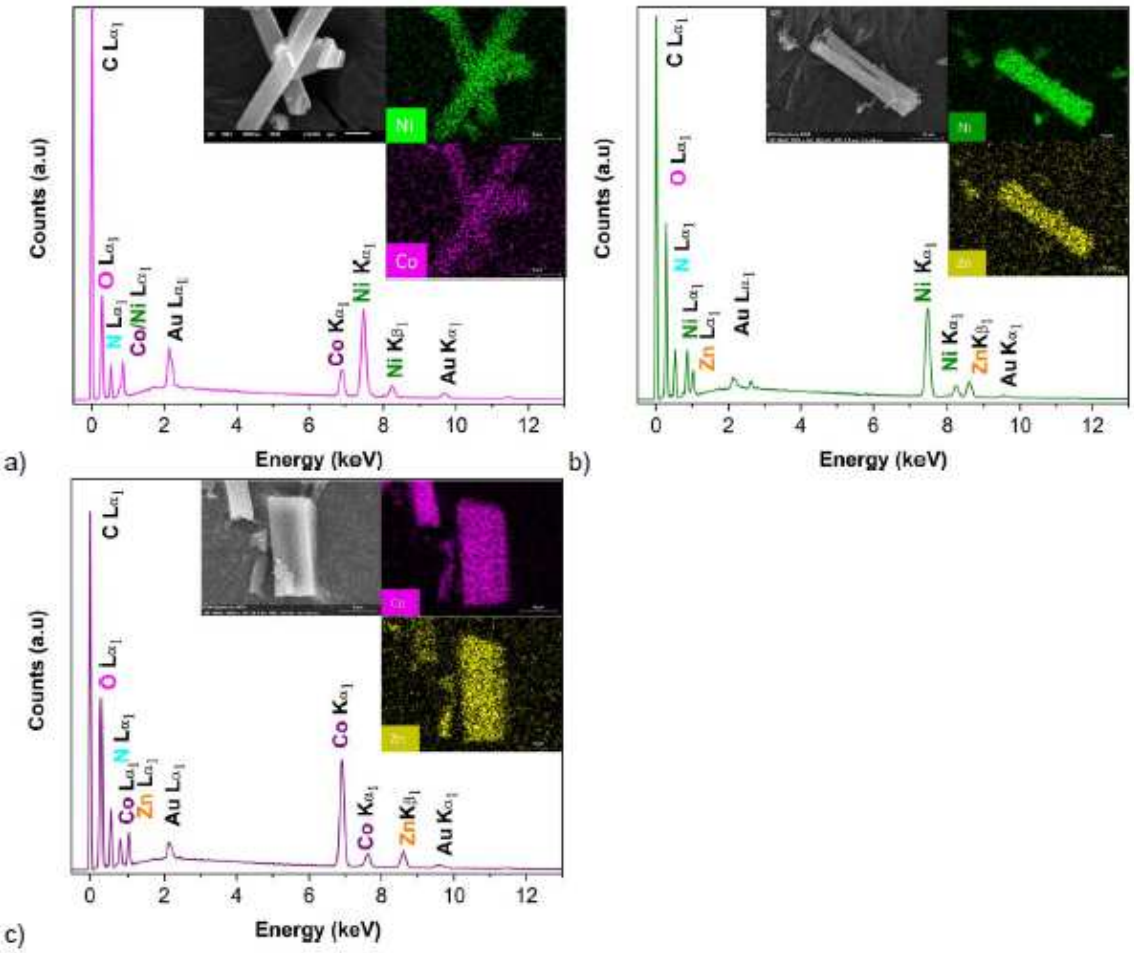

Figure S5. The energy dispersive X-ray spectra (SEM-EDX) and EDX scanning element mappings of a) NiCoMOF, b) NiZnMOF and c) CoZnMOF in the selected area of the given SEM image. The samples were gold-sputtered to ensure sufficient conductivity.

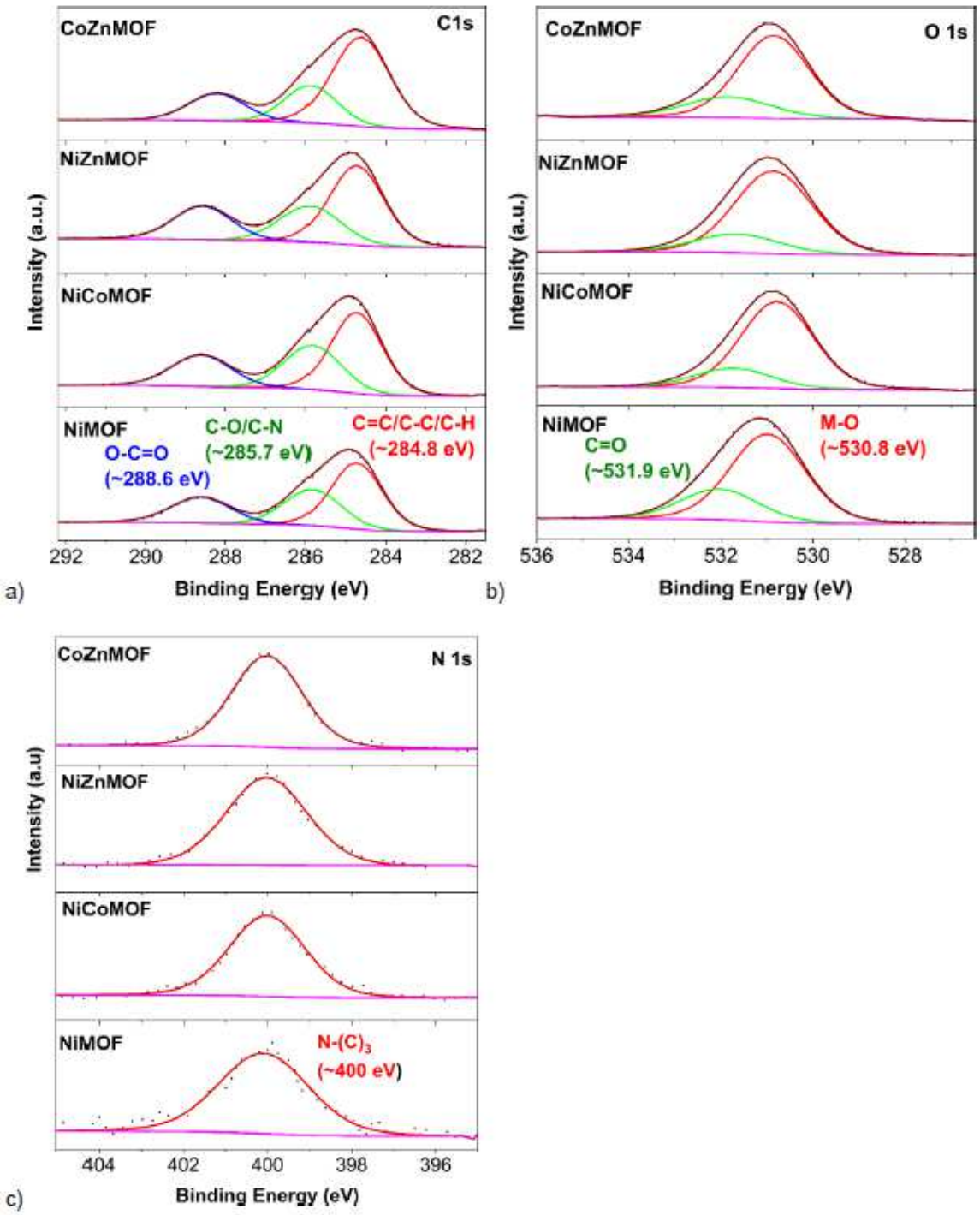

Figure S6. High-resolution X-ray photoelectron spectra (XPS) of a) C 1s, b) O 1s and c) N 1s of the monometallic and bimetallic MOFs.

The C 1s peaks observed at 284.3, 285.6, 286.7, 287.8, and 289.0 eV were related to C-C/C=C/C-H, C-O/C-N, C-O-C, C=O and O-C=O, respectively, in BDC. The O 1s peaks were observed at 530.8 and 531.9 eV, and these peaks were related to typical M-O-C bonds and C=O, respectively. The N 1s spectrum consists of one peak with a binding energy of 400 eV which corresponds to the presence of tertiary N, bonded to carbon ($N-C_3$),[6,7] as in DABCO.

Table S4. The molar metal ratio of the bimetallic MM'MOF materials according to SEM-EDX, AAS, XPS and stoichiometric (theoretical) ratio.

Sample [a]	M:M'	SEM-EDX	AAS	XPS	Theoretical
NiCoMOF	Ni:Co	4.0	4.0	3.9	4.0
NiZnMOF	Ni:Zn	3.8	3.7	3.6	4.0
CoZnMOF	Co:Zn	4.2	3.8	3.7	4.0

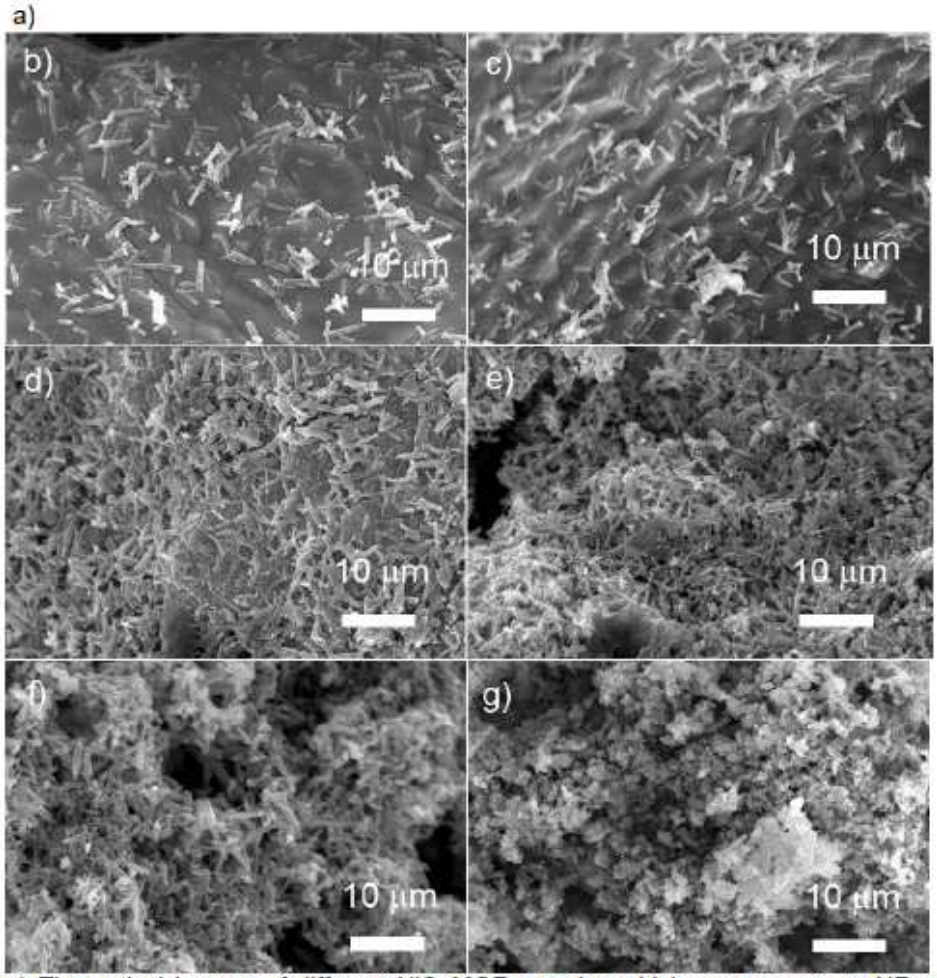

Figure S7. a) The optical images of different NiCoMOF samples which were grown on NF with different microwave heating times of 12, 15, 20, 25, 30 and 40 min corresponding to and yielding the different mass loading of 4.5, 12.6, 15.0, 16.6, 18.7 and 28.6 mg_{MOF}/g_{NF}, respectively. SEM image of b) NiCoMOF/NF-4.5, c) NiCoMOF/NF-12.65, d) NiCoMOF/NF-15.0, e) NiCoMOF/NF-16.6, f) NiCoMOF/NF-18.7 and g) NiCoMOF/NF-28.6 with 10 µm scale bars. These images b)-g) are given here enlarged from the inset images in Figure 6 in the main text.

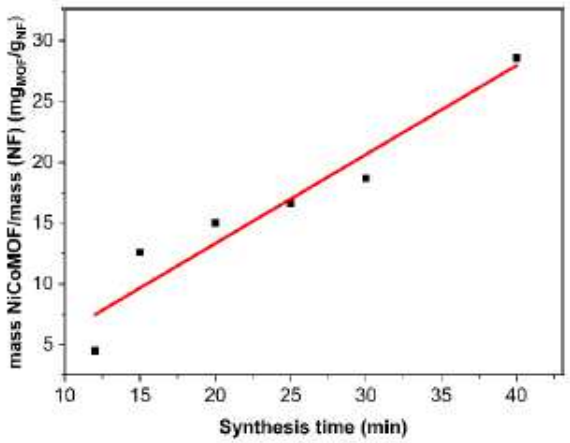

Figure S8. The curves of the $mass_{NiCoMOF}/mass_{NF}$ (mg_{MOF}/g_{NF}) versus additional microwave heating time (12, 15, 20, 25, 30, 40 min of common heating time before) (cf. Table S2).

Phase-pure β-(Ni,Co)(OH)$_2$ sample from NiCoMOF in KOH (1 mol L^{-1}) at 120 °C, denoted (NiCo)(OH)$_2$-120 °C

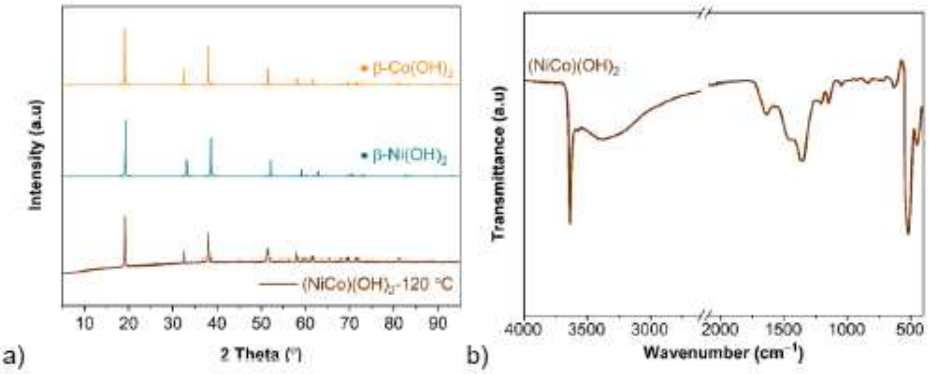

Figure S9. a) PXRD and b) FT–IR spectra of (NiCo)(OH)$_2$-120 °C. In the PXRD also the reflections from β–Ni(OH)$_2$ (ICDD 14-0117) and β-Co(OH)$_2$ (ICDD 30-0443) are included.

FTIR of the MOF-derived materials after thermal treatments (Figure S9b) shows two broad bands at ~3400 and ~3600 cm^{-1} which correspond to the stretching vibrations of adsorbed water molecules and to O–H stretching vibrations, as in metal hydroxide. The strong bands at 516 and 450 cm^{-1} are attributed to M-OH bending vibrations in M(OH)$_2$.[8]

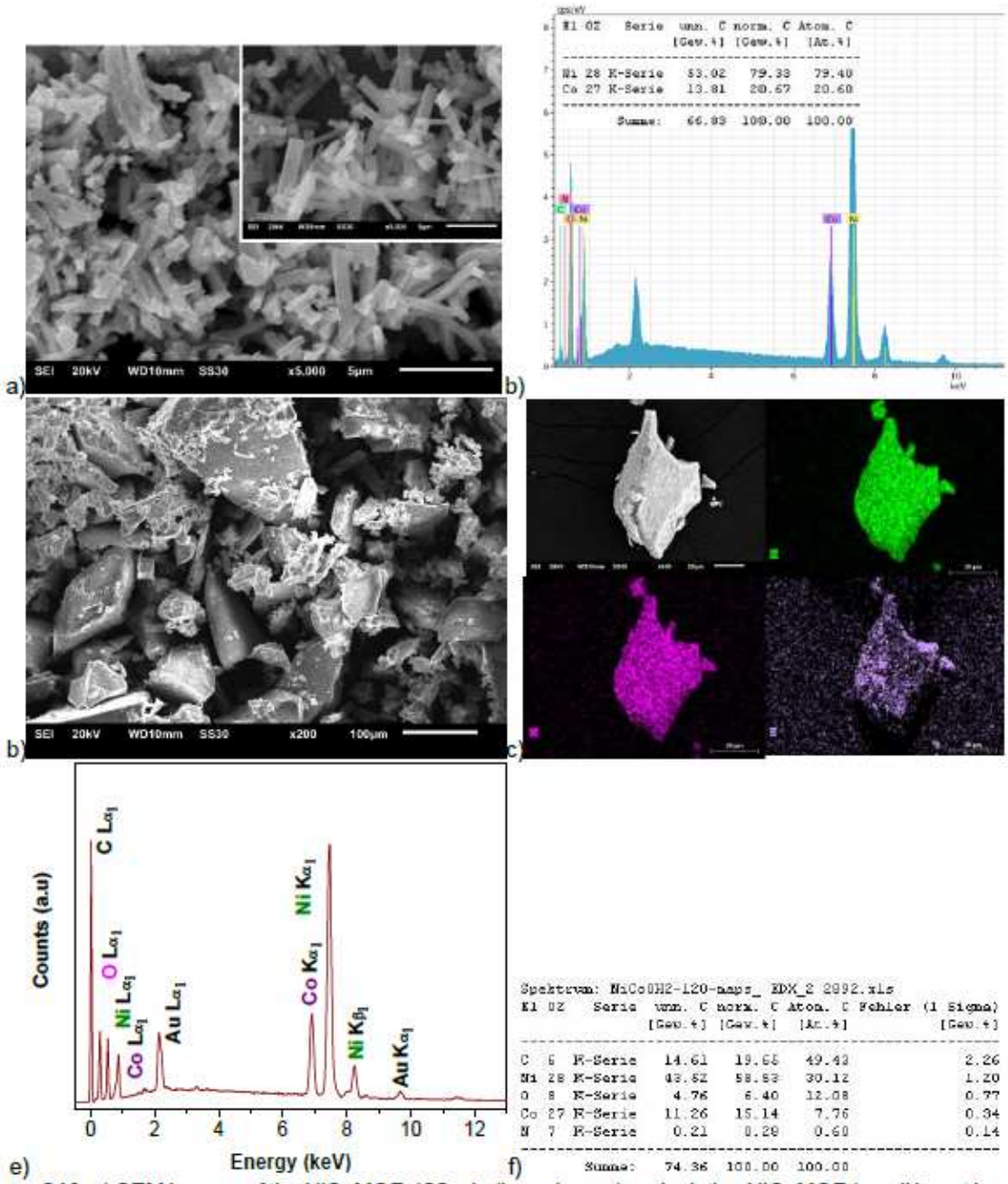

Spektrum: NiCoOH2-120-maps_ EDX_2 2892.xls

El	OZ	Serie	unn. C [Gew.%]	norm. C [Gew.%]	Atom. C [At.%]	Fehler (1 Sigma) [Gew.%]
C	6	K-Serie	14.61	19.65	49.43	2.26
Ni	28	K-Serie	43.82	58.83	30.12	1.20
O	8	K-Serie	4.76	6.40	12.08	0.77
Co	27	K-Serie	11.26	15.14	7.76	0.34
N	7	K-Serie	0.21	0.29	0.60	0.14
		Summe:	74.36	100.00	100.00	

Figure S10. a) SEM images of the NiCoMOF-120 min (large image) and pristine NiCoMOF (small insert image) after 120 min of KOH treatment time at room temperature. b) SEM-EDX of NiCoMOF-120 min. c) SEM image, d) EDX scanning element mappings and e) SEM-EDX of $(NiCo)(OH)_2$-120 °C in the selected area of the given EDX mapping. The samples were routinely gold-sputtered.

The morphology of $(NiCo)(OH)_2$-120 °C *via* scanning electron microscopy (SEM) is shown in Figure S10c. The rod shape of NiCoMOF (Figure 2 and Figure S10a) was still retained after the alkaline but not after the additional thermal treatment after which it changed into a shard-like topology in $(NiCo)(OH)_2$-120 °C (Figure S10c). The EDX scanning element mappings and SEM-EDX spectrum of $(NiCo)(OH)_2$-120 °C in Figure S10d,e revealed the uniform distribution of Ni, Co, and O throughout the derived particles. The molar ratio of Ni:Co ratio by SEM-EDX is: 3.9:1 which was also confirmed by an AAS measurement.

Electrochemical characterization of bimetallic MM'MOFs

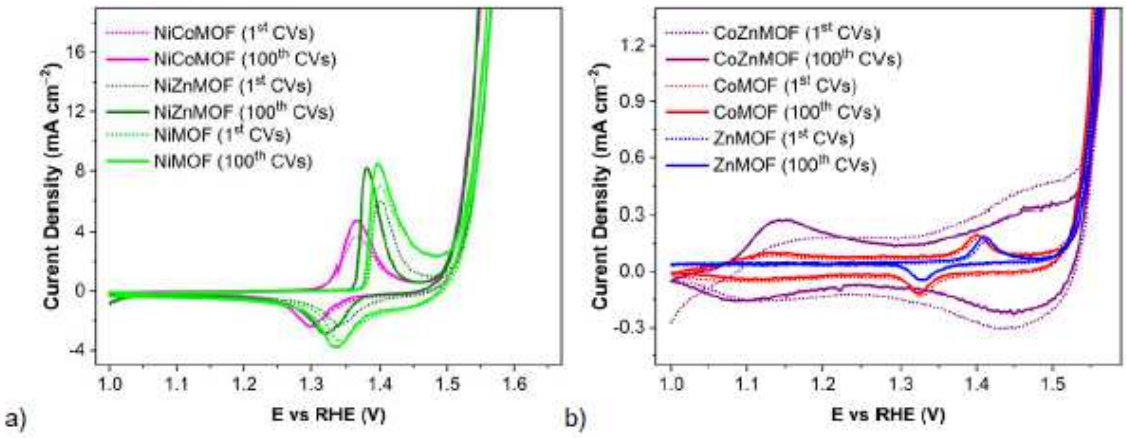

Figure S11. Comparison of CV curves collected after the 1st and 100th CV cycle for a) NiCoMOF, NiZnMOF and NiMOF and b) CoZnMOF, CoMOF and ZnMOF.

The polarization curves of the Ni-based MOFs were examined in 1 mol L^{-1} KOH at a scan rate of 10 mV s^{-1} (Figure S11a). Anodic peaks observed within the potential range of 1.25-1.45 V versus the reversible hydrogen electrode (RHE) signify the oxidation of Ni^{2+} to $Ni^{3+/4+}$.[9,10] This process happens together with the formation of the nickel surface (*) bound O*-radical (from a surface bound hydroxy radical, *OH) which is an essential intermediate and couples sequentically with two OH^- groups to generate the dioxygen, O_2 for the oxygen evolution:[10]

(active Ni^{2+} species on surface)* + $OH^- \rightarrow Ni^{2+}$-OH* + e^-

Ni^{2+}-OH* + $OH^- \rightarrow Ni^{3+}$-O* + H_2O + e^-

Ni^{3+}-O* + $OH^- \rightarrow Ni^{3+}$-OOH* + e^-

Ni^{3+}-OOH* + $OH^- \rightarrow Ni^{2+}$* + O_2 + H_2O + e^-

Notably, the Ni^{2+} to $Ni^{3+/4+}$ peak potential in the bimetallic NiCoMOF and NiZnMOF is altered as the metal atoms change from Co to Zn. This observation suggests that the two metals interact and this can effectively regulate the surface oxidation process, thereby influencing the OER activity. The pair of redox peaks within the potential region of ~1.1–1.2 V can be assigned to the Co^{2+}/Co^{3+} redox couple, whereas another pair of redox peaks within the potential region of ~1.35–1.55 V can be attributed to those of Co^{3+}/Co^{4+} (Figure S11b).[11,12] Notably, the anodic peaks in the CoZnMOFs are more defined to compare with its counterparts CoMOF and ZnMOF, indicating a significant active surface for electrocatalytic oxygen evolution.[13]

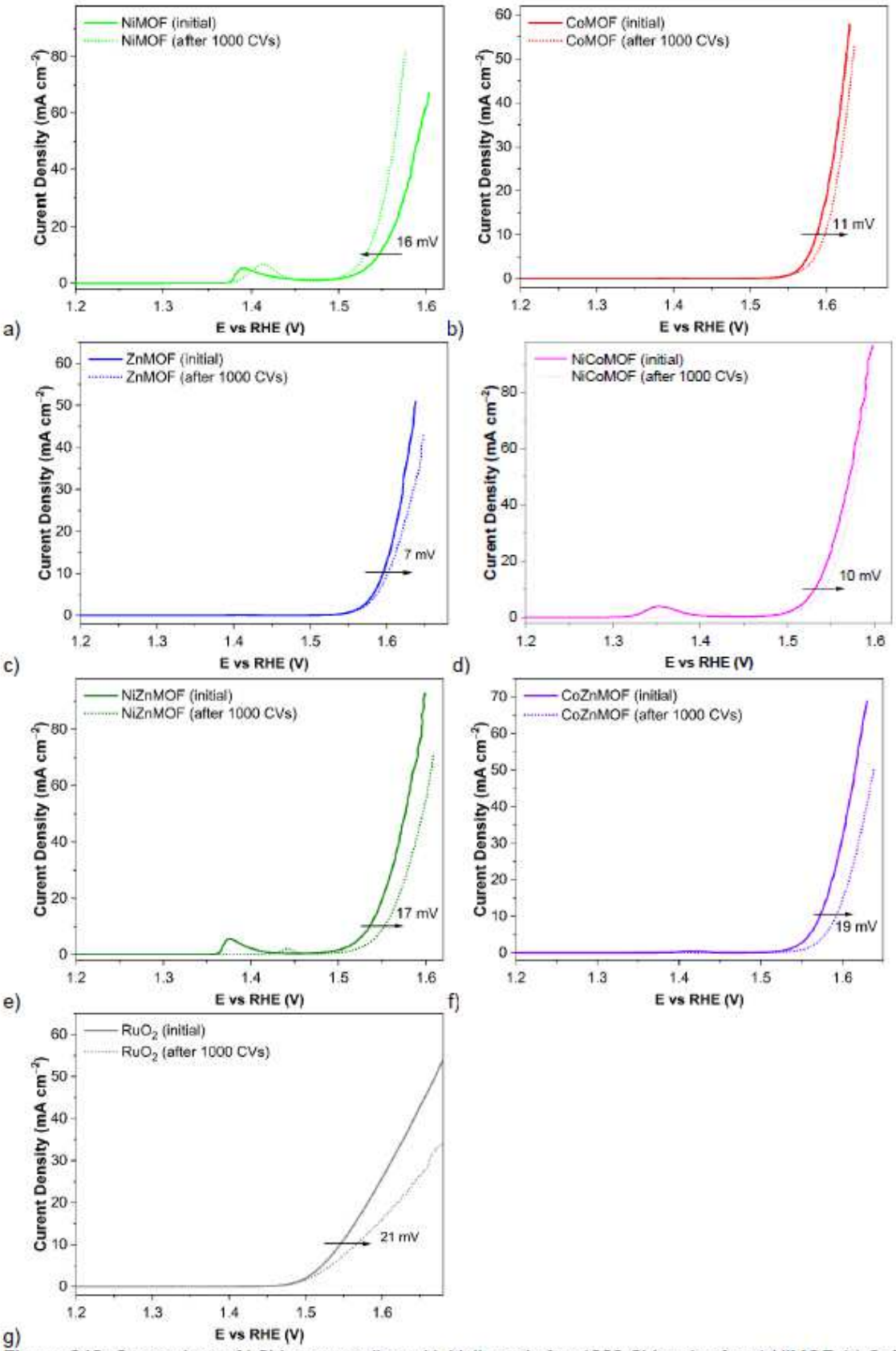

Figure S12. Comparison of LSV curves collected initially and after 1000 CV cycles for a) NiMOF, b) CoMOF, c) ZnMOF, d) NiCoMOF, e) NiZnMOF, f) CoZnMOF and g) RuO_2.

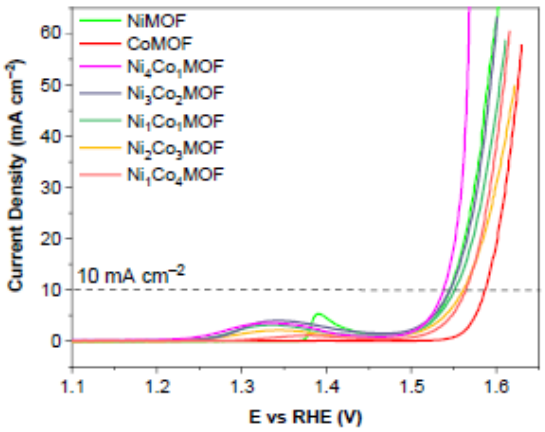

Figure S13. LSV polarization curves of as-synthesized monometallic Ni-, Co- and bimetallic NiCo-MOF with different Ni:Co molar ratios on RD-GCE at a scan rate of 5 mV s^{-1}.

Turnover frequency, TOF determination

For preparation of the active materials on the RD-GC electrode, there are 4.5 x 10^{-2} mg of NiMOF on the RD-GCE electrode with about 0.01 mg Ni element (n= 1.63 x 10^{-4} mmol) on the RD-GCE electrode (Faraday constant F = 96485 s A/mol).

The TOFs were determined using formula (4) which was already given above.

Taking the NiMOF as an example (equation (8)), the surface area of GC electrode (A) is 0.196 cm^{-2} and the current density (j) at an overpotential of 320 mV is 12.2 mA cm^{-2}.

$$TOF = \frac{12.2 \times 0.196}{4 \times 1.63 \times 10^{-4} \times 96485} s^{-1} = 0.038\ s^{-1} \quad (8)$$

Table S5. Summarized electrochemical data of monometallic and bimetallic MOFs after the electrochemical activation process.

Material	Overpotential (mV) (at 10 mA cm^{-2})	Tafel slope (mV dec^{-1})	R_p (Ω)	R_s (Ω)	R_{far} (Ω)	TOF (s^{-1}) at an overpotential of 320 mV
NiMOF	315	55	7	21	28	0.038
CoMOF	356	57	-	187	187	0.002
ZnMOF	365	61	-	275	275	0.002
NiCoMOF	301	42	1.5	10.7	12.2	0.074
NiZnMOF	306	46	1.6	14.3	15.9	0.062
CoZnMOF	342	50	-	122	122	0.009
RuO_2	315	91	-	23	23	-

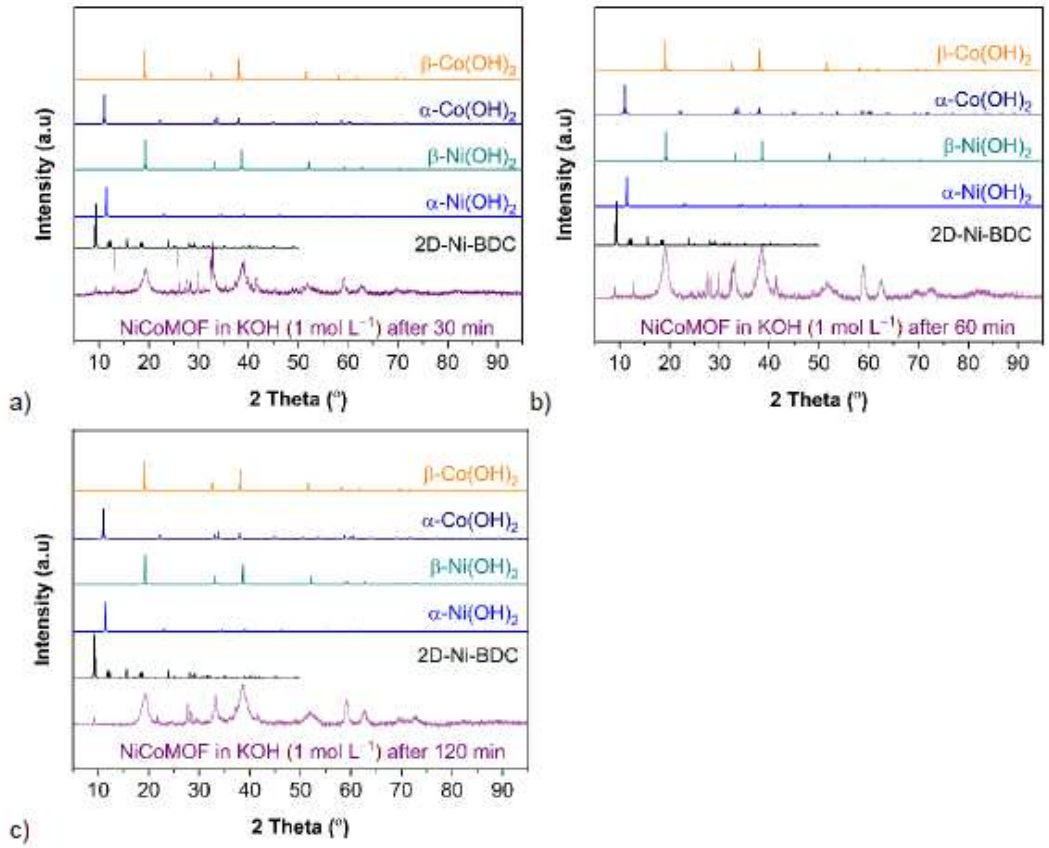

Figure S14. PXRD patterns of the experimentally derived metal oxide/hydroxides from NiCoMOF after a) 30 min, b) 60 min and c) 120 min in 1 mol L^{-1} KOH. For comparison the simulated diffractograms are given for 2D-NiBDC (CCDC Nr. 638866),[14] α–$Ni(OH)_2$ (ICDD: 38-0715), β–$Ni(OH)_2$ (ICDD: 14-0117), α–$Co(OH)_2$ (ICDD: 46-0605) and β-$Co(OH)_2$ (ICDD: 30-0443).

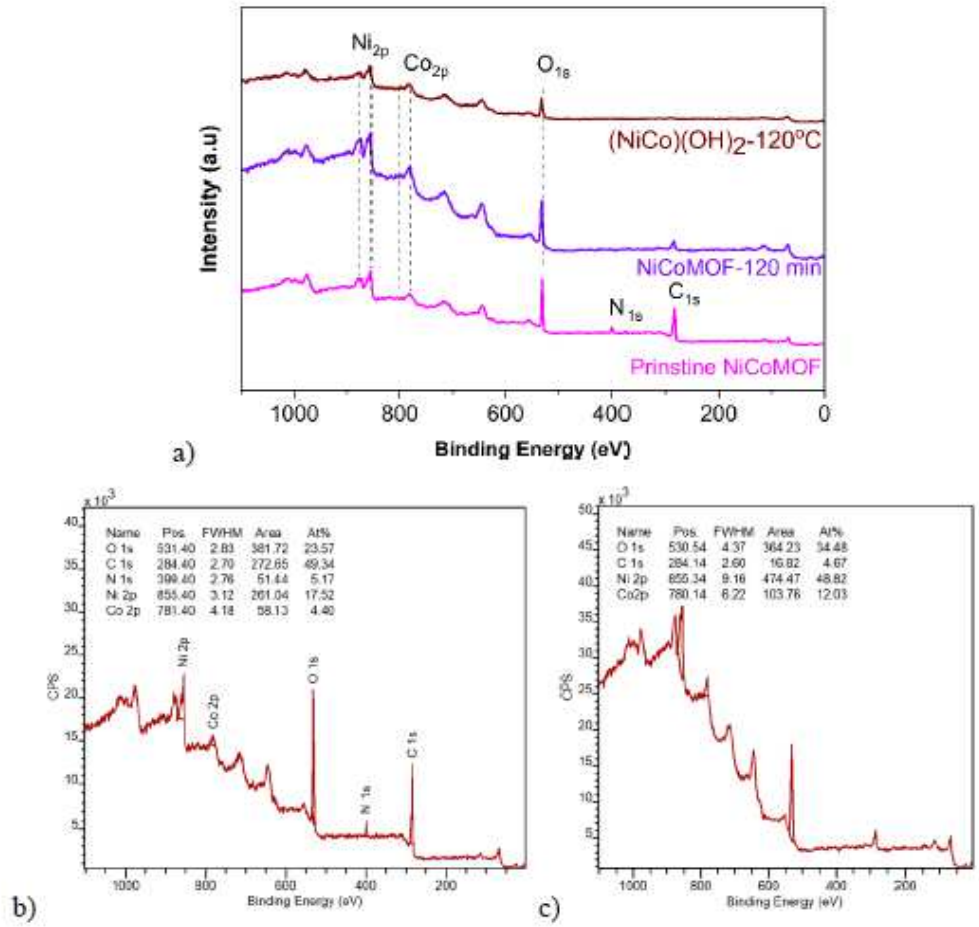

Figure S15. a) Survey XPS spectra of pristine NiCoMOF, NiCoMOF-120 min and $(NiCo)(OH)_2$-120 samples. b) Survey XPS spectrum of pristine NiCoMOF with quantitative contribution analysis. c) Survey XPS spectrum of NiCoMOF-120 min with quantitative contribution analysis. For comparison with the parallel CHN analysis the At% values in the diagrams were recalculated by assuming the presence of theoretical 3.61 at% H in b) and 2.17 at% H in c) because the hydrogen content cannot principally detected by XPS.

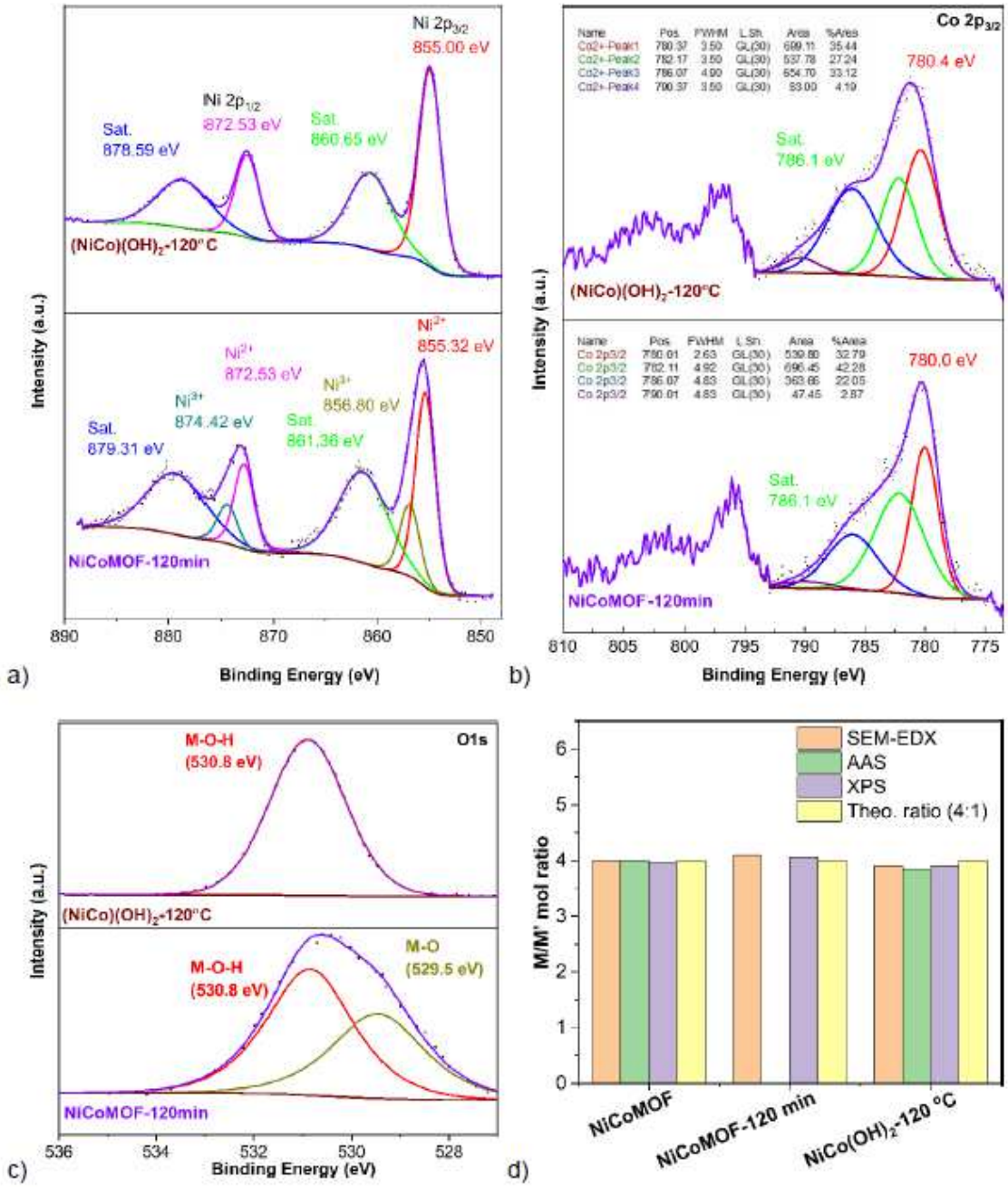

Figure S16. High-resolution XPS spectra of a) Ni 2p, b) Co 2p and c) O1s of NiCoMOF-120 min and $(NiCo)(OH)_2$-120 °C samples. d) Ni and Co composition of the NiCoMOF, NiCoMOF-120 min and $(NiCo)(OH)_2$-120 °C materials according to SEM-EDX, AAS, XPS and stoichiometric (theoretical) ratio.

The XPS survey spectrum of NiCoMOF-120 min and $(NiCo)(OH)_2$-120 °C in Figure S15 shows the presence of Ni, Co, C and O elements. The Ni 2p spectrum of the $(NiCo)(OH)_2$-120 °C sample in Figure S16a consists of two major peaks at ~855 eV (Ni $2p_{3/2}$) and ~872.5 eV (Ni $2p_{1/2}$) corresponding to Ni^{2+} and its shakeup satellites (denoted as "Sat."). With the oxidation state of Ni^{2+} a binding energy region of 855.0 or 855.3 eV is obtained. In the sample NiCoMOF-120 min also a peak at 856.8 eV can be fitted which corresponds to Ni^{3+}.[15]

Apparently, the presence of oxygen in the air induces minor oxidation together with the alkaline hydrolysis. However, upon subsequent thermal treatment, at 120 °C the Ni^{3+} is reduced again to Ni^{2+} which is the sole contribution fitted to the peak at 855.0 eV.[16]

The Co 2p (Figure S16b) spectrum includes two contributes at ~781 eV (Co $2p_{3/2}$) and 796 eV (Co $2p_{1/2}$), each with shake-up satellite peaks (~786 and ~801 eV). As noted in the main text, the oxidation state of cobalt cannot be unequivocally determined from the binding energies of the peaks. The fitting of the main Co $2p_{3/2}$ peak between 779-782 eV to two (or three) contributions cannot be assigned to the two oxidation states.[17,18,19] Instead, cobalt(III) oxides were distinguished from cobalt(II) oxides by the absence of the multielectron excitation satellite at 785-786 eV to the Co $2p_{3/2}$ line in the former. In Figure 4c the areas of the satellites for NiCoMOF, CoZnMOF and CoMOF (green curves) are between 32-34 % of the total Co $2p_{3/2}$ line with agreement with the presence of predominantly (if not solely) Co^{2+}.[18,19] For the sample of NiCoMOF-120 min in Figure S16b the area of the satellite at 786 eV is only 22 % of the total Co $2p_{3/2}$ line which upon comparison indicates the presence of partial Co^{3+},[18,19] in line with the Ni^{3+} found in the same sample. For $(NiCo)(OH)_2$-120 °C the satellite area at 785 eV is again 33% of the total Co $2p_{3/2}$ line suggesting the presence of mainly Co^{2+} which agrees with the sole finding of Ni^{2+} in this probe.

As shown in Figure S16c, the O 1s spectral contributions at the binding energy of 531.0 eV are assigned to metal hydroxide (M-O-H) in good agreement with PXRD results (Figure S9) and with previous results of $NiCo(OH)_2$.[20,21,22] The spectrum of O1s for the sample of NiCoMOF-120 can be de-convoluted into two peaks at 531.1 and 531.8 eV, that is, a contribution of metal oxide (M-O) can be fitted to the broad O 1s signal which is in agreement with the partial metal oxidation to Ni^{3+} and Co^{3+}, suggesting the presence of metal oxide/hydroxides. Again, this contribution disappears upon thermal treatment concomitant with reduction to Ni^{2+} and Co^{2+}

Furthermore, the Ni: Co atomic ratio of NiCoMOF, NiCoMOF-120min and $(NiCo)(OH)_2$-120 °C was detemined using XPS, AAS and EDX. As shown in Figure S16d and Figure S10, the Ni:Co atomic ratio (~4:1) of NiCoMOF before and after KOH treatment and after additional thermal treatment remained constant (cf. Table S6 and Figure S10).

Table S6. Element analysis of NiCoMOF materials before and after KOH treatment after 120 min (NiCoMOF-120 min) at room temperature according to combustion CHN and XPS.

Elements	Elemental analysis (wt %)		XPS (at %)		Theoretical (at %)	
	Before KOH treatment	After KOH treatment (120 min, RT)	Before KOH treatment	After KOH treatment (120 min, RT)	Before KOH treatment	$Ni_{0.8}Co_{0.2}(OH)_2$
C	46.48	0	47.6	4.5	47.11	0
H	3.55	3.98	n.a.	n.a.	3.61	2.17
N	4.94	0	5.0	0	5.00	0
O	-	-	22.7	33.2	22.95	34.52
Ni	-	-	16.9	47.1	16.8	50.6
Co	-	-	4.2	11.6	4.2	12.7

n.a. = not available as H cannot be detected by XPS.

The strong decrease of At% of carbon and nitrogen to zero in the CHN analysis after the KOH treatment indicates the complete removal of the organic linkers from the derived metal hydroxide by dissolution into the alkaline medium with 1 mol L^{-1} KOH.

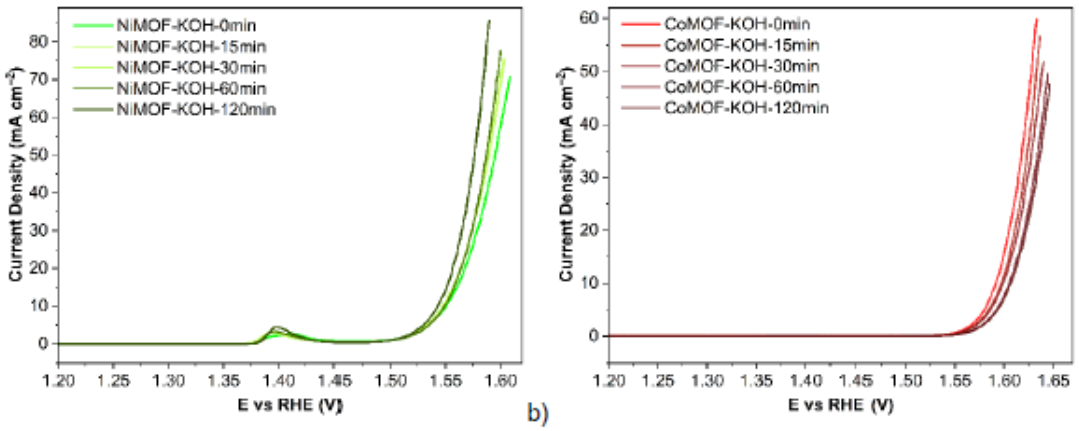

Figure S17. Polarization curves of a) NiMOF and b) CoMOF-coated electrodes (RD-GCE) in the electrolyte KOH (1 mol L^{-1}) after different pre-treatment times of 0, 15, 30, 60 and 120 min without applying a potential.

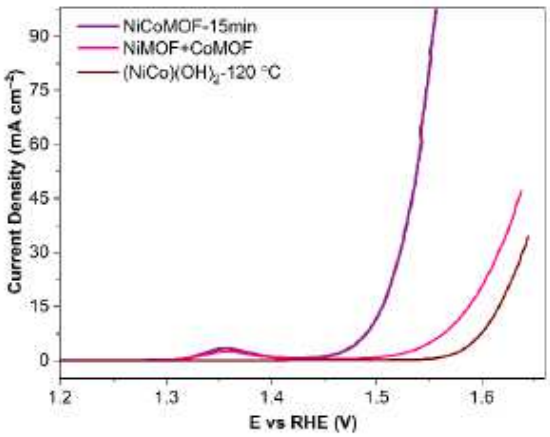

Figure S18. Polarization curves of the catalysts derived from NiCoMOF after 15 min in KOH 1 mol L^{-1} at room temperature, from a physical mixture of NiMOF+CoMOF (named as NiMOF+CoMOF) with Ni:Co molar ratio 4:1 and from $(NiCo)(OH)_2$-120°C. The $(NiCo)(OH)_2$-120°C was obtained by immersing 30 mg of the NiCoMOF in 30 mL of 1 mol L^{-1} KOH solution at a temperature of 120 °C for 24 h (see above). All samples were conditioned before the LSV measurement with the same pre-treatment time in KOH of 15 min and 100 CVs for precatalytic activation.

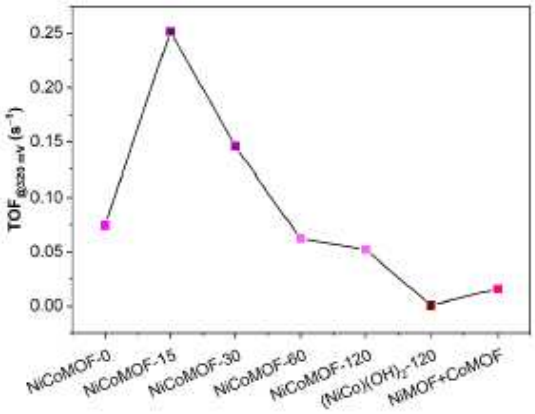

Figure S19. TOF values of the MOF-derived electrocatalysts at an overpotential of 320 mV of NiCoMOF after pre-treatment times in KOH of 0, 15, 30, 60 and 120 min, of $(NiCo)(OH)_2$-120°C and of the physical mixture of NiMOF+CoMOF.

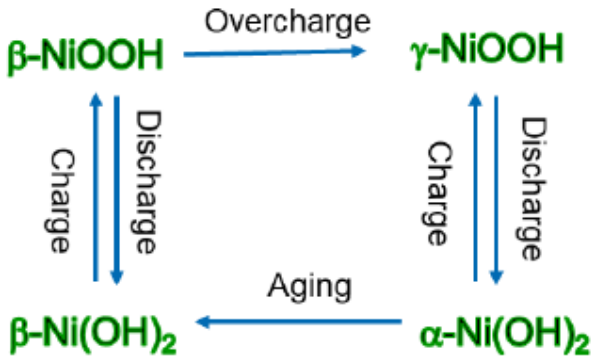

Figure S20. Bode scheme for the transformation of $Ni(OH)_2$/NiOOH

The Bode scheme [23] describes the transformations among the phases during the OER process, in which the Ni oxidation state changes from Ni(II) in $Ni(OH)_2$ to Ni(III) in NiOOH and back from NiOOH to $Ni(OH)_2$ in an alkaline solution. For instance, when β-$Ni(OH)_2$ is oxidized it also loses a proton (H^+) to become β-NiOOH. A different situation occurs between α-$Ni(OH)_2$ and γ-NiOOH, where α-$Ni(OH)_2$ endures an aging effect and transforms into β-$Ni(OH)_2$ in alkaline solution. Under long-term overcharging, β-NiOOH is also transformed into γ-NiOOH.

Electrochemical characterization NiCoMOF/NF

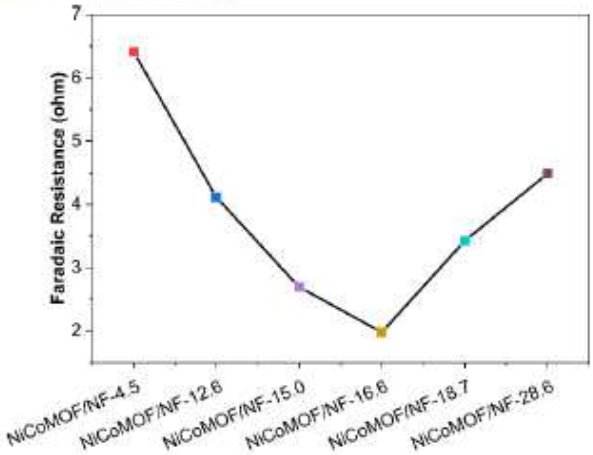

Figure S21. Fitted values of resistances of NiCoMOF/NF with different mass loading of 4.5, 12.6, 15.0, 16.6, 18.7 and 28.6 mg of MOF per g of NF

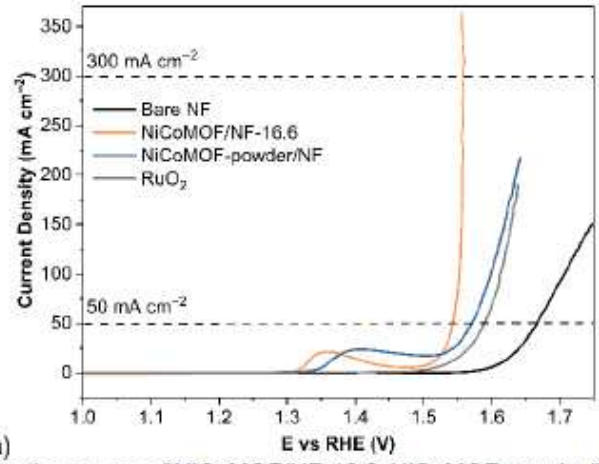

a)

Figure S22. The LSV polarization curves of NiCoMOF/NF-16.6, NiCoMOF-powder/NF, RuO_2/NF and bare NF. NiCoMOF powder and commercial RuO_2 coated on NF were named NiCoMOF-powder/NF and RuO_2/NF, respectively. All electrodes had a similar loading on NF with 16.6 mg_{MOF}/g_{NF}.

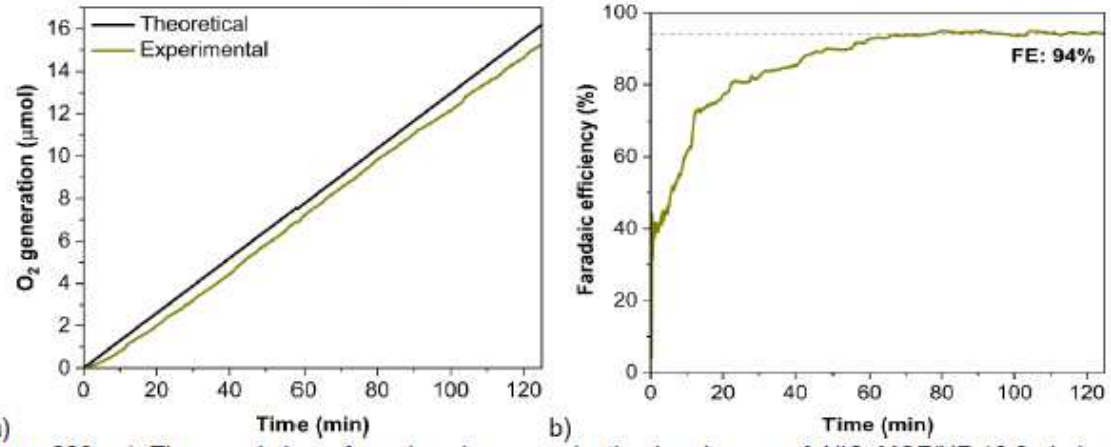

a) b)

Figure S23. a) Time evolution of produced oxygen in the headspace of NiCoMOF/NF-16.6 during a chronopotentiometry at the constant current density of 50 mA cm^{-2} for 2 h and comparison to the theoretical value when assuming 100% faradaic efficiency. b) The O_2 production reached a steady state condition after about 1 h of the chronopotentiometry test. This corresponds to a 94% faradaic efficiency.

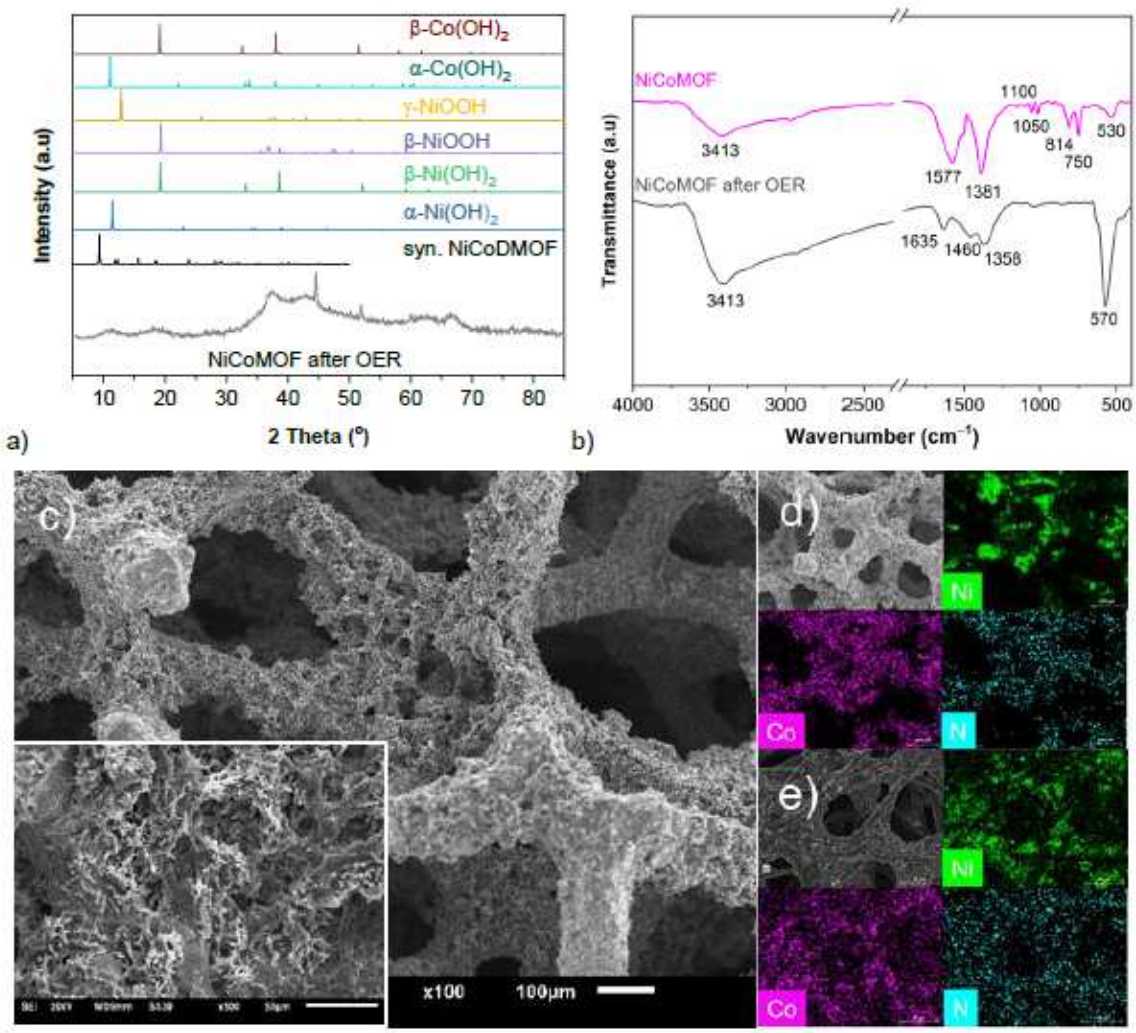

Figure S24. a) PXRD, b) FTIR of NiCoMOF powder, c) SEM images and d) EDX-mapping NiCoMOF/NF-15 min. (e) SEM with EDX-mapping of NiCoMOF/carbon cloth after the chronopotentiometry (CP) test over 50 h.

The FTIR of the NiCoMOF after 50 h of chronopotentiometry (CP) test showed two broad bands at around 3400-3600 cm^{-1}, which correspond to the stretching vibrations of the adsorbed water molecules and to the O-H stretching vibrations as in $(NiCo)(OH)_2$. New absorption bands appear at 1635, 1460 and 1358 cm^{-1} which is assigned to the banding vibrations of the adsorbed water molecules of δO-H hydroxyl group. The bands at 1100 cm^{-1} and 1055 cm^{-1} could be due to the ν_{as}C-N and ν_{as}C-N vibrations of DABCO virtually disappeared as did the bands at 814 cm^{-1} and 750 cm^{-1}, which correspond to the $\nu(C\text{-}C)_{Ar}$ and $\delta(C\text{-}H)_{Ar}$ vibrations of the BDC linker, respectively. The absorption band at 570 cm^{-1} are assigned to the M–O stretching vibration for due to the formation of metal oxide/hydroxides.

Table S7. Comparison of NiCo-based electrocatalysts for OER.

Catalysts [a]	Substrate	Overpotential (mV) [b]	Synthesis time (h)	Ref.
NiCoMOF	RD-GCE	H_{10}: 301	0.2	This work
NiCoMOF/NF-16.6	NF	η_{50}: 313	0.42	This work
PVP4%-CoNi-MOF-74	GCE	η_{10}: 310	0.3	[24]
NiCoMOF/CF-40L	CF	η_{50}: 287	23.3	[25]
$Ni_{0.5}Co_{0.5}$-MOF-74	RD-GCE	η_{10}: 270	3	[26]
NiCoMOF	NF	η_{10}: 316	12	[27]
NiCoBDC	CF	η_{10}: 281	12	[28]
NiCoBDC-NH_2	CF	η_{10}: 281	12	
NiCoBTC	CF	η_{10}: 245	12	
NiCoNDC	CF	η_{10}: 288	12	
NiCo-DOBDC	CF	η_{10}: 261	12	
NiCoHYDC	CF	η_{10}: 303	12	
Ni_{10}CoBTC	GCE	η_{10}: 378	48	[29]
NiCoMOF	NF	η_{50} : 270	12	[30]
2D-CoNi-single-layer $(NiCo)_2BDC_2DABCO)$	CC	η_{10} : 825	48	[31]
NiCoMOF/NF	NF	η_{50}: 339	24	[32]
NiCoP/NC-1:1	GCE	η_{10}: 330	5.5	[33]
NiCoMOF	NF	η_{30}:425	3	[34]
NiCoMOF/CC	CC	η_{50}: 325	4	[35]
NiCo-MOF	NF	η_{50}: 320	12	[36]
NiCoMOF/NF	NF	η_{50}:343	12	[37]
$NiCo_2O_4$/NF	NF	η_{50}:332	8	[38]
NiCoFe/Ni-BDC-NF	NF	η_{50}:450	24	[39]
$CoNi_{0.48}$MOF/CFP	CFP	η_{50}:296	12	[40]
$Ni_{0.7}Co_{1.4}(Se_{0.85}O_{0.15})_4$	NF	η_{50}: 335	6	[41]

[a] RD-GCE: rotating disk glassy carbon electrode, GCE: Glassy carbon electrode, NF: nickel foam, CF: Cu foam, CC: Carbon cloth, CFP: carbon fiber paper; CF: Carbon fiber, η_{50} : at a current density of 50 mA cm^{-2}, η_{10}: at a current density of 10 mA cm^{-2}

[b] in 1 mol L^{-1} KOH electrolyte.

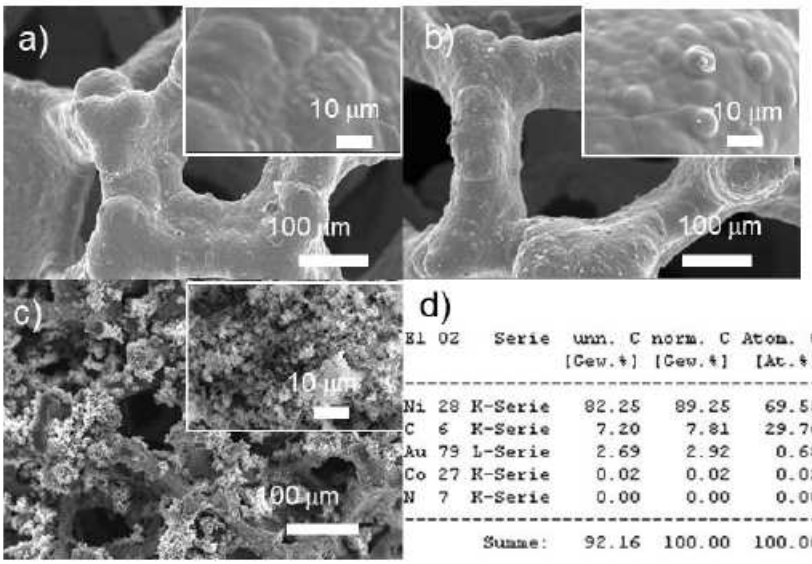

d)

El	OZ	Serie	unn. C [Gew.%]	norm. C [Gew.%]	Atom. C [At.%]
Ni	28	K-Serie	82.25	89.25	69.55
C	6	K-Serie	7.20	7.81	29.76
Au	79	L-Serie	2.69	2.92	0.68
Co	27	K-Serie	0.02	0.02	0.02
N	7	K-Serie	0.00	0.00	0.00
		Summe:	92.16	100.00	100.00

Figure S25. SEM image of a) bare NF, b) BDC-DABCO/NF and c) NiCoMOF/NF-4.5. d) SEM-EDX listing of BDC-DABCO/NF. The synthesis time for BDC-DABCO/NF was 40 min at 120 °C. The samples were routinely gold-sputtered. The carbon in BDC-DABCO/NF in the SEM-EDX listing results from the carbon-tape which was used for sample deposition.

References

[1] K. Brandenburg, Diamond 4.6, Crystal and Molecular Structure Visualization. Copyright 1997-2022 Crystal Impact GbR, Bonn, Germany. Available online: https://www.crystalimpact.com/diamond/ (accessed on 10 August 2022).

[2] P. Maniam, N. Stock, *Inorg. Chem.* **2011**, *50*, 5085–5097.

[3] F. Zou, S. L. Chao, Y. X. Wang, Y. L. Wang, Q. X. Guan, W. Li, *Environ. Sci. Nano* **2017**, *4*, 46–51.

[4] J. Long, K. Shen, L. Chen, Y. Li, *J. Mater. Chem. A* **2016**, *4*, 10254–10262.

[5] J. Guerrero-Medina, G. Mass-González, L. Pacheco-Londoño, S. P. Hernández-Rivera, R. Fu, A. J. Hernández-Maldonado, *Microporous Mesoporous Mat.* **2015**, *212*, 8–17.

[6] Y. Jiao, C. Qu, B. Zhao, Z. Liang, H. Chang, S. Kumar, R. Zou, M. Liu, K. S. Walton, *ACS Appl. Energy Mater.* **2019**, *2*, 5029–5038.

[7] Y. Wu, X. Song, S. Xu, Y. Chen, O. Oderinde, L. Gao, R. Wei, G. Xiao, *Dalton Trans.* **2020**, *49*, 312–321.

[8] P. Xu, X. J. Han, B. Zhang, Z. S. Lv, X. R. Liu, *J. Alloys Compd.* **2007**, *436*, 369–374.

[9] O. Diaz-Morales, D. Ferrus-Suspedra, M. T. M. Koper, *Chem. Sci.* **2016**, *7*, 2639–2645.

[10] J. Yan, L. Kong, Y. Ji, J. White, Y. Li, J. Zhang, P. An, S. Liu, S.-T. Lee, T. Ma, *Nat. Commun.* **2019**, *10*, 2149.

[11] S. Palmas, F. Ferrara, A. Vacca, M. Mascia, A. M. Polcaro, *Electrochim. Acta* **2007**, *53*, 400–406.

[12] E. Castro, C. Gervasi, *Int. J. Hydrogen Energy.* **2000**, *25*, 1163–1170.

[13] X. Liu, Z. Chang, L. Luo, T. Xu, X. Lei, J. Liu, X. Sun, *Chem. Mater.* **2014**, *26*, 1889–1895.

[14] A. Carton, A. Mesbah, T. Mazet, F. Porcher, M. François, *Solid State Sci.* **2007**, *9*, 465–471.

[15] X. Yu, J. Zhao, L.-R. Zheng, Y. Tong, M. Zhang, G. Xu, C. Li, J. Ma, G. Shi, *ACS Energy Lett.* **2018**, *3*, 237–244.

[16] X. Yi, V. Celorrio, H. Zhang, N. Robertson, C. Kirk, *J. Mater. Chem. A* **2023**, *11*, 22275–22287.

[17] J. Yang, H. Liu, W. N. Martens, R. L. Frost, *J. Phys. Chem. C* **2010**, *114*, 111-119.
[18] M. C. Biesinger, B. P. Payne, A. P. Grosvenor, L. W. Lau, A. R. Gerson, R. S. Smart, *Appl. Surf. Sci.* **2011**, *257*, 2717–2730.
[19] R. Lontio Fomekong, P. Kammi Yontchoum, T. J. Matemb Ma Ntep, H. M. Tedjieukeng Kamta, P. Kenfack Tsobnang, S. Krüger, J. Šturala, Z. Sofer, C. Janiak, B. Saruhan, A. Delcorte, J. N. Lambi, *Adv. Energy Sustainability Res.* **2024**, *5*, 2300232.
[20] M. C. Biesinger, B. P. Payne, L. W. M. Lau, A. Gerson, R. C. St. Smart, *Surf. Interface Anal.* **2009**, *41*, 324–332.
[21] N. Song, S. Hong, M. Xiao, Y. Zuo, E. Jiang, C. Li, H. Dong, *J. Colloid Interface Sci.* **2021**, *582*, 535–542.
[22] Y. Yang, M. Zhou, W. Guo, X. Cui, Y. Li, F. Liu, P. Xiao, Y. Zhang, *Electrochim. Acta* **2015**, *174*, 246–253.
[23] H. Bode, K. Dehmelt, J. Witte, *Electrochim. Acta* **1966**, *11*, 1079–1087.
[24] Q. Chen, Z. Xue, F. Wei, Q. Cheng, R. Wang, T. Hu, C. Guan, B. Ouyang, S. Xu, B. Fan, X. Li, *Int. J. Hydrogen Energy.* **2024**, *51*, 1327–1336.
[25] D.-J. Li, Q.-H. Li, Z.-G. Gu, J. Zhang, *J. Mater. Chem. A* **2019**, *7*, 18519–18528.
[26] S. Zhao, C. Tan, C.-T. He, P. An, F. Xie, S. Jiang, Y. Zhu, K.-H. Wu, B. Zhang, H. Li, J. Zhang, Y. Chen, S. Liu, J. Dong, Z. Tang, *Nat. Energy* **2020**, *5*, 881–890.
[27] W. Li, H. Zhang, K. Zhang, Z. Cheng, H. Chen, G. Tan, X. Feng, L. Wang, S. Mu, *Chem. Commun.* **2023**, *59*, 4750–4753.
[28] J. Zhou, Z. Han, X. Wang, H. Gai, Z. Chen, T. Guo, X. Hou, L. Xu, X. Hu, M. Huang, S. V. Levchenko, H. Jiang, *Adv. Funct. Mater.* **2021**, *31*, 2102066.
[29] L. Sondermann, W. Jiang, M. Shviro, A. Spieß, D. Woschko, L. Rademacher, C. Janiak, *Molecules* **2022**, *27*.
[30] P. Thangasamy, S. Shanmuganathan, V. Subramanian, *Nanoscale Adv.* **2020**, *2*, 2073–2079.
[31] W. Pang, B. Shao, X.-Q. Tan, C. Tang, Z. Zhang, J. Huang, *Nanoscale* **2020**, *12*, 3623–3629.
[32] T. Sun, S. Lin, Z. Xu, L. Li, *CrystEngComm* **2021**, *23*, 7650–7657.
[33] D. Chen, J. Luo, Q. Sun, C. Han, Q. Li, J. Qian, *Int. J. Hydrogen Energy.* **2022**, *47*, 18700–18707.
[34] D. Liu, H. Xu, C. Wang, H. Shang, R. Yu, Y. Wang, J. Li, X. Li, Y. Du, *Inorg. Chem.* **2021**, *60*, 5882–5889.
[35] J. Wu, Z. Yu, Y. Zhang, S. Niu, J. Zhao, S. Li, P. Xu, *Small* **2021**, *17*, 2105150.
[36] M. Jothi, P. Gnanasekar, J. Kulandaivel, *Energy & Fuels* **2022**, *36*, 13713–13721.
[37] D. Xiong, M. Gu, C. Chen, C. Lu, F.-Y. Yi, X. Ma, *J. Chem. Eng.* **2021**, *404*, 127111.
[38] H. Chen, S. Qiao, J. Yang, X. Du, *Mol. Catal.* **2022**, *518*, 112086.
[39] E. Sadeghi, N. S. Peighambardoust, S. Chamani, U. Aydemir, *ACS Mater. Au* **2023**, *3*, 143–163.
[40] S. Zhang, D. Lv, A. Zhou, Di Wang, D. Cai, *J. Alloys Compd.* **2023**, *943*, 169091.
[41] S. Abdpour, L. Rademacher, M. N. A. Fetzer, T. H. Beglau, C. Janiak, *Solids* **2023**, *4*, 181–200.

3.4. Co-Author contributions

X-ray Photoelectron Spectroscopy (XPS) and SEM measurements were performed.

Metal–organic framework structures of fused hexagonal motifs with cuprophilic interactions of a triangular Cu(i)$_3$(pyrazolate-benzoate) metallo-linker.

Saskia Menzel, Tobias Heinen, Ishtvan Boldog, Thi Hai Yen Beglau, Shanghua Xing, Alex Spieß, Dennis Woschko, Christoph Janiak. *CrystEngComm* ***2022****, 24, 3675–3691.*

Summary:

In this work, the reaction of the N,O-heteroditopic bifunctional ligand 4-(3,5-dimethyl-1H-pyrazol-4-yl)benzoic acid (H_2- mpba) with CuIJNO$_3$)$_2$·2.5H$_2$O and ZnIJNO$_3$)$_2$·4H$_2$O or ZnIJCH$_3$COO)$_2$·2H$_2$O in DMF results in concomitant formation of three difference bimetallic MOFs with open structures, [Me$_2$NH$_2$]ijZn$_4$(CuI $_3$IJmpba)$_3$}$_3$IJMe$_2$NH)-(DMF)$_2$] (1), [Zn$_6$(CuI $_3$IJmpba)$_3$}$_4$IJDMF)$_5$] (2) and [Zn$_3$(CuI $_3$IJmpba)$_3$}$_2$IJDMF)$_3$-IJH$_2$O)]ijZn$_4$IJμ$_4$-O){CuI $_3$IJmpba)$_3$}$_2$IJH$_2$O)$_4$] (3). The in situ formed softer CuI atoms coordinate with the softer pyrazolate nitrogen donor atoms of the pyrazolate–carboxylate ligand, leaving the carboxylate groups for linking to the Zn atoms.

Own contribution to the publication:

- Performing XPS measurements
- Evaluation and interpretation of the XPS spectra with CasaXPS software
- Preparing graphs and literature research for the related XPS part in the manuscript
- Reviewing and correcting the final manuscript as a co-author

Synthesis and Characterization of a Crystalline Imine-Based Covalent Organic Framework with Triazine Node and Biphenyl Linker and Its Fluorinated Derivate for CO_2/CH_4 Separation.

Stefanie Bügel, Malte Hähnel, Tom Kunde, Nader de Sousa Amadeu, Yangyang Sun, Alex Spieß, Thi Hai Yen Beglau, Bernd M. Schmidt, Christoph Janiak. *Materials* **2022**, *15*, 2807.

Summary:

A catalyst-free Schiff-Base- reaction was used to synthesise two imine-linked covalent organic frameworks (COFs). The condensation reaction of 1,3,5-tris-(4-aminophenyl)triazine (TAPT) with 4,4′-biphenyldicarboxaldehyde led to the structure of HHU-COF-1 (HHU = Heinrich Heine University). The fluorinated analogue HHU-COF-2 was obtained with 2,2′,3,3′,5,5′,6,6′-octafluoro-4,4′-biphenyldicarboxaldehyde. Solid-state NMR, IR, XPS and elemental analysis confirmed the successful formation of the two network structures. The crystalline materials are characterised by high BET surface areas of 2352 m^2/g for HHU-COF-1 and 1356 m^2/g for HHU-COF-2. The products of a larger-scale synthesis were used to produce mixed matrix membranes (MMMs) with the polymer Matrimid. CO_2/CH_4 permeation tests showed a

moderate increase in CO_2 permeability with constant selectivity for HHU-COF-1 as the dispersed phase, while the application of the fluorinated COF led to an increase in CO_2/CH_4 selectivity from 42 for the pure Matrimid membrane to 51 for 8 wt% HHU-COF-2 and an increase in permeability from 6.8 to 13.0 Barrer for the 24 wt% MMM.

Own contribution to the publication:

- Performing XPS measurements
- Evaluation and interpretation of the XPS spectra with CasaXPS software
- Preparing graphs and literature research for the related XPS part in the manuscript
- Reviewing and correcting the final manuscript as a co-author

Synthesis of tin nanoparticles on Ketjen Black in ionic liquid and water for the hydrogen evolution reaction.

Lars Rademacher, Thi Hai Yen Beglau, Özgür Karakas, Alex Spieß, Dennis Woschko, Tobias Heinen, Juri Barthel, Christoph Janiak. *Electrochem. Comm.* **2022**, *136*, 107243.

Summary:

This study examined the influence of various ionic liquids (ILs) on the synthesis of composite materials consisting of metallic tin nanoparticles (Sn-NPs) and Ketjen Black (KB) carbon black, as well as the electrocatalytic properties of the produced materials. The imidazolium-based ILs were employed as electrosteric stabilisers for the NPs formed during the reduction of tin(II) chloride with sodium borohydride. The synthesis of finely dispersed tin nanoparticles (Sn-NPs) with a size range of 40–90 nm was achieved, which were embedded in larger KB agglomerates. The use of imidazolium-based ILs resulted in different influences on the chemical and structural properties of the composites compared to Sn/KB produced in HCl/H_2O (Sn/KB_H_2O). In terms of the HER, the comparative sample Sn/KB_H_2O exhibited superior performance, with an overpotential of only 136 mV (Pt/C: 46 mV), in comparison to the composites produced in ILs. Following electrochemical stability tests, the composites synthesized in ILs demonstrated enhanced performance, with decreased overpotentials down to 166 mV. In contrast, Sn/KB_H_2O exhibited a decline in performance, with an overpotential of 184 mV. The results indicated a stronger interaction of the IL residues with the surface of the Sn-NPs and a release of IL-blocked active sites during the stability tests.

Own contribution to the publication:

- Performing SEM and SEM-EDX measurements
- Performing XPS measurements
- Evaluation and interpretation of the XPS spectra with CasaXPS software
- Preparing graphs and literature research for the related XPS part in the manuscript.
- Reviewing and correcting the final manuscript as a co-author.

Microwave-assisted synthesis of iridium oxide and palladium nanoparticles supported on a nitrogen-rich covalent triazine framework as superior electrocatalysts for the hydrogen evolution and oxygen reduction reaction.

Lars Rademacher, Thi Hai Yen Beglau, Tobias Heinen, Juri Barthel, Christoph Janiak. *Frontiers in Chemistry* **2022**, 10.

Summary:

In this work, iridium oxide (IrOx-NPs) and palladium nanoparticles (Pd-NPs) with sizes ranging from 2 to 13 nm were immobilised onto a CTF, based on the 2,6-dicarbonitrilpyridine (DCP) monomer, and tested for their potential application in the HER and ORR. In particular, CTFs serve as promising support materials due to their structural diversity, high porosity, and electrical conductivity. The properties of CTFs are significantly controlled by the chosen monomer and the applied synthesis route. In this work, CTFs were synthesised through an ionothermal process at temperature stages of 600 or 750°C in the presence of zinc chloride, which acted as a catalyst and a pore-forming agent. The deposition of IrOx- or Pd-NPs on the shard-like CTF particles was achieved through a microwave-assisted thermal decomposition reaction in the IL [BMIm][NTf_2] or in propylene carbonate (PC). The synthesis of the CTFs at different temperatures resulted in varying influences on the properties of the CTFs and the resulting composites. The composites exhibited excellent performance towards the HER with low overpotentials ranging from 47 to 325 mV (standard material Pt/C: 46 mV) and towards the ORR with high half-wave potentials between 810 and 872 mV (Pt/C: 884 mV). Notably, the IrOx samples demonstrated high performance in the HER, whereas the Pd samples exhibited superior performance in the ORR. These results highlight the promising properties of M-NP/CTF composites, which may lead to the development of materials with high electrocatalytic activity and stability.

Own contribution to the publication:

- Performing SEM, SEM-EDX, SEM-mapping measurements;
- Performing XPS measurements;
- Evaluation and interpretation of the XPS spectra with CasaXPS software;
- Preparing graphs and literature research for the related XPS part of the manuscript;
- Reviewing and correcting the final manuscript as a co-author.

Scalable synthesis of SWCNT via CH_4/N_2 gas: The effects of purification on photocatalytic properties of CNT/TiO_2 nanocomposite

Sakineh Ghasemzadeh, Hassan Hosseini-Monfared, Massomeh Ghorbanloo, Thi Hai Yen Beglau, Lars Rademacher, Alex Spieß, Dennis Woschko, Christoph Janiak. *J. Environ. Chem. Eng.* **2022**, *10*, 108440.

Summary:

Single-walled carbon nanotubes (SWCNTs) were synthesised using a catalysed CVD method over Mo-Fe-MgO and Mo-Fe-Al_2O_3 catalysts. A systematic investigation on the purification of SWCNTs was carried out using 20 methods, applying different acids, acid concentrations, temperatures and processing times. The method of consecutive HCl treatment, air oxidation and second HCl treatment was successful for the purification of SWCNTs. The purification process was effective in removing catalyst support materials, embedded metal catalysts and carbon materials other than nanotubes from the synthesised SWCNTs. Subsequently, the effects of SWCNTs purification on. the photocatalytic activity of CNTs-based nanocomposites were investigated. A SWCNT/TiO_2 composite with 15 wt% of purified SWCNTs was synthesised, which showed the highest photocatalytic activity in decomposing the dye rhodamine B under optimised conditions. The photocatalytic activity of the composite material of purified SWCNT/TiO_2 was significantly higher than that of non-purified SWCNT/TiO_2 and pure TiO2. Overall, this study elucidated the scalable synthesis of SWCNTs, an effective purification method for CCVD-produced SWCNTs, and the effects of purification on the photocatalytic activity of CNT-based nanocomposites for wastewater treatment.

Own contribution to the publication:

- Performing XPS measurements
- Evaluation and interpretation of the XPS spectra with CasaXPS software
- Preparing graphs and literature research for the related XPS part of the manuscript.
- Reviewing and correcting the final manuscript as a co-author.

A New Family of Layered Metal-Organic Semiconductors: Cu/V-Organophosphonates

Patrik Tholen, Lukas Wagner, Jean G. A. Ruthes, Konrad Siemensmeyer, Thi Hai Yen Beglau, Dominik Muth, Yunus Zorlu, Mustafa Okutan, Jan Christoph Goldschmidt, Christoph Janiak, Volker Presser, Özgür Yavuzçetin, Gündoğ Yücesan. *Small* **2023**, *19* (47), 2304057.

Summary:

In this work, the layered redox-active, antiferromagnetic metal organic semiconductor crystals with the chemical formula [Cu(H_2O)$_2$V(μ-O)(PPA)$_2$], where PPA stands for phenylphosphonate, that we designed and synthesized are described in this paper. The phenyl groups of the phenyl phosphonate linker serve to separate the metal phosphonate layers, as evidenced by the crystal structure of [Cu(H_2O)$_2$V(μ-O)(PPA)$_2$]. The diffuse reflectance spectra Tauc plot

demonstrates an indirect band gap of 2.19 eV for $[Cu(H_2O)_2V(\mu\text{-}O)(PPA)_2]$. The photoluminescence (PL) spectra display a complex landscape of energy levels, with peaks observed at 1.8 and 2.2 eV. The hybrid ionic and electronic conductivity values of $[Cu(H_2O)_2V(\mu\text{-}O)(PPA)_2]$ have been calculated to range between 0.13 and 0.6 S m^{-1}. The short-range antiferromagnetic order between the Cu(II) and V(IV) ions is demonstrated by $[Cu(H_2O)_2V(\mu\text{-}O)(PPA)_2]$ through temperature-dependent magnetisation measurements. Furthermore, $[Cu(H_2O)_2V(\mu\text{-}O)(PPA)_2]$ exhibits photoluminescence, with a photoluminescence quantum yield of 0.02%. The high $[Cu(H_2O)_2V(\mu\text{-}O)(PPA)_2]$ is demonstrated.

Own contribution for the publication:

- Reproduction and optimizing synthesis conditions of Cu/V-Organophosphonates materials.

Iron-containing Nickel Cobalt Sulfides, Selenides and a Sulfoselenide as Active and Stable Electrocatalysts for the Oxygen Evolution Reaction in Alkaline Solution

Soheil Abdpour, Lars Rademacher, Marcus. N. A. Fetzer, Thi Hai Yen Beglau, Christoph Janiak, *Solids* **2023**, 4, 181 - 200.

Summary:

Iron-containing nickel sulfides, selenides and sulfoselenides were synthesised via a simple two-step hydrothermal reaction (temperature ≤ 160 °C) for application as electrocatalysts in the OER in alkaline solution (1 mol L^{-1} KOH). The study showed that iron-containing nickel cobalt sulfides and selenides exhibited better OER performance with lower overpotentials compared to iron-free nickel cobalt sulfides and selenides, highlighting the significant role of iron in improving the OER of nickel cobalt electrocatalysts. In addition, the ferrous nickel-cobalt sulfoselenide $Fe_{0.5}Ni_{1.0}Co_{2.0}(S_{0.57}Se_{0.25}O_{0.18})_4$ exhibited exceptional OER performance with η_{50} = 277 mV, outperforming the benchmark RuO_2 electrode with η_{50} = 299 mV. The superior performance of the sulfoselenide was attributed to its low charge transfer resistance (R_{ct}) of 0.8 Ω at 1.5 V compared to the reversible hydrogen electrode (RHE). In addition, the sulfoselenide showed remarkable stability with only a minimal increase in overpotential (η_{50}) from 277 mV to 279 mV after a 20h chronopotentiometric test.

Own contribution to the publication:

- Performing XPS measurements
- Evaluation and interpretation of the XPS spectra with CasaXPS software.
- Preparing graphs and literature research for the related XPS part of the manuscript.
- Reviewing and correcting the final manuscript as a co-author.

Impregnation of textile cotton material with Cymbopogon citratus-mediated silver nanoparticles and investigations by light, electron and hyperspectral microscopies.

Jean Yves Sikapi Fouda, Agnes Antoinette Ntoumba, Philippe Belle Ebanda Kedi, Thi Hai Yen Beglau, Marcus Fetzer, Till Strothmann, Tchangou Armel Florian, Sone Enone Bertin, Vandi Deli, Emmanuel Jean Teinkela Mbosso, Gustave Leopold Lehman, Emmanuel Albert Mpondo Mpondo, Gisele Etame Loe, Francois Eya'ane Meva and Christoph Janiak. *Journal of Pharmacognosy and Phytochemistry* **2023**, *12* (5), 135–146.

Summary:

The goal of this project is to create an inexpensive, eco-friendly cotton fabric that has been treated with green, synthetic silver nanoparticles derived from the leaves of Cymbopogon citratus. PXRD and UVs were used to analyze the silver nanoparticles. The analytical distinctions between cotton textiles that were impregnated and those that weren't were evaluated using TEM and light. When used with emission spectroscopy to distinguish in situ impregnated cotton material from cotton fabric, hyperspectral microscopy indicates the presence of silver nanoparticles, providing information for material quality monitoring. The in situ impregnated cotton material exhibits the lowest sizes, while the high-density dispersions of silver nanoparticles within the cotton materials are displayed by TEM. The maximum emission of the in situ nanomaterial differs from that of the cotton fabric, and dark field microscopy may be used to see the particles. The cotton textiles' capacity to retain solutions containing nanoparticles and water were ascertained. The results of the experiment indicate that the cotton cloth that was impregnated in situ exhibited exceptional washing resistance.

Own contribution for the publication:

- Performing SEM, SEM-EDX, SEM-mapping measurements
- Reviewing and correcting the final manuscript as a co-author

Anti-inflammation study of cellulose-chitosan biocomposite-based Tetrapleura tetraptera (Taub) dried fruits aqueous extract

Jean Baptiste Hzounda Fokou, Annick Christianne Nsegbe, Beglau Thi Hai Yen, Marcus N. A. Fetzer, Elise Nadia Mbogbe, Maeva Jenna Chameni Nkouankam, Pamela Ngadie Mponge, Marie Tryphene Magaly Ngo Yomkil Baleng, Sylvie Pascale Songue, Chris Rosaire Ninpa Kuissi, Juliette Koube, Bertin Sone Enone, Agnes Antoinette Ntoumba, Francois Eya'ane Meva, Christoph Janiak. *BioNanoScience*, **2024**, S. 1-11

Summary:

In this work, Nanotechnology is making remarkable advances in the medical realm. The discovery of innovative ways for delivering plant components has advantages such as improved bioavailability, solubility, prolonged release, and potential. To the best of our

knowledge, there has been no publication on nanocomposites derived from Tetrapleura tetraptera, despite its several ethnopharmacological applications, including the treatment of inflammatory illnesses. The goal of this work was to create nanocomposites made of chitosan and cellulose that have anti-inflammatory properties. The biocomposites demonstrated an encapsulation effectiveness of 69.4%. UV-Vis revealed a peak at 290 nm, confirming their creation. Infrared spectrophotometry confirmed the presence of a mixed polysaccharide and polyphenol system. There were no indicators of toxicity or fatalities, hence the lethal dosage 50 (LD50) exceeds 2000 mg/kg. The biocomposite displays anti-inflammatory action in vitro with a maximum inhibition of 99.5%, and in vivo with a maximum inhibition of 98.7% at a dosage of 200 mg/kg. The manufactured biocomposites derived from the aqueous extract of Tetrapleura tetraptera fruits show anti-inflammatory activity with satisfactory safety.

Own contribution for the publication:

- Performing SEM, SEM-EDX, SEM-mapping measurements
- Reviewing and correcting the final manuscript as a co-author

Ruthenium nanoparticles on covalent triazine frameworks incorporating thiophene for the electrocatalytic hydrogen evolution reaction.

Lars Rademacher, Thi Hai Yen Beglau, Bahia Ali, Linda Sondermann, Till Strothmann, István Boldog, Juri Barthel, Christoph Janiak, *J. Mater. Chem. A* **2024**, *12* (4), 2093–2109.

Summary:

In this work, The chemical, structural, and electrocatalytic characteristics of different thiophene-based CTFs and composites containing ruthenium nanoparticles (Ru-NPs) were examined. Ruthenium is of special importance due to its superior performance in the hydrogen evolution process (HER) and much cheaper cost when compared to other noble metals. For this objective, CTFs bridged by thiophene (Th-CTF), phenylthiophene (PhTh-CTF), bithiophene (BTh-CTF), or quaterthiophene units (QTh-CTF) were synthesized by ionothermal techniques at 400 or 600°C, and then decorated with Ru-NPs in a microwave process employing PC. CTF-1, which is made up of bridging phenyl units, was employed as a comparison material. The new composites with Ru-NPs ranging from 2 to 9 nm displayed excellent electrocatalytic activity against the HER with low overpotentials, reaching 30 mV in 0.5 mol L^{-1} H_2SO_4 (Pt/C: 9 mV) and 3 mV in 1 mol L^{-1} KOH (Pt/C: 26 mV).

Own contribution to the publication:

- Performing SEM, SEM-EDX, SEM-mapping measurements
- Performing XPS measurements.
- Reviewing and correcting the final manuscript as a co-author.

Bimetallic CPM-37(Ni,Fe) metal–organic framework: enhanced porosity, stability and tunable composition.

Soheil Abdpour, Marcus NA Fetzer, Robert Oestreich, Thi Hai Yen Beglau, István Boldog, Christoph Janiak. *Dalton Transactions* **2024.**

Summary:

In this work, a novel synthesis of mixed metal nickel-iron MOFs, specifically bimetallic CPM-37(Ni,Fe) with varying iron content, was undertaken for the first time as precursors for electrode materials in OER. Notable high BET were exhibited by the bimetallic CPM-37(Ni,Fe) samples, with values of 2039, 1955, and 2378 m^2 $g^{-}1$ for CPM-37(Ni_2Fe), CPM-37(NiFe), and CPM-37(NiFe2), respectively. Conversely, the monometallic counterparts, CPM-37(Ni) and CPM-37(Fe), exhibited markedly lower surface areas, with values of 87 and 368 m^2 g^{-1}, respectively. The mixed-phase nickel and iron hydroxide/oxides derived from bimetallic CPM-37(Ni,Fe) samples during OER exhibited superior performance, with CPM-37(Ni_2Fe) (Ni/Fe ~ 2) emerging as the most promising catalyst. The catalyst exhibited a small overpotential of 290 mV at 50 mA cm^{-2}, along with a low Tafel slope of 39 mV dec^{-1} and good electrochemical performance stability. This was demonstrated by an overpotential increase from 290 to 304 mV over 20 hours of chronopotentiometry. After 20 h of chronopotentiometry, the overpotential was 304 mV at 50 mA cm^{-2}, which outperformed the benchmark RuO_2 electrode, which exhibited an overpotential increase from 300 to 386 mV after 20 h of chronopotentiometry.

Own contribution to the publication:

- Performing XPS measurements
- Supporting evaluation and interpretation of the XPS spectra with CasaXPS software
- Reviewing and correcting the final manuscript as a co-author.

Mechanochemical synthesis and application of mixed-metal copper–ruthenium HKUST-1 metal–organic frameworks in the electrocatalytic oxygen evolution reaction.

Sondermann, L.; Smith, Q.; Strothmann, T.; Vollrath, A.; Beglau, T. H. Y.; Janiak, C. *RSC Mechanochem.* **2024.** doi:10.1039/D4MR00021H.

New electrode materials for hydrogen generation are being studied to make expensive noble-metal components more efficient. Here, different copper–ruthenium combinations of the metal–organic framework HKUST-1 were made through a mechanochemical method. This method allowed for the mixed-metal MOFs to be made in an hour. Characterisation through X-ray diffraction, N_2-adsorption, SEM, TGA and FTIR confirmed the formation of a MOF with the

HKUST-1 topology, but with lower porosity. The MOFs were tested as catalysts for the oxygen evolution reaction (OER) and performed as well as the industry standard ruthenium oxide (RuO_2). An overpotential of 314 mV and a Tafel slope of 55 mV dec^{-1} were achieved, along with a charge-transfer resistance of 13.6 Ω. RCT = 52.8 Ω and FE = 70% (RuO_2 FE = 66%) show that the Cu_{10}Ru-BTC catalyst is effective for the OER. All the catalysts showed good stability in a chronopotentiometric measurement over 12 hours.

Own contribution to the publication:

- Performing XPS measurements
- Supporting evaluation and interpretation of the XPS spectra with CasaXPS software

4. Overall Summary

The OER is considered the bottleneck of electrolytic water-splitting. Thus, there is a need for the development of innovative, low-cost approaches to design active and durable electrocatalysts based on abundant transition metal oxides. Although much effort has been devoted to this goal, most materials reported with high catalytic activity require time and energy-demanding, multi-step synthetic approaches. The most effective strategy would be the one-step preparation of highly active electrocatalysts without any complicated templating and energy-intensive calcination processes.

Herein, an iron-doped nickel-based MOF was prepared with a highly-conductive modified Ketjenblack (mKB) support (denoted as Ni(Fe)-MOF/mKB) by a one-step solvothermal method. The introduction of KB provided the true solution to overcoming the intrinsic drawbacks of pristine MOFs and KB for electrocatalysis, in particular (i) a low electrical conductivity, (ii) a predominant microporosity disturbing a permeability of electrolyte ions into pores and a mass transfer of evolved gases from inner pores to bulk electrolyte, and (iii) a poor wettability. The Ni-MOF/mKB14 composite (14 wt. % of mKB) demonstrated an overpotential of 294 mV at a current density of 10 mA cm^{-2} and Tafel slope of 32 mV dec^{-1}, which is comparable with commercial RuO_2 commonly used as a benchmark material for OER. The Ni(Fe)MOF/mKB14 (0.57 wt.% Fe) had an even lower overpotential of 279 mV at a current density of 10 mA cm^{-2}. The low Tafel slope of 25 mV dec^{-1} as well as a low reaction resistance from electrochemical impedance spectroscopy (EIS) measurement confirm the excellent OER performance of this composite. When the Ni(Fe)MOF/mKB14 electrocatalyst was impregnated into commercial nickel foam (NF), overpotentials of 247 and 291 mV at current densities of 10 and 50 mA cm^{-2}, respectively, were realized with constant applied voltages for 30 h at the current density of 50 mA cm^{-2}. The superior OER performance is associated with the transformation of Ni(Fe)MOF into highly functionalized α/β-$Ni(OH)_2$/β/γ-NiOOH and FeOOH inherited from the MOF structure. The demonstrated MOF/mKB material preparation strategy is applied to develop of high-performance electrode materials for other advanced energy storage systems. The simple synthetic concept is very flexible and can be also extended to various structured materials including different types of MOFs to be applied for water-splitting, artificial photosynthesis, nitrogen fixation, etc., which has great potential for practical commercialization of the process as well.

Herein, we report the hydrothermal synthesis of two new semiconductive metal phosphonate frameworks namely Co_2[1,4-NDPA] and Zn_2[1,4-NDPA], and we have shown that alternating the identity of metal ions in isostructural semiconductive metal phosphonate frameworks can be used to tune band gap and semiconductive properties. Both powdered compounds have absorption onsets at around 500 nm (2.5 eV), derived from photoluminescence optical

Kubelka-Munk spectra data, which is strongly localized at the naphthalene moieties. Furthermore Co2[1,4-NDPA] shows a second onset at 700 nm (1.7 eV) which has to be identified as ligand-field transitions localized at the Co center with its low energetic $4A^2(4F) \rightarrow 4T1(4P)$ ligand field transition of tetrahedrally coordinated d7-Co(II). We have furthermore used the new semiconducting metal phosphonate frameworks as precatalysts for the OER reaction. We have shown that both, Co_2[1,4-NDPA] and Zn_2[1,4-NDPA], are remarkable precatalysts for the OER reaction in water splitting with overpotentials of 374 mV for Co_2[1,4-NDPA] and 408 mV for Zn_2[1,4-NDPA] for a glassy carbon rotating electrode system and 312 mV and 371 mV on NF at a current density 10 mA cm^{-2}. The Tafel slope of 43 mV dec^{-1} in 1 mol L^{-1} KOH at a current density of 10 mA cm^{-2} of the Co_2[1,4-NDPA] precatalyst indicates its superior reaction kinetics compared to the commercial benchmark material RuO_2 or other compound families like metal phosphides and some reported MOFs in the literature. Besides, its good reaction kinetics, electrocatalyst derived from Co_2[1,4-NDPA] also shows remarkably improved activity, compared to RuO_2 on NF for water splitting reaching a current density of 200 mA cm^{-2} at 1.63 V. This work also demonstrated the exceptionally high stability of the derived active species of β-$Co(OH)_2$ and β-CoOOH catalysts by using Co_2[1,4-NDPA] as a precatalyst in 1 mol L^{-1} KOH for 30 h at a constant current density of 50 mA cm^{-2}. Several features may contribute to the excellent OER performance of the Co_2[1,4-NDPA] compared to the concurrently studied RuO_2, β-$Co(OH)_2$ and physically mixed β-$Co(OH)_2$ with the ligand 1,4-NDPA-H4. For example, Co_2[1,4-NDPA] precatalyst might hypothetically generate a more uniform distribution of β-$Co(OH)_2$ and 1,4-NDPA-H_4 ligand on the surface of the glassy carbon electrode creating superior OER activities compared to the concurrently studied catalytically active species. All these results demonstrate that both materials, but especially the Co_2[1,4-NDPA] are potential candidates for industrial applications as precatalysts for OER in water electrolysis.

In summary, a new series of bimetallic MOFs was successfully prepared using a rapid synthesis method within only 12 min. These bimetallic MOFs offer flexibility in adjusting the molar ratio of metal nodes, which are uniformly distributed throughout the frameworks. Furthermore, the pillars within this series of MOFs are customizable. As expected, the introduction of a second metal ion allows for the modification of the intrinsic characteristics of the original MOFs, preserving their initial morphology and pore structure. Notably, the bimetallic NiCoMOF demonstrates superior catalytic activity for the OER. Electrochemical assessments show that the pristine structure of MOFs can affect OER performance during prolonged alkali treatment, impacting the kinetics of transformation from disordered α-$(NiCo)(OH)_2$ to ordered β-$(NiCo)(OH)_2$ under alkaline conditions. Moreover, taking advantage of the MW synthesis method, the NiCoMOFs were in situ grown on the surface of NF. The

OER efficiency can be optimized effectively via tuning the thicknesses of MOFs on NF by employing MW synthesis times. The NiCoMOF/NF within only 25 min of synthesis time show superior OER activity with required overpotentials of 313 and 328 mV to achieve current densities of 50 and 300 mA cm^{-2} and excellent stability after 50 h , which surpasses the state-of-the-art RuO_2 and other MOF-derived catalysts for the OER. These promising results not only prove that the properties of MOFs can be tailored by the incorporation of a second metal into the MOF structure but also present a new strategy for developing promising highly efficient electrocatalysts in practical applications.

5. References

[1] M. S. Faber, S. Jin, *Energy Environ. Sci.* **2014**, *7*, 3519–3542.

[2] C. Tan, X. Cao, X.-J. Wu, Q. He, J. Yang, X. Zhang, J. Chen, W. Zhao, S. Han, G.-H. Nam, M. Sindoro, H. Zhang, *Chem. Rev.* **2017**, *117*, 6225–6331.

[3] REN21. 2024. Renewables 2024 Global Status Report Collection. *https://www.ren21.net/gsr-2024/*

[4] N. S. Lewis, D. G. Nocera, *PNAS* **2006**, *103*, 15729–15735.

[5] S. Agrawal, R. Soni in *Energy*, **2021**, pp. 131–150.

[6] Z. de Souza, B. Venkatesh, *Planning and Operation of Active Distribution Networks;* Springer, **2022**.

[7] M. T. M. Koper, *Nature Chemistry* **2013**, *5*, 255–256.

[8] C. G. Morales-Guio, L.-A. Stern, X. Hu, *Chem. Soc. Rev.* **2014**, *43*, 6555–6569.

9 IEA (2023), Global Hydrogen Review 2023*,* IEA, Paris *https://www.iea.org/reports/global-hydrogen-review-2023,*

[10] N.-T. Suen, S.-F. Hung, Q. Quan, N. Zhang, Y.-J. Xu, H. M. Chen*, Chem. Soc. Rev.* **2017**, *46*, 337–365.

[11] C. Panda, P. W. Menezes and M. Driess, *Angew. Chem., Int. Ed.*, **2018**, 57, 11130–11139.

[12] H. Wendt, G. Imarisio, *J. Appl. Electrochem.* **1988**, *18*, 1–14.

[13] M. M. Najafpour, G. Renger, M. Hołyńska, A. N. Moghaddam, E.-M. Aro, R. Carpentier, H. Nishihara, J. J. Eaton-Rye, J.-R. Shen, S. I. Allakhverdiev, *Chem. Rev.* **2016**, *116*, 2886–2936.

[14] G. Glenk, S. Reichelstein, *Nature Energy* **2019**, *4*, 216–222.

[15] Office of energy efficiency & renewable energy, US. https://www.energy.gov/eere/fuelcells/h2scale (accessed July 2024)

[16] S. Jin, *ACS Energy Letters* **2019**, *4*, 1443–1445.

[17] N.-T. Suen, S.-F. Hung, Q. Quan, N. Zhang, Y.-J. Xu, H. M. Chen, *Chem. Soc. Rev.* **2017**, *46*, 337–365.

[18] M. Koper, B. Roldan, Research needs towards sustainable production of fuels and chemicals, *EnergyX*, **2019**.

[19] M. S. Burke, S. Zou, L. J. Enman, J. E. Kellon, C. A. Gabor, E. Pledger, S. W. Boettcher, *J. Phys. Chem. Lett.* **2015**, *6*, 3737–3742.

[20] F. Lu, M. Zhou, Y. Zhou, X. Zeng, *Small* **2017**, *13*, 1701931.

[21] The Sustainable Development Goals Report 2021, United Nations, https://unstats.un.org/sdgs/report/2021/The-Sustainable-Development- Goals-Report-2021.

[22] Z. W. Seh, J. Kibsgaard, C. F. Dickens, I. B. Chorkendorff, J. K. Nørskov, T. F. Jaramillo, *Science* **2017**, *355*, eaad4998.

[23] K. Zeng, D. Zhang, *PECS***2010**, *36*, 307–326.

[24] Z. Yan, H. Liu, Z. Hao, M. Yu, X. Chen, J. Chen, *Chem Sci,* **2020,***11, 10614–1062*.

[25] I. C. Man, H.-Y. Su, F. Calle-Vallejo, H. A. Hansen, J. I. Martínez, N. G. Inoglu, J. Kitchin, T. F. Jaramillo, J. K. Nørskov, J. Rossmeisl, *ChemCatChem* **2011**, *3*, 1159–1165.

[26] P. W. Menezes, C. Panda, C. Walter, M. Schwarze, M. Driess, *Adv. Funct. Mater.* **2019**, *29*, 1808632.

[27] J. Suntivich, E. E. Perry, H. A. Gasteiger, Y. Shao-Horn, *Electrocatalysis* **2013**, *4*, 49–55.

[28] A. J. Bard, L. R. Faulkner, H. S. White, Electrochemical methods: fundamentals and applications*; John Wiley & Sons*, **2022**.

[29] M. G. Walter, E. L. Warren, J. R. McKone, S. W. Boettcher, Q. Mi, E. A. Santori, N.

[30] J. Wang, Analytical Electrochemistry, 3rd edn, Wiley-VCH, Hoboken, N.J. USA, **2006**.

[31] S. Anantharaj, S. R. Ede, K. Sakthikumar, K. Karthick, S. Mishra, S. Kundu, *ACS Catalysis* **2016**, *6*, 8069–8097.

[32] T. Reier, M. Oezaslan, P. Strasser, *ACS Catal.* **2012**, *2*, 1765–1772.

[33] J. Zhou, L. Zhang, Y.-C. Huang, C.-L. Dong, H.-J. Lin, C.-T. Chen, L. H. Tjeng, Z. Hu, *Nature Communications* **2020**, *11*, 1984.

[34] J. Liang, Y.-Z. Wang, C.-C. Wang, S.-Y. Lu, *J. Mater. Chem.A* **2016**, *4*, 9797–9806.

[35] J. Du, G. Liu, F. Li, Y. Zhu, L. Sun, *Adv. Sci.* **2019**, *6*, 1900117.

[36] S. Hou, R. M. Kluge, R. W. Haid, E. L. Gubanova, S. A. Watzele, A. S. Bandarenka, B. Garlyyev, *Chem. Electro. Chem.* **2021**, *8*, 3433–3456.

[37] Q. Shao, J. Yang, X. Huang, *Chem. Eur. J.* **2018**, *24*, 15143–15155.

[38] N.-T. Suen, S.-F. Hung, Q. Quan, N. Zhang, Y.-J. Xu, H. M. Chen, *Chem. Soc. Rev.* **2017**, *46*, 337–365.

[39] J. T. Mefford, X. Rong, A. M. Abakumov, W. G. Hardin, S. Dai, A. M. Kolpak, K. P. Johnston, K. J. Stevenson, *Nat. Commun.* **2016**, *7*, 11053

[40] H. Liu, X. Li, C. Peng, L. Zhu, Y. Zhang, H. Cheng, J. Cui, Q. Wu, Y. Zhang, Z. Chen, W. Zou, W. Gu, H. Huang, J. Wang, B. Ye, Z. Fu, Y. Lu, *J. Mater. Chem. A* **2020**, *8*, 13150–13159.

[41] N. Zhang, Y. Chai, *Energy Environ. Sci.* **2021**, *14*, 4647–4671.

[42] A.Grimaud, W. T. Hong, Y. Shao-Horn, J. M. Tarascon, *Nat. Mater.* **2016**, *15*, 121–126.

[43] M. Wohlfahrt-Mehrens, J. Heitbaum, *J. Electroanal. Chem. Interfacial Electrochem.* **1987**, *237*, 251–260

[44] Y. Tian, S. Wang, E. Velasco, Y. Yang, L. Cao, L. Zhang, X. Li, Y. Lin, Q. Zhang, L. Chen, *iScience* **2020**, *23*, 100756.

[45] S. Cherevko, T. Reier, A. R. Zeradjanin, Z. Pawolek, P. Strasser, K. J. J. Mayrhofer, *Electrochem. Commun.* **2014**, *48*, 81–85

[46] H. N. Nong, T. Reier, H.-S. Oh, M. Gliech, P. Paciok, T. H. T. Vu, D. Teschner, M. Heggen, V. Petkov, R. Schlogl, T. Jones, P. Strasser, *Nat. Catal.* **2018**, *1*, 841–851.

[47] D. B. Hibbert, C. R. Churchill, *J. Chem. Soc. Faraday Trans.* 1984, *80*, 1965–1975.

[48] F. Song, L. Bai, A. Moysiadou, S. Lee, C. Hu, L. Liardet, X. Hu, *JACS* **2018**, *140*, 7748–7759.

[49] S. Anantharaj, S. Noda, V. R. Jothi, S. Yi, M. Driess, P. W. Menezes, *Angew. Chem. Int. Ed.* **2021**, *60*, 18981–19006.

[50] K. S. Joya, Y. F. Joya, K. Ocakoglu, R. van de Krol, *Angew. Chem. Int. Ed.* **2013**, *52*, 10426–10437.

[51] D. Voiry, M. Chhowalla, Y. Gogotsi, N. A. Kotov, Y. Li, R. M. Penner, R. E. Schaak, P. S. Weiss, *ACS Nano* **2018**, *12*, 9635–9638.

[52] D. Senthil Raja, X.-F. Chuah, S.-Y. Lu, *Adv. Energy Mater.* **2018**, *8*, 1801065.

[53] H. Sun, Z. Yan, F. Liu, W. Xu, F. Cheng, J. Chen, *Adv. Mater.* **2020**, *32*,1806326.

[54] S. Anantharaj, S. Noda, M. Driess, P. W. Menezes, *ACS Energy Letters* **2021**, *6*, 1607–1611.

[55] E. Antolini, *ACS Catalysis* **2014**, *4*, 1426–1440.

[56] D. D. Macdonald, *Electrochimica Acta* **2006**, *51*, 1376–1388.

[57] V. F. Lvovich, Impedance spectroscopy: applications to electrochemical and dielectric phenomena; *John Wiley & Sons*, **2012**.

[58] X. Zhao, P. Pachfule, S. Li, T. Langenhahn, M. Ye, C. Schlesiger, S. Praetz, J. Schmidt, A. Thomas, *JACS* **2019**, *141*, 6623–6630.

[59] U. Divya Madhuri, T. P. Radhakrishnan, *ChemElectroChem* **2019**, *6*, 1984–1989.

[60] S. Anantharaj, S. R. Ede, K. Sakthikumar, K. Karthick, S. Mishra, S. Kundu, *ACS Catalysis* **2016**, *6*, 8069–8097.

[61] S. Wang, A. Lu, C.-J. Zhong, *Nano Converg.* **2021**, *8*, 4.

[62] C. Janiak, J. K. Vieth, *New J. Chem.* **2010**, *34*, 2366–2388.

[63] K. K. Gangu, S. Maddila, S. B. Mukkamala, S. B. Jonnalagadda, *Inorganica Chimica Acta* **2016**, *446*, 61–74.

[64] B. F. Hoskins, R. Robson, *JACS* **1990**, *112*, 1546–1554.

[65] O. M. Yaghi, H. Li, *JACS* **1995**, *117*, 10401–10402.

[66] M. Munakata, T. Kuroda-Sowa, M. Maekawa, A. Hirota, S. Kitagawa, *Inorg. Chem.* **1995**, *34*, 2705–2710.

[67] H. Li, M. Eddaoudi, M. O'Keeffe, O. M. Yaghi, *nature* **1999**, *402*, 276–279.

[68] S. S.-Y. Chui, S. M.-F. Lo, J. P. H. Charmant, A. G. Orpen, I. D. Williams, *Science* **1999**, *283*, 1148–1150.

[69] The Comprehensive Repository of Validated and Curated Small Molecule Organic and Metal-organic Crystal Structures, https://www.ccdc.cam.ac.uk/solutions/software/csd/

[70] J. Zhou, B. Wang, *Chem. Soc. Rev.* **2017**, *46*, 6927–6945.

[71] Y.-S. Bae, R. Q. Snurr, *Angew. Chem. Int. Ed.* **2011**, *50*, 11586–11596.

[72] M.-M. Hu, Z. Zhang, J. D. Atkinson, M. J. Rood, L. Song, Z. Zhang, *J. Chem. Eng.* **2019**, *360*, 89–96.

[73] Y. Yang, N. Burke, S. Ali, S. Huang, S. Lim, Y. Zhu, *RSC Advances* **2017**, *7*, 12629–12638.

[74] A. Rabenau, *Angew. Chem. Int. Ed.* **1985**, *24*, 1026–1040.

[75] S. Gökpinar, T. Diment, C. Janiak, *Dalton Trans.* **2017**,46, 9895-9900.

[76] A. K. Das, R. S. Vemuri, I. Kutnyakov, P. B. McGrail, R. K. Motkuri, *Sci. Rep.* **2016**, 6, 28050.

[77] N. Stock, S. Biswas, Chem. Rev. 2012, 112, 933-969.

[78] M. P. Suh, H. J. Park, T. K. Prasad, D.-W. Lim, *Chem. Rev.* **2012**, *112*, 782-835.

[79] J. A. Mason, M. Veenstra, J. R. Long, *Chem. Sci.* **2014**, *5*, 32-51.

[80] K. Sumida, D. L. Rogow, J. A. Mason, T. M. McDonald, E. D. Bloch, Z. R. Herm, T.-H. Bae, J. R. Long, *Chem. Rev.* **2012**, *112*, 724-781.

[81] A. Nuhnen, D. Dietrich, S. Millan, C. Janiak, *ACS Appl. Mater. Interfaces*, **2018**, *10*, 33589-33600.

[82] P. Horcajada, R. Gref, T. Baati, P. K. Allan, G. Maurin, P. Couvreur, G. Férey, R. E. Morris, C. Serre, *Chem. Rev.* **2012**, *112*, 1232-1268.

[83] L. E. Kreno, K. Leong, O. K. Farha, M. Allendorf, R. P. Van Duyne, J. T. Hupp, *Chem. Rev.* **2012**, *112*, 1105-1125.

[84] M. D. Allendorf, A. Schwartzberg, V. Stavila, A. A. Talin, *Chem. Eur. J.* **2011**, *17*, 11372-11388.

[85] V. Stavila, A. A. Talin, M. D. Allendorf, *Chem. Soc. Rev.* **2014**, *43*, 5994-6010.

[86] Jeremias, F.; Khutia, A.; Henninger, S. K.; Janiak, C. *J. Mater. Chem.* **2012**, *22*, 10148-10151.

[87] J. Y. Lee, O. K. Farha, J. Roberts, K. A. Scheidt, S. B. T. Nguyen, J. T. Hupp, *Chem. Soc. Rev.* **2009**, *38*, 1450-1459.

[88] Q Yang, Q. Xu, S. H. Yu, H. L. Jiang, *Angew. Chem. Int. Ed.*, **2016**, *55*, 3685-3689.

[89] L. Zeng, X. Guo, C. He, C. Duan, *ACS Catal.*, **2016**, *6*, 7935-7947.

[90] A. Mahmood, W. Guo, H. Tabassum, R. Zou, *Adv. Energy Mater*. **2016**, *6*, 1600423-1600449.

[91] S. Dou, X. Li, X. Wang, *ACS Materials Letters* **2020**, *2*, 1251–1267.

[92] B. D. McCarthy, A. M. Beiler, B. A. Johnson, T. Liseev, A. T. Castner, S. Ott, *Coord. Chem. Rev.* **2020**, *406*, 213137.

[93] S. Jin, *How to effectively utilize MOFs for electrocatalysis;* ACS Publications, *4*, **2019**.

[94] D. Li, H.-Q. Xu, L. Jiao, H.-L. Jiang, *EnergyChem* **2019**, *1*, 100005.

[95] J. Liu, S. Hou, W. Li, A. S. Bandarenka, R. A. Fischer, *Chem. Asian J.* **2019**, *14*, 3474–3501.

[96] P.-Q. Liao, J.-Q. Shen, J.-P. Zhang, *Coord. Chem. Rev.* **2018**, *373*, 22–48.

[97] Huo, Y. Wang, L. Yan, Y. Xue, S. Li, M. Hu, Y. Jiang, Q.-G. Zhai, *Nanoscale* **2020**, *12*, 14514–14523.

[98] W. Zheng, L. Y. S. Lee, *ACS Energy Letters* **2021**, *6*, 2838–2843.

[99] Y. Guan, J. Lai, G. Xu, *ChemElectroChem* **2021**, *8*, 2764–2777.

[100] H. B. Aiyappa, J. Thote, D. B. Shinde, R. Banerjee, S. Kurungot, *Chem. Mater.* 2016, *28*, 4375–4379.

[101] J. Jiang, L. Huang, X. Liu, L. Ai, *ACS Appl. Mater. Interfaces* **2017**, *9*, 7193–7201.

[102] D. Xing, Y. Wang, P. Zhou, Y. Liu, Z. Wang, P. Wang, Z. Zheng, H. Cheng, Y. Dai, B. Huang, *Appl. Catal. B* 2020, *278*.

[103] Y. K. Hwang, D.-Y. Hong, J.-S. Chang, S. H. Jhung, Y.-K. Seo, J. Kim, A. Vimont, M. Daturi, C. Serre, G. Férey, *Angew. Chem., Int. Ed.* **2008**, *120*, 4212–4216.

[104] L. Tao, C.-Y. Lin, S. Dou, S. Feng, D. Chen, D. Liu, J. Huo, Z. Xia, S. Wang, *Nano Energy* **2017**, *41*, 417–425.

[105] D. Li, H.-Q. Xu, L. Jiao, H.-L. Jiang, *EnergyChem* **2019**, *1*, 100005.

[106] S. Dou, C.-L. Dong, Z. Hu, Y.-C. Huang, J. Chen, L. Tao, D. Yan, D. Chen, S. Shen, S. Chou, S. Wang, *Adv. Funct. Mater.* **2017**, *27*, 1702546.

[107] F.-L. Li, P. Wang, X. Huang, D. J. Young, H.-F. Wang, P. Braunstein, J.-P. Lang, *Angew. Chem., Int. Ed.* **2019**, *131*, 7125–7130.

[108] W. Cheng, X. Zhao, H. Su, F. Tang, W. Che, H. Zhang, Q. Liu, *Nature Energy* **2019**, *4*, 115–122.

[109] S. Mukherjee, S. Hou, S. A. Watzele, B. Garlyyev, W. Li, A. S. Bandarenka, R. A. Fischer, *ChemElectroChem* **2022**, *9*, e202101476.

[110] Y. Mousazade, M. R. Mohammadi, P. Chernev, R. Bagheri, Z. Song, H. Dau, M. M. Najafpour, *Inorg. Chem.* **2020**, *59*, 15335–15342.

[111] J. Tian, F. Jiang, D. Yuan, L. Zhang, Q. Chen, M. Hong, *Angew. Chem. Int. Ed.* **2020**, *59*, 13101–13108.

[112] M. Liu, L. Kong, X. Wang, J. He, J. Zhang, J. Zhu, X.-H. Bu, *Nano Research* **2021**, *14*, 4680–4688.

[113] Q. Qian, Y. Li, Y. Liu, L. Yu, G. Zhang, *Adv. Mater.* **2019**, *31*, 1901139.

[114] K. Rui, G. Zhao, Y. Chen, Y. Lin, Q. Zhou, J. Chen, J. Zhu, W. Sun, W. Huang, S. X. Dou, *Adv. Funct. Mater.* **2018**, *28*, 1801554.

[115] C. Qu, B. Zhao, Y. Jiao, D. Chen, S. Dai, B. M. deglee, Y. Chen, K. S. Walton, R. Zou, M. Liu, *ACS Energy Lett.* **2017**, *2*, 1263–1269

[116] X. Liu, F. Xia, R. Guo, M. Huang, J. Meng, J. Wu, L. Mai, *Adv. Funct. Mater.* **2021**, *31*, 2101792.

[117] J. Zhou, Y. Dou, X.-Q. Wu, A. Zhou, L. Shu, J.-R. Li, *Small* **2020**, *16*, 1906564.

[118] M. Liu, L. Kong, X. Wang, J. He, X.-H. Bu, *Small* **2019**, *15*, 1903410.

[119] M. Liu, L. Kong, X. Wang, J. He, J. Zhang, J. Zhu, X.-H. Bu, *Nano Res.* **2021**.

[120] A. I. Khan, D. O'Hare, *J. Mater. Chem.* **2002**, *12*, 3191–3198.

[121] S. Zhao, C. Tan, C.-T. He, P. An, F. Xie, S. Jiang, Y. Zhu, K.-H. Wu, B. Zhang, H. Li, J. Zhang, Y. Chen, S. Liu, J. Dong, Z. Tang, *Nat. Energy* **2020**, *5*, 881–890

[122] K. S. Park, Z. Ni, A. P. Cote, J. Y. Choi, R. Huang, F. J. Uribe-Romo, H. K. Chae, M. O'Keeffe, O. M. Yaghi, *Proc. Natl. Acad. Sci. USA* **2006**, *103*, 10186–10191.

[123] W. Zheng, M. Liu, L. Y. S. Lee, *ACS Catalysis* **2020**, *10*, 81–92.

[124] G. Cai, W. Zhang, L. Jiao, S.-H. Yu, H.-L. Jiang, *Chem* **2017**, *2*, 791–802.

[125] C.-P. Wang, H.-Y. Liu, G. Bian, X. Gao, S. Zhao, Y. Kang, J. Zhu, X.-H. Bu, *Small* **2019**, *15*, 1906086.

[126] F. Sun, G. Wang, Y. Ding, C. Wang, B. Yuan, Y. Lin, *Adv. Energy Mater.* **2018**, *8*, 1800584.

[127] T. Qiu, Z. Liang, W. Guo, H. Tabassum, S. Gao, R. Zou, *ACS Energy Letters* **2020**, *5*, 520–532.

[128] Q. Liang, J. Chen, F. Wang, Y. Li, *Coord. Chem. Rev.* **2020**, *424*, 213488.

[129] M. Liu, W. Zheng, S. Ran, S. T. Boles, L. Y. S. Lee, *Adv. Mater. Interfaces* **2018**, *5*, 1800849.

[130] N. K. Chaudhari, H. Jin, B. Kim and K. Lee, *Nanoscale*, **2017**, 9, 12231–12247.

[131] Y.-K. Li, G. Zhang, W.-T. Lu and F.-F. Cao, *Adv. Sci.,* **2020**, 7, 1902034.

[132] J. Xing, K. Guo, Z. Zou, M. Cai, J. Du and C. Xu, *Chem. Commun.*, **2018**, 54, 7046–7049.

[133] D. Senthil Raja, X.-F. Chuah, S.-Y. Lu, *Adv. Energy Mater.* **2018**, *8*, 1801065.

[134] M. H. Hassan, A. B. Soliman, W. A. Elmehelmey, A. A. Abugable, S. G. Karakalos, M. Elbahri, A. Hassanien, M. H. Alkordi, *ChemComm* **2019**, *55*, 31–34.

[135] J. Meng, Y. Zhou, H. Chi, K. Li, J. Wan, Z. Hu, *ChemistrySelect* **2019**, *4*, 8661–8670.

[136] X. Zheng, Y. Cao, D. Liu, M. Cai, J. Ding, X. Liu, J. Wang, W. Hu, C. Zhong, *ACS Applied Materials & Interfaces* **2019**, *11*, 15662–15669.

[137] S. Sohrabi, S. Dehghanpour, M. Ghalkhani, *J. Mater. Sci.* **2018**, *53*, 3624–3639.

[138] H. Peng, X. Yang, Y. Ma, J. Liu, Y. Wang, H. Tan, Y. Li, *CrystEngComm* **2018**, *20*, 5387–5394.

[139] C. Wang, M. Zhou, Y. Ma, H. Tan, Y. Wang, Y. Li, *Chem. Asian J.* **2018**, *13*, 2054–2059.

[140] L. Sondermann, W. Jiang, M. Shviro, A. Spieß, D. Woschko, L. Rademacher, C. Janiak, *Molecules* **2022**, *27*.

[141] S. Öztürk, G. Moon, A. Spieß, E. Budiyanto, S. Roitsch, H. Tüysüz, C. Janiak, *ChemPlusChem* **2021**, *86*, 1106–1115.